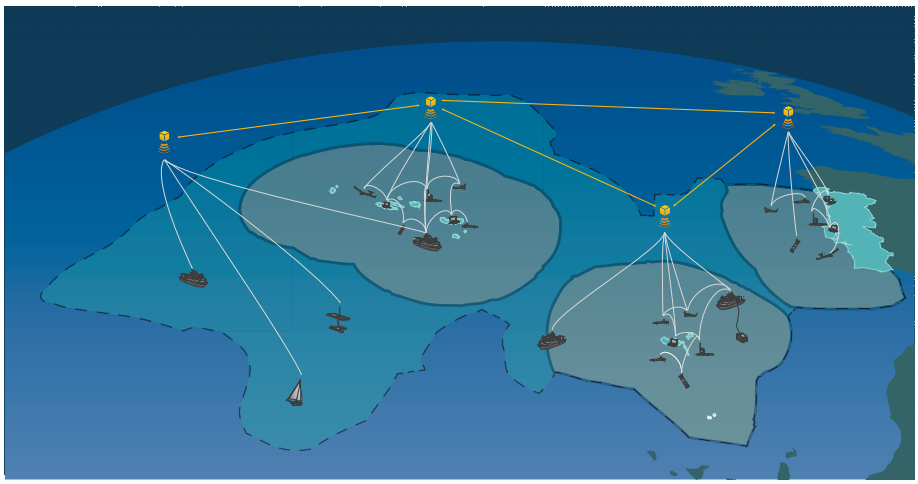


Design, thermal analysis and integration of small satellites with a network of autonomous vehicles

André Gomes da Costa Guerra
Doutoramento em Física
Departamento de Física e Astronomia
2018

Orientador
Orfeu Bertolami Neto, Professor Catedrático, FCUP

André Gomes da Costa Guerra

Design, thermal analysis and integration of small satellites with a network of autonomous vehicles



Supervisor: *Professor Orfeu Bertolami Neto*

Thesis submitted to the Faculty of Sciences of the University of Porto
in partial fulfilment of the requirements for the degree of Doctor in Physics

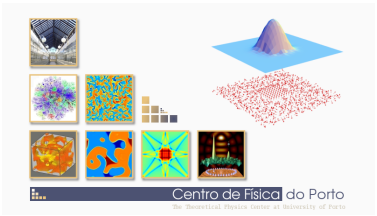
Centro de Física do Porto
Department of Physics and Astronomy
Faculty of Sciences of the University of Porto

2018

© 2018
André Gomes da Costa Guerra
ALL RIGHTS RESERVED

Institutions (where the work was carried out):







Universidade Vigo

Funding:

The work developed for this thesis was supported by the *Fundação para a Ciência e a Tecnologia* (Portuguese Agency for Research) fellowship PD/BD/113536/2015.



To my grandmother,
my parents,
my brother
and Carolina.

Preface

One of the objectives of this work is to make a strong case for the use of small satellites, in particular micro and nano satellites (with mass smaller than 100 kg), and their key role in oceanography. The opportunity arises because these spacecraft are becoming more affordable, with the use of commercial-off-the-shelf technologies, for instance, and also since potential sensors and instruments are rapidly evolving, which makes some candidate ocean observing missions possible in the near future.

Although there have been numerous fields where small satellites have been extensively used, including monitorisation of terrestrial domains, communication and engineering testing, with many missions launched or schedule to be launched, after an extensive survey (published in *A.G.C. Guerra, F. Francisco, J. Villate, F. Aguado Agelet, O. Bertolami, K. Rajan, On small satellites for oceanography: A survey, Acta Astronaut. 127 (2016) doi:10.1016/j.actaastro.2016.06.007*) few platforms were found to really perform ocean observation. However, remote sensing with mini and conventional satellites (with mass greater than 100 kg and 1 000 kg respectively) has been a tool for oceanographers to study large scale dynamic phenomena (*e.g.* gyres and fronts) for many years. Therefore, an effort to understand what are the typical sensors for remote sensing and which ones could be adapted to nano and micro spacecraft was undertook.

Some candidate instruments were identified. Two of the most accessible ones are ocean imagers, *e.g.* to measure ocean colour, and global navigation satellite system receivers, *e.g.* for altimetry. As a complement to these instruments, automatic identification system receivers can be an added asset, opening up surveillance mission opportunities, as has been demonstrated by several missions. Some of the most complicated instruments to adapt to these platforms, but which would bring numerous advantages (scientific, economical and security), are radar-based ones, with a focus on Synthetic Aperture Radar.

A constellation of small satellites, each with identical or complementary sensors and working together with large spacecraft, could provide a comprehensive and continuous view of some sites or even the global oceans, making them an extension of oceanographic study and sensing.

Besides just performing measurements, micro and nano satellites can support *in situ* observations, by working in an integrated fashion with autonomous vehicles. This has been the focus of the paper *A.G.C. Guerra, A.S. Ferreira, M. Costa, D. Nodar-López, F.A. Agelet, Integrating small satellite communication in an autonomous vehicle network: A case for oceanography, Acta Astronaut. (2018). doi:10.1016/j.actaastro.2018.01.022*, where a scenario with these two multifaceted assets, combined in an incremental way, is proposed. This could ultimately alleviate logistical expenses of remote oceanographic operations, by taking advantage of two fundamental characteristics of

small satellites: their higher flexibility and lower cost when compared to conventional spacecraft. To develop this cooperative scenario, a partnership was set up with the *Laboratório de Sistemas e Tecnologia Subaquática* from the University of Porto, devoted to multi vehicle operations, and with the University of Vigo, that developed a satellite communication system.

The first step to create a system of systems was to adapt a software defined radio to the autonomous vehicle network of the *Laboratório de Sistemas e Tecnologia Subaquática*, in particular to their unmanned air vehicle, creating a highly reliable and constantly available communication link. Hardware has been developed for that purpose and, likewise, a function to acquire, process and send data to the satellite has been written for the laboratory software toolchain.

With this test platform, several trials, both in the laboratory and in the field, were prepared. These have been successful, and act as a proving ground for this integrated system. Improvements to the current communication system have also been proposed. When a nano satellite is fully operational the connection could be extended and a truly cooperative network created, with application in sea operations, both *in situ* and for remote sensing.

These spacecraft are also excellent tools for improving the skills of young engineers or for introducing students to the space industry. One of the tools that helps the fast and reliable development of spacecraft is concurrent engineering, already widely used, in particular by the European Space Agency. This method brings together people from different backgrounds for specific spacecraft systems or assignments, to collaboratively design a satellite mission. Challenged by the University of Vigo, a thermal study and design of a few case studies was initiated.

From this collaboration several tasks were performed, both to gather expertise and to propose new approaches. The knowledge gathered is also discussed in this document, together with a practical case for a nano satellite, reflected on the paper *A.G.C. Guerra, D. Nodar-López, R. Tubó-Pardavila, Thermal analysis of the electronics of a CubeSat mission, (2018). arXiv:1803.10468* (submitted to Applied Thermal Engineering). Part of the work performed was either for an European project, and subject to non disclosure agreements, or is being prepared for a patent submission, and cannot be disclosed beforehand.

At the same time, and apart from analysing the internal effects of the spacecraft thermal environment, work on the external effects has also been developed. In particular, in the paper *A.G.C. Guerra, F. Francisco, P.J.S. Gil, O. Bertolami, Estimating the thermally induced acceleration of the New Horizons spacecraft, Phys. Rev. D. 95 (2017) 124027. doi:10.1103/PhysRevD.95.124027*, the thermal induced residual accelerations are estimated for the New Horizons spacecraft, using a combination of a pointlike source method and a Monte Carlo simulation. This has been already applied for the Pioneer and Cassini probes, in fact solving the Pioneer anomaly problem. Besides the accelerations, attitude effects of the thermal radiation emitted are also discussed. The results showed that when reaching Pluto, the thermal emissions produce a residual acceleration of the order of $1 \times 10^{-9}\,\mathrm{m/s^2}$, when the spacecraft is spin stabilised (*i.e.* when no manoeuvres are being made). A rotational effect may also be distinguishable, when communicating with the spacecraft, although for the obtained range this might be somewhat difficult to detect.

This thesis comprises published work corresponding to the following papers:

- A.G.C. Guerra, F. Francisco, J. Villate, F. Aguado Agelet, O. Bertolami, K. Rajan, On small satellites for oceanography: A survey, Acta Astronaut. 127 (2016) 404−423. doi: 10.1016/j.actaastro.2016.06.007.
- A.G.C. Guerra, A.S. Ferreira, M. Costa, D. Nodar-López, F.A. Agelet, Integrating small satellite communication in an autonomous vehicle network: A case for oceanography, Acta Astronaut. (2018). doi: 10.1016/j.actaastro.2018.01.022.
- A.G.C. Guerra, D. Nodar-López, R. Tubó-Pardavila, Thermal analysis of the electronics of a CubeSat mission, (2018). arXiv: 1803.10468 (submitted to Applied Thermal Engineering).
- A.G.C. Guerra, F. Francisco, P.J.S. Gil, O. Bertolami, Estimating the thermally induced acceleration of the New Horizons spacecraft, Phys. Rev. D. 95 (2017) 124027. doi: 10.1103/PhysRevD.95.124027.

During his doctoral work, besides the above mentioned papers, the candidate co-authored the following papers that are unrelated to the work of this thesis:

- C. Bernardo, N.F. Castro, M.C.N. Fiolhais, H. Gonçalves, A.G.C. Guerra, M. Oliveira, A. Onofre, Studying the W_{tb} vertex structure using recent LHC results, Phys. Rev. D. 90 (2014) 113007. doi: 10.1103/PhysRevD.90.113007.
- A.G.C. Guerra, P.S. Carvalho, Orbital motions of astronomical bodies and their Centre of Mass from different reference frames: a conceptual step between the Geocentric and Heliocentric models, Phys. Educ. 51 (2016) 11. doi: 10.1088/0031-9120/51/5/055012.
- A.G.C. Guerra, A.B. García, A.C. Esteban, F. Fabozzi, M. Goli, J. Greif, A.B. Ivanov, L. Jonsson, K. Leschinski, V. Lofstad, M. Martin-Lagarde, J. McClean, M. Reganaz, J. Seibezeder, E. Stoop, G. Van Looveren, J. Wiis, Magrathea: Dust growth experiment in micro-gravity conditions, (2018). arXiv: 1803.10477.

The work developed has been presented at the following conferences/workshops/schools:

- On a small satellite to integrate multiple capabilities for ocean monitoring, in: 1st Doctoral Congress in Engineering, Porto, (2015).
- On a small satellite to integrate multiple capabilities for ocean monitoring, in: MAP-fis Conference 2015, Braga, (2015).
- Ocean Monitoring with Small Satellites, MAP-fis Conference 2016, Aveiro. (2016).
- Ocean Monitoring With Small Satellites, in: 8th European CubeSat Symposium, London. (2016)
- Monitoring the Oceans with Small Satellites, in: Ciência 2017 - Encontro com a Ciência e Tecnologia em Portugal, Lisboa. (2017).
- SmallSats for Oceanography - The Science Pull, Schmidt Ocean Institute visit to Laboratório de Sistemas e Tecnologia Subaquática, Porto. (2017).
- Networking New Capabilities of Unmanned Aircraft and Small Satellites to Improve Maritime Domain Awareness, Marine UAS Summer School, Lisboa. (2017).

Acknowledgements

Over the last few years, during the course of my PhD, I had the privilege of working with several people in many different places. Without them, this thesis would not be possible, and I would like to thank all of them for their support. Even though I cannot mention everyone here, it is important to highlight a few people that somehow influenced the outcome of my work.

Now that I am closing this chapter, I could not go without thanking the person who introduced me to the idea of a PhD and guided me through all of the process, my supervisor, Professor Orfeu Bertolami. With his support and encouragement I was able to work within different areas and learn several new things. Moreover, he has always been available when I needed some advice, either about the work being developed or on future endeavours, and has proven time and time again to stand with my best interests in mind. He has also reviewed all my works, including this thesis, giving much needed inputs and suggestions, making the final texts look better and more professional. All of that hopefully prepared me for what comes next.

I could have not done all of this work alone, and thus I would like to thank my co-authors Paulo Gil, Frederico Francisco, Jaime Villate and Kanna Rajan for their commitment to our work.

Part of this work has been done in the LSTS, and for that I have to thank João Sousa. He has welcomed me there, gave me a place to carry out the work, and sponsored several trips both to show my work and to meet new people. At the LSTS I worked closely with António Sérgio Ferreira and Maria Costa, whom I have to give a special thanks for helping me write several documents, teaching me how to work with Dune/Neptus, and making all the satellite communication protocol a reality. Still, there are several people from LSTS who somehow contributed to my work and all that I learned there, especially Manuel Ribeiro, Paulo Dias, José Pinto, Jorge Neiva, Marina Oliveira and Paulo Lopes. I must thank Catarina Morais for dealing with all the bureaucracy, making my time there and all the travels much smoother.

I also want to thank Fernando Aguado for both his collaboration and for inviting me to work at UVigo and Cinae. There, I had the opportunity to meet Diego Nodar and Ricardo Tubó with whom I collaborated actively in two papers, and the rest of the team that made those works possible, in particular Aarón Nercellas, Franco Pérez and Antón Vázquez.

Although I went to both of those places, I always came back to the institutions that welcomed me first and made the work feasible, both the written one as well as the spoken one, FCUP and the CFP. From those two places I would like to thank Miguel Costa, João Lopes dos Santos, Cláudio Gomes, Niaz Ali Khan, and all of my colleagues. But all of our work would not come through without the support of Maria Armanda Silva, Florbela Martins, Filomena Dara and Armanda Sá.

Although not part of this thesis, I had the pleasure to work in other fields and for that I would like to acknowledge the work I developed with Paulo Simeão de Carvalho, César Bernardo, Nuno Castro, Miguel Fiolhais, Hugo Gonçalves, Miguel Oliveira, António Onofre and with the Green team of Alpbach Summer School 2017 (John McClean, Jonas Greif, Marine Martin-Lagarde, Mattia Reganaz, Esmee Stoop, Fabio Fabozzi, Marta Goli, Lisa Jonsson, Gwenaël Van Loover, Adrián Banos, Adrián Castanón, Anton Ivanov, Kieran Leschinski, Victoria Lofstad, Julia Seibezeder).

Finally, in the last few months I was welcomed by CEiiA and in particular by the team at the Aerospace & Ocean Engineering unit. I have to thank all of them for their support, insights and letting me have the time to write this thesis. Of all of them, a special thanks goes to Paulo Figueiredo, Miguel Machado, Andre João, Raquel Magalhães and Tiago Rebelo.

Sei que o texto já vai longo, mas a vida não é só feita de trabalho. Queria aproveitar para agradecer também àquelas pessoas que me acompanharam durante todo este processo, ainda que seja impossível mencioná-las todas aqui.

Antes de mais tenho que agradecer ao Armando Gonçalves e ao Gaspar Gonçalves que me acolheram da melhor forma em sua casa quando comecei o doutoramento. Não me deram simplesmente um sítio para dormir. Os dois fizeram com que me sentisse em casa e mantivéssemos uma vivência familiar (e até ter o "privilégio" de passear a Noa). No entanto, queria fazer uma referência especial ao Armando, que através da sua boa disposição, à vontade, abertura, amizade e paciência moldou bastante a minha forma de estar e como interajo com os outros. Obrigado Armando!

Apesar de ainda muito ligado ao trabalho, gostaria de fazer uma ressalva a duas Catarinas que me ajudaram durante o meu doutoramento e foram importantes até para o processo de escrita deste documento, a Catarina Dias e a Catarina Cosme.

Quero agora agradecer a uma pessoa que, de apenas conhecida, revelou-se uma grande amiga, claro está a Bárbara Lima. Nestes últimos anos tive a felicidade de conhecê-la verdadeiramente, tendo-se mostrado uma pessoa extraordinária. Por todos os conselhos, conversas, cumplicidades e desabafos, tanto do meu lado como do teu, e ainda mais por te teres dado a conhecer, o meu grande obrigado!

Com a Bárbara veio o João, e não podia deixar de agradecer a sua boa disposição, sentido de humor (ainda que muitas vezes disfarçado) e o companheirismo. Espero que se venha a tornar uma grande amizade, da minha parte já o é.

Como não podia deixar de ser, tenho que dirigir um grande obrigado à minha família que como sempre está lá para me apoiar em todas as fases. Claro está que não podia deixar de mencionar a minha avó Celeste que tem sempre na ponta da língua um conselho, um ditado, ou qualquer coisa que lhe passe no espírito. Se não for para dizer algo, pelo menos partilha uma notícia que leu. Quero também deixar uma nota muito especial para o meu avô. Apesar de já cá não estar fisicamente, está presente em tudo o que faço!

Dadas as vicissitudes da vida, agora devo também agradecer à minha "extensão familiar", em particular ao Carlos, à Sílvia e à Margarida, que me acolheram no seu seio de braços abertos, e deram-me a conhecer uma vida diferente e muito divertida. De cada vez que vou lá passar um tempo, volto com as energias renovadas!

Agradeço agora ao meu pai por todo o seu apoio, incentivo e por simplesmente acreditar em mim. Está sempre a desafiar-me para fazer mais, mesmo quando não diz nada, e espero vir a ganhar tanto quanto ele acha que eu já deveria estar a receber!

À minha mãe por todo o carinho e apoio que me dá, mas também por todas as brincadeiras e por me aturar em todas as minhas aventuras. Mesmo quando as coisas parecem muito negras ou complicadas, está lá para dar uma força ou qualquer outra coisa que necessite. Espero continuar a ser o cientista louco que ela acha que sou. Já o disse quando terminei o mestrado, mas volto a dizer, sem ela a minha vida seria completamente diferente!

Como não podia deixar de ser, e apesar de virem no fim, dedico estas últimas palavras às duas pessoas que por inerência e por escolha minha são muito importantes para mim.

Primeiro para o meu irmão, Diogo Guerra, por uma lista demasiado longa de coisas, mas acima de tudo por estar sempre lá. Aliás, tenho igualmente de agradecer pelo grande esforço que fez para ler toda esta tese, que eu sei que não é coisa fácil. De qualquer forma, tenho que confessar: adoro as nossas tardes a jogar PS4 quando cá vens! E mesmo sabendo que é preciso, custa-me sempre muito quando te vais embora. Não podia pedir melhor irmão, que me acompanha e se deixa acompanhar em tudo! Apesar de não o mostrarmos no dia a dia, mesmo com toda a gente a dizer que o devíamos fazer, espero que ele saiba o quanto gosto dele!

Por último àquela singela rapariga a quem dava boleia ocasionalmente, me pediu amizade e depois o primeiro beijo, e finalmente tornou-se minha namorada e agora noiva, Carolina Augusto! Tu que suportas todas as horas fora de casa, em casa mas a trabalhar, ou simplesmente a descansar. Para além disso aturas todas as minhas manias e os meus nervosismos, sempre com bom humor e uma resposta apaziguadora. Todos os dias trazes algo de novo à minha vida e todos os dias me fazes sorrir, seja por algo que dizes ou algo que fazes. Adoro todas as tuas pequenas peculiaridades, que me conquistaram e me levam todos os dias a gostar mais de ti. Agora és a primeira a lá estar e a última também, e eu espero retribuir todos os dias todo o amor que me dás! Mais não posso ou devo dizer, pois há que guardar algo para o dia 3 de Novembro...

André Gomes da Costa Guerra

Resumo

De acordo com o levantamento efectuado a nível mundial de missões com pequenos satélites, em particular de micro e nano satélites (com massas menores do que $100\,\mathrm{kg}$), verifica-se que estes tiveram um impacto muito reduzido na oceanografia. No entanto, estas plataformas podem ser um elemento essencial num futuro próximo, dado o seu custo reduzido, potencializado por o extenso uso de componentes *off-the-shelf*. Assim, através de uma investigação do tipo de sensores usados actualmente para observação remota, averiguou-se quais seriam passíveis de ser adaptados para estas plataformas. Baseado nesses factores, potenciais missões são sugeridas, incluindo cor do oceano e altimetria. Com a progressiva redução de preço e aumento das capacidades destes sensores, e através da adaptação de sensores desenvolvidos para veículos autónomos, idealiza-se uma constelação de pequenos satélites a observar os oceanos, quase em tempo real com uma cobertura quase global. Isto torná-los-ia uma das ferramentas particularmente útil para os oceanógrafos. Ao mesmo tempo, os pequenos satélites podem ter um papel activo na coordenação de activos terrestres, assegurando que estes estão no local certo no momento certo. De forma a criar-se este sistema integrado de operação, desenvolveu-se uma plataforma de testes para um sistema de comunicação entre veículos autónomos e pequenos satélites, nomeadamente com a adaptação de um rádio programável num veiculo aéreo não tripulado. Vários testes laboratoriais e no terreno foram realizados para verificar o comportamento deste protocolo, o que permitiu identificar alguns pontos em que se poderia melhorar o sistema, e que já estão a ser implementados. Este protocolo de comunicação permitiria também possivelmente diminuir os custos associados à operação dos veículos autónomos, dispensando-os do uso dos dispendiosos sistemas convencionais de comunicação por satélite. Do lado dos satélites, o trabalho foi focado no desenho do subsistema de controlo térmico, baseado numa abordagem de engenharia concorrente. Dadas as pequenas dimensões destas plataformas, e do tamanho e experiência das equipas envolvidas, este subsistema tende a ser menosprezado, o que pode ser crítico quando o satélite é lançado. Diversas análises foram realizadas para um caso de estudo, tendo em conta os modos de operação e as soluções de controlo propostas. Paralelamente, foi efectuado um estudo de como as emissões térmicas de uma sonda podem interferir com a sua trajectória. Para determinar as acelerações residuais, derivadas da emissão de radiação, um método já usado na resolução da anomalia das sondas *Pioneer* foi aplicado à sonda New Horizons. Este método foi estendido para verificar possíveis problemas de atitude. Os resultados evidenciam a existência de uma aceleração residual da ordem de $1 \times 10^{-9}\,\mathrm{m/s^2}$.

Palavras-chave: Micro satélites, Nano satélites, Oceanografia, Sensores, Propostas de missão, Veículos autónomos, Comunicações por satélite, Sistema térmico, Análises térmicas, Sondas interplanetárias, New Horizons, Aceleração induzida.

Abstract

According to a survey of missions performed with small satellites, in particular with micro and nano satellites (with mass less than $100\,\mathrm{kg}$), these have had a small impact in oceanography studies up to now. However, these platforms can be an essential element in a near future, given their reduced cost, and can be leveraged by the extensive use of commercial off-the-shelf components. Thus, through an analysis of current remote sensing instruments, it was assessed which ones could be more easily adapted to these platforms, and potential missions are suggested, including ocean colour and altimetry. With the progressive cost reduction and the increase in sensor capabilities, and through the adaptation of sensors developed for autonomous vehicles, a small satellite constellation to monitor the oceans, in near real time and with an almost global coverage, is envisioned. At the same time, small satellites can have an active role in ground assets coordination, making sure they are at the right spot at the right time. To start building up this integrated operational system, a test platform to implement a communication protocol between autonomous vehicles and small satellites was developed, by adapting a software defined radio on an unmanned air vehicle. Several laboratory and field tests have been performed to verify the protocol behaviour, and some improvements have been suggested, and are already being implemented. This communication protocol will, in principle, allow for reducing operational costs associated with autonomous vehicles, by replacing costly conventional satellite communication systems. On the spacecraft themselves, the work was focussed on the design of the thermal control subsystem, based on a concurrent engineering approach. Due to their small dimensions, and the experience and size of the teams involved, this subsystem tends to be overlooked, which is critical when the satellite is finally launched. Several analyses for a case study were performed, considering both the operational modes and the thermal solutions proposed. In parallel, a study of the impact of thermal radiation emissions on a spacecraft trajectory has been undertaken, in particular for interplanetary orbits. To determine the residual accelerations, caused by the spacecraft thermal emissions, a previously developed method used to solve the Pioneer anomaly was applied on the New Horizons spacecraft. This method has been extended to also determine possible thermal induced attitude variations. The results have shown that there is in fact a residual acceleration of the order of $1 \times 10^{-9}\,\mathrm{m/s^2}$.

Keywords: Micro satellites, Nano satellites, Oceanography, Sensors, Mission proposals, Autonomous vehicles, Satellite communication, Thermal system, Thermal analysis, Interplanetary spacecraft, New Horizons, Induced accelerations.

Contents

Preface vii

Resumo xv

Abstract xvii

List of Figures xxiii

List of Tables xxvii

Nomenclature 1

1 Introduction 1

1.1 Motivation for small satellite oceanography . . . 1

1.1.1 The case for small satellite SAR . . . 2

1.2 Coordinated observation with autonomous platforms . . . 3

1.2.1 Communication network . . . 4

1.2.2 The Portuguese case . . . 6

1.3 Spacecraft design – Thermal analysis and ensued accelerations . . . 7

1.3.1 Thermal radiation implications . . . 8

1.4 Objectives and outline . . . 9

2 Small Satellites 11

2.1 Brief history and classification . . . 11

2.2 Space mission analysis and design . . . 13

2.3 Features and components . . . 15

2.3.1 Structure and mechanisms . . . 17

2.3.2 Propulsion system . . . 18

2.3.3 Attitude Determination & Control System . . . 19

2.3.4 Electric Power System . . . 20

2.3.5 Thermal system . . . 21

2.3.6 Command & Data Handling . . . 21

2.3.7 Communication systems . . . 22

2.4 Small satellites advantages and disadvantages . . . 24

3 Monitoring the Oceans with Small Satellites **27**
3.1 Remote sensing oceanography . . . 27
3.2 Survey of ocean observation missions with small satellites . . . 28
3.2.1 Ocean imaging with small satellites . . . 30
3.2.2 Data relay with small satellites . . . 31
3.2.3 Vessel tracking and AIS equipped small satellites . . . 31
3.2.4 Small satellite constellations . . . 34
3.3 Oceanography main observables and sensors . . . 35
3.3.1 Ocean colour . . . 35
3.3.2 Ocean altimetry . . . 37
3.3.3 Ocean surface winds . . . 40
3.3.4 Sea surface temperature . . . 42
3.3.5 Ocean salinity . . . 43
3.3.6 GNSS Reflectometry . . . 45
3.3.7 The case of (and for) SAR . . . 46

4 An Integrated Operation Scenario **49**
4.1 Mission scenarios . . . 49
4.2 LSTS network system . . . 50
4.2.1 Software toolchain . . . 51
4.2.2 Autonomous vehicle system . . . 53
4.3 Commercial communication systems . . . 54
4.3.1 INMARSAT . . . 55
4.3.2 Iridium . . . 56
4.3.3 Argos . . . 57
4.4 The HumSat system . . . 59
4.4.1 User segment . . . 60
4.4.2 Space segment . . . 61
4.5 System integration and test . . . 62
4.5.1 Software . . . 62
4.5.2 Hardware . . . 63
4.5.3 Tests and results . . . 64

5 Thermal Analysis of Spacecraft and Small Satellites **71**
5.1 The thermal subsystem – Objectives and design . . . 71
5.2 Space thermal environment . . . 73
5.2.1 Radiation energy balance . . . 73
5.2.2 Thermal conductivity and contact conductance . . . 79
5.3 Thermal control technology . . . 82
5.3.1 Passive methods . . . 82
5.3.2 Active methods . . . 85

5.4 Computational analysis methods . . . 85
5.5 A practical case . . . 87
5.5.1 Geometric model . . . 87
5.5.2 Assumptions and simulated cases . . . 90
5.5.3 Results and discussion . . . 93
5.5.4 Analysis summary . . . 98
5.6 Another approach to thermal analysis and induced accelerations . . . 99
5.6.1 Pointlike source method . . . 99
5.6.2 New Horizons model . . . 102
5.6.3 Results and discussion . . . 107

6 Conclusions **113**
6.1 Design and development of small satellite missions . . . 113
6.2 Oceanography and network operations . . . 114
6.3 Thermal design and its effects . . . 116
6.4 Future Work . . . 117
6.4.1 Communication integrated network . . . 117
6.4.2 Thermal analysis . . . 118

References **119**

A SAR Principles **143**

B Modelling the Thermal Effects on the Attitude of the Spacecraft **147**
B.1 Thermal moment relative to the centre of mass . . . 147
B.2 Rotation dynamics induced by thermal effects . . . 147
B.2.1 Three-axis mode case . . . 148
B.2.2 Spin stabilised case . . . 148

List of Figures

1.1 Network of several robotic platforms across several domains for an integrated view of the ocean. . . . 3
1.2 Simplified schematic of a communication architecture between a network of autonomous systems and small satellites. . . . 5
1.3 Boundaries of the proposal for the extension of the Portuguese continental shelf. . . . 6

2.1 Main goals of the 7 472 spacecraft launched from 1957 to 2013. . . . 11
2.2 Schematic of the main spacecraft subsystems, with their respective components. . . . 16
2.3 Computer aided design schematic of the 3U CubeSat structure from Innovative Solutions in Space. . . . 17
2.4 CubeSat propulsion module integrated into a 1U structure. . . . 18
2.5 Set of reaction wheels for a CubeSat. . . . 20
2.6 Computer aided design schematic of a pack of high capacity lithium-ion batteries for CubeSats, including an autonomous heater system, from GomSpace. . . . 21
2.7 Computer aided design schematic of a on-board computer for small satellite missions from GomSpace. . . . 22
2.8 Computer aided design schematics of a communication system from GomSpace. . . . 23

3.1 Ocean colour instrument schematics. . . . 36
3.2 Schematic of the method of operation of an altimetry aboard a spacecraft. . . . 38
3.3 RapidScat scatterometer schematics of operations. . . . 41
3.4 Viewing geometry of the **EnviSat** Advanced Along-Track Scanning Radiometer. . . . 43
3.5 Signal sources interfering with salinity measurements for the **Aquarius** mission. . . . 44
3.6 GNSS-Reflectometry concept. . . . 45
3.7 Synthetic aperture radar principle. . . . 46

4.1 Portuguese operational scenario composed of several assets, including small satellites, showing their communication links. . . . 50
4.2 Visual representation of the LSTS toolchain layers. . . . 52
4.3 X8 Skywalker autonomous aerial vehicle ready for launch (using a catapult). . . . 53
4.4 Global coverage map of the Global Xpress INMARSAT network. . . . 55
4.5 Illustration of Iridium NEXT spacecraft with main dimensions and components. . . . 57
4.6 Elta platform messaging transceivers for the Argos 3 version. . . . 58
4.7 Ground station for the HumSat spacecraft at the University of Vigo. . . . 60

4.8 HumSat automatic and autonomous platforms. 60
4.9 HumSat transmitter board photo, with modules identification. 61
4.10 Xatcobeo satellite photography. 62
4.11 Schematic flow of the SatComms driver task. 63
4.12 Block diagram of the X8 avionics and the HumSat SDR connections. 64
4.13 Workbench test setup with the main components used. 65
4.14 Both networks of the test setup for the communication dry-run scenario. 66
4.15 Block diagram of the communication links for the communication dry-run scenario. . 66
4.16 X8 vehicle equipped with the HumSat SDR and the UHF antenna. 68
4.17 Field trials operational setup. 68

5.1 Flow diagram of thermal analysis design steps. 72
5.2 Schematic of view factor parameters for two elemental surfaces. 76
5.3 Schematic of the angle between surface's normal and planet centre. 76
5.4 Albedo flux (for $a_E = 0.38$) on a surface element in Earth's orbit. 77
5.5 Temperature evolution for a flat plate normal to the Sun at 1 AU as a function of material optical characteristics (*i.e.* absorptivity and emissivity). 78
5.6 Schematic of a detail of a contact between two materials. 80
5.7 Illustration of a filling material applied in a contact interface. 81
5.8 Absorptivity versus emissivity for different surface thermal control coatings. 83
5.9 Typical composition of a multilayer thermal blanket. 84
5.10 Thermal strap different configurations. 84
5.11 Heater made of a flexible metal printed circuit sandwiched between Kapton layers. 85
5.12 Basic model structure, with each component labelled. 87
5.13 Main electric components of the main PCB. 89
5.14 Amplifier, shielding and a zoom of the thermal strap, all on the RF PCB. 90
5.15 Schematic of the options simulated. 92
5.16 Temperature evolution for a full orbital period for all electronic components when the amplifier is off. 93
5.17 Temperature evolution of the main chip for all transient cases, including a zoom of the first 45 minutes. 94
5.18 Temperature evolution for the amplifier, without a thermal strap, during the first 5 minutes, working either with a 5/20 seconds cycle or a 10/20 seconds one. 94
5.19 Comparison of the temperature evolution for the amplifier with and without the thermal strap, working with a 10/20 seconds cycle, for the first 5 minutes. 95
5.20 Maximum temperature evolution of the amplifier with different operational cycles, with and without the thermal strap. 95
5.21 Temperature distribution of the amplifier after a full orbital period (90 minutes). . . . 96
5.22 Thermal strap temperature distribution after 90 minutes. 97
5.23 Temperature distribution of the RF PCB, which supports the amplifier, after 90 minutes. 97
5.24 Temperature distribution of the amplifier shield casing after 90 minutes. 98

5.25 Artistic impression of the New Horizons spacecraft. 102
5.26 Model of the New Horizons used for the analysis, showing the antenna, main body, and RTG. 103
5.27 RTG electrical power output evolution with time. 104
5.28 Schematic of the eight times sixteen Lambertian sources distribution used to represent the RTG thermal emissions. 105
5.29 Schematic of the sixteen Lambertian sources used for the main body top wall. . . . 106
5.30 Thermal acceleration probability distribution, for the time of encounter with Pluto, in the Y direction, overlaid by the derived normal distribution. 109
5.31 Thermal acceleration exponential fit for $20\,\text{years}$ since launch along the spacecraft Y axis, with the 2σ confidence region around it, and with measured data. 109

A.1 Schematic of a side looking imaging radar system aboard a spacecraft, with the most relevant parameters. 143

B.1 Transformation between the inertial reference frame and the spacecraft's reference frame, using the Euler angles and frequencies. 149

List of Tables

2.1 Spacecraft classification according to its mass, cost, and development time. 12
2.2 Summary of the CubeSat standard classes, size and respective mass. 13
2.3 Mission design and development phases of any space programme according to ESA. 14

3.1 Summary of ocean observing small satellites, including mass, power, mission and payload (oceanography related), and launch date. 29
3.2 Characteristics of past, current, and future ocean colour instruments. 37
3.3 Decommissioned, current and future altimeter characteristics and corresponding mission support sensors. 39
3.4 Characteristics of decommissioned instruments and active ones, in mini satellites, to measure ocean surface winds. 41
3.5 Ocean surface temperature instrument characteristics, either decommissioned, currently active or future ones. 43
3.6 Currently active earth observing spacecraft equipped with SAR payloads. 47

4.1 Main characteristics and specifications of the X8 Skywalker vehicle. 54
4.2 Main characteristics of the satellite communication systems described. 59
4.3 Communication Dry-Run validation tests. 67
4.4 Field mission script. 69

5.1 PCBs position and dimensions. 88
5.2 Dimensions and positions of the main and secondary rods. 88
5.3 Electronic packages position and characteristics. 90
5.4 Power consumption of each component for the two main different cases. 92

Nomenclature

This is a list of several symbols and abreviations used within the body of the document. The relevant symbols' values and units are shown on the right margin.

Acronyms/Abbreviations

ADCS	Attitude Determination & Control System.
AIS	Automatic Identification System.
ARM	Advanced RISC Machine
ASV	Autonomous surface vehicles.
AUV	Autonomous underwater vehicles.
C&DH	Command & Data Handling.
CCD	Charge-coupled device.
CEOS	Committee on Earth Observation Satellites.
Comm	Communication.
COTS	Commercial off-the-shelf.
CPU	Central processing unit.
DDR3L SDRAM	Double data rate type three synchronous dynamic random-access memory.
DLR	German Aerospace Center.
DND	Canadian Department of National Defence.
DORIS	Doppler Orbitography and Radiopositioning Integrated by Satellite.
DPC	Deferred Procedure Call.
DTN	Disruptive Tolerant Networking.
DUNE	Unified Navigational Environment.
EMEPC	Estrutura de Missão para a Extensão da Plataforma Continental.
EPO	Expanded PolyOlefin foam.
EPS	Electric Power System.
ESA	European Space Agency.
FCUP	Faculdade de Ciências da Universidade do Porto.
FEM	Finite element method.
FEUP	Faculdade de Engenharia da Universidade do Porto.
FOV	Field of view.
FPGA	Field-programmable gate array.
GEO	Geostationary Earth orbit.
GMSK	Gaussian Minimum Shift Keying modulation.
GNSS	Global Navigation Satellite System.
GNSS-R	Global Navigation Satellite Systems Reflectometry.
GSM	Global System for Mobile Communications.
GSO	Geosynchronous orbit.
HITL	Hardware-in-the-Loop.
IAA	International Academy of Astronautics.
IMC	Inter-Module Communication.
IMO	International Maritime Organisation.
IR	Infrared.
ISR	Intelligence, Surveillance, and Reconnaissance.
ISRO	Indian Space Research Organization.
ISS	International Space Station.

ITU	International Telecommunication Union.
JAXA	Japanese Aerospace Exploration Agency.
LAPAN	Indonesian space agency.
LEO	Low Earth orbit.
LGS	Local ground station.
LIDAR	Light Detection and Ranging.
LP	Lumped-parameter representation.
LRA	Laser Retroreflector Array.
LSTS	Laboratório de Sistemas e Tecnologia Subaquática.
MCC	Mission control centre
MDA	Maritime Domain Awareness.
MEMS	Micro-Electro-Mechanical Systems.
MLI	Multilayer thermal blankets.
NASA	National Aeronautics and Space Administration.
NIR	Near infrared spectrum.
NOAA	National Oceanographic and Atmospheric Administration.
P-POD	Poly Picosatellite Orbital Deployer.
PCB	Printed circuit board.
PGS	Pyrolytic graphite sheet.
PPN	Parameterized post-Newtonian formalism.
R&D	Research and development.
RF	Radio frequency.
RGS	Remote ground station.
RMS	Root mean square.
RTG	Radioisotope Thermoelectric Generators.
SAR	Synthetic Aperture Radar.
SDR	Software defined radio.
SNR	Radar signal-to-noise ratio.
SoC	System on a chip.
SST	Sea suface temperature.
SWIR	Short-Wave Infrared channels.
TS	Thermal strap.
TTL	Transistor−Transistor Logic.
UART	Universal Asynchronous Receiver-Transmitter.
UAV	Unmanned aerial vehicles.
UHF	Ultra-high frequency.
UN	United Nations.
UNOOSA	UN Office for Outer Space Affairs.
UVigo	Universidade de Vigo.
VHF	Very high frequency.
VIS	Visible spectrum.

Electronic Symbols

DIN	Digital receive pin.
DOUT	Digital transmit pin.
GND	Ground power pin.
IOREF	Input/Output reference pin.
RX	Receive.
TX	Transmit.
VIN	Voltage in power pin.

Remote Sensing Greek Symbols

δ_A	Radar azimuth resolution.	
δ_R	Radar range resolution.	
λ	Radar pulse wavelength.	
τ	Radar pulse time length.	
θ	Radar antenna incident angle.	

Remote Sensing Roman Symbols

B	Radar pulse bandwidth.	
c	Speed of light.	$299.8 \times 10^6\,\mathrm{m/s}$

D	Length of the antenna in the spacecraft motion direction.	
d	Length of the antenna perpendicular to the spacecraft motion direction.	
h	Spacecraft orbital altitude.	
R	Distance to the centre of the swath area.	
R_i	Range distance to point i in the swath area.	
S	Swath width.	

Thermal Conductivity Greek Symbols

α	Absorptivity.	
ϵ	Material's emissivity.	
η	Solar array efficiency.	
ρ	Material density.	$\mathrm{kg/m^3}$
σ	Surface roughness.	µm
σ_0	Stefan-Boltzmann's constant.	$5.669 \times 10^{-8}\,\mathrm{W/(m^2\,K^4)}$
θ	Angle between incident radiation and surface normal.	

Thermal Conductivity Roman Symbols

A	Area.	$\mathrm{m^2}$
a_E	Earth's albedo.	36.5%
C	Capacitance.	J/K
c_p	Specific heat.	$\frac{\mathrm{J}}{\mathrm{kg.K}}$
E	Young's module.	Pa
F_v	Nominal preload of a fastener.	N
G	Thermal conductor.	$\frac{\mathrm{W}}{\mathrm{K}}$
G_S	Mean solar flux.	$1\,367\,\mathrm{W/m^2}$
q_{IR}	Earth's infrared radiation flux.	$246\,\mathrm{W/m^2}$
h	Spacecraft orbital altitude.	m
H_c	Microhardness.	Pa
h_c	Contact conductance.	W/K
k	Thermal conductivity.	$\frac{\mathrm{W}}{\mathrm{m.K}}$
m	Asperity slope.	
P	Applied pressure.	Pa
Q	Heat flow.	W
q	Heat flux.	$\mathrm{W/m^2}$
R	Thermal resitance.	K/W
r_E	Earth's radius.	$6\,371 \times 10^3$ m
T	Temperature.	K
t	Thickness.	m
V	Volume.	$\mathrm{m^3}$
Δx	Distance between two points.	m

Thermal Conductivity Subscripts

A	Albedo.
cond	Conduction.
cross	Cross sectional.
d	Dissipated.
E	Earth.
Gen	Generated.
int	Interstitial material.
rad	Radiation.
app	Apparent.
eff	Effective.
surf	Surface.
S	Sun.
s	Effective values.

Pointlike Source Method Symbols

α	Material "shininess" constant.	
$\mathbf{a}$	Thermal radiation acceleration.	$\mathrm{m/s^2}$
A	Area.	$\mathrm{m^2}$
AU	Astronomical units.	149.6×10^9 m
δ	Perturbed/Small component.	
$\dot{\psi}$, $\dot{\nu}$, $\dot{\sigma}$	Euler angles (precession, nutation, and spin).	
$\mathbf{e}$	Unit direction vector.	

E	Poynting vector flux.	$\mathrm{W/m^2}$
f_A	Area fraction.	
$\mathbf{F}_{\mathrm{rad}}$	Thermal radiation force.	N
ΔG	Parabolic antenna gain.	dB
I	Illumination value.	
i	Light source intensity.	
$\mathbf{I}$, A, B, C	Principal moments of inertia of the inertia tensor.	$\mathrm{kg/m^2}$
k	Optical properties.	
$\mathbf{l}_m$	Direction of a light source m.	
$\mathbf{M}$	Thermal moment.	N m
m	Mass.	kg
p_{rad}	Radiation pressure.	$\mathrm{N/m^2}$
$\mathbf{r}$	Position vector to the centre of mass.	m
$\mathbf{r}_m$	Direction of a reflected ray originated from a light source m.	
$\mathbf{S}$	Time-averaged Poynting vector field for a radiation source.	$\mathrm{W/m^2}$
S	Surface.	
θ	Angle variation from boresight.	
t	Time.	years
$\theta_{3\mathrm{dB}}/2$	Antenna half power beamwidth.	
$\mathbf{v}$	Direction of the observer.	
ω	Spacecraft spin rate.	rpm
W	Power.	W
$\dot{\omega}$	Spacecraft spin acceleration.	
$\mathbf{n}$	Surface normal vector.	
$\mathbf{x}$	Position vector.	m

Pointlike Source Method Subscripts

0	Nominal value.
a, d, s	Ambient, diffusive and specular characteristics.
Hyp	Hypothesis.
ilum	Illuminated surface.
Lamb	Lambertian radiation source.
NH	New Horizons.
rad	Radiation.
rd	Reflected diffusive component.
rs	Reflected specular component.
SC	Spacecraft.
X, Y, Z	Cartesian components.

CHAPTER 1

Introduction

This introductory chapter gives the motivations behind the work developed for this thesis. It starts by introducing why small satellite technology could be advantageous to perform remote sensing oceanography. The chapter then follows into a discussion on how and why small satellites can augment autonomous vehicle operations in the ocean, giving the concrete example of Portugal. Additionally, it also presents what was done on small satellite design, in particular the importance of thermal analysis for the satellite subsystems and what are the implications of the thermal emissions of a spacecraft. The chapter concludes with the objectives of the thesis and an outline of the document.

1.1 Motivation for small satellite oceanography

One of the greatest societal problems of the last decades, and for decades to come, is climate change. We are witnessing an unprecedented rate of change, for which there is still no definitive explanation. Thus, it is necessary to pursue global studies of the fundamental components of the Earth's biosphere, so that we understand our planet better. One of those components are the oceans, that account for 70% of the Earth's surface and are the primary sink for greenhouse gases [1]. Moreover, considering that 44% of the world population lives in coastal areas, a number expected to grow 25% by 2050 [2], they are affected by the interactions at the sea-land interface.

Even though ocean science has become critical for climate change studies, many other fields benefit from large temporal and spatial resolution oceanography research. Changes of the ocean's features, including surface height, temperature, salinity, colour, amongst others, have a deep impact on the coastal ecosystem and on the global ecological system [3]. Furthermore, economic, safety and security issues, including pollution episodes (*e.g.* blooms, anoxic zones and anthropogenic events), fishing locations, or even extended ship traffic (either from trade or trafficking), demand a constant and worldwide ocean surveillance.

Currently, one of the prime methods for Earth and ocean observation, providing large amounts of data every day, and credited for giving us a whole new understanding of our planet, is remote sensing spacecraft [3, 4]. Despite the exponential growth in data available today [5], remote sensing has been accessible to oceanographers since the dawn of space exploration, giving them

the opportunity to study dynamic large scale physical phenomena (like gyres and fronts), or other biological and geochemical processes. However, these sensing spacecraft tend to be very complex, taking years to develop, build, and launch, making them so costly that only large governmental or multi-national agencies can afford them, like the European Space Agency (ESA) or the American National Aeronautics and Space Administration (NASA).

However, as it will be discussed in Chapter 2, since the 1970s and 1980s smaller and affordable spacecraft have been developed. In fact, with the use of components which were not originally developed for space, the capabilities of these small satellites have grown at almost the rate at which new technology is released. Furthermore, due to small satellite characteristics, these can take advantage of new smaller form-factor sensors developed for other platforms, *e.g.* terrestrial, aerial and underwater autonomous vehicles. The small satellite market, in particular of the micro and nano classes, has grown 205% from 2016 to 2017, and more than 263 spacecraft are expected to be launched in 2018 [6]. This is especially leveraged by academia needs, which are driving recent developments.

Although possible application fields for these spacecraft have been growing, including communication and engineering developments, after a survey of recent or proposed small satellite missions (presented in Chapter 3), oceanography has not been one of those fields. Therefore, a collection of oceanography sensors, to measure the features mentioned above, and how they could be adapted to fit on small platforms, based on current and expected future knowledge, is also presented in Chapter 3.

1.1.1 The case for small satellite SAR

A particular relevant sensor whose data has numerous applications is the Synthetic Aperture Radar (SAR). The potential for a small satellite equipped with SAR is very large, as it will boost oceanography and climate studies, by providing new ways to monitor these changing environments. At the same time, surveillance operations would benefit from this combination (of a SAR and a small satellite), since it would allow for a greater Maritime Domain Awareness (MDA) over territorial waters of seaward-facing nations. Moreover, SAR would help mitigating pollution events, and even give access to polar regions for search and rescue missions, for example. That is why some focus is given to SAR, both in Chapter 3 and Appendix A.

Nowadays, most spacecraft equipped with SAR have mass ranging from $1\,200\,\mathrm{kg}$ to $2\,300\,\mathrm{kg}$, carrying antennas with about $12\,\mathrm{meters}$ of span. Only recently have technological developments allowed for a plane antenna of $5\,\mathrm{meters}$, or a deployable umbrella shaped one (with less than $0.5\,\mathrm{kg}$), to be used for SAR (the last one on **TecSAR**, a military satellite) [7]. But the sheer size of the sensor is only one of the issues with SAR. For example, the power consumption when it is active, to obtain a reasonable signal-to-noise ratio and a meaningful resolution, is prohibitively high. Even conventional spacecraft only activate the SAR for short orbital periods, over predefined regions. All of these poses significant challenges when moving from large to small satellites.

1.2 Coordinated observation with autonomous platforms

The advent of autonomous vehicles, and their development in quality and quantity due to open-source alternatives to commercial solutions, has proven to have several advantages. Not only are these vehicles now capable of surveying larger and sometimes inaccessible areas, but also faster and at a much smaller cost, supporting in this way traditional assets in their study of some spatio-temporal varying phenomena. Examples of the plethora of operational scenarios where autonomous vehicles are already proving valuable assets include surveillance [8], search and rescue [9], oceanographic and atmospheric studies [10, 11].

The autonomous vehicles evolution has been so accelerated that the current paradigm is the deployment of several heterogeneous vehicles, instead of a single one. Although these multi-vehicle operations are an important step, this brings several new challenges and possibilities, which are now the subject of numerous studies, as is the case for highly mobile ad-hoc networks [12].

An example, and a crucial challenge in oceanography, is the continuous, close to real-time, observation of a water column across all mediums (*i.e.* air and water) and in their interface, instead of single point measurements. Furthermore, besides the scale of the ocean patch that needs to be observed, it is frequently necessary to follow some targeted phenomena (*e.g.* plumes or fronts), over periods that can extend up to months. To achieve this, it has already been proven that a multiple vehicle operation is essential [13–17], together with an excellent coordination (both in time and space), and control across several domains (space, aerial, surface and underwater) is needed. Still, this cannot be achieved without the support of remote sensing data, as illustrated in Figure 1.1.

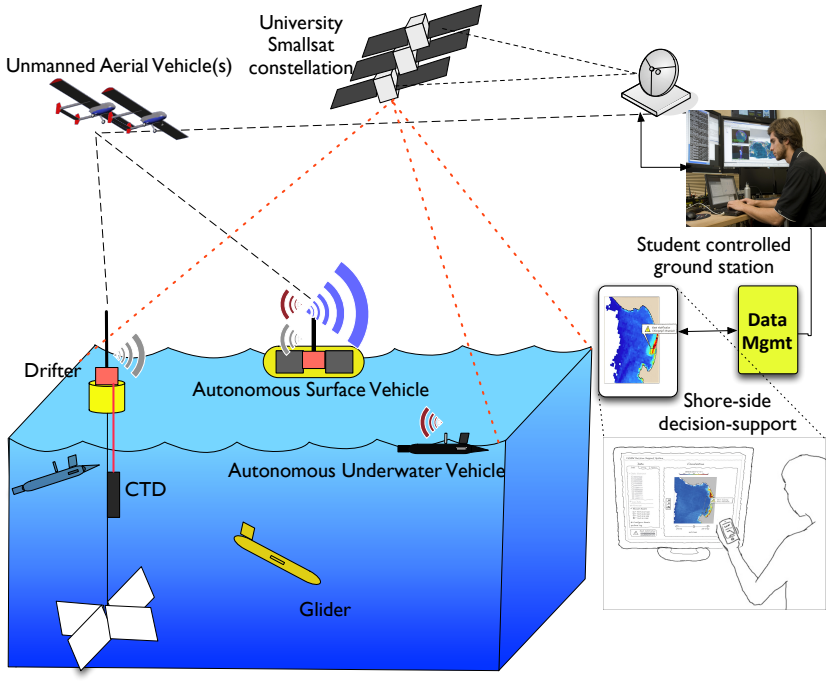


Figure 1.1 – *Network of several robotic platforms across several domains for an integrated view of the ocean.*

Another relevant example, crucial to many governments and organisations worldwide, is to have an effective MDA, namely the protection of critical marine infrastructures and the enforcement of maritime laws, including the deterrence and prevention of illegal activities [18]. This is particularly relevant for Europe considering that, according to the European Commission, 75% of Europe's external trade and 37% of the internal one is seaborne [19]. Overall, the economic activities that depend on the sea, commonly referred by the European Union as the Blue Economy, represents 5.4 million jobs and close to 500 billion Euros gross added value per year [19].

Although there are already several sources of information available to answer these needs, like maritime radars, patrolling vessels, ground based Automatic Identification System (AIS), and other Intelligence, Surveillance, and Reconnaissance (ISR) sensors [20, 21], most maritime infrastructures still do not have a rapid and thorough response to the current necessities [22]. In fact, this surveillance network, using manned vessels to identify unknown targets, is often highly inefficient. New processes, including the combination of AIS, autonomous platforms, and remote observation (mostly SAR imagery), have been suggested as efficient alternatives to this situation. And even though countries like Norway are already starting exercises to test these approaches [23], others with substantial exclusive maritime economic zones, like Japan and Indonesia, are still using traditional methods [23−25].

Small satellites are flexible and versatile enough to be the best tool to integrate with robotic *in situ* assets (including Autonomous Underwater Vehicles, AUVs, Autonomous Surface Vehicles, ASVs, and Unmanned Aerial Vehicles, UAVs), and thus provide coordinated observation, making sure that these assets are "at the right place at the right time" (a topic further developed in Chapter 4). This would yield an unprecedented view of the largest part of the Earth ecosystem. However, some technological and computational developments are still needed to have reliable methods of observation and data collection, using small satellites. Nonetheless, these developments could not only be applied to robotic ground assets, pushing the engineering state of the art, but would also propel ocean science and maritime security and defence.

Besides making a stronger network, combining all these multifaceted vehicles with new hardware and software (including methods of multi-vehicle control), a new observational capacity can be created, by which data gathered can be available in an whole new format. For example, an oceanographer could in principle select whatever scales he or she wishes, from small temporal ones (where Harmful Algal Blooms can be seen), to large spatial scales (so that coherent Lagrangian structure movements are perceived) [26]. Moreover, with new ways to treat data and perform analytics, phenomena trends unknown before can appear. All of this can be achieved in a cost-effective manner.

1.2.1 Communication network

One of the first challenges of large scale, multiple and heterogeneous vehicle coordinated operations is network interoperability, in particular when dealing with multi-hop networks (*i.e.* networks where vehicles can be simultaneously middle and end nodes) [27, 28]. Even if this interoperability

is properly achieved, physical communication limitations as range and bandwidth always exist. Consequently, it is a common practice that each asset has several simultaneous communication channels [29], for increased redundancy, creating a robust communication network, and so the limitation of each channel can be overcome.

When discussing remote or spatially large operations, a channel that cannot be overlooked is the satellite link, since satellite communication systems provide a global and reliable means of transmitting data (or voice). Indeed, satellite communications can empower, or replace, local gateways, making it a paramount component of a robust network, and a vital part of any group working in remote locations.

Although there are already some well known communication systems for maritime applications, most are expensive systems, both to use and to maintain. Therefore, a communication system based on a constellation of small satellites (Figure 1.2), even with the limitations that they have (which restricts the types of data transmitted, for instance), can be tailored to the specificities of the autonomous vehicles and their missions, and be potentially cheaper than other established systems (maintaining still some of their features). Furthermore, these small satellites can be equipped with other sensors, making the spacecraft an active component of the operations (as discussed before).

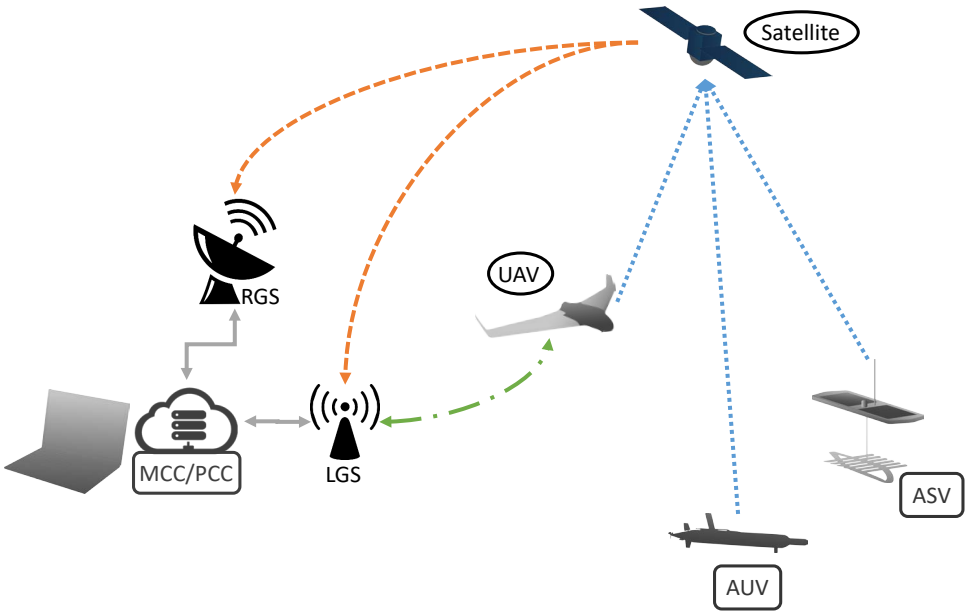


Figure 1.2 – *Simplified schematic of a communication architecture between a network of autonomous systems and small satellites, where the Local Ground Station (LGS), the Remote Ground Station (RGS) and the Mission/Payload Control Centre (MCC/PCC) are identified.*

There is already a system which was created to support small scientific and humanitarian operations, and that can be easily adapted to be part of an already established autonomous vehicle network, the HumSat system [30]. One of the features that the second version of the HumSat system has that makes it a good candidate is two way communication, which allows for both receiving instrument data and to send mission commands to the vehicle.

To have both autonomous vehicles and small satellite communicating, a HumSat Software Defined Radio (SDR) was integrated on an UAV. The advantage of using a SDR, more precisely the HumSat SDR, is the capacity to reconfigure it as needed, creating in practice a system of systems. Thus, if a small satellite is not available, for instance, any other node (vehicle) of the network can act as a storage node, relaying the data gathered when a viable link is available. To test the system developed, several workbench tests were performed, together with field trials.

1.2.2 The Portuguese case

A highly motivating factor to lay the ground for coordinated observations between autonomous vehicles and small satellites is Portugal's claim to the United Nations (UN) for an Extension of its Continental Shelf, prepared by the *Estrutura de Missão para a Extensão da Plataforma Continental* (EMEPC) [i]. With more than 500 years of an ocean exploration legacy, clearly related to its geography, and with the renewal of ocean related activities in the last decade, Portugal put forward a claim for a vast swath of the mid-Atlantic (about four million square kilometres). If the claim is successful, Portugal will have rights and responsibilities over an area extending beyond the Azorean archipelago, represented in Figure 1.3, where it is estimated that about 65% of all maritime traffic to and from Europe will pass.

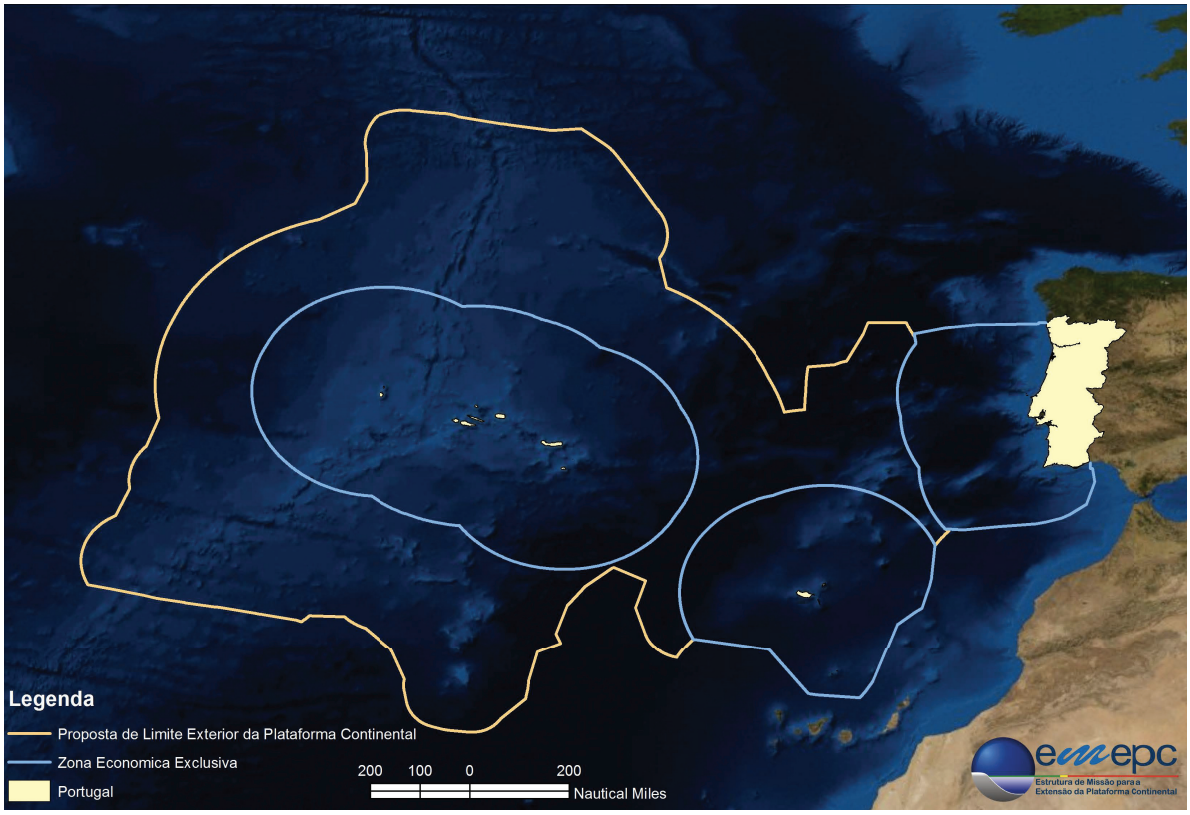


Figure 1.3 – *External bounds of the proposal for the extension of the Portuguese continental shelf (made available by EMEPC [31]).*

[i] More information can be found at `http://www.emepc.pt/` (in Portuguese).

Using traditional methods, both ship and aircraft, to carry out scientific research and surveillance for this area is neither sustainable nor effective. Even with a fleet of autonomous vehicles, it would not be possible to have a clear and comprehensive picture of the processes that take place in this region. Considering that the areas around both the Azores and Madeira archipelagos can be taken as representatives of the world changing climate, and the influence it may have in extreme weather conditions, it is imperative to augment all of these ground assets with an integrated all-weather constellation of remote observation small satellites.

1.3 Spacecraft design – Thermal analysis and ensued accelerations

A full space mission involves many players and goes through several phases to get from a mission statement to its final operations (as discussed in Section 2.2). During these phases all mission components, including the ground, launch and space segment, are either developed or go through a procurement process. Looking at the space segment, *i.e.* the spacecraft itself, it is necessary to design, produce and assemble all the required subsystems that make the spacecraft fulfil the mission requirements.

Among these subsystems, and critical for the success of any space mission, the thermal control system is responsible for making sure that every piece of the spacecraft is within its survival temperature range. This limit represents the temperatures that a component can withstand without any permanent damage, even if not powered, which has to be determined beforehand. Usually most components also have an operational temperature, where they can function without any performance reduction. For example, when working outside their operational temperature, electrical devices, or batteries, have reduced efficiencies and shorter life spans. Increasing temperatures, and temperature gradients, can even deform the spacecraft structure, which can lead to total mission failure.

During the spacecraft design and development it is the job of a thermal engineer to determine if the components selected are all operating within their allowed temperatures. Therefore, thermal analysis has to be performed for every spacecraft iteration, for both the components used and their arrangement inside the spacecraft. These can go from simple thermal balance hand calculations to more computational intensive simulations, as presented in Chapter 5. The spacecraft models created can be as complex as needed, and although the increase in complexity can bring more accurate results there is a penalty in computer solving time.

For small satellite missions, some with mass ranging from $1\,\mathrm{kg}$ to $12\,\mathrm{kg}$, the thermal control system is sometimes not well studied or even ignored. For spacecraft that heavily relies on Commercial Off-The-Shelf (COTS), not only for their high performance and low cost, but also for being lightweight integrated solutions, this might be a gross mistake. These COTS components have been designed to operate in our environment, and taking them to space can have unforeseen implications. Therefore, it is important to study how to maintain their temperature stable, including

de-rating requirements like maximum joint temperature, for example.

To show how temperature control can have an important impact on spacecraft design, a case study of a small satellite carrying a Field-Programmable Gate Array (FPGA) device is posed in Section 5.5.

1.3.1 Thermal radiation implications

Thermal analysis is fundamental to properly sizing any spacecraft, and to make sure it operates, as discussed above. Even more so when studying interplanetary spacecraft, as it may be much closer to the Sun, and thus hotter, or much farther away, and thus colder. Furthermore, the spacecraft thermal environment has also important implications for interplanetary travel, since it has a measurable impact on the trajectory of the spacecraft itself [32−36].

What started this discussion was the so-called Pioneer anomaly, a detectable acceleration of unknown origin, when reported, which remained unsolved for about a decade [37, 38]. After several hypotheses to answer this anomaly were presented, the solution was finally obtained by studying the anisotropic heat radiation emitted by the spacecraft itself, using a pointlike source method (reviewed in Section 5.6).

Most probes for the outer planets use Radioisotope Thermal Generators (RTGs) as the power source, since the solar panel area needed to produce the same amount of energy increases with the square of the distance to the Sun. Examples of these missions include the Jupiter and Saturn visits, by Pioneer 10 and 11 launched in the 1970s, the round through all four gas giants, with Voyager 1 and 2, and the Jupiter and Saturn (and their moons) studies, by Galileo and Cassini spacecraft launched in 1989 and 1997, respectively. Apart from generating a reasonable amount of energy, RTGs also produce a considerable excess of heat, since the thermocouples (*i.e.* the mechanism used to convert heat into energy) are very inefficient. This heat is emitted in the form of radiation producing a very small acceleration, which in turn can have a considerable effect on the spacecraft's trajectory, if nothing is done to correct it.

Although all spacecraft discussed above used RTGs, the anomalous acceleration was only perceived on the Pioneer spacecraft and not on the Voyager ones, a fact justified by the way each mission was designed. While the heavier and more sophisticated Voyagers had active pointing control, the Pioneers were spin stabilised (see Section 2.3.3) and had long periods without any manoeuvre. Thus, it was possible to determine their trajectory with a very high precision.

When Cassini was launched one of the objectives was to perform an experiment to determine the γ parameter[ii], of the Parametrised Post-Newtonian (PPN) formalism, with the best accuracy so far, which was called the Cassini Solar Conjunction experiment [39]. To perform it, a long free fall trajectory period was required. With this experiment a similar anomalous acceleration was detected, later also attributed to a thermal origin [40].

[ii] The γ parameter represents the amount of space curvature produced by one unit of rest mass.

Much more recently, in January 2006, a new spacecraft carrying RTGs and headed to the now demoted dwarf planet Pluto was launched, the New Horizons probe [41]. This was the first ever spacecraft sent to Pluto, which in fact had never been visited before. It took nine and a half years to reach Pluto, with its closest approach in July 2015, and to have the opportunity to perform a series of scientific studies on the planet and on its moon, Charon. Along the trajectory there were several periods of "hibernation", when the spacecraft was in free flight, making it a prime candidate to detect thermal origin accelerations. An initial report has already mentioned an anomalous acceleration for certain periods between February 2008 and May 2013 [42]. Therefore, it was imperative to model the thermal radiation accelerations and compare them to the New Horizons radiometric data. This would give the impact of this acceleration on the trajectory of the New Horizons, which can be used, for instance, on the trajectory computations done for the planned mission extension.

Using the pointlike method, already applied to the Pioneers and Cassini, a range for the thermal accelerations of the New Horizons was obtained, using a model of the spacecraft and its Pluto bound mission. The expected effects are discussed in Section 5.6.3. A new and simplified study of the implications for the attitude of the spacecraft is also briefly discussed.

1.4 Objectives and outline

This thesis had a broad purpose, which is inherited of the two major subjects selected, small satellites and oceanography. Furthermore, the two topics should be dealt using both a scientific/engineering perspective and an economic one, as these cannot be separated. Only a systems engineering approach, combining different disciplines, could tackle the interaction of both subjects, seen by the different perspectives. The first objective of this thesis was thus settled to be:

> *Study the feasibility of using micro and nano satellites (with mass smaller than* $100\,\mathrm{kg}$*) for ocean observations.*

The first stage to fulfil this objective was to understand what are small satellites, their components, and the advantages and disadvantages of such platforms. Moreover, it was also necessary to understand how small satellites are designed and the ensued assumptions taken. This is the topic covered in Chapter 2, and which partially reflects some of the material of Ref. [43].

The second stage was to survey what had been done before on oceanography with small satellites, and is the focus of Chapter 3 (reflecting the rest of the work of Ref. [43]). This not only sets a starting point for future work, but also updates the current knowledge of what is feasible in this rapidly evolving field. At the same time, it was important to determine what instruments are commonly used for remote sensing. Only then would it be possible to assess how they could be adapted to these platforms, and how much research is still needed to accomplish it.

With this survey as a base, the second part of the developed work was twofold.

On the one hand, it was important to look at the small satellites application in maritime operations. This can be translated into a second objective, namely:

> *Set out the basis for a cooperative network between small satellites and autonomous vehicles.*

To fulfil this it was settled that the best approach would be to start by creating a communication link between them. This is not only the most straightforward way to start integrating these two systems (small satellites and autonomous vehicles), but it also has a relevant practical application. In particular, with a small satellite communication channel the operations of the autonomous vehicles can be further extended, but ultimately at a lower cost than with current conventional satellite communication options. Thus, in Chapter 4 operation scenarios are devised and both systems are presented, with a brief comparison to current commercial communication systems. Finally, the test platform developed, to infer the capabilities and limitations of this proposed system of systems, is presented, together with the tests made. This chapter reflects the work developed in Ref. [44].

On the other hand, the design of the platform itself is meaningful to build up national capabilities to answer future challenges (like the extension of the continental shelf). Therefore, a third objective can be transcribed into:

> *Understand how the thermal control system is designed, based on a concurrent engineering approach, and what are its influences.*

The selection of the thermal control subsystem, among all of them, is justified by its importance within the spacecraft and its design. Moreover there is a clear lack of knowledge about the system within nano satellite development teams. Therefore, it was necessary to firstly understand what are the tasks and objectives of the subsystem, and how the design process works. This was followed by a review of two heat transfer mechanisms in space, and a survey of the types of technologies used for small satellites and their limitations. Finally, after learning the type of methods and their setup, all this is materialised with a practical case (developed in Ref. [45]), which also serves to assess the subsystem relevance. All of this is the focus of Chapter 5.

In parallel, the influence of the thermal radiation emitted by a spacecraft was also studied, and is the subject of Section 5.6 and the paper [46]. This had already been successfully done for past missions, using a pointlike methodology. At the time it was proven that those emissions had an impact in the spacecraft trajectory. However, it was time to apply it to a currently flying spacecraft, in particular the New Horizons one, further validating the method. Moreover, it was decided to understand if the emitted radiation would also have implications in the spacecraft attitude, extending the method to compute thermal induced momenta. This can then be applied to future developments, and potentially improve the accuracy of trajectory algorithms (essential for some types of manoeuvres, *e.g.* flyby ones).

CHAPTER 2

Small Satellites

With the motivation and potential usages of small satellites addressed in the previous chapter, the objective of this one is to give an overview of what is in fact a small satellite. The definition of a particular group of small satellites, the CubeSat, is also given, together with a brief discussion on what was the evolution from the first small satellites to the modern ones. Because Chapter 1 also refers to mission design, an overview of what are the necessary steps to successfully design a space mission is given here, with an emphasis on the initial concept design. The discussion is then focused on what are the main spacecraft subsystems and their most important characteristics, in particular for small satellites. Finally, the advantages and disadvantages of these platforms are examined. Most of what is presented here has been published in part in Ref. [43].

2.1 Brief history and classification

Since 1957, when **Sputnik** was launched, more than 7 000 spacecraft have been sent to orbit. While more than half are military and communication satellites, as shown in Figure 2.1, many have scientific and research purposes. This potential has been harvested right from the start, for example, using **Sputnik**'s radio signals to determine electron density on the ionosphere [47, 48].

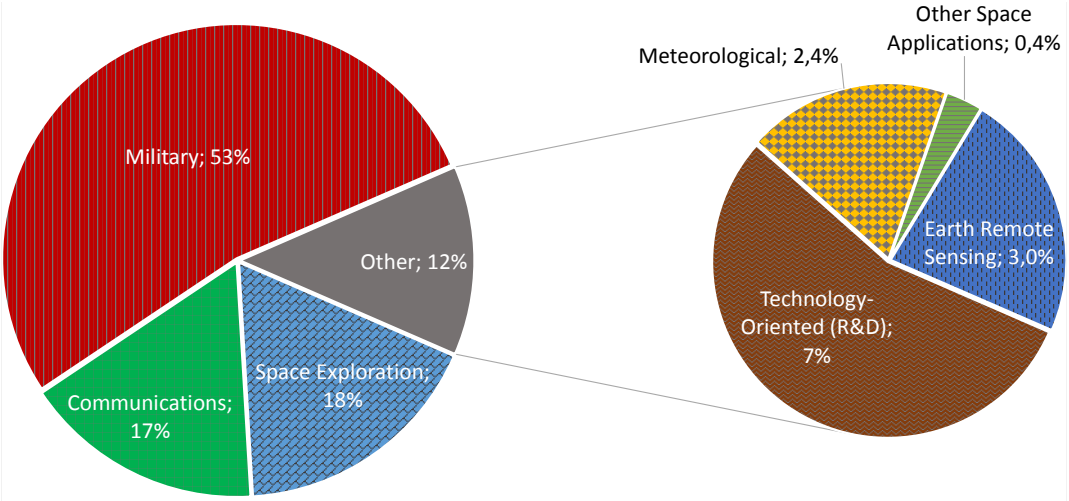


Figure 2.1 – *Main goals of the* 7 472 *spacecraft launched from 1957 to 2013 (data from Ref. [49]).*

Among all of these satellites, several sizes, mass, and types of spacecraft were launched. Hence, in an attempt to create a standard, the International Academy of Astronautics (IAA) defined conventional satellites as those which have a mass higher than 1 000 kg, and small satellites as those which are bellow that limit [50]. Within the small satellites, five classes were also created by the IAA: mini satellites, with mass between 100 kg and 1 000 kg; micro satellites, whose mass ranges from 10 kg to 100 kg; nano satellites, with mass smaller than 10 kg; and pico satellites, with mass smaller than 1 kg [51]. As shown in Table 2.1, there is a correlation between spacecraft mass, the total mission cost and the development time.

Table 2.1 – *Spacecraft classification according to its mass [51], cost [52], and development time [53].*

Satellite Class		Mass [kg]	Cost [M€]	Development Time [years]
Conventional		> 1 000	> 100	> 6
Small Satellites	Mini	100 - 1 000	7 - 100	5 - 6
	Micro	10 - 100	1 - 7	2 - 4
	Nano	1 - 10	0.1 - 1	2 - 3
	Pico	< 1	< 0.1	1 - 2

The cost associated with each class accounts for the launch cost, which is about 20% of the total budget, the spacecraft platform and payloads, making about 70% of the total, and the ground systems at about 10%. While the payload and platform costs reflect not only production, but also mission complexity, development time, and infrastructure [54], the launch cost has a direct dependency on the mass. For example, launching a conventional satellite to Low Earth Orbit (LEO) costs 21 000 €/kg, on average, and 29 000 €/kg for GeoSynchronous Orbits (GSO) [52]. Conversely, small satellites do not usually pay for a full launch, and go as secondary payloads to LEO, in what is called “piggyback”, or ride-share, making the integration with the launcher a relevant parameter for launch cost [55].

Although the first spacecraft were small, modern micro, nano, and pico satellites were made possible especially after the 1970 revolution of very-large-scale integration, which allowed sophisticated functions to be performed by smaller, lighter and less consuming electronic components [52]. This started back in 1961 with the first micro amateur radio satellite, the 10 kg Orbiting Satellite Carrying Amateur Radio (**OSCAR**) 1, and continued to evolve up to the end of the 1970s, with **OSCAR-8** (about 27 kg). However, they were still simple spacecraft, with limited functionalities, and not even equipped with an on-board computer, for example. It was only in 1981 that this panorama change, when the University of Surrey launched the first small satellite with an in-orbit re-programmable computer, the **UoSAT-OSCAR-9** (**UoSAT-1**), which weighted 54 kg.

After the **UoSAT-1** there was a boom in small satellite launches, particularly with an increasing number of universities starting their own satellite programmes. Even though this was an auspicious time for small satellites, with missions coming in increasingly different mass, sizes and power, a lack of knowledge, practice and standards led to a high percentage of spacecraft failures. By the turn of the century, this put in jeopardy the use of these spacecraft, as they were not only

losing credibility, but also becoming a hazard for conventional satellites. Therefore, the Stanford University and the California Polytechnic State University undertook a standardisation effort, and put forward in 1999 the CubeSat standard [56].

A CubeSat is measured in what is called "Units" (U), with a 1U corresponding to the smallest size ($10\,\text{cm} \times 10\,\text{cm} \times 11.35\,\text{cm}$) and mass (bellow $1.33\,\text{kg}$). Other sizes admitted by the standard include 1.5U, 2U, 3U and 3U+, as shown in Table 2.2, although larger ones also exist. One of the keys for the standard success, as a low cost platform, is the very simple standard interface with the launcher adaptor, the Poly Picosatellite Orbital Deployer (P-POD). This launcher adaptor can be integrated in almost any launcher, and is basically a fully closed aluminium box, which has a loaded spring for releasing the CubeSats, and an electrical system to open the pod door. Besides this launcher adaptor, a Printed Circuit Board (PCB) form factor was widely adopted, the PC/104. The hardware for a CubeSat, including all subsystems (as discussed in Section 2.3), can vary between $50\,000\,€$ to $200\,000\,€$ at present time.

Table 2.2 – *Summary of the CubeSat standard classes, size and respective mass (from Ref. [56]).*

Class	Size [cm^3]	Mass [kg]
1U	$10 \times 10 \times 11.35$	< 1.33
1.5U	$10 \times 10 \times 17.02$	< 2
2U	$10 \times 10 \times 22.7$	< 2.66
3U	$10 \times 10 \times 34.05$	< 4
3U+	$10 \times 10 \times 37.65$	< 4

2.2 Space mission analysis and design

Almost all space missions go through the same life cycle, although the nomenclature for the different phases are not the same, and depend on the organisation. According to ESA standards, a space mission runs through all the phases listed in Table 2.3. A mission cannot be launched if it does not fulfil all these milestones. Still, even if technically it respects all requirements, it can be cancelled due to funding cuts.

Several organisations participate in the development of all mission phases. The end users or customers are the ones who actually use the data obtained with the spacecraft and thus set the requirements. The system operators and developers are responsible for building, testing and controlling the spacecraft when in orbit, and are in charge of the ground facilities. Sometimes there are also sponsors, who basically finance the mission and are present in some of the reviews.

Independently of the name used, the first phase of a space programme is focused on developing the initial concept (phase 0/A of Table 2.3). The main elements of the mission are defined in this phase, together with an initial design of the spacecraft. Usually several alternative concepts are proposed and analysed, followed by a selection of a single concept, balancing the customer needs and the engineering feasibility. The selection process also includes schedule, costs, and

Table 2.3 – *Mission design and development phases of any space programme according to ESA [57].*

Phase	Name	Associated milestones
0	Mission Analysis	Mission Definition Review (MDR)
A	Feasibility	Preliminary Requirements Review (PRR)
B	Preliminary Definition	System Requirements Review (SRR) Preliminary Design Review (PDR)
C	Detailed Definition	Critical Design Review (CDR)
D	Production/Qualification	Qualification Review (QR) Acceptance Review (AR) Operational Readiness Review (ORR)
E	Utilization	Flight Readiness Review (FRR) Launch Readiness Review (LRR) Commissioning Result Review (CRR) End of Life Review (ELR)
F	Disposal	Mission Close-out Review (MCR)

policies constraints. All requirements must also be defined, as they drive all the developments and, in fact, all design decisions must be traced back to the original requirements.

Currently, ESA has adopted a concurrent engineering approach to this initial phase, where there is an integrated design process, emphasising the response to user expectations [58]. Within a multidisciplinary environment, with people distributed by different roles, and with an integrated design model and software, decisions are reached by consensus following an established process. Moreover, choices that might have an impact in several parameters, or problems that could invalidate the design, or even different options to fulfil a mission, are identified in a faster way and assessed from an early project phase, saving costs and time [59]. Apart from representatives of the different spacecraft subsystems (discussed in the next section) and instruments, concurrent design sessions are attended by a team leader, a systems engineer, a mission analyst, a ground systems and operations engineer, a programmatic and assembly integration and verification responsible, a technical risk assessment person, a simulation engineer, a configuration responsible, and a technical author[i]. The final customer, that will use the spacecraft or that has commissioned the study, is also present at some of the sessions.

After validating that the mission can fulfil the preliminary requirements, it moves to two design phases. The preliminary one is where the global system parameters and their arrangement are defined (phase B of Table 2.3), whereas the detailed design phase is to completely define all mission components. By the end of this latter phase, classified by ESA as phase C, the design of all the components of the spacecraft must be ready for production or for procurement from approved suppliers. Some hardware and software may have already been tested during this phase.

[i] Role and responsibility of each person can be found on ESA standards (Ref. [60]) or at the web page of ESA concurrent design facility (Ref. [58])

The next step is the actual production and building of the spacecraft equipment, both hardware and software (phase D in Table 2.3). Each component on its own, and then the spacecraft as a whole, goes through a series of qualification tests, including, but not limited to, thermal vacuum and vibration tests. The ground segment, *i.e.* the control and operations centre, any data repository and auxiliary equipment, and the ground stations, are also built or procured.

As soon as all the systems are assembled and verified, the spacecraft waits for its launch opportunity and is ready to enter phase E of Table 2.3. The waiting period differs if the spacecraft is the launcher main payload or if it is sharing the launch. During this period the spacecraft will be carried to the launch site and integrated into the launcher vehicle. This phase ends with the actual launch.

Once in orbit, and released by the launcher, the mission enters the commissioning phase, where all the systems are again tested and validated. Depending on the mission complexity, orbital changes might be performed, and instruments recalibrated. Only when the operation control has certified that the spacecraft is operating in normal conditions, do standard operations and the actual mission begin.

When the spacecraft has fulfilled its initial goals, and sometimes has completed the goals set for mission extensions, it is necessary to dispose of it. This is the last phase of the mission and is defined by ESA as phase F. There are cases, when the spacecraft starts to fail, where this last phase has to be started before the full mission is actually completed. Currently, this is a mandatory procedure for all spacecraft, since according to international regulations any satellite orbiting Earth must be de-orbited up to $25\,\text{years}$ after completing their mission, to minimise space debris around the planet [61].

A small satellite mission must also go through all of these phases, but usually they are faster, as is seen in Table 2.1, and involve less stakeholders. However, team organisation, work process and documentation cannot be underrated, as sometimes is by smaller teams. These are very important when designing a spacecraft, and may represent the difference between a successful or an unsuccessful mission. In fact, concurrent design sessions should also be performed, although for nano satellites these can represent most of the time spent from concept to launch, since the use of COTS makes the detailed design and production phases shorter. This is one of the reasons why there are several educational funding programmes for micro and nano satellite mission projects in the early phases, *e.g.* from ESA Academy [62].

2.3 Features and components

Small satellites share most of the conventional satellite characteristics and systems, although adjusted for the size and power of the platforms. Usually they are divided in two parts, the *payload* and the *bus*. The booster adapter, commonly designed for each one, is sometimes considered a part of the spacecraft [54]. While the payload senses and/or interacts with the object under study, and includes all the mission specific experiments, instrumentation and software, the bus comprises

all essential subsystems for the satellite and payload operation. For missions with similar payloads, a standard adaptable bus design is commonly used, suffering none or minor adjustments between each mission. However, this does not mean that a bus can fit any type of mission. Nevertheless, there are a few subsystems that are always present within any bus, namely:

1. Structure and Mechanisms;
2. Attitude Determination & Control System;
3. Electric Power System;
4. Thermal control system;
5. Command & Data Handling;
6. Communication.

A particular subsystem that is almost always present on conventional spacecraft, but sometimes does not exist on small satellites, is the propulsion subsystem.

A brief description of each of these subsystem is given here, combining information from [52, 54, 63−65], while the payload discussion is left for Section 3.3. When relevant, common limitations of these systems for micro and nano satellites are also discussed, especially since they can restrict the missions to be developed. For visual aid, a schematic of the subsystems addressed here, together with their usual components, is illustrated in Figure 2.2.

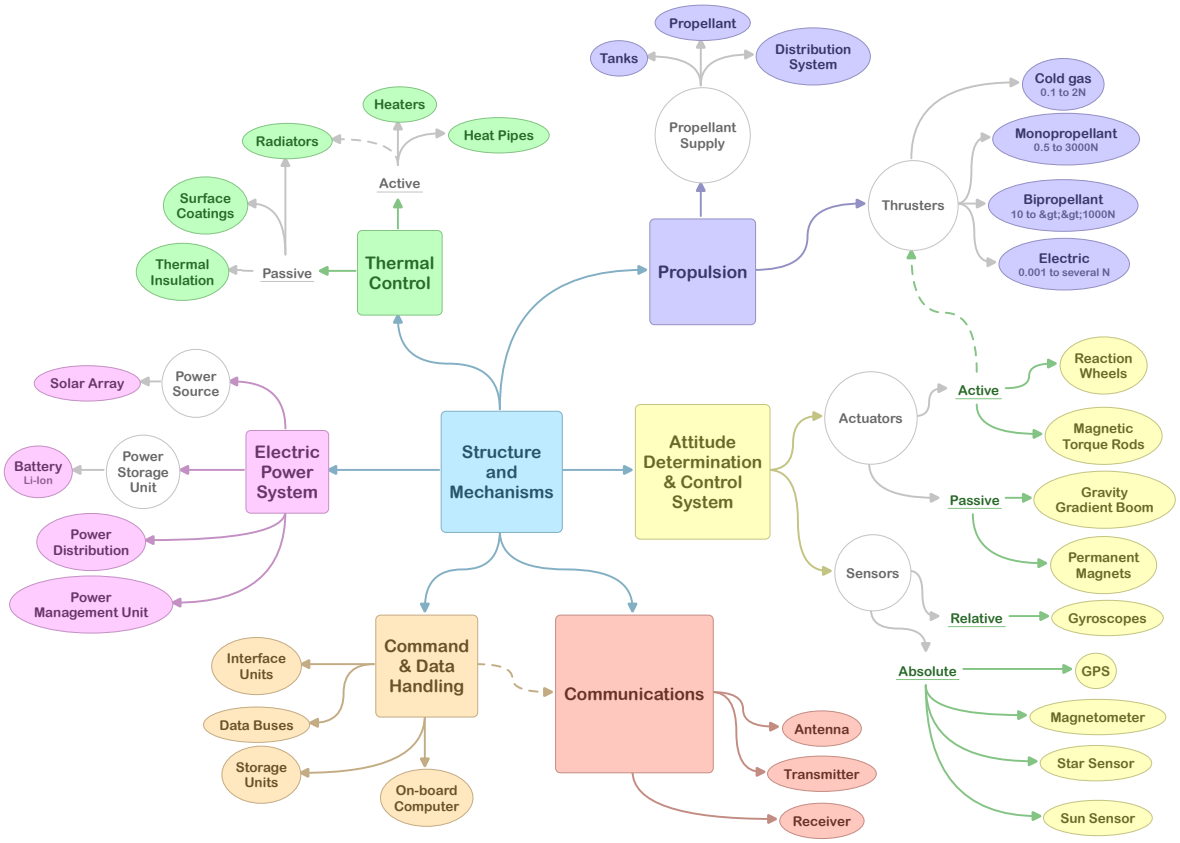


Figure 2.2 – *Schematic of the main spacecraft subsystems (squares), with their respective components (ellipses).*

2.3.1 Structure and mechanisms

The physical skeleton of the spacecraft that houses, supports, and protects all other components is under the responsibility of the structure and mechanisms subsystem. Therefore, the structure design must answer many other systems and payload requirements, as it determines not only the exterior but also the interior configuration. However, there are a few cases where the payloads are the ones adapted to the platform dimension and configuration. This is particularly true for CubeSats, since the standard does not allow for many deviations.

The shape most widely used is a cuboid, especially for 3-axis stabilised spacecraft, although cylinder and other shapes have already been used. Since the mass is always a parameter to be minimised, almost all side panels are usually light with only one being more massive, for making the link with the launch vehicle. All components are either attached to the exterior panels, or to an internal bearing structure. As a rule of thumb, this subsystem represents between 10% and 15% of the total spacecraft dry mass.

CubeSats are built using four main pillars (trusses or stiff rods), that carry all the loads, with face plates (either closed or open) just to separate or protect the inside components from the environment (as depicted in Figure 2.3).

One of the institutions at the forefront of small satellite design is the University of Surrey, which machines each subsystem as identical boxes. Those are then stacked and held by tie-rods, forming the main body. The solar panels and all instrumentation are then mounted to this structure.

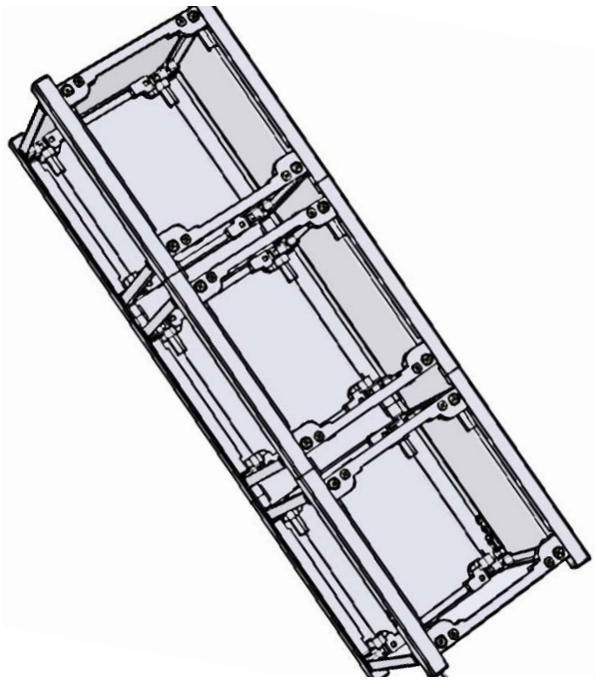


Figure 2.3 – *Computer aided design schematic of the 3U CubeSat structure from Innovative Solutions in Space [66].*

2.3.2 Propulsion system

When a spacecraft is launched it is subjected to several forces that cause its orbit to change. Moreover, sometimes it is not released by the launcher to its final orbit, or has to perform de-orbit manoeuvres at end of its life. Thus, most spacecraft include a propulsion system, which can be used to change or fix their orbit, or also for controlling their attitude. In particular, those in GSO must have thrusters, since those have several station keeping manoeuvres throughout their lifetime.

There are several types of propulsion systems, each using different technologies, classified according to several parameters, including total impulse, thruster characteristics (number, orientation, and thrust levels), total mass, power demand, reliability and lifetime. The most common propulsion systems are cold gas (yielding between $0.1\,\mathrm{N}$ and $2\,\mathrm{N}$), monopropellant systems (capable to provide $0.5\,\mathrm{N}$ to $3\,000\,\mathrm{N}$), and bipropellant ones (supplying from $10\,\mathrm{N}$ to much more than $1\,000\,\mathrm{N}$). In the last few years electric systems (that can only yield up to a few Newtons) have been developed and started to be deployed in several spacecraft. These systems are ordered by performance, even though electric propulsion needs a larger power supply (about $40\,\mathrm{W/kg}$ when using solar panels) than the chemical ones, resulting in an increase of mass.

Although there have been small satellites equipped with propulsion systems, as small as CubeSats, the simplest ones do not have any thrust capabilities. An example of a miniaturised cold gas system has been set up for the $6.5\,\mathrm{kg}$ **SNAP-1** nano spacecraft. A hydrazine propulsion module, shown in Figure 2.4, is also under development for CubeSat constellations deployment [67].

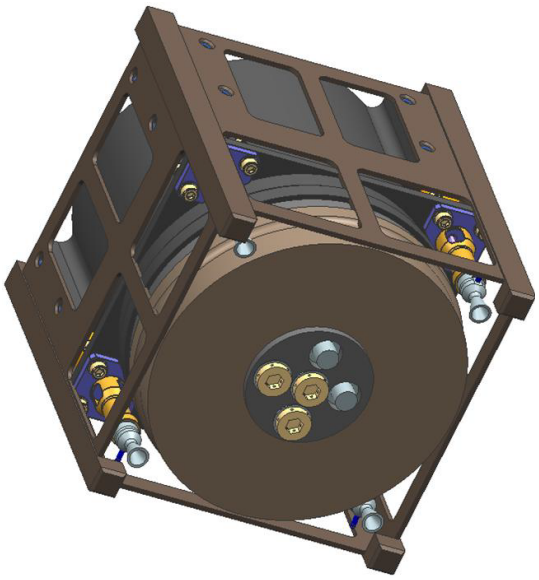


Figure 2.4 – *CubeSat propulsion module integrated into a 1U structure (image from Ref. [67]).*

2.3.3 Attitude Determination & Control System

The Attitude Determination & Control System (ADCS), also called Guidance, Navigation & Control, is responsible for sensing and controlling the angular orientation of the spacecraft (*i.e.* the direction it points to). There are satellites which also use the ADCS to determine the orbit, and even control it when a propulsion system is present. Nonetheless, the characteristics of the subsystem are dictated by the needs of the mission and its payload. Among the main characteristics are the accuracy of the system (*i.e.* the difference between the perceived and the real attitude), the stability (*i.e.* the capacity of the system to keep attitude rates), and the agility (*i.e.* the time the system takes to respond to a change in attitude). As with other systems, the mass, power, and redundancy will also drive the selection of a particular ADCS.

Conversely, there are spacecraft without any ADCS subsystem, *e.g.* the **Sputnik 1**. To solve some problems that arise from a continuously changing attitude, the spacecraft must be designed accordingly, for example, using omnidirectional antennas and solar panels covering all its faces.

To determine the attitude of a spacecraft there are several sensors available, and usually a combination of a few is used. Two of the most common sensors used are Sun sensors (which determine the vector spacecraft/Sun with respect to a body fixed reference frame), and Global Navigation Satellite System (GNSS). Other sensors include magnetometers (which measures the Earth magnetic field and compares it to an internal map), and star trackers (that matches photographs of star fields with internal databases), although the latter ones are more uncommon due to size, power and performance constraints. Sometimes relative sensors, like gyroscopes, are combined with the previous absolute ones.

There are two main ways to perform attitude control, passively or actively. Passive methods can work using actuators like permanent magnets (which align themselves with the Earth field) and gravity gradient booms (which by a mass distribution cause the spacecraft to be pointing to Earth). Another passive approach is putting the spacecraft to spin around an axis and using its gyroscope effect, a process called spin stabilisation. Common to all passive methods is the fact that they do not require any power to operate. However, these are more unstable than active control systems, and tend to oscillate around an axis.

Active control systems are much more stable and agile, and tend to be used on conventional spacecraft, usually more than one for redundancy. Among these there are thrusters (in particular cold gas ones), reaction wheels or control moment gyroscope (which use the conservation of angular momentum to point the spacecraft in a particular direction), and magnetic torque rods (a system similar to permanent magnets and especially used to unload or desaturate, *i.e.* decelerate, reaction wheels).

While micro satellites have mostly used active control systems (*e.g.* reaction wheels and magnetic torque rods), and more than two sensors (*e.g.* GNSS, a magnetometer, a gyroscope and Sun sensors), smaller spacecraft, like CubeSats, tend to prefer passive systems (*e.g.* magnetic ones) and few sensors (mostly magnetometers and Sun sensors). Nevertheless, there are already

reaction wheels available for CubeSats, as the set represented in Figure 2.5.

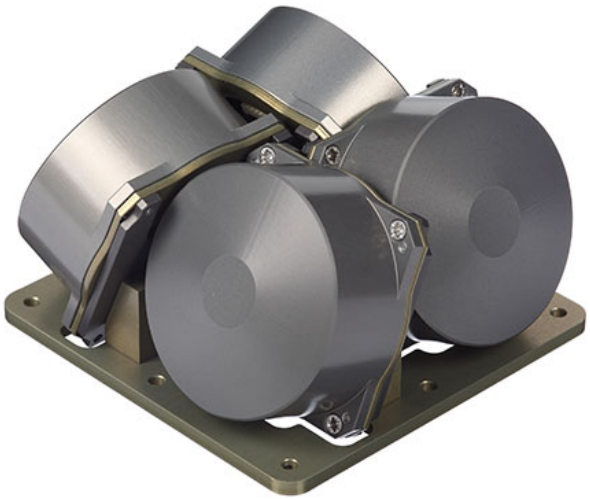


Figure 2.5 – *Set of reaction wheels for a CubeSat (image from Ref. [68]).*

2.3.4 Electric Power System

Another core system of any spacecraft, which has to be totally autonomous and function even under failure conditions, is the Electric Power System (EPS). Responsible for generating and distributing energy to all equipment, the EPS design influences what can be carried by the spacecraft. In turn it must be designed to accommodate both nominal as well as peak power requirements. As the EPS efficiency tends to degrade over time, those requirements shape the end-of-life figures. Apart from all equipment needs, the orbit of the spacecraft does also dictate what type of power system can be used.

The type of EPS depends mostly on the power source used, and although there are a few ones available, *e.g.* Radioisotope Thermoelectric Generators, the most used one is photovoltaic. As mentioned before, simpler spacecraft use body-mounted solar arrays (usually multi junction gallium arsenide, GaAs, or triple junction cells), while conventional spacecraft tend to use deployable rigid arrays.

Another important component of the EPS is the power storage unit, especially with photovoltaic cells, which depend on solar irradiation. Most satellites use rechargeable batteries, *e.g.* lithium-ion (like the ones illustrated in Figure 2.6), nickel-cadmium, and nickel-metal hydride, as storage units. Apart from storing, these units are also designed to respond to peak power needs, commonly higher than what the power source can provide.

The rest of the EPS includes the power distribution equipment, and the power management unit, which is the controller of the system and responsible for conversion, conditioning, and charging and discharging.

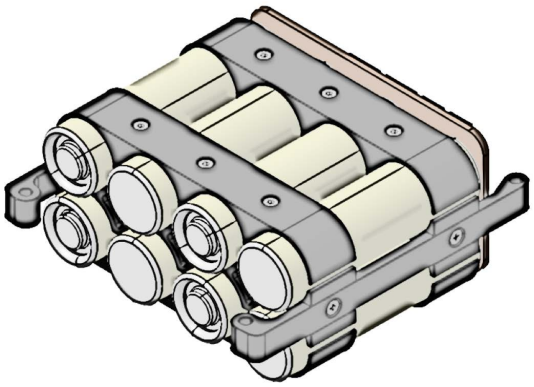


Figure 2.6 – *Computer aided design schematic of a pack of high capacity lithium-ion batteries for CubeSats, including an autonomous heater system, from GomSpace [69].*

2.3.5 Thermal system

A spacecraft in orbit is exposed to a harsh environment, in particular in what concerns the heat received and lost to the surroundings. Although this is not always properly accounted for, most spacecraft have a thermal system to ensure that the temperature inside remains within a predefined range. That range, and thus this system characteristics, are driven by the spacecraft equipment, and their operational and survival temperatures.

There are several methods and components that can be used to achieve a proper heat balance. As before, passive solutions are usually preferred for micro and nano satellites as there are high mass savings, and they do not occupy much space. Nonetheless, active control has been used, in particular joule heating of the battery (like the one used in Figure 2.6), or when the payload includes photodiodes (as their thermal requirements are usually very stringent).

A lengthier discussion on thermal analysis and this system can be found in Chapter 5.

2.3.6 Command & Data Handling

The control of most spacecraft subsystems is performed by the Command & Data Handling (C&DH) system. Besides controlling and distributing the commands received, and performing housekeeping, the C&DH is sometimes responsible for gathering and storing payload data. Usually this means that high processing capabilities are needed for the central processor, together with large storage capacity.

Several characteristics have to be taken into consideration when designing this system, in particular, performance and reliability. As for the thermal subsystem, Space is also harsh for electronic components, and that is why the C&DH equipment should be tolerant to faults, and be able to self-heal (*i.e.* be able to overcome some failures or anomalies), if possible. Power and size of the full C&DH (*i.e.* main processor, data bus and storage units), will also influence the rest of the spacecraft, and thus must be accounted for. Conversely, the communication subsystem used, especially its data rates, has a great impact on the C&DH.

While conventional spacecraft tend to have space graded systems, and usually with high redundancy, micro and nano satellites have to rely on COTS components. Commonly used COTS include FPGAs, ARM and PIC controllers, so to have both high storage and processing capabilities, although at the expense of system durability.

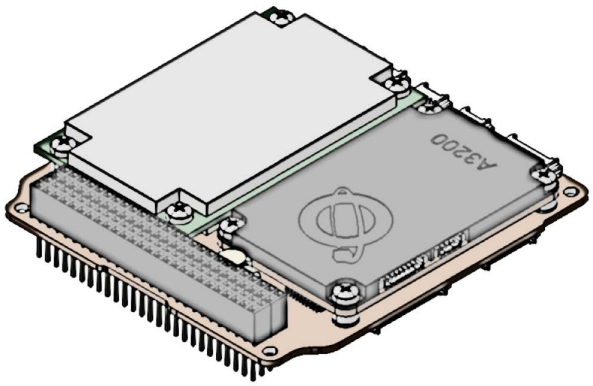


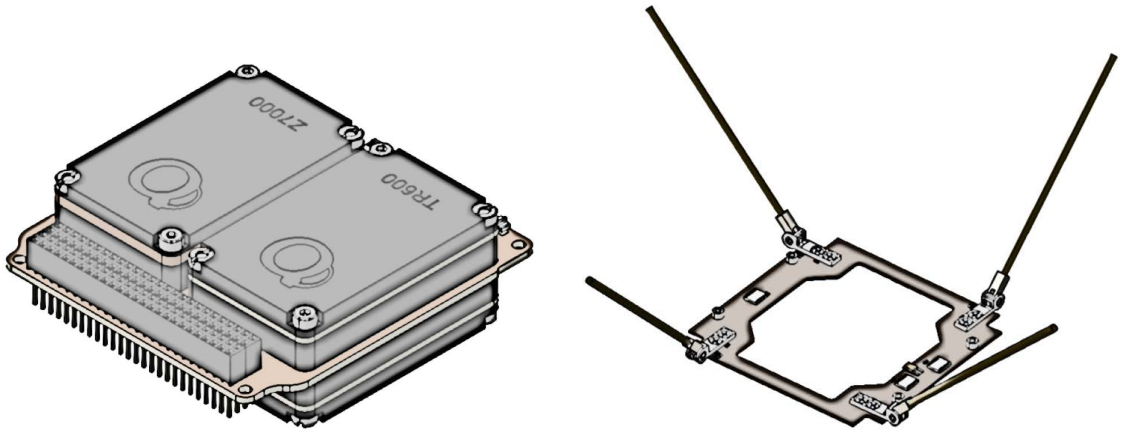
Figure 2.7 – *Computer aided design schematic of a on-board computer for small satellite missions from GomSpace [69].*

2.3.7 Communication systems

Even if all spacecraft systems run properly, a mission would most likely be lost if the spacecraft did not communicate with the ground (or other spacecraft). Thus, a reliable and redundant Communication (Comm) system, or sometimes called Tracking, Telemetry and Command system, is of the utmost importance. System parameters include data rates, radio frequency and modulation, and transmitting power, among others (*e.g.* coding, communication path length and error rate allowance). These must be properly sized to maximise spacecraft downlink and uplink capabilities, as they will limit the outcome of a mission. As can be expected, the communication bandwidth of a spacecraft is closely related to the transmitting power and to the inverse of the distance to ground antennas.

Although a fundamental part of a Comm system is the antenna's size and type (*i.e.* directional, hemispheric, or omnidirectional), the receiver and the transmitter also play an important role, in particular for software defined radios. Nowadays there are several COTS available for these components, each with its own characteristics.

Conventional spacecraft tend to use bands which allow very high data rates, as is the case for C, X and Ku bands. Micro and nano satellites have limited power and size, which makes the S-band the most common one, with data rates of about 1 Mbps. Nevertheless, there are some spacecraft using those higher data rate bands, for example, the **RISESat** with its 2.5 Mbps X-band, and the very high **QSat-EOS** 30 Mbps Ku-band Comm system (see Section 3.2 for more details on these spacecraft). Conversely, about 75% of CubeSats use a UHF (Ultra-High Frequency) communication band, and 10% VHF (Very High Frequency), with a typical data rate of 9.6 kbps (even though higher ones can be achieved with more power, *e.g.* the **VesselSat** 512 kbps UHF system). The remaining 15% CubeSats are using S-band frequencies, with data rates of 256 kbps.



(a) *Transceiver* **(b)** *Antennas*

Figure 2.8 – *Computer aided design schematics of a communication system from GomSpace [69].*

2.3.7.1 Regulating small satellite communication

Besides the reasons stated above, the Comm system is also very important since it is one of the systems with most impact on the spacecraft surroundings. If any another system is wrongly configured or programmed, its greatest impact would be on the spacecraft itself, whereas a badly configured Comm system might have a severe impact on other important communication systems (either space-borne or ground-based). In fact, with growing numbers of CubeSat and small satellite launches, there is an increasing concern with the lack of adherence of these missions to international laws, regulations and procedures. This was already stated in the 2015 Prague declaration on Small Satellite Regulation and Communication Systems [70]. Nevertheless, back in 1971 regulations were made to hold liable any spacecraft that causes a collision during its life time, in the Liability Convention resolution 2777 (XXVI) [71], and many countries made insurance for these cases compulsory.

One aspect that aided the lack of compliance with communication regulations is the complex and time consuming procedure to register the use of a frequency with the responsible United Nations agency, the International Telecommunication Union (ITU). Furthermore, the timing and cost of such a process is not suitable for short and low-cost missions. Therefore, several members of the small satellite community urged the ITU to examine all of its procedures, taking into account the particularities of the small satellite missions.

No studies have provided definite answers to support frequency management for small satellite missions, as there are no relevant spacecraft specific characteristics, since these are rapidly changing [72]. Nonetheless, in an attempt to answer these needs, the UN Office for Outer Space Affairs (UNOOSA) and the ITU compiled and issued a best practice guide, including a summary of laws and regulations that small satellites must obey [73]. It was further recommended, by the Provisional Final Acts of the World Radiocommunciation Conference, that spacecraft with a lifetime

of less than three years should use the 150.05 MHz to 174 MHz and 400.15 MHz to 420 MHz frequency range for telemetry, tracking and command [74].

2.4 Small satellites advantages and disadvantages

Conventional satellite missions are usually very long ones, with a developing phase longer than six years, and very costly, more than 100 M€, as was shown in Table 2.1. This means that many years of investment, project and planning are behind every successful launch. Furthermore, from the moment a particular sensor or technology is selected until the spacecraft is actually launched, a long time will have passed, and newer technologies may exist.

It is in some of these aspects that small satellites excel, in particular micro and nano ones (since mini satellites are still very close to the conventional ones). With substantially shorter developing times, frequent mission opportunities exist, with faster scientific and data return. Furthermore, new technologies can be used, and thus state of the art payloads can be flown. This is leveraged by the use of COTS microelectronic technologies, and more recently by Micro-Electro-Mechanical Systems (MEMS) technology, which significantly increased the sophistication and capabilities of small satellites [52]. Besides the technology that can be used, shorter developing times allow these platforms to answer more potential user needs, as more missions can be designed and launched [50].

Another important aspect of small satellites is clearly their lower cost, which in turn represents a greater flexibility. For example, instead of a single spacecraft with several sensors, multi spacecraft with one or two payloads can be designed, making the mission less susceptible to single failures [75]. Moreover, going from thousands of million euros to a few or less than 1 M€ also means the difference between a mission only affordable to national institutions or multi-national partnerships, or one developed and operated by an university or even at a department level. In fact, their lower cost (including managing and operational costs), increased flexibility and reduced complexity have made small satellites the tool for teaching and research [52]. Many of the small satellites launched today are designed, tested, and operated by students, even at the undergraduate level, with an increasingly involvement of local and small industries [50]. Actually, small satellite projects are the prime testing ground for system engineering and team work in a multidisciplinary environment.

The usually lower orbit that these spacecraft tend to be launched to is also an advantage of this platform. Although the lifetime is shortened by these LEO orbits, the power needed for ground assets to communicate with the spacecraft is less demanding, even without the use of high gain antennas. Therefore, small satellites can be an important tool to link remote *in situ* experiments with ground stations many kilometres away (an aspect further developed in Chapter 4).

Despite these relevant advantages, small satellites can never replace conventional spacecraft, and are more complementary platforms. As with any other platform, small satellites have some conspicuous disadvantages, as for example, the limited dimensions and power available. These

not only restrict the instrumentation that can be fitted in, but also what those instruments can perform and the amount of data that can be downlinked. An additional disadvantage of these platforms comes from the way they are launched (*i.e.* as secondary payloads). As they are not the primary contractors of a launch, small satellites do not usually have any control neither over the target orbit nor the schedule. This means the missions must be designed for a range of orbits instead of being optimised for a particular one [76].

CHAPTER 3

Monitoring the Oceans with Small Satellites

With a clearer picture of what is a small satellite and what are its advantages and disadvantages, the discussion here is turned to what can be accomplished within oceanography with these platforms (and represents the remaining part of Ref. [43]). An introduction of what remote sensing has done for oceanography is given at the beginning of the chapter, including how it integrates with conventional methods, as well as with autonomous vehicles. A survey of what has already been done with small satellites is then presented, with a brief description of each satellite found. The chapter ends with what are the common remote sensing observables and their respective instruments, together with simple exercises on how they could be adapted to the constrains of micro and nano satellites.

3.1 Remote sensing oceanography

Even before remote sensing satellites had been idealised, the study of the oceans relied on conventional ship-based and static methods. Still today, these are important tools for performing accurate *in situ* measurements. However, there are several ocean phenomena that, either for their spatial or temporal scales, or just their natural variability, require both synoptic and large spatial and temporal measurements, and thus these methods are not cost-effective, sustainable, or even adequate.

Autonomous vehicles, underwater, surface, or aerial ones, slowly but steadily extended the reach of those traditional methods, making large surveys faster and more cost effective. Although this represents an important step, they do not provide the needed mesoscale (*i.e.* $> 50\,\mathrm{km}^2$) observation capability, the maturity and robustness, neither the rapid response, that is required to understand some bio-geochemistry processes [16, 77]. Moreover, they do not provide a maritime domain and situation awareness, for example, to answer to disaster situations like oil spills.

A way to overcome some observational limitations of the traditional methods, and of the autonomous vehicles, is to use synthetic ocean models [78]. However, these have their own limitations, in particular, the poor capability to represent complex mixing phenomena.

The first remote sensing spacecraft was the **TIROS** (Television Infrared Observing Satellite) 1. It was a weather satellite, launched 3 years after **Sputnik 1**, with a mass smaller than $200\,\mathrm{kg}$ [47].

These spacecraft came to complement and augment traditional methods of monitoring and observing the ocean (*e.g.* moorings, Lagrangian drifters, and manned ships), and eventually became an indispensable tool for Earth Observation [79]. Satellites provide a wide range of high resolution data, which made possible regional or global scale studies, over periods of days, months, or even years. Even though the focus here is oceanography, there have been missions covering numerous Earth science fields, from meteorology to geology and biology [80]. Furthermore, radar equipped spacecraft, including LIDAR (Light Detection and Ranging) and SAR, were a boon for MDA, and respective maritime authorities.

Through the years there was a consistent demand for spacecraft capable of gathering more measurements and with higher resolutions, leading to a growth in mass, cost and complexity. The peak of this curve was reached in 2002, with the 7.9 tonnes **EnviSat** mission from ESA [63]. Besides the growing cost and mass, each spacecraft was also getting more complex. For example, there are numerous engineering issues when trying to put several different instruments, each with its own requirements, inside a confined volume. Consequently, in the last few years both ESA and NASA are favouring spacecraft with less instruments and a maximum mass of about 1 tonne.

3.2 Survey of ocean observation missions with small satellites

With the observed evolution of small satellites, these could become a promising tool for remote sensing operations. Therefore, to have a better understanding of what can be achieved with these platforms, it was imperative to do a survey of what had been done before.

The goal is to understand the small satellite impact on ocean observations and oceanography, which does not mean that the discussion concerns only oceanographic variables. As before, the focus is on micro, nano and CubeSat missions (*i.e.* bellow 100 kg), as these are the types of small satellites that differ the most from conventional satellites. Nevertheless, the survey covered all program ranges, *i.e.* mission still in the design phase and those already launched, both successfully operating or which were unsuccessful. Small satellite constellation missions were also considered.

The data presented here was gathered until around the end of 2015, mainly from online databases (the Earth Observation Portal[i], the Union of Concerned Scientist satellite database[ii], and the Nanosatellite Database[iii]), together with a broad survey of available literature and the web. When specific mission references were available, which was not always the case, they were used to cross check the databases information.

From all gathered data, the field that has seen more small satellite missions launched is traffic monitoring (using AIS), as can be seen in Table 3.1. Only two other fields had (or will have) missions, ocean imaging and data storage and relay. Details of the missions found, covering these fields, are discussed in the following sections.

[i] https://directory.eoportal.org/web/eoportal/satellite-missions
[ii] http://www.ucsusa.org/nuclear-weapons/space-weapons/satellite-database.html
[iii] http://www.nanosats.eu/

Table 3.1 – *Summary of ocean observing small satellites, including mass, power, mission and payload (oceanography related), and launch date. Missions are still operational if not stated otherwise.*

Satellite	Mass [kg]	Power [W]	Size [cm][a]	Mission	Payload	Launch
SeaHawk[‡]	4	–	$10 \times 10 \times 34$	Monitor ocean health and technology demonstration	Imager	2018
ZACube-2[‡]	4	–	$10 \times 10 \times 34$	Vessel tracking and ocean colour	AIS and imager	2018
RISESat[‡]	60	100	$50 \times 50 \times 50$	Fisheries and environment studies	Multi-band camera	2018
M3MSat	85	80	$80 \times 60 \times 60$	Augmenting maritime surveillance capabilities	AIS	2016
AAUSat5[⋆]	0.88	1.15	$10 \times 10 \times 11$	Vessel tracking	AIS	2015
LambdaSat[⋆]	1.5	1.5	$10 \times 10 \times 11$	Vessel tracking	AIS	2015
LAPAN-A2	68	32	$50 \times 47 \times 36$	AIS payload for the equatorial region	AIS	2015
AISat	14	15	$10 \times 10 \times 11$	Helical antenna technology demonstration	AIS	2014
QSat-EOS	50	70	$50 \times 50 \times 50$	Ocean eutrophication	VIS and NIR camera[b]	2014
AAUSat3[⋆]	0.8	1.15	$10 \times 10 \times 11$	Vessel tracking	AIS	2013
COPPER[+]	1.3	2.5	$10 \times 10 \times 11$	Infrared Earth images	Uncooled Microbolometer Array	2013
WNISAT-1	10	12.6	$27 \times 27 \times 27$	Monitoring Arctic Sea state	VIS and NIR cameras	2013
Aeneas	3	2	$10 \times 10 \times 34$	Track cargo containers	Antenna and corresponding electronics	2012
VesselSat 2	29	–	$30 \times 30 \times 30$	Collect space-borne AIS message data	AIS	2012
SDS-4	50	60	$50 \times 50 \times 45$	Demonstrate space-based AIS	AIS	2012
exactView 1	98	–	$63 \times 63 \times 60$	Commercial constellation of AIS spacecraft	AIS	2012
exactView 6/5R/12/11/13	13	15	$25 \times 25 \times 25$	Commercial constellation of AIS spacecraft	AIS	2011/13/14
VesselSat 1	29	–	$30 \times 30 \times 30$	Collect space-borne AIS message data	AIS	2011
AISSat-1	6.5	0.97	$20 \times 20 \times 20$	Assess feasibility of situational awareness service	AIS	2010
NTS/CanX-6[⋆]	6.5	5.6	$20 \times 20 \times 20$	Demonstrate AIS detection technology	AIS	2008
WEOS	50	14.5	$52 \times 52 \times 45$	Data relay from cetacean probes	UHF Antenna	2002

[a] Size of the main structure (not accounting for deployed mechanisms, *e.g.* antennas).
[b] Visible (VIS) and Near InfraRed (NIR).
[‡] To be launched.
[⋆] Concluded operations.
[+] Mission failed.

3.2.1 Ocean imaging with small satellites

There have been many micro and nano satellites equipped with imaging sensors (*e.g.* Planet Labs launched in a single event more than 88 [81]), and even though images acquired with these can be used for oceanographic research, very few have been actually designed for ocean observation. Only in 2013 was the first CubeSat with an ocean imaging sensor about to be launched, **COPPER**, but the missions ultimately failed, and thus no CubeSat actually exists with this capability [63]. Conversely, there have been two micro satellites, **WINISAT-1** which was a commercial purpose mission, and **QSat-EOS** which used data acquired for other purposes to monitor ocean quality.

RISESat. The Japanese programme FIRST (Funding Program for World-Leading Innovative R&D on Science and Technology) is financing Tohoku University to develop the Rapid International Scientific Experiment Satellite (**RISESat**) [82]. Although initially planned for 2016, it has still not been launched [83]. The mission has two main goals: the technological development of a demonstration platform (as the bus is planned to be re-used for future missions), and the integration of several scientific payloads, totalling $10\,\mathrm{kg}$, from different countries and mainly devoted to Earth observation. The spacecraft measures about $50\,\mathrm{cm} \times 50\,\mathrm{cm} \times 50\,\mathrm{cm}$, has a maximum mass of $60\,\mathrm{kg}$, and using gallium arsenide multi-junction cells, it is expected to generate more than $100\,\mathrm{W}$. Because of the payloads expected to be carried a X-band communication system was added, besides the UHF and S-band used for housekeeping. Due to mission considerations, a de-orbit mechanism will also be installed, or otherwise it would not re-enter Earth in the mandatory $25\,\mathrm{years}$ (the maximum re-enter time allowed for a spacecraft, after completing its mission) [84, 85]. Among the payload (which include a High Precision Telescope, a Dual-band Optical Transient Camera, a Three-dimensional Telescope, a Space Radiation micro-Tracker, a micro-Magnetometer, a Very Small Optical Transponder, and a Data Packet Decoder) the only devoted to oceanography, in particular for fisheries and environmental studies, is the Ocean Observation Camera (OOC). This is a multi-band camera with a wide field of view, which yields an approximately $65\,\mathrm{km}$ swath, and a spatial resolution of about $100\,\mathrm{m}$ [82]. With a small mass and power consumption, approximately $1\,\mathrm{kg}$ and $3\,\mathrm{W}$, it uses for each lens a $659 \times 494\,\mathrm{pixels}$ Watec CCD (Charge-Coupled Device) [83].

QSat-EOS. Already launched in 2014, the **QSat-EOS** was developed by graduate students of Kyushu University, in Japan, mainly to monitor disasters (apart from other secondary objectives, including studies of Earth's magnetic field) [86, 87]. The data acquired by the $50\,\mathrm{kg}$ spacecraft, is also used for detecting harmful algal blooms and ocean eutrophication (*i.e.* a sort of pollution caused by excess of nutrients [88]).

COPPER. As mentioned before, the Close Orbiting Propellant Plume and Elemental Recognition CubeSat mission, launched in 2013, did not succeed (since communications could not be established). One of main objectives was to understand if commercially available compact uncooled microbolometer detector arrays could be used by CubeSats in order to acquire infrared

images. An additional goal was to understand the space radiation effects on electronic devices [89]. If the microbolometer had worked, the images would have been used to provide space situational awareness, making it a pathfinder mission for the long term Argus flight programme [90].

WNISAT-1. A commercial venture between Weathernews Inc. of Tokyo (one of the largest weather companies of Japan) and AXELSPACE (a university company), designed a simple and compact satellite for monitor the Arctic Sea state, in particular for ice coverage, the **WNISAT-1** (Weathernews Inc. Satellite-1) [91]. Launched in 2013, it provides frequent updates of sea state to shipping customers crossing the Arctic Sea [92]. The spacecraft used COTS as much as possible, with minimum redundancies, and was designed to be simple to operate.

3.2.2 Data relay with small satellites

Apart from sensing the ocean, relaying data from *in situ* experiments, or other assets, to ground stations is another important task that spacecraft can perform. An example of such a mission is the one of the Chiba Institute of Technology in Japan, the Whale Ecology Observation Satellite (**WEOS**). Other missions include the **ParkinsonSat** [93], the nano satellites **TUBSAT-N** and **N1** [94], the twin 8.2 kg **CONASAT** spacecraft [95], and the Federation Satellite (**FedSat**) [96].

A particularity of the **TUBSAT-N** and **N1** missions is the launcher used, which was a Russian converted ballistic missile launched from a submarine. This allows for spacecraft to be launched with any orbit inclination desired, without having to perform any change of orbit manoeuvres, although making spacecraft form-factor critical (because of the limited rocket size and power).

WEOS. Although the space segment of the **WEOS** mission was successful, the true goal of the mission was never achieved. This was a 50 kg spacecraft, designed, built and operated by students, launched in 2002, which was supposed to track whales' probe signals. By transmitting GPS position, diving depth and sea temperature (using UHF), it could be used to study the migration routes of the whales [97]. However, the probes could never be attached to the whales, and only dummy buoys were tracked by the spacecraft.

3.2.3 Vessel tracking and AIS equipped small satellites

The automatic identification system is designed to provide MDA, prevent collisions and allow maritime traffic control [21, 98]. It is a mandatory system to vessels operating in international waters (both passenger ships and others with mass over 300 tonnes), and for 500 tonnes ships and over in most national waters [23].

This is a ship-to-ship and ship-to-shore system, which sends the Maritime Mobile Service Identity of each vessel (*i.e.* position, heading, time, rate of turn, and cargo) to other vessels and to shore beacons in range [99]. It has a typical range of 50 km to 100 km, which means it is commonly

used around maritime choke points or near the shore line. However, it can be made simpler using a self-organised time division multiple access scheme, and thus each transmitter can communicate with others without any interference, within the same 100 km cell [98].

Moving an AIS receiver to space can provide not only a global view of the maritime traffic (with implications to national security and shipping tasks), but also support search and rescue missions, apart from some environmental studies. That is why ship-to-space AIS communication was in fact suggested in the fourth revision of the system recommendations [23]. However, some problems arise from this change. For example, in high traffic areas jamming problems can appear, since a space-based system usually has a Field Of View (FOV) far wider than those 100 km. Two other common problems are the Doppler shift, derived from the high relative velocity of the spacecraft to the vessel [24], and the weaker signal, as it needs to travel distances longer than 100 km to reach LEO satellites. The signal is also weaker because of the polarisation mismatch between the spacecraft antenna and the vessel signal. This is a common problem of remote sensing observations, and is caused by a frequency dependent Faraday rotation of the polarisation plane of all signals crossing the ionosphere. Nevertheless, while there are few payloads designed for oceanography flying in micro and nano spacecraft, the same cannot be said of the AIS systems, with much research in this area being carried out nowadays [100].

Aside from the spacecraft discussed below, there are a few of which there is not much information available. Among these are the United Kingdom's 3U CubeSats **Triton 1** and 2 [101], the 9.3 kg Chinese nano satellite of the National University of Defence Technology, **TianTuo 1** [102], the 6U Canopus Systems US **Perseus-M 1** and 2 missions [103, 104], and the Dauria Experimental 1 (**DX 1**) 27 kg spacecraft (with 40 cm $\times$ 40 cm $\times$ 30 cm), built by Dauria Aerospace [105].

ZACube-2. The objectives for the **ZACube-2** include tracking of AIS signals, using a SDR, and study ocean colour and fire monitoring, using for this a medium resolution imager. Ultimately, it will serve as a demonstrator for the nano satellite programme created by Cape Peninsula University of Technology (CPUT) in South Africa, for which the **ZACube-2** is the second spacecraft [106].

M3MSat. Launched back in 2016, and built upon a previous mission (the Near Earth Object Surveillance Satellite), the Maritime Monitoring and Messaging Microsatellite (**M3MSat**) is monitoring AIS signals for the Canadian Department of National Defence (DND) and a Canadian founded commercial venture, Exactearth. The main purpose is to expand the range of AIS and create an improved Recognized Maritime Picture, with the integration of ISR sensors [99]. Furthermore, as most small satellites, it serves as a demonstrator, which allows to gain knowledge about these platforms and a flight heritage.

AAUSat. Research on AIS systems has also been done in the Department of Electronic Systems of Aalborg University (AAU). An education programme there has launched three satellites, **AAUSat3** and **AAUSat5** from the International Space Station (ISS), in October 2015, and

AAUSat4. Each had an improved AIS, however only the latter is still operational and in orbit.

LambdaSat. Also launched from the ISS in March 2015, the **LambdaSat** was a Silicon Valley, California, student endeavour to demonstrate an AIS system. It also served to space qualify graphene, without any protection against solar and space radiation, and a three-fault tolerant spacecraft [22, 107]. After 30 days of operations, the mission was successfully concluded with the spacecraft re-entering the atmosphere.

LAPAN-A2. The Indonesian space agency (LAPAN) wanted to develop its own small satellite for Earth observation, disaster control and maritime traffic control (using AIS) [25]. Therefore, it sent their own engineers to the Technical University of Berlin to help develop **LAPAN-TUBSAT** or **A1**, a precursor to **LAPAN-A2**, and thus gain expertise to successfully launch it in 2015 [108].

AISat. The German Aerospace Center (DLR), together with the Institute of Space Systems, the Institute of Composite Structures and Adaptive Systems, the Bremen University of Applied Sciences, and two private companies (The Schütze Company and Joachims), designed the Automatic Identification System Satellite (**AISat**) to monitor AIS signals [109]. One of the particularities of this mission is the use of a helical antenna, instead of a conventional one, apart form the use of the DLR adapted CubeSat platform, the Clavis bus.

Aeneas. With an elliptical orbit of 480 km in its nearest point, the **Aeneas** nano satellite tracks cargo containers all over the world, which have been equipped with a 1 W Wi-Fi type transceiver [110]. Launched in 2012, it was developed by the students of the University of Southern California, from the Space Engineering Research Center, and iControl Inc. (which provided the primary payload) [111].

VesselSat. A Luxembourg company, LuxSpace Sarl, has been working with space-based AIS detection to monitor maritime traffic from many years, starting with three non-separable payloads aboard the Polar Satellite Launch Vehicle, the **Rubin 7**, 8 and 9 [112]. In 2011 and 2012, they launched their two micro satellites, **VesselSat 1** and 2 [113].

SDS-4. The Small Demonstration Satellite 4 (**SDS-4**), launched in 2012, was intended to validate not only an AIS system, but also the high performance bus [100]. It was part of a 2006 programme started by the Japanese Aerospace Exploration Agency (JAXA), called the Small Demonstration Satellite programme. An objective of that programme was to create a standard 50 kg, on which future missions could be based, and to try out the next generation of space technologies [24]. The mission was a success, and the spacecraft remained operational much after its designed lifetime [114].

AISSat-1. Norway put in a 630 km Sun-synchronous polar orbit (*i.e.* passing above the same place about the same time of day) its first satellite for monitoring AIS signals in 2010 [20, 23]. This was a joint venture with the University of Toronto, and its Institute for Aerospace Studies/Space Flight Laboratory (UTIAS/SFL), to perform surveillance of the more than 2 million square kilometres Norwegian waters. As it was such a success, with **AISSat-1** operating for five years after its launch, two more were launched, **AISSat-2** in 2014, and **AISSat-3** in 2016.

NTS/CanX-6. Besides the **AISSat** missions and **M3MSat** spacecraft, the UTIAS/SFL of the University of Toronto and COM DEV Ltd (a company researching AIS systems) had already tested the reception of AIS signals in space back in 2007/2008, with the Nanosatellite Tracking Ships (**NTS**) [98]. This nano satellite was actually designed, produced and launched in less than seven months, as the platform was based on the Generic Nanosatellite Bus (GNB) of the previous SFL **CanX-2** nano satellite, and although still operational it is no longer used actively. This short period between design and launch was also possible due to the top-down approach to mission requirements (lifetime, data throughput, attitude, schedule, and resources), and bottom-up analysis to maturity, readiness, and hardware limitations (including on-board memory, downlink rate, power, volume, and others).

3.2.4 Small satellite constellations

Although made up of single spacecraft, constellations can be considered a different category from the above ones, since they combine observations of a single target made by several spacecraft to create a coherent larger image. Thus, constellations allow for some scientific studies which would not be feasible if only one spacecraft was used. Furthermore, with a constellation it is possible to maintain a permanent global coverage, allowing for systems like the GNSS, **Iridium** (which is discussed in Section 4.3), or the **exactView** AIS system presented below.

SOCON. A project started a few years ago, and still being developed, is the **SOCON** (Sustained Ocean Observation from Nanosatellites), of which the 3U **SeaHawk** is the forerunner of the envisioned constellation of ten small satellites [115]. The **SeaHawk** payload, the HawkEye Ocean Colour Sensors (which will measure ocean colour), is expected to be seven to 15 times better, costing about eight times less, than its predecessor, carried be the **OrbView-2** satellite.

CYGNSS. Already on the micro satellite class, the **CYGNSS** (Cyclone Global Navigation Satellite System) is composed by eight identical 25 kg spacecraft [116]. Launched by a single vehicle in 2016, it relates atmospheric conditions, radiation and convective dynamics, and ocean surface properties (from GNSS signals bouncing of the ocean) with tropical cyclone formation [117].

exactView. To develop a service that could give a comprehensive view of maritime traffic anywhere in the world, with revisit time (*i.e.* the time that it takes for a satellite to cross the same

point on Earth) of about only 90 minutes, exactEarth has built a constellation of AIS spacecraft and payload, the **exactView**. It started with the experimental **NTS (EV0)**, already discussed, and the 2011 **EV2** payload aboard the **ResourceSat 2** satellite. Afterwards it requested SpaceQuest to develop **EV6** and **5R**, which were later named **AprizeSat-6** and 7, and in 2012 **exactView1** (**EV1**). In 2013 **AprizeSat 8** begun operations (becoming **EV12**), and in 2014 **EV11** and 13 (**AprizeSat 9** and 10) were launched. Finally two more spacecraft and one payload were added to the constellation, the **EV7** spacecraft (which is the name give by exactEarth to the **M3MSat** satellite), the **EV8** payload aboard the Spanish spacecraft **Paz**, and the 2015 **EV9** satellite [118].

AprizeSat. Apart from the spacecraft given to exactEarth, the **AprizeSat** constellation is made of 64 satellites, carrying AIS and communication payloads. The objective is to build a data communication system and to track and monitor different assets [119].

3.3 Oceanography main observables and sensors

It has been established that there are not many examples of micro and nano satellites used for ocean observation. In fact, the main source of remote sensing data have been conventional satellites, acquiring large amounts of continuous data, and being mainly operated by ESA, NASA, and the National Oceanographic and Atmospheric Administration (NOAA) [120, 121]. Nevertheless, in the last few years there has been a move to small satellites, of the mini satellite class [52]. Even though micro or nano spacecrafts are still underestimated, they could be integrated with conventional satellites to allow for a much more cost-effective way to perform oceanography.

Several observables are commonly acquired by remote sensing satellites, including sea surface temperature, ocean colour, winds, and sea-state, giving a wide and comprehensive view of the ocean [122]. Furthermore, remote sensing is an integral part of the life of any oceanographer, since it feeds synthetic ocean models (*e.g.* the Regional Ocean Modelling System [123]), which can guide the deployment of manned or robotic assets [124, 125].

To understand what could be done with small satellites, it is relevant to discuss what are these main ocean observables and the satellite sensors currently used to acquire them. The main data sources used for this section are Refs. [3, 63, 122, 126−129].

3.3.1 Ocean colour

The colour of the ocean is closely related to the concentrations and types of sediments, organic material and phytoplankton on the upper water-column. This region is especially important since the presence of phytoplankton with chlorophyll leads to high primary productivity [129]. In fact, increase in anthropomorphic input, either coming from sewage, fertiliser run off or commercial dumping, has severe consequences on the organisms living there and, in particular, in phytoplankton concentration, which has an impact in primary productivity [130, 131], for example.

Besides primary production, ocean colour data can also be used as a proxy for phenomena like mesoscale eddies (which are large circular currents, 10 km to 500 km in diameter, persisting a few days to some months) or fronts (that are very distinct boundaries between mass of water in the middle of the ocean). Upwelling (a phenomena characterised by the rise of cold water from the deep to the surface), and internal waves (which are gravity waves that propagate inside the ocean and are only possible when there is a density stratification of the water) can also be inferred.

To measure ocean colour it is necessary to sample several spectrum bands, including ultraviolet, visible and near infrared, with a high spectral resolution (*i.e.* the minimum difference between two wavelengths or frequencies that a sensor can distinguish). By combining the information of the different bands, it is possible to separate ocean colour data from the atmospheric interference. Nonetheless, ocean colour sensors have some limitations, including difficulties with the calibration and signal to noise ratio, in particular in the blue and green regions, and the need to have a cloud free view of the ocean. These shortcomings limit the capacity of the sensor to make precise measurements, which results in a 50% accuracy. One of most common sensors are a multispectral radiometer, which samples a well defined and narrow limited number of wavelengths to form a picture of the incoming light. Another one is an imaging spectrometer (like the one represented in Figure 3.1), that generates substantially more data since it works by sensing across a continuous spectrum with an established spectral resolution.

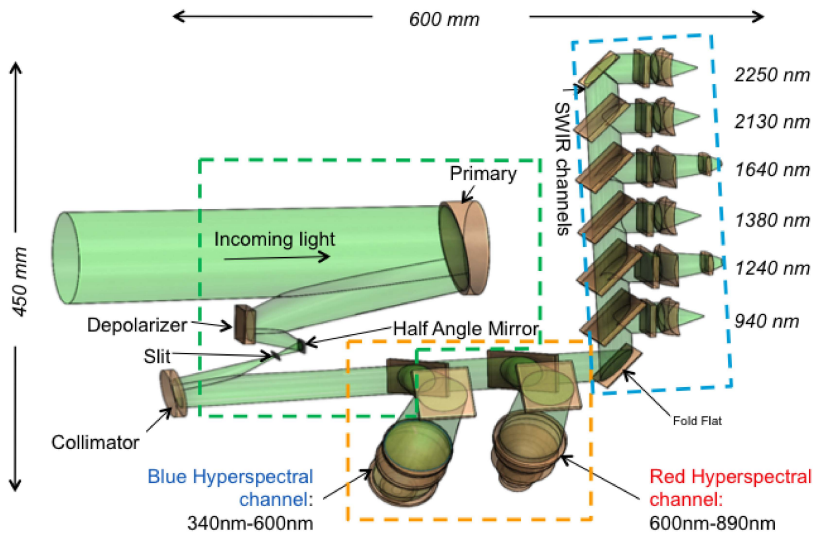


Figure 3.1 – *Ocean colour instrument schematics, including Short-Wave Infrared (SWIR) channels (image from Ref. [132]).*

The first ocean colour remote sensing data was acquired with the Coastal Zone Color Scanner (aboard the **NIMBUS-7** spacecraft) in 1978 [129]. Even though it ceased operations in 1986, working on alternate days to save power, it was only about ten years later, in 1996, that other sensors were launched. These were the Japanese Ocean Color and Temperature Sensor (on the 3 560 kg **ADEOS-1**), and the German Modular Optical Scanner (on the 922 kg **IRS-P3**). With these launches, and the support of the Committee on Earth Observation Satellites (CEOS), the

International Ocean-Colour Coordinating Group was founded to oversee and support ocean colour research and technology [133]. Its mission includes setting standards for sensor calibration and measurement validation, apart from combining the efforts of data providers, space agencies, and users (which can be either scientists or managers).

More recently several large spacecraft (well above the 1 000 kg) have carried ocean colour instruments (*e.g.* **EnviSat**, **Aqua**, and **COMS-1**). Conversely, only two mini satellites examples were found in this survey, the Indian Space Research Organization (ISRO) 970 kg **OceanSat-2** spacecraft [134], and **Haiyang-1B** (a 443 kg Chinese spacecraft) [135]. Both carry radiometers, with instrument characteristics (including spatial resolution and mass) shown in Table 3.2.

Table 3.2 – *Characteristics of past, current, and future ocean colour instruments.*

Sensor (Satellite – Mass [kg])	Figures of merit[a] (Past/Future)	COCTS [135] (HY-1B – 443)	OCM-2 [134] (OceanSat-2 – 970)	HawkEye [136] (SeaHawk – 4)
Spatial Resolution [km]	1.5/0.7	1.1	0.36	0.15 – 0.075
Swath [km]	1 328/1 474	2 800	1 420	750
Wavelength [μm]	0.404 – 5.42	0.402 – 0.885	0.404 – 0.885	–
Mass [kg]	122/242	50	78	–
Power [W]	99/206	29.3	134	–

[a] Average figures of merit of decommissioned and future sensors [122, 127, 133].

Based on data of other instruments and recent developments, it is clearly perceived that a ocean colour instrument can be carried by a micro or nano satellite. There are two examples of measuring ocean colour with CubeSats, the **SeaHawk** (carrying the already mentioned HawkEye Ocean Colour instrument) and the **ZACube-2**, both scheduled to be launched this year. The HawkEye, shown also in Table 3.2, is expected to have, for its 540 km orbit, a 75 m per pixel ground resolution, which amounts to a ground swath of 300 km $\times$ 750 km (with its 4 096 $\times$ 10 000 pixels in each image) [136]. One of the challenges for this spacecraft is the downlink of the aggregated 655 Mb of data, which has already been compressed from the 4.6 Gb raw data produced by the eight linear CCDs (measuring eight VIS and NIR bands similar to the SeaWiFS instrument).

3.3.2 Ocean altimetry

Measurements made by altimeters have a plethora of applications, both in oceanography and weather and climate patterns. The first example, and most obvious one, is the retrieval of the ocean surface topography (*i.e.* sea level and wave height). Nevertheless, altimetry can also yield submarine topography (bathymetry), and ocean current maps. Moreover, through small sea surface displacements (relative to the mean elevation) and scaler wind speed, altimetry is one of the most reliable ways to observe mesoscale eddies.

Altimetry is usually performed with an instrument pointed vertically downward (nadir pointing) sampling along the spacecraft ground track, the radar altimeter. Like any other radar, these emit short pulses with a fixed frequency. By measuring the signal travel time, from the sensor to the ocean and back, the distance between the spacecraft and the sea surface can be extrac-

ted. That range is then combined with precise gravity fields (*e.g.* the one created by **GRACE** measurements [137]) and orbit position, to have the relative sea surface height with respect to Earth's reference ellipsoid (as shown in Figure 3.2). Besides the time, the sensor also records the magnitude and the shape of the signal received, as these can be used to apply corrections (*e.g.* atmosphere and ionospheric free electrons and sea state ones) and for instrument calibration. Estimates of wave height and wind speed are obtained from sea surface roughness, measured for length scales of a few millimetres to centimetres (related to the radar wavelength), and sea surface height variability.

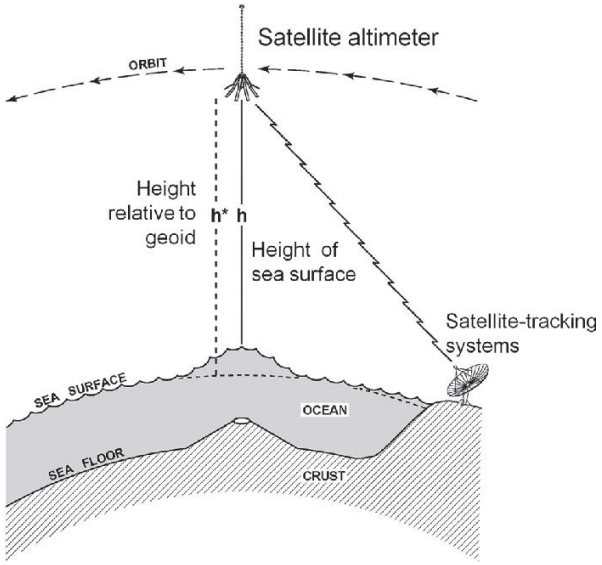


Figure 3.2 – *Schematic of the method of operation of an altimetry aboard a spacecraft (image from Ref. [138]).*

In the past, missions performing altimetry involved either more than $2\,000\,\mathrm{kg}$ conventional spacecraft (*e.g.* **SeaSat**, **ERS-1**, and **ERS-2**), or $500\,\mathrm{kg}$ mini satellites (*e.g.* **GEOS-3** and **GEOSAT**). However, these spacecraft did not have the accuracy of the more recent missions, often in the $2\,\mathrm{cm}$ to $3\,\mathrm{cm}$ range, for open ocean, since coastal waters have other interferences (like the noise coming from ground communication systems) [139]. Accuracies of newer spacecraft can reach $1\,\mathrm{cm}$, for measurements done with timing precisions of $6 \times 10^{-11}\,\mathrm{s}$. The difference between those past and the more recent missions is the use of dual frequency radars (C and Ku-band). Examples of already decommissioned dual band missions are the $2\,388\,\mathrm{kg}$ **TOPEX/Poseidon** mission (operational from 1992 to 2005), the **Jason-1** with $500\,\mathrm{kg}$ (active between 2001 to 2013) [140], and the aforementioned largest spacecraft ($8\,140\,\mathrm{kg}$) and active between 2003 and 2012, the **EnviSat** [141]. Three altimetry mini satellites are currently active: the evolution of **Jason-1** ($553\,\mathrm{kg}$, C and Ku-bands, **Jason-2**) [142], a $720\,\mathrm{kg}$ dual Ku-band antenna (**CryoSat-2**) [143], and finally a innovative Ka-band altimeter that does not require substantial ionospheric corrections, the **SARAL** ($407\,\mathrm{kg}$) [144]. The most relevant characteristics of some of these spacecraft is shown in Table 3.3.

Considering the characteristics of the spacecraft mentioned above, the most successful ones are compact (*i.e.* with low drag resistance), and carry various supporting sensors. This yields a total payload mass of about $100\,\mathrm{kg}$, with a power consumption of $150\,\mathrm{W}$, and one $1.1\,\mathrm{m}$ antenna in

Table 3.3 – *Decommissioned, current and future altimeter characteristics and corresponding mission support sensors.*

Sensor (Satellite – Mass [kg])	Figures of merit[a] (Past/Future)	Poseidon-3[b] [142] (Jason-2 – 553)	AltiKa[b] [144] (SARAL – 407)	Optimised [145] (Micro Satellite – 45)
Spatial Resolution [km]	–/8.5	–	–	–
Swath [km]	13/68	30	8	–
Bands	Ku/C or Ka	Ku/C	Ka	Ku
Accuracy [cm]	6.1/2.4	2	1.8	2.5
Mass [kg]	108/142	70	40	13
Power [W]	134/329	78	75	24
Antenna [m]	1.2/2.5	1.2	1	0.4
Supporting Sensors	Radiometer, GPS, DORIS, LRA[c]			GPS

[a] Average figures of merit of decommissioned and future sensors [122, 127, 128].
[b] These are representative of current capacities of mini satellites.
[c] SARAL does not have GPS and AltiKa also works as a radiometer.

diameter. These values are obtained by averaging the characteristics of the still active mini satellite missions, and account also for all the supporting sensors, which include a radiometer (for atmospheric corrections), an inertial unit (to measure spacecraft accelerations), a Doppler Orbitography and Radiopositioning Integrated by Satellite or DORIS system (for precise orbit determination), and sometimes a Laser Retroreflector Array (LRA). Although the last two have the same purpose (*i.e.* to give the orbit of the spacecraft with high precision), the LRA is used as a reference target for satellite laser ranging measurements, while the DORIS instrument exchanges signals with reference ground beacons spread over the world. With the evolution of GNSS systems, some newer spacecraft have been replacing or augmenting the DORIS system with GNSS receivers.

If the same accuracy is desired, it appears close to impossible to perform altimetry using micro satellites (not even mentioning nano ones). However, there have been several studies to try to miniaturise Ka-band radar altimeters, since by creating an altimeter constellation it would be possible (with an almost continuous observation) to perceive some ocean phenomena not observed nowadays (due to the temporal resolution of those phenomena). For example, in 1999 the **GENDER** twelve small satellite constellation (with a mass smaller than 150 kg each) was proposed, even though there the goal was not to have the full sea surface topography, but only significant wave height and wind speed [146, 147]. Another study (also shown in Table 3.3), carried out by two institutes responsible for previous altimeter missions, suggested a 45 kg micro satellite (consuming 70 W), with errors of around 5.6 cm [145]. Finally, in 2012, even a 12 kg 6U CubeSat was proposed [148].

Although the accuracies achieved are not close to the current altimeters, several authors still believe that nano satellites can have a beneficial impact on altimetry data, just because of the increase in spatial measurements. By simply scaling down the 78 W **Jason-2** altimeter, to a 1 W instrument, capable of fitting in a nano satellite, the accuracy would decrease to 16.7 cm, without accounting for orbit position determination errors, from the 2 cm obtained by **Jason-2** [149]. Nevertheless, this is the worst case scenario, and could be potentially minimised by introducing atmospheric corrections provided by suitable models (whose accuracy are about 1 cm to 3 cm).

3.3.3 Ocean surface winds

Studying the winds at the surface of the ocean has both scientific implications, *e.g.* for atmospheric, ocean surface waves, and circulation models, as well as economical ones, as it can be used in weather and climate forecasting for offshore oil operations, ship movement and routing.

Remote sensing measurements of surface winds are always indirect, and work by measuring the electromagnetic signal either backscattered or emitted by the ocean, in particular in the microwave C, X, and Ku bands (as these are the most effective ones). This yields surface wave state, which in turn acts as a proxy for surface winds, although the accuracy depends on the wind speed. Therefore, to retrieve surface winds (both speed and direction) there are two main methods: passive microwave radiometers or active radar instruments (*e.g.* scatterometers and SAR). For each of these methods there is always a trade-off between spatial resolution and swath.

The sea surface shape and orientation, together with water temperature and its dielectric properties, influences the radiation signal emitted by the ocean. By passively measuring this radiation, simpler radiometers (*i.e.* those that are only able to scan vertical or horizontal polarisation) can retrieve wind speed values. To also have wind direction it is necessary to look twice at the same patch of the ocean from different orientations. Conversely, there are radiometers capable of reading all four Stokes parameters (*i.e.* vertical and horizontal polarisation components of the electric field, plus corresponding real and imaginary parts of the correlation between them). Combining those four together fully describes the properties of an arbitrarily polarised electromagnetic wave. Thus, this fully polarimetric radiometer only needs a single measurement to have both magnitude and direction of the surface wind vector, under some conditions.

So the instrument is not dependent of the electromagnetic signal emitted by the ocean, and thus to be more effective, it is necessary to actively produce it. The simplest form of such an instrument is the scatterometer, which is also the most effective remote sensing radar. Its principal is to measure the average backscatter of microwaves by the ocean, emitted with an incidence angle between $20°$ and $70°$. As for the simpler radiometer, to retrieve wind speed and direction with a scatterometer the same patch of the ocean, in this case in a wide FOV, has to be measured several times, with different polarisations or from different directions (see Figure 3.3). The data is then processed, to correct for noise, atmospheric attenuation, and ambiguities, and fed into some selected models.

The other active instrument used for measuring ocean surface winds is the SAR (whose work principle is explained in Section 3.3.7). One of the main differences between the scatterometer and SAR is that the latter only observes the ocean from one direction. Therefore, to have useful data and apply scatterometer backscatter models, SAR measurements need to be combined with previously known wind direction data.

Remote sensing observations of surface winds begun in 1978, and since then there have been many spacecraft launched with either of these sensors. In particular, as radiometers (and sometimes scatterometers) are needed for altimetry missions, those spacecraft usually have dual

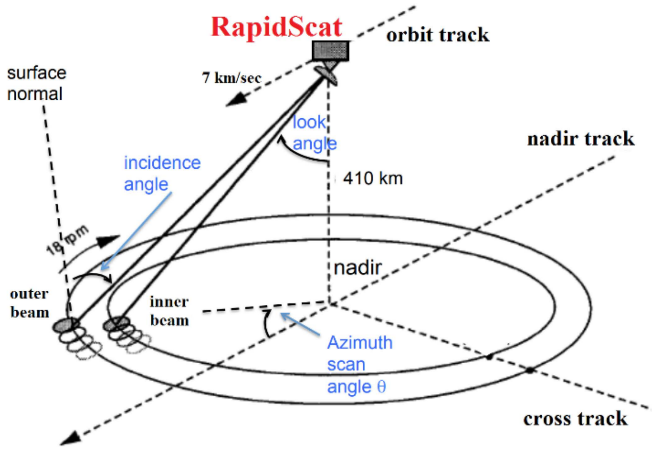


Figure 3.3 – *RapidScat scatterometer schematics of operations (image from Ref. [150]).*

objectives. Although there have been missions with high (more than 2 000 kg) launch mass (*e.g.* **HY-2A**, **RADARSAT-2**, and **TRMM**), there are several in the mini satellite class (with Table 3.4 showing some relevant characteristics of both scatterometers and radiometers flown or currently active). Carrying pencil beam scatterometers, which rotate the antenna performing circular scans (for multiple observations), there is the example of the 970 kg **QuikSCAT** mission [151], and the **OceanSat-2** [134]. Whereas the other type of scatterometer, a fixed vertical fan beam pointing several beams at the ocean simultaneously, using several antennae, has been carried by the **ADEOS-1** spacecraft. Conversely, the **DMSP** missions (750 kg to 1 220 kg) [152], the **Jason 1** and 2 [140, 142], and the 828 kg **Coriolis** spacecraft [153], were all equipped with a mechanically scanning radiometer (which has a single parabolic reflector, a cluster of feed horns and microwave detectors, all mounted in a gimbal). For radiometers there is also a fixed alternative, flown in the 670 kg **SMOS** mission [154], which combines the data coming from an array of small antennae electronically to have a multiple view of the ocean. Finally, as mentioned above, the AltiKa altimeter of the **SARAL** mission is capable of working as a radiometer and collect surface wind data [144].

Table 3.4 – *Characteristics of decommissioned instruments and active ones, in mini satellites, to measure ocean surface winds.*

Sensor (Satellite – Mass [kg])	Figures of merit[a] (Past)	SeaWinds[b] [151] (QuikScat – 970)	WindSat[c] [153] (Coriolis – 828)
Spatial Resolution [km]	50	50	25
Swath [km]	1 000	1 800	1 000
Wind Accuracy (Wind speed) [m/s]	2 (4 – 20)	2 (3 – 20)	2 (3 – 25)
Wind Direction Accuracy [deg]	20	20	20
Bands	Ku/C	Ku	C/X/K/Ka
Frequency [GHz]	13.9/5.3	13.4	6.8/10.7/18.7/23.8/37
Mass [kg]	230	205	341
Power [W]	197	250	350
Antenna [m]	1.7	1	1.8

[a] Average figures of merit of decommissioned sensors [122, 127, 129].
[b] The only active scatterometer nowadays in a mini satellite.
[c] An example of a currently active fully polarimetric radiometer in a mini satellite.

Performing an interpolation exercise, with current technology (and without intensive research) a scatterometer is most certainly out of the scope of a micro or nano satellite, as this is an instrument with double the mass of a micro satellite (238 kg), that consumes about 221 W, and uses a 120 cm antenna. The radiometer, although more feasible, since it has an average mass of 118 kg, a power consumption of about 122 W, and a reflector of 116 cm, would have several technical and mechanical difficulties, and a dubious utility due to the decrease in measurement accuracy (as some studies have suggested). Nonetheless, more research on this has to be performed.

3.3.4 Sea surface temperature

Among ocean surface currents, salinity, colour and other physical and biogeochemistry phenomena, Sea Surface Temperature (SST) has been classified as an essential climate variable by the Global Observing System for Climate. The data that can be retrieved with SST includes ocean circulation phenomena (*e.g.* current systems, eddies, jets, and upwelling regions), besides being critical for atmospheric models, either global (*e.g.* for studying the El Niño Southern Oscillation cycle) or local (*e.g.* guiding ship routing and hurricane forecast). In particular, SST changes the boundary conditions of these models, since it influences atmospheric water vapour and heat fluxes, and thus moderates the global climate system.

To measure SST is necessary to observe the natural infrared radiation emitted by the ocean, either using an optical infrared system (as the ones for ocean colour), or a radiometer (like the ones for surface winds). The main difference between both is the requirement of a cloud free observation with infrared instruments (and an on-board black body of known temperature for calibration), whereas microwave radiometers can observe even through rain cloud cover (although it needs to use appropriate channels and perform atmospheric corrections). However, radiometers have an important limitation, they are only effective on open ocean, since there is a significant reduction of signal to noise ratio within about 75 km of land (as was discussed for the altimeter). Nevertheless, for most studies a temperature difference of at least 0.5 K is necessary, and achievable with current instrumentation. For short revisit time, to have an increasing number of readings of a specific place (required by most studies), satellite data needs to be combined with *in situ* data (*e.g.* with buoys, AUVs and ships).

Most spacecraft carrying out SST measurements have mass above the 1 000 kg small satellite limit (*e.g.* **EnviSat**, whose instrument FOV is depicted in Figure 3.4, and **Terra**), although there are two recent mini satellites equipped with SST radiometers and imagers, the 696 kg **Meteosat-7** [155], and **EO-1** (a 572 kg spacecraft) [156], respectively. The radiometer is a pencil beam one (*i.e.* spinning with the spacecraft), which has three high resolution thermal infrared, water vapour absorption and visible range bands. The imagers equipped in **EO-1** are a panchromatic and multi spectral imager (called ALI), and the hyper spectral imager Hyperion (that has two spectrometers). Characteristics of all these instruments, with some figures of merit of past and future ones, can be seen in Table 3.5.

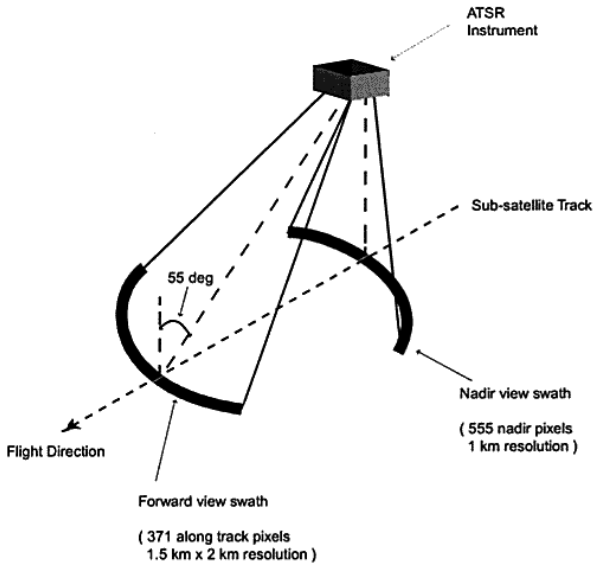


Figure 3.4 – *Viewing geometry of the **EnviSat** Advanced Along-Track Scanning Radiometer, ATSR (image from Ref. [157]).*

Table 3.5 – *Ocean surface temperature instrument characteristics, either decommissioned, currently active or future ones.*

Sensor (Satellite – Mass [kg])	Figures of merit[a] Past/Future	MVIRI [155] (Meteosat-7 – 696)	ALI [156] (EO-1 – 572)	Hyperion [156] (EO-1 – 572)
Spatial Resolution [km]	15/0.9	5	0.03	0.03
Swath [km]	1 030/2 200	–	37	7.5
Accuracy [K]	0.65/0.35	1	–	–
Wavelength [μm]	0.6 – 12	0.5 – 12.5	0.48 – 2.35	0.4 – 2.5
Mass [kg]	190/196	63	106	49
Power [W]	205/173	17	100	78

[a] Average figures of merit of decommissioned and future sensors [122, 126, 127].

Analysing the mechanical characteristics of these instruments it is possible to say that they could be adapted for micro satellites, even though there is no record of micro or nano satellite missions performing SST measurements. However, there is a characteristic not shown in Table 3.5 which is challenging for these platforms, namely the amount of generated data (which has to be downlinked later). For example, the **Meteosat-7** MVIRI radiometer has a data transmission rate of about 330 kbps, much similar to the ALI imager, although it can reach 2.7 Mbps in burst mode. Each image acquired by Hyperion has about 75 MB. Nevertheless, there as been studies suggesting that simpler infrared sensors (microbolometers) could be an option for CubeSat missions.

3.3.5 Ocean salinity

Another essential variable for ocean modelling and analysis is salinity, which influences the density and stability of surface water (combined with SST). Thus, processes like ocean mixing and water-mass formation (*e.g.* the meridional overturning circulation) are affected by it [126, 158]. This has noticeable repercussions on the planet climate, in particular, in the global hydrological cycle.

As there is a strong correlation between salinity and SST, if the brightness temperature is known to about 0.1 K, it is possible to determine salinity concentrations using this parameter (or radiance of microwave radiation) [129]. Also as SST, passive microwave radiometers can be used for measuring salinity, while in this case the most suitable frequency is 1.41 GHz, in the L-band. Nevertheless, radiometer measurements have to be corrected for sea surface roughness, ionospheric effects (inducing Faraday rotation), and heavy rain (as shown in Figure 3.5), to generate valid and relevant salinity measurements (*i.e.* with accuracies of at least 0.2 psu[iv]). Remote sensing measurements are calibrated using moored buoys equipped with salinity instrumentation.

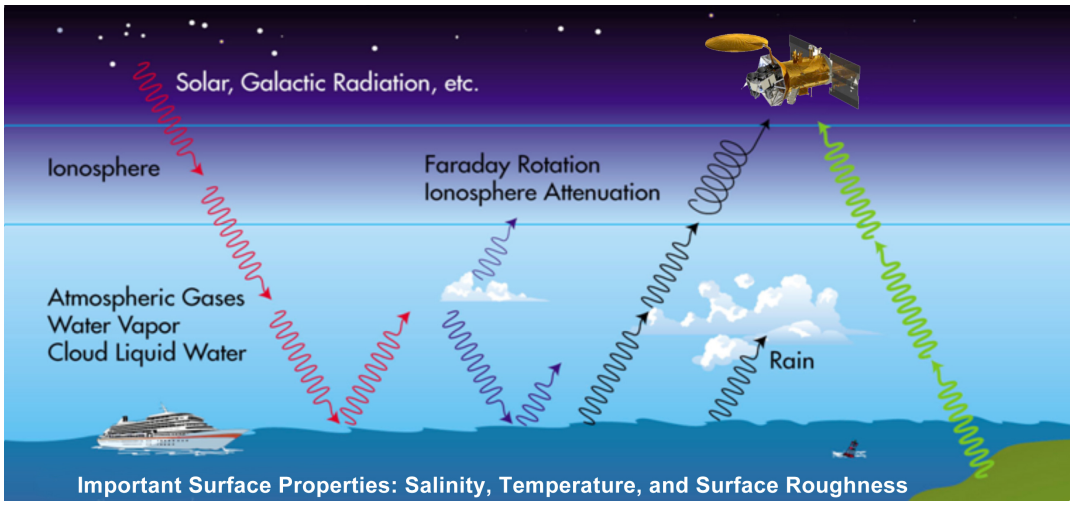


Figure 3.5 – *Signal sources interfering with salinity measurements for the **Aquarius** mission (image from Ref. [159]).*

A conventional spacecraft mission, the 1 515 kg **SAC-D/Aquarius**, was one of the two missions that recently performed salinity measurements. However, due to bus equipment failure, the mission halted its operations in 2015. The other spacecraft that is still active is the **SMOS** mission with the Microwave Imaging Radiometer using Aperture Synthesis [154]. As was mentioned before, this is a fan beam radiometer, that by electronically combining the data received by 69 antenna/receiver modules distributed in a deployable three arm structure, generates a two dimensional interferometer microwave image. The instrument has a mass of 369 kg, with a power consumption of 375 W, and each arm extends to a 8 m length.

Already discussed in Section 3.3.3 and Section 3.3.4, to fit a radiometer in a micro satellite (not even discussing a nano one) would be difficult, and, even if possible, the measurements validity of such small instrument is doubtful. Some research has also to be performed when discussing the use of microbolometers on micro and nano satellites to measure salinity. In particular, if the spectral resolution that can be achieved is enough to use the brightness temperature measurement correlation with salinity.

[iv] The unit for measuring seawater salinity is called “precision salinity units”, and the standard says that 35 psu, has a conductivity ratio of unity at 15 °C at 1 atmosphere, for 32.435 6 grams of KCl (potassium chloride) per kilogram of solution.

3.3.6 GNSS Reflectometry

Most of the remote sensing instruments seen so far are difficult if not impossible to adapt for a micro or nano satellite. Those that are possible have strong limitations because of the frequency band they use (*e.g.* imagers cannot perform observations with clouds of heavy rainfall). Therefore, some studies suggest that it is possible to use Global Navigation Satellite Systems Reflectometry (GNSS-R) to overcome these limitations and make some relevant measurements [117]. With the worldwide availability of GNSS signals, GNSS-R could be used as a complement to other instruments, but as the expected accuracy is lower, never as a substitute. While the use of GNSS-R to measure surface wind speed and direction was proposed in 1988 [160], its use for altimetry only came up in 1993 [161], and even more recently for other ocean studies (including ocean salinity, ocean circulation and sea ice) or land ones [63, 117, 162, 163].

The working principle of GNSS-R is very similar to any other radar, since it measures the scattering of a signal reflected by a rough surface to retrieve information about it. If the surface was smooth, the signal would be reflected in a single direction, and is called specular point reflection. For the oceans, the information obtained is sea and wave height, and indirectly near surface meteorological conditions. However, unlike radars, GNSS-R does not need to produce its own signal, and passively receives the GNSS signals reflected by the ocean to form an image of the scattering cross section in time and frequency, called Delay Doppler Map [117]. For this technique to work, and centimetre scale accuracy achieved, the backscattered signal has to be combined with the original GNSS, coming directly from the GNSS constellation (as seen in Figure 3.6), as this works as a coherent reference [160, 161].

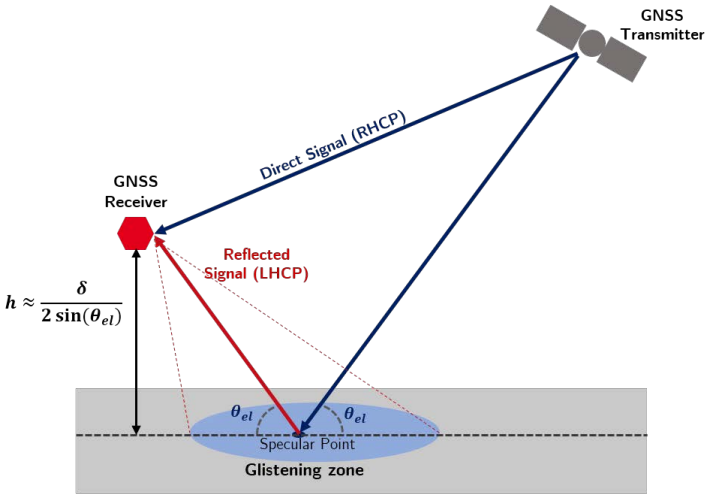


Figure 3.6 – *GNSS-Reflectometry concept (image from Ref. [164]).*

Although a 12 kg and 4.8 W GNSS-R micro satellite mission was proposed in 2002, using two GNSS receivers (a nadir pointing one and another turned to the zenith) and a solid-state data recorder [161], when the apparatus finally flew, in 2003, it was on the 88 kg **UK-DMC**. The system was only operational for 20 s each orbit, yet enough to prove the concept [160, 165]. In 2012, a

constellation of twelve non-polar orbiting nano satellites was proposed for altimetry, the GNSS Ocean Wind and Altimetry [160]. This constellation was expected to have a spatial resolution of about 30 km, a less than two days revisit time, and accuracies between 7 cm and 20 cm, for ocean topography, and more than 70 m/s, for wind speed. Again, only a single instrument, with a mass of around 1.5 kg, and approximately 10 W power consumption, was launched with the 157 kg **TechDemoSat-1** in 2014, for a more robust and extensive test [162]. More recently, in 2016, the already described **CYGNSS** constellation was launched, carrying a GNSS-R instrument, and is still operational [117]. In that same year a single 5.4 kg nano satellite, dedicated to GNSS-R, called ^{3}**Cat-2** (consuming 5.5 W and an expected payload data volume of 13.8 Mb/day [166]) was also launched, even though in this case only a beacon is known to be received.

3.3.7 The case of (and for) SAR

A synthetic aperture radar has many applications and has become one of the most important sensors for both scientific and security purposes. For oceanography, SAR can give valuable information on surface and internal waves, shoals, sea ice, rainfall, and the location of large marine mammals [167, 168], apart from being extremely successful in determining surface winds on coastal zones. Although it has also been used to determine ocean currents, using Doppler readings, the algorithms used are still very challenging [122]. As SAR can also detect man-made platforms, estimate local bathymetry, and monitor the marine environment, it is also used for military applications [169], maritime domain awareness, and marine spatial planning [170].

A SAR, like any other radar imaging systems, works by emitting a sequence of short microwave pulses and measuring their reflection, usually using the same antenna. However, by synthesising several short individual readings of the same target, as illustrated in Figure 3.7, SAR can create a single high resolution image, which for other radars would only be possible with a much larger antenna (more details on this are found in Appendix A). Using microwave signals, it is possible to observe with any type of cloud cover, without major energy loss.

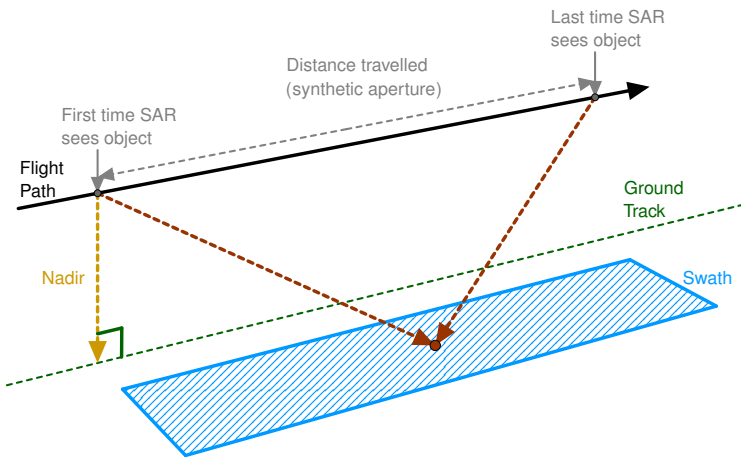


Figure 3.7 – *Synthetic aperture radar principle (image adapted from Ref. [171]).*

The first launch of a SAR equipped spacecraft was in 1978, NASA's 2 290 kg **SEASAT**, and even though it only lasted for four months (ceasing operations due to a bus malfunction), was followed by many other missions [172]. Modern major operating spacecraft are all flying in low, near polar, sun synchronous orbits, and are very massive, as shown in Table 3.6. Due to SAR peak power requirements, the system usually only operates around 10 minutes each full 100 minutes period orbit.

Table 3.6 – *Currently active earth observing spacecraft equipped with SAR payloads.*

Satellite	RADARSAT 2 [173]	TSX/TDX [174]	COSMO-SkyMed [175]	KOMPSAT-5 [176]	Sentinel 1 [177]
Launch date	2007	2007	2007	2013	2014
Sat. Mass [kg][a]	2 200	1 230/1 340	1 700	1 400	2 300
Sat. Altitude [km][a]	798	514	620	550	693
SAR Mass [kg][a]	750	394	–	520	945
Peak Power [W][a]	1 650	2 260	–	1 700	4 075
Swath [km]	20 – 500	30 – 260	30 – 200	30 – 100	80 – 400
Resolution [m]	3 – 100	1.7 – 10	1 – 100	1 – 20	5 – 40
System Band	C	X	X	X	C

[a] Figures from [127].

The use of SAR by each spacecraft is very short, and thus very localised. However, it has so many user requests for so many locations, that ESA decided to stop trying to answer to user needs and focus its **Sentinel-1** spacecraft on some selected and fixed areas of interest. Conversely, spacecraft like **TerraSAR-X** or **RADARSAT 2** still try to be open for specific area requests by the scientific community. Nonetheless, while **TerraSAR-X** releases some of the images to the public, **RADARSAT 2** ones are less freely accessible (despite being one of instruments with better accuracy and resolution).

CHAPTER 4

An Integrated Operation Scenario

Some of the reasons behind combining small satellites and autonomous vehicles have already been discussed in Chapter 1. This is further expanded in this chapter, by proposing mission scenarios and describing what has been done to combine both systems. However, before discussing system integration and the tests performed, a brief overview of both the UVigo HumSat system and the LSTS vehicles and toolchain is given here. For completeness, other conventional satellite communication systems and how they compare to the HumSat one are also presented. This chapter closely follows what has been published in Ref. [44].

4.1 Mission scenarios

When countries have large ocean areas under their jurisdiction, such as Portugal (with its current 1.72 million square kilometres area, or the proposed extension to 4 million square kilometres) or Canada (with an area totalling almost 6 million square kilometres and with over 1 600 ships per day transecting their extended continental shelf [99, 178]), they not only must maintain a constant surveillance over it, but also promote scientific studies ranging from the ocean bottom to its surface [179]. Moreover, they should keep monitoring continuously their evolution. Therefore, a diverse network of multi-vehicle systems, including both a robust autonomous network and small satellites, operating in an integrated and coordinated fashion, is fundamental. Especially since using only conventional methods entails a large investment, monetary and human.

A fundamental piece of an integrated and autonomous network, in particular for remote sea operations, is a robust and stable communication infrastructure. Any maritime mission scenario, like the one sketched in Figure 4.1, is composed of several active layers of communication, from short-range (*e.g.* Wi-Fi and radio frequency), through medium-range (*e.g.* Global System for Mobile communication, GSM, and 4G), up to long range (*e.g.* satellite communication). Furthermore, any of the links used are not frozen, and with the coming and going of different assets to the operational area, these must be re-arranged as needed.

The goal here is to show that by replacing costly conventional satellite communication systems with new small satellites, the cost overhead of this link can be significantly reduced. Furthermore, with small satellites there is more control over its capabilities and functionalities, and the potential

to reduce maritime operations cost and complexity. With these spacecraft it is not only possible to work in a plug-and-play communication mode, fundamental to create a system of systems, but also to equip them with their own on-board payload, making them an active part of the observation and data collection capabilities of the network.

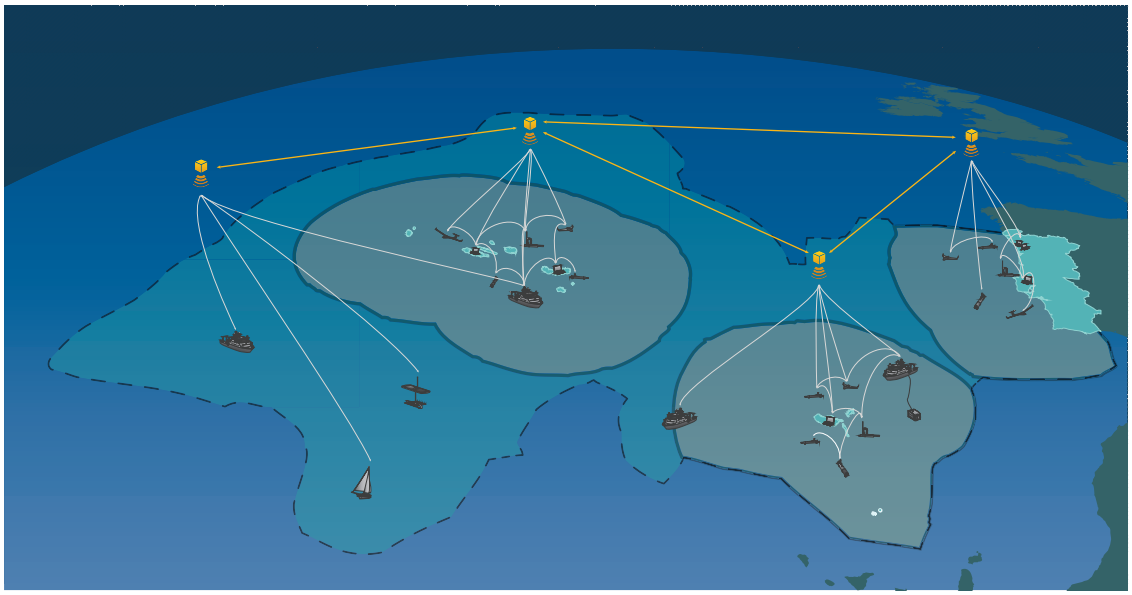


Figure 4.1 – *Portuguese operational scenario composed of several assets, including small satellites, showing their communication links.*

To study the use of small satellite communication by an autonomous vehicle network, a single spacecraft test platform will be used. Even though a constellation is needed to fulfil the goals stated above, this has an increased cost and time to build, making it unsuitable for an initial test. Several UAVs, equipped with the payload of the small satellite, can be used instead to understand the scalability of the network and its major issues (*e.g.* bandwidth and radio network capacity), although the range and scope would not be as far-reaching as with satellites.

The need of UAVs, and the required plug-and-play functionalities, are strong reasons for the use of a pre-existent software toolchain, devised to handle such operational setups, like the one of *Laboratório de Sistemas e Tecnologia Subaquática* (LSTS). Moreover, using the LSTS X8 UAV, and transmitting the vehicle's position and velocity only, makes the test and the integration easier, while at the same time the data can be cross checked with the one sent through the already present Wi-Fi and GSM communication channels. Nevertheless, more and different metadata can be sent, since the communication protocol designed is agnostic to the type of data, apart from supporting message segmentation and reassembly, to transmit data too extensive for a single message.

4.2 LSTS network system

With regular large scale exercises and tests [180], LSTS has developed a comprehensive software toolchain and a few low-cost vehicle solutions. It is currently composed by a multi-disciplinary

research team, from electrical to mechanical engineers, including computer scientists, all faculty members and students.

All LSTS vehicles are designed, or adapted, to support network operation scenarios, and to use both modular hardware and software. This not only facilitates the development and maintenance of the vehicles themselves, but also streamlines all operations and exercises. Furthermore, the toolchain software, used both on the vehicles and at the ground stations (to command and control all types of vehicles in an uniform manner), is all open source[i], promoting a higher integration with software and hardware developers.

4.2.1 Software toolchain

Building on the experience of coordinating the operation of several heterogeneous vehicles, a unique toolchain was developed [29]. The idea behind the toolchain was to establish a mixed-initiative control software (*i.e.* humans in the planning and control loops) [181], for different types of unmanned vehicles (from ocean to air), all operating in a communication challenging environment. With the support for Disruptive Tolerant Networking (DTN) protocols [182], the toolchain is made up of several layers of different software, as depicted in Figure 4.2. This provides a user friendly interface that can be operated by anyone, anywhere in the world. Each element of the toolchain has its own function, namely:

Ripples. Used as a web entry point, running in any desktop and mobile devices, it provides a communication hub for data dissemination and global situation awareness. Information displayed in the browsers, about the deployed assets, includes position, mission intelligence and collected data, and is updated in real-time. All data shared by remote assets is collected and stored in Ripples, which allows to coordinate geographically distributed teams, even if there are severe restrictions in the communication network.

Neptus. The Neptus software works as a distributed command and control infrastructure, where all types of vehicles are monitored and controlled by one or more operators. Written in Java and running in Linux or Windows operating systems (an app version is being developed), Neptus supports every phase of any mission, including planning, simulation, execution and post-mission analysis. Apart from a base environment, new functionalities or displays can be added via plug-ins, allowing each user to adapt the software to fit mission-specific requirements.

IMC. The Inter-Module Communication (IMC) protocol was designed and implemented so that every network element, vehicles, sensors and human operators, can be interconnected. Therefore, through an abstraction of the hardware and communication heterogeneity, a standard message format is available to be filled, serialized and transferred over different communication channels.

[i] The source software is available online at the GitHub repository, found at `https://github.com/LSTS`.

Since any element has access to the messages circulating within the network, the information about the environment, vehicle state, or updated objectives is shared in real-time, helping the network to pursue common goals cooperatively.

DUNE. The last layer of the toolchain is the software running on-board the vehicles, the Unified Navigational Environment (DUNE). It oversees all vehicle activities, including communication, navigation, control, manoeuvring, and plan execution, apart from managing all hardware interactions (*e.g.* with sensors, payload and actuators). Written to be CPU architecture independent, as well as from the operating system, it is composed of several tasks, each with its particular function.

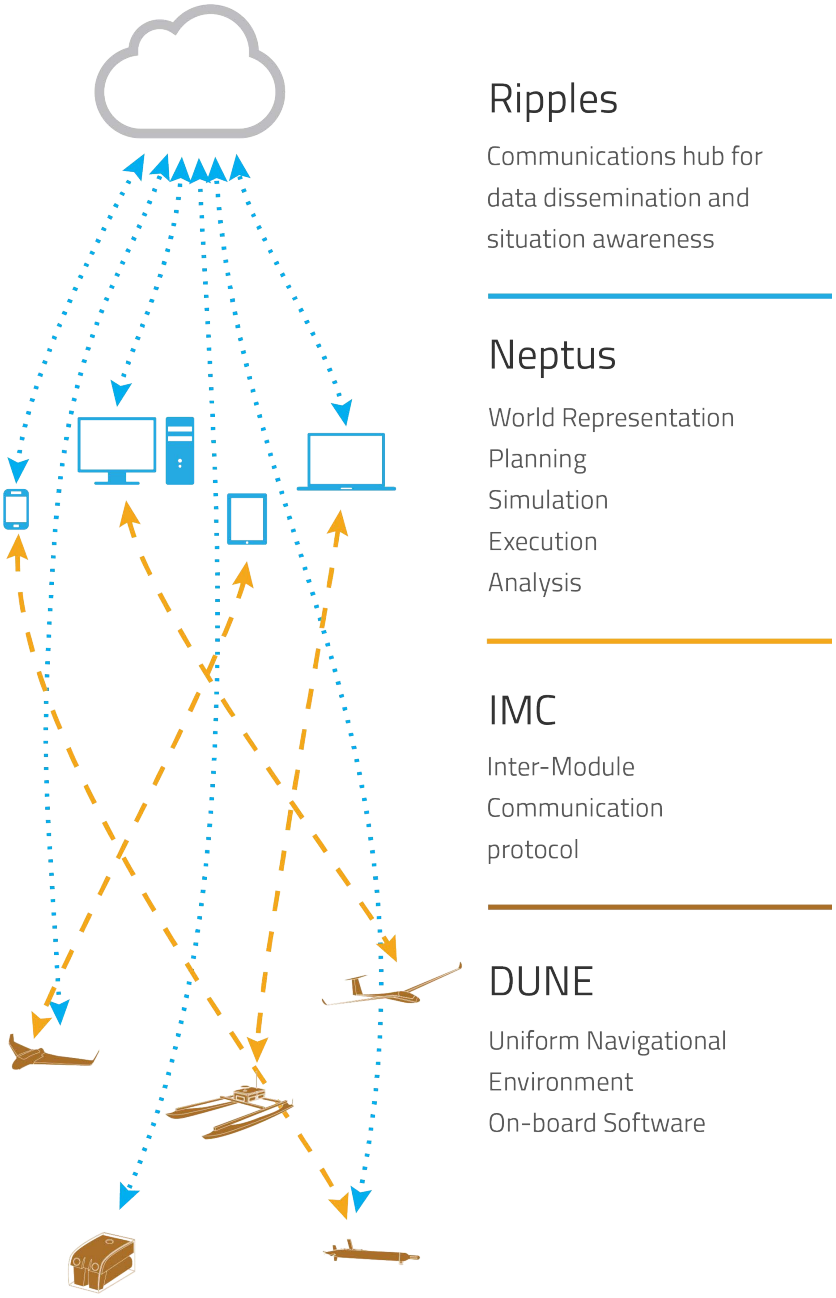


Figure 4.2 – *Visual representation of the LSTS toolchain layers.*

4.2.2 Autonomous vehicle system

The selection of the platform to serve as testbed of a small satellite communication protocol, among the various vehicles available at the LSTS, was straightforward. The decision was to use small UAVs, not only because the hardware integration is simpler, but also because the communication links are easy to configure (for example, a clear view of ground station and space is always available, without having to modify the vehicle behaviour).

From some of the UAVs LSTS already operated, the preferred one nowadays is the delta wing X8 Skywalker (seen in Figure 4.3). With already a large experience within various types of operational scenarios, the X8 is a COTS vehicle modified by LSTS to fit its needs. Although the X8 is designed with a glider shape and size, and it has very light logistical operation setup (making it as simple as a one-man single laptop setup configuration), it is capable of a large array of missions. In particular it was optimised for low altitude reconnaissance scenarios, with live video feed, and for remote sensor scenarios. The operations are so simple that for a first flight, covering the mounting of the UAV and turning on all consoles, only takes about 20 min, whereas subsequent flights takes 5 min to prepare.



Figure 4.3 – *X8 Skywalker autonomous aerial vehicle ready for launch (using a catapult).*

That multitude of missions are also made possible by its wide oval internal area, capable of easily accommodate many payloads (a benefit for testing the prototype small satellite communication). Made almost all of Expanded PolyOlefin (EPO) foam, as listed in Table 4.1, there are also small wood connectors to slide the wings into the main body. There is no documented turbulence restrictions, no minimum visibility conditions for operation, neither strict outside air temperature limitations (apart from the ones determined by the LSTS equipment flying inside, 0 °C to 40 °C). Because the temperatures are limited, and the X8 would not operate in an environment propitious for icing condition, there is no in-flight icing problems.

Table 4.1 – *Main characteristics and specifications of the X8 Skywalker vehicle.*

Parameter	Value
Model Designation	X8 Skywalker
Design	Fixed wing delta wing
Material	EPO Foam
Motor Type	Electric
Fuel/Energy	LiPo battery
Length	0.80 m
Wingspan	2.12 m
Body Diameter	Oval (from 0.15 m to 0.30 m)
Brakes	None
Hydraulic System	None
Parachute	None
Weight Empty	1.2 kg
Mean Take-Off Weight	4.3 kg
Indicated Air Speed (Min|Cruise|Max)	15 | 18 | 23 (m/s)
Wind Tolerance (Head|Cross|Gust)	17 | 15 | 19 (m/s)
Maximum Endurance	50 min
Maximum Range	20 000 m
Maximum Altitude	350 m
Maximum rate of climb	2 m/s
Maximum rate of descent	3 m/s
Maximum bank angle	30 deg
Turn radius | Turn rate limits	31 m | 32 deg/s

4.3 Commercial communication systems

Due to the contributions of visionaries such as Arthur C. Clarke, in 1945, or pioneers like John Pierce of Bell Laboratories, in 1954, the concept of satellite communication gained strength at late 1950s, early 1960s [183]. By 1964, an international organisation to develop and oversee satellite communication between different countries and telecommunication entities had been created, INTELSAT [183]. A fully European system followed, with EUTELSAT definitive agreement being signed in 1985 [183]. A need for a maritime mobile service was recognised by the International Maritime Organisation (IMO), which lead to the establishment in 1978 of an international organisation to develop, oversee, and regulate maritime satellite communication, INMARSAT.

By that time, it was already evident that satellite communication was a lucrative business on a global scale. Consequently, a large number of global mobile satellite personal communication systems were created, with proposals of constellations of satellites between 2 and 10 billion dollars [183].

Although most systems are thought to process large volumes of data, either video, voice or data (*e.g.* Iridium), there are systems designed just for data collection (*e.g.* Argos). The objective for these data storage and forward systems is to allow a spacecraft to receive small amounts of data from several small ground terminals. That data would then be downlinked to a ground station either immediately or later, depending if the spacecraft is in view of a ground station at the time or not.

4.3.1 INMARSAT

INMARSAT was the first satellite communication service thought to fulfil maritime needs. The main, and initial, objective was to provide international maritime mobile satellite services. This allows ship to maintain a constant communication channel with shore, even when in the middle of the ocean (and particularly at an emergency), apart form providing efficient ship management [184]. The system was later expanded to supply both aeronautical and land services [185]. The target market is now very wide, including governments, oil, gas and mining industries, merchant shipping, and broadcast media, dealing with large volumes of communication [186]. Since its foundation the organisation had a significantly growth, in particular as a response to the market evolution and the set up of private endeavours. Thus, it was the first intergovernmental organisation to be established as a private company [183].

Arranged in a four-ocean-region configuration (illustrated in Figure 4.4) [183], it counts today twelve operational satellites, from different generations [187]. The newest spacecraft network, which entered in operation in 2015, is called Global Xpress, and has three satellites plus a spare one at a Geostationary Earth Orbit (GEO), *i.e.* at an altitude of about $35\,800\,\mathrm{km}$ [186]. An INMARSAT Global Express spacecraft has about $6\,100\,\mathrm{kg}$, measuring $6.98\,\mathrm{m} \times 33.8\,\mathrm{m}$. Part of these dimensions account for the five solar panels which, after $15\,\mathrm{years}$ in orbit, can still produce over $13\,\mathrm{kW}$. To maintain its GEO orbit it is equipped with a Xenon ion propulsion system. To route all data received by the satellites to the end customer several ground stations are available worldwide.

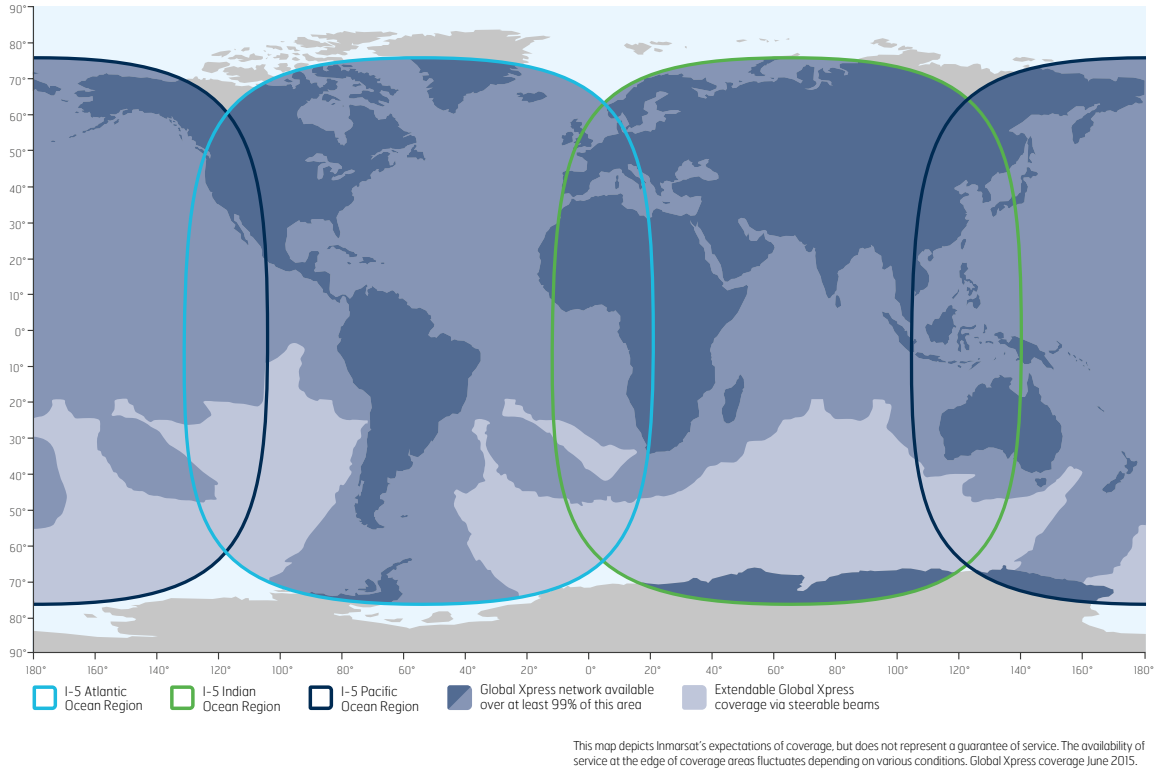


Figure 4.4 – *Global coverage map of the Global Xpress INMARSAT network (image from Ref. [186]).*

To communicate with the satellites, the customers can rely on several types of equipment, from handheld satellite phones (*e.g.* the IsatPhone 2) to radios (*e.g.* the Fleet One Handset) [186]. The latter have to be linked to fixed $2.5\,\text{kg}$ antennas (measuring $27.5\,\text{cm} \times 22.1\,\text{cm}$), and can provide up to $100\,\text{kbits/s}$, while consuming around $100\,\text{W}$ [188]. There are smaller options, with modems of just $12.6\,\text{cm} \times 12.6\,\text{cm} \times 4.9\,\text{cm}$ (for powered vehicles) or $43.2\,\text{cm} \times 14.7\,\text{cm} \times 2.5\,\text{cm}$ (for a modem equipped with batteries), used for messaging services, *e.g.* the IsatM2M service [189]. These smaller modems can weight up to $1.3\,\text{kg}$, including batteries, while the antennas measure $12.6\,\text{cm} \times 9.3\,\text{cm} \times 7.4\,\text{cm}$. Nevertheless, since the satellites are at about $35\,800\,\text{km}$ away, the terminals require more power to transmit (up to $9\,\text{W}$).

4.3.2 Iridium

Within satellite communication services, Iridium is one of the most well known. The premise, introduced in 1987, was to have a global satellite phone system, before cellular telecommunication networks had been globally deployed [190]. The original plan was that a constellation of 77 low Earth satellites was required to have global coverage. The parallelism between this configuration and the chemical element was what actually gave the name to the system [191]. It took nine years to set up the network, and a factory was even build to have an assembly line, in an effort to standardise all satellites. After a complicated start, with the company declaring bankruptcy just one year after the first call, the system was re-launched in 2001, providing global voice and data coverage to specialist applications, including rescue services, military, and missions to remote areas.

When the first call was made, in 1998, the system was using 66 satellites (without counting spares), all considered the most advance telecommunication satellites at the time, distributed by 11 orbital planes [183]. In fact, one of the unique characteristics of this system is that the satellites are capable of exchanging messages between them, with each satellite linked to four others [190]. This creates a robust network in space, which is independent of the ground stations distribution and availability. When a user sends a message to another one, the satellite passing above receives the message and transmits it to another satellite, and so forth, until it reaches the spacecraft over the end user, instead of being retransmitted to ground immediately [192].

Iridium satellites are orbiting at an approximate altitude of $780\,\text{km}$ (*i.e.* they are LEO spacecraft). Although the first satellites had life spans of five years [191], the new ones, called Iridium NEXT (depicted in Figure 4.5), are closer to $12.5\,\text{years}$ [193]. These are smaller (only $2.4\,\text{m} \times 9.4\,\text{m}$ when deployed), lighter (with a mass of just $860\,\text{kg}$), and require less power to operate (about $2.2\,\text{kW}$), when compared to INMARSAT. With the launch of these recent spacecraft, new features have been studied, including carrying secondary payloads (*e.g.* altimeters and imagers) [192].

Because the satellites are much closer to Earth, the commercialised user terminals, provided by other companies, are also smaller, with omnidirectional antennas, and using less power (a premise of the Iridium system [190]). Although the initial idea was that a phone could provide both terrestrial communication as well as satellite ones, changing between them depending on availab-

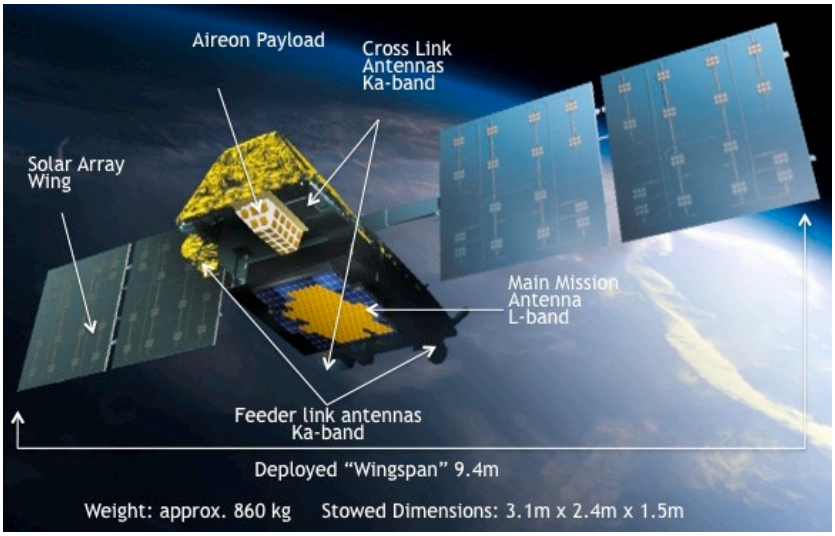


Figure 4.5 – *Illustration of Iridium NEXT spacecraft with main dimensions and components (image from Ref. [194]).*

ility, currently the most advanced systems (an equipment with $1.35\,\mathrm{kg}$ and a $12.5\,\mathrm{kg}$ antenna) are used just for satellite communication. This includes a broadband connection and three independent voice lines [194]. This system has a capability for data transfer rates up to $134\,\mathrm{kbits/s}$, with a power consumption around $31\,\mathrm{W}$. Conversely, there are also much smaller transceivers, used mainly for short data (less than $340\,\mathrm{bytes}$) transmitted by short bursts (with data rates of about $2.4\,\mathrm{kbits/s}$) [194]. Another example of a company providing Iridium communication equipment is Rock Seven, with its $0.076\,\mathrm{kg}$ and $7.6\,\mathrm{cm} \times 5.2\,\mathrm{cm} \times 1.9\,\mathrm{cm}$ RockBlock transceiver (an adaptation of the Iridium 9602 transceiver) [195], which consumes less than $1\,\mathrm{W}$ when transmitting [194].

Common access plans include a lease of the system and charges for each transmission, *i.e.* either duration or volume of data exchanged. While Rock Seven charges $\$10\,/\mathrm{month}$ nowadays, plus $\$0.14\,/\mathrm{message}$ (with a message containing a maximum of $50\,\mathrm{bytes}$) [196], CLS Group, for the large bandwidth real-time system, already charges about $1\,€/\mathrm{kbytes}$ of transmitted data [197]. There are other companies that have voice plans, charging $\$0.75\,/\mathrm{minute}$ to $\$1.50\,/\mathrm{minute}$, for outgoing calls, and several dollars per minute for incoming ones.

4.3.3 Argos

Initially a partnership between the French Centre National d'Etudes Spatiales (CNES) and both NOAA and NASA agencies, Argos now also includes Eumetsat and ISRO [198]. The system was designed specifically to perform research and protect the environment, by collecting and relaying meteorological and oceanographic data. There is a large number of buoys equipped with Argos deployed all over the world, and Argos 2 terminals are small enough to be even used to tag wildlife, like turtles and birds. Other applications include fisheries, and sometimes maritime security.

Although created by those institutions, Argos is operated and managed by the CLS Group. A single charge of about $4\,€/\mathrm{day}$ is made to the user when transmitting data, with a maximum of

63 €/month [197]. Although there is no volume limitation, the number of satellite passes limits the data that a user can send per day.

The second version of the system provides global coverage and Doppler location capability. If the user wants it, it can link a GNSS to the Platform Terminal Transmitter, to have a higher location accuracy. Yet, the terminals are configured to transmit messages at a regular interval, and do not have a downlink acknowledgement. However, with Argos 3, the new version of the system, two way communication is already possible, and the terminals (now called Platform Messaging Transceivers), only transmit data when they receive an acknowledgement by the satellite (*i.e.* when it is in view of the transceiver) [199].

Argos 3 transceivers come in two versions, a lighter one (with a mass of 0.08 kg measuring 1.8 cm × 4.3 cm × 10 cm), manufactured by Elta exclusively for CLS (shown in Figure 4.6) [200], or a heavier one (2.5 cm × 6 cm × 8 cm with a mass of 0.16 kg) and produced by Kenwood [201]. Both transceivers have the same power consumption (around 5 W), use UHF (≈ 402 MHz for transmitting and ≈ 466 MHz for receiving), and a structured message composition (not exceeding 31 bytes per message [197]). The data rate is close to 400 bits/s [197], with a typical transmission lasting 920 milliseconds.



Figure 4.6 – *Elta platform messaging transceivers for the Argos 3 version (image from Ref. [201]).*

When compared to the previous systems, one of the main differences is that Argos does not have dedicated satellites, depending on other large spacecraft (*e.g.* 4 087 kg **MetOp** and 2 232 kg **NOAA** 5th generation [127]) to function. These spacecraft have all 800 km Sun-synchronous orbits, and are equipped with Argos payloads (a 16 kg receiver and a 8 kg transmitter), besides their main payloads. With these payloads, the system can provide a data rate of up to 4.8 kbits/s [199], which means that, together with the orbit of the satellites, up to 3.1 kbytes are upload each pass (in interactive mode with downlink acknowledgement) [197]. Adding this up, with the average number of passes per day, dependent on the transceiver latitude, about 10 kbytes can be transmitted [197].

In terms of ground segment, the system has three main ground stations to receive all user data aboard the spacecraft, even though there are several regional ones capable of data relay (*i.e.* receive data if the station and transmitter are under the same footprint).

4.4 The HumSat system

In 2011 the University of Vigo (UVigo), the California Polytechnic State University, the National Autonomous University of Mexico, and the Regional Center for Education in Space Science and Technology in Latin America and Caribbean Countries, started a project to develop a communication system based on the small satellite form factor, the HumSat system [30]. This project, mainly supported by UNOOSA and ESA (with a help by the International Astronautical Federation), still in development, is different from the systems presented above (mainly in the components size). Nonetheless, there are many similarities with the Argos concept, as Table 4.2 shows.

Table 4.2 – *Main characteristics of the satellite communication systems described (data from Refs. [194, 196, 197, 199]).*

System	Orbit Altitude [km]	Comm. Type	Transmitting Power† [W]	Data rate† [kbits/s]	Data Amount per Message† [bytes]	System of systems
INMARSAT	35 800 (GEO)	Voice	100	100	–*	No
		Data	9	–*	6 400	
Iridium	780 (LEO)	Voice	31	134	–*	No
		Data	1	2.4	50	
Argos	800 (LEO)	Data	1	4.8	31	No
HumSat	600 (LEO)	Data	1	1.2	32	Yes

† Values shown are top limits.
* Information not available.

When the concept was presented, the main goal was humanitarian, namely by providing a free non-guaranteed store and forward data system to serve areas not covered by telecommunication services [202]. Nevertheless, it was already designed to support remote sensors (equipped with the HumSat transmitters discussed in Section 4.4.1) to relay their data to the end users, by storing short UHF messages and later sending them to a ground station, without the need for a ground communication network [30].

Nowadays the system has fulfilled its technological demonstration, and is slowly moving to commercial applications, with the advent of HumSat 2.0 [202], and the deployment of a constellation of small satellites. With this new version UVigo is trying to maximise the number of users, besides implementing two-way communication, among other capabilities. These extra features include data relay between terminals, new access schemes, encrypted communication, prioritization, error correction algorithms, management of terminal network, and fixed and mobile terminals support.

With the space segment (described in Section 4.4.2), UVigo has also build a standardise ground station at the university campus (Figure 4.7). This is equipped with two redundant stations capable of receiving four simultaneous polarisation signals (even though to command and downlink information a small antenna would suffice), and a set of operational software and tools to control all HumSat spacecraft [202]. The ground station has VHF, L and S-band capabilities, on top of the UHF ones, so it can be used to support other small satellite operations.

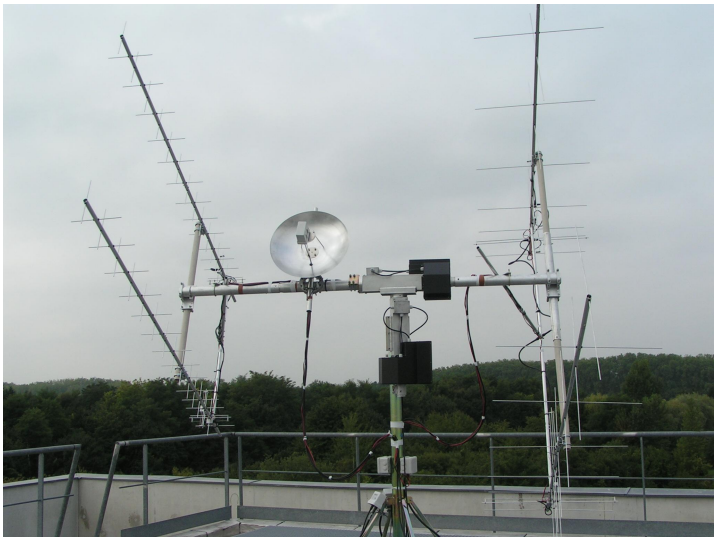


Figure 4.7 – *Ground station for the HumSat spacecraft at the University of Vigo.*

4.4.1 User segment

For the current version of the HumSat there are two available transmitters, or user terminals: an automatic or autonomous platform (shown in Figure 4.8) and a simple board. While the former is a plug and play solution, relaying any data passed by a user sensor, the latter one is connected directly to the user equipment (using its own hardware), and a driver has to be integrated in the user software [202].



Figure 4.8 – *HumSat automatic and autonomous platforms.*

The simple HumSat transmitter board, depicted in Figure 4.9, has three main modules: a Radio Frequency (RF) stage (which U.FL connector links the board to an antenna), a control stage (with an interface similar to the Arduino Shield one), and a power stage. The full board measures $13\,\text{cm} \times 5.3\,\text{cm}$, has a mass of $30\,\text{g}$, and consumes only up to $3.2\,\text{W}$ when transmitting at $30\,\text{dBm}$. If just $27\,\text{dBm}$ are required for transmission, the board would consume $2.4\,\text{W}$, while in standby its consumption is less than $0.14\,\text{W}$. This simple board is the best option for the integration work developed here, because it has to be integrated into an UAV, and thus it should be light, small and require low power.

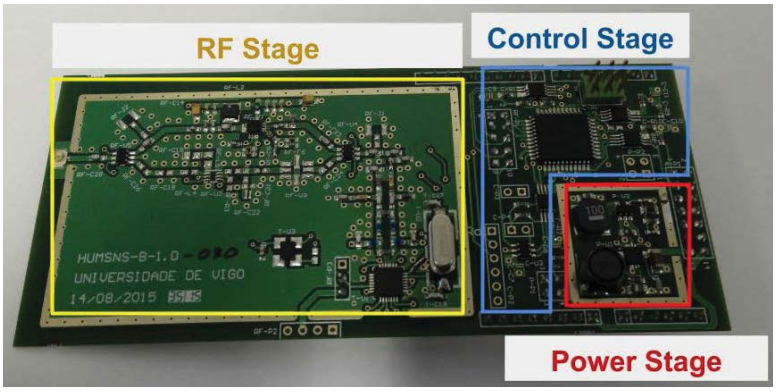


Figure 4.9 – *HumSat transmitter board photo, with modules identification.*

This board has to be powered using an unregulated line from 4.3 V to 17 V, using the VIN (voltage in) and the GND (ground) pins, as it regulates its own logic accordingly. To communicate with the board a Universal Asynchronous Receiver/Transmitter (UART) serial bus has to be used, via the Digital Transmit (TX) and Receive (RX) pin (DOUT and DIN pin respectively). The recommended bit rate is 9.6 kbits/s, and the communication voltage levels should be fed to the Input/Output Reference pin (IOREF).

The board communicates with the spacecraft using a GMSK (Gaussian Minimum Shift Keying) modulation, with a transmission data rate of up to 1.2 kbits/s. Although configurable, the frequency range of the RF output signal is between 400 MHz and 470 MHz, with a maximum power of 30 dBm.

In the new version of the terminals, within HumSat 2.0, a similar electrical configuration will be used, although the hardware is expected to be smaller and capable of handling higher data rates. Besides the two transmitters available, there are new smart terminals being developed, with the capability of being dynamically integrated with newer sensors [202].

4.4.2 Space segment

The similarities with Argos finish when discussing the space segment, in particular in what concerns the spacecraft that are used. HumSat is based on small satellites, more exactly CubeSats, instead of relying on conventional satellites. Although a constellation was always assumed, only a few ones have been launched so far, and neither were operating at the same time.

The first CubeSat carrying a HumSat payload, **HumSat-D**, was launched in 2013, and was supposed to serve as a demonstrator and to be a standard for the system constellation [202]. It was a 10 cm × 10 cm × 11 cm, 1 kg CubeSat, based on the previous bus designed by UVigo, **Xatcobeo** (seen in Figure 4.10). With solar cells in almost every spacecraft face, it produced around 3 W, enough to power both the bus and the communication payload. This payload was made of a single electronic board, and one turnstile omnidirectional antenna (with four monopoles), so that no attitude control was needed. Operational for over a year, it was launched as a secondary payload from a Dnepr-1 rocket, released to a 600 km altitude orbit [203].

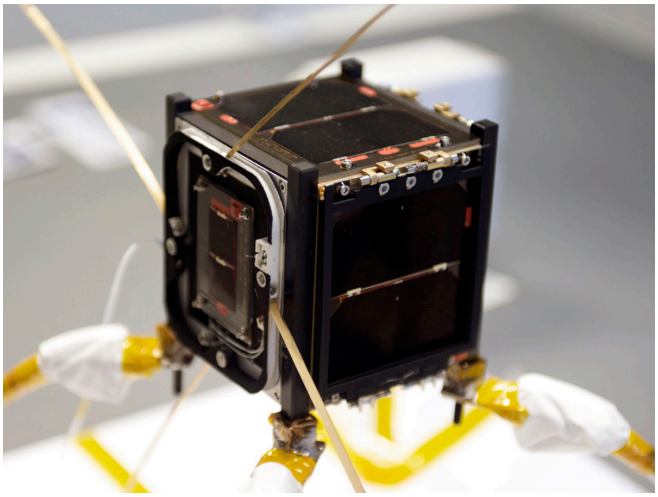


Figure 4.10 – *Xatcobeo satellite photography (image from ESA-UVigo/INTA).*

After *HumSat-D*, and based on the acquired experience (*e.g.* the detected external interferences in the UHF band), a new enhanced payload was launched inside the **Serpens** spacecraft. This $10\,\text{cm} \times 10\,\text{cm} \times 34\,\text{cm}$ and $3\,\text{kg}$ CubeSat was built by the University of Brasilia, with UVigo support and funded by the Brazilian space agency, to test new system functionalities and combinations of payload and user terminals (to be used in future implementations).

4.5 System integration and test

The integration of both systems, the UAV and the HumSat SDR, involves first the software and then the hardware link. Afterwards, several bench and field tests were carried out, to both validate the full setup and to determine possible improvements or shortcomings, that could be useful for the next version of the integrated system and of the HumSat.

4.5.1 Software

The software written for the UAV to communicate with the SDR was done within the LSTS software toolchain, described in Section 4.2. The main task was named SatComms and was placed inside the Transports (communication and logging) section of DUNE's code organization.

The current version of the task is used to collect and parse all data to be sent by the satellite link, apart from determining when the spacecraft is above the vehicle and messages can be transmitted [204]. A driver, using UVigo's libraries, was also added to the task to manage the interaction with the HumSat SDR transmitter. SatComms basic workflow is depicted in Figure 4.11.

When the task is activated the user is able to modify several parameters related to the SDR configurations and spacecraft orbit characteristics (including period, communication window and last passage). The type of data to be transmitted by the task, and if it is to be sent when the satellite is in view, are also options available to the user.

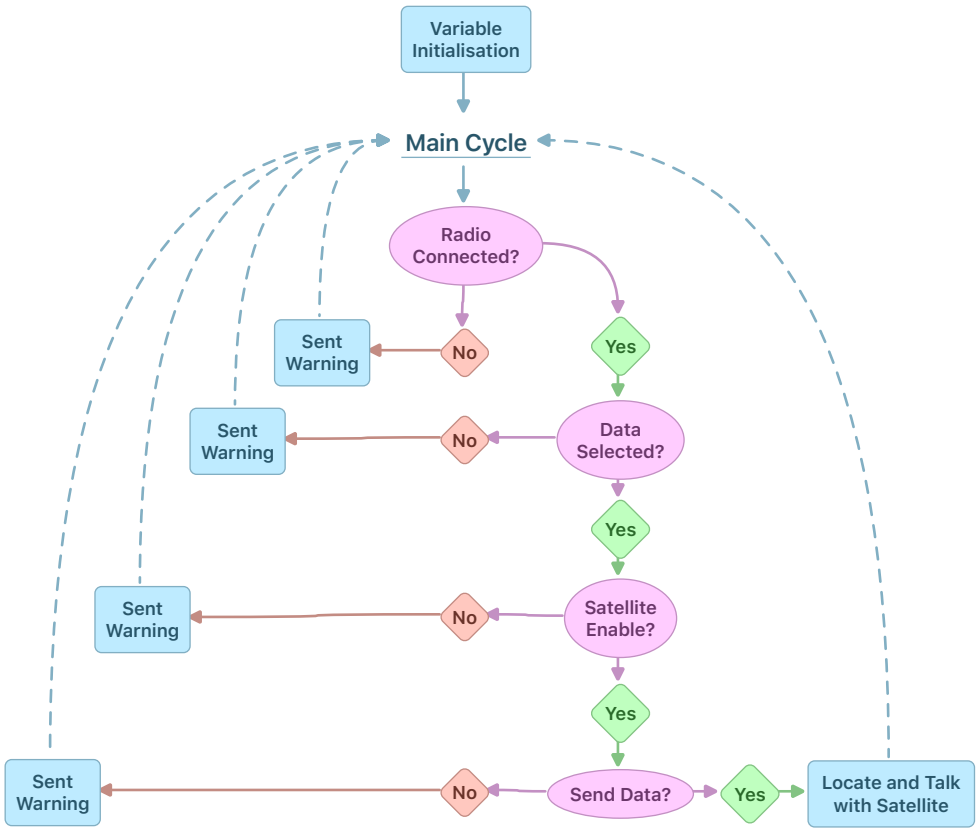


Figure 4.11 – *Schematic flow of the SatComms driver task.*

One of the HumSat shortcomings and major concerns, the 32 bytes message limit, was overcome by fragmenting the data to be sent into smaller parts, which are reassembled back to its original state later. This option was selected as it was already implemented in the toolchain, besides being a solution independent of the data type to be parsed and transmitted.

4.5.2 Hardware

Mounting the HumSat SDR onto the X8 payload bay, and linking both in terms of hardware, is a simple process, since the UAV main Central Processing Unit (CPU) and the SDR have a 3V3 TTL (Transistor-Transistor Logic) serial communication. Figure 4.12 details the electronic connections for the X8 and where the SDR is placed.

A missing component from the previous discussion is the SDR antenna. Firstly, a UHF antenna has to be used, since the HumSat uses that frequency. However, there are many radiation patterns and a selection has to be based on the user needs. Since the UAV would use the HumSat SDR to communicate with both the spacecraft above and other sensors bellow, at least two directions have to be covered. Therefore, no directional antenna should be used and, at the same time, omnidirectional antennas are not required, since the forward and aft directions do not need to

be covered. This leaves the dipole antenna as the best option and, for this particular case, a UHF Dipole 433 MHz model [205] was selected. It was installed on the nose of the vehicle and connected to the U.FL connector of the SDR, as seen in Figure 4.16.

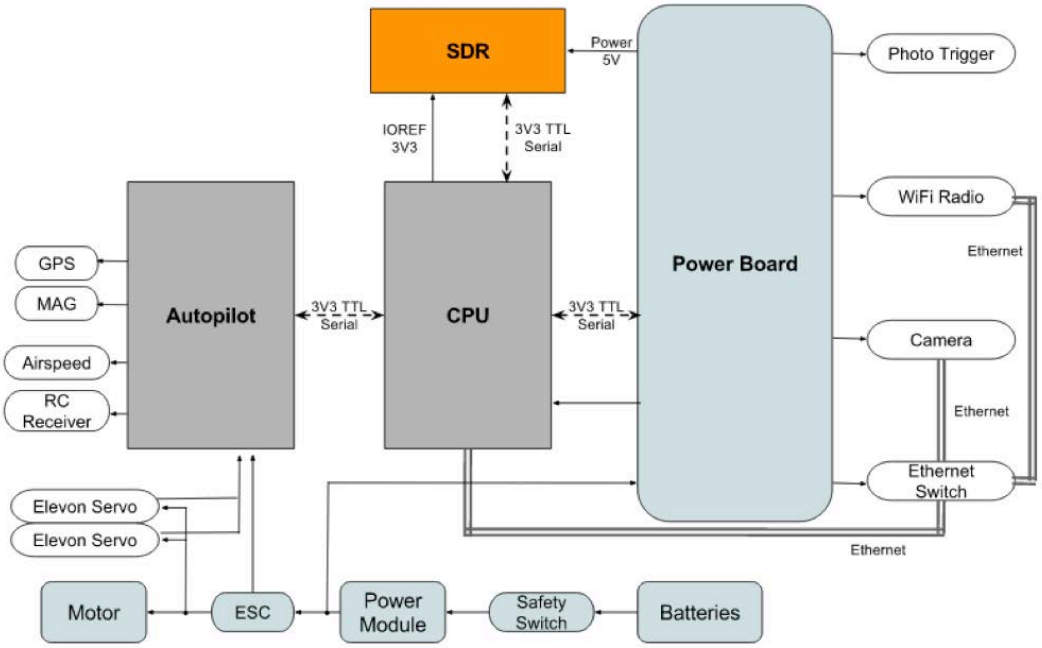


Figure 4.12 – *Block diagram of the X8 avionics and the HumSat SDR connections.*

4.5.3 Tests and results

To test the integration work a set of incremental steps were devised, starting with workbench tests, a communication dry-run, and ending with some field trials. However, a replacement of the real spacecraft had to be used which would mimic the spacecraft payload behaviour, since the satellite launch was scheduled only for the end of 2018. Although the communication protocol is agnostic to the type of data being sent, and thus works in any maritime scenario, the field tests were performed over land, since the project funding these developments is focused on forest fire combat [206].

4.5.3.1 Workbench tests

The first batch of tests were with a Hardware-in-the-Loop (HITL) setup, to verify every implementation step in a simulated environment. In particular, the test was focused on data fragmentation, transmission and reconstruction.

The components required for this test, most seen in Figure 4.13, include an exact replica of the UAV avionics used (a X8 Testbed), the HumSat SDR (with a simple dummy antenna), the spacecraft payload simulator provided by UVigo, and a Neptus Workstation (*i.e.* basically a laptop running Neptus).

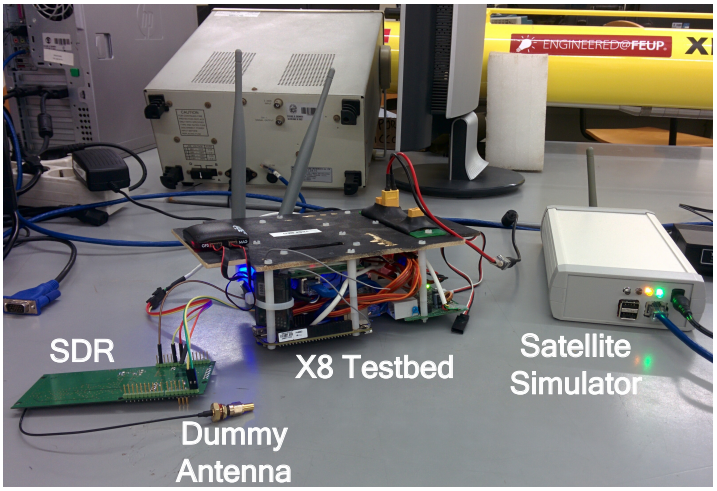


Figure 4.13 – *Workbench test setup with the main components used (the X8 Testbed connected to the HumSat SDR, and UVigo's satellite simulator).*

For these tests all components are connected to the same Wi-Fi network, with the simulator configured to send the data received by it to a particular IP and port (corresponding to the Neptus Workstation). Although the initial tests had some problems, after solving them, Neptus was able to receive all message fragments and reconstructed the initial data.

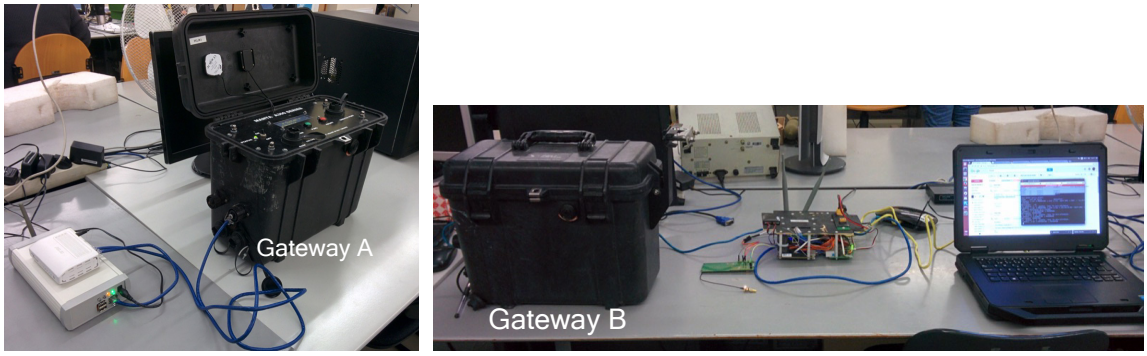
The problems occurring with the first tests were related to the SDR sending multiple times (four to be precise) the same message, for added redundancy. This had to be sorted out by Neptus, so it could handle repeated fragments correctly.

4.5.3.2 Communication dry-run

With the software architecture validated, the next step was to emulate a real operational scenario. In a real situation, the X8 (equipped with the SDR) would be connected to the same network of the Neptus Workstation (although this is not truly necessary), while the spacecraft (in this case the simulator) would be transmitting to a ground station in a different network. That latter would send the data collected to the LSTS server, which acts as a data router, retransmitting the messages received by the ground station to the Neptus Workstation in the field. To simulate this arrangement, apart from the components used in the previous test, two communication gateways[ii] had to be used (as shown in Figure 4.14), as these are capable of providing 3G connection (each with its own IP), creating thus isolated networks.

To setup this test the spacecraft payload simulator is connected to one gateway (gateway A), as shown in Figure 4.14a, while the X8 Testbed (with the SDR) and the Neptus Workstation (playing the role of a remote DPC, Deferred Procedure Call) are connected to the communication gateway B, Figure 4.14b. The X8 Testbed and Neptus are on the same network only for logistical convenience, as a local workstation is required to command the testbed.

[ii] The LSTS uses a portable communication hub, called Manta Communication Gateway (`http://lsts.pt/support_systems/manta`), which can have multiple active communication channels at the same time.



(a) *Network A* **(b)** *Network B*

Figure 4.14 – *Both networks of the test setup for the communication dry-run scenario.*

On the schematic for the communication links, Figure 4.15, the satellite simulator receives data from the HumSat SDR (using UHF) and transmits it to the LSTS server, through gateway A. The server, located at the laboratory and connected to the Internet, routes the messages received from gateway A IP to gateway B IP, which in turn delivers all server incoming traffic to the Neptus Workstation. Since Neptus can distinguish between the received traffic, it can tell what comes from the UAV and what is being sent by the spacecraft. In fact, Neptus can only receive data sent with the SDR through the LSTS server communication routing.

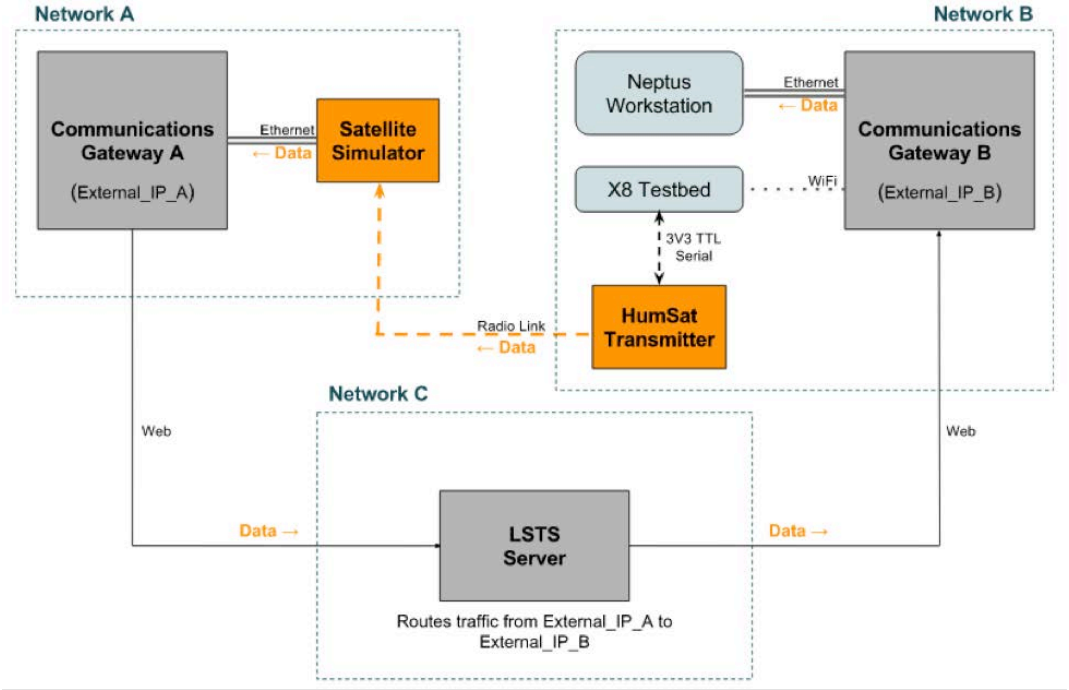


Figure 4.15 – *Block diagram of the communication links for the communication dry-run scenario.*

The test sequence, with desired outcome and results, is listed in Table 4.3. All tests were passed, even if not at the first trial.

Table 4.3 – *Communication Dry-Run validation tests.*

Test	Description	Expected Outcome	Results
Configuring network interface in Simulator	Manual configuration of eth0	Connection established between gateway and simulator	OK
Configuring Simulator *NeptusConnections*	Configure IP and port values	Connection established with LSTS server	OK
Connecting communication gateways to internet	Enable "Mobile Internet" in both gateways and give external IPs to POC at LSTS	Mobile Internet successfully established and external IP attributed	OK
Routing incoming communication [client]	Add iptable rule to route incoming data from LSTS server to Neptus workstations	Iptable rule successfully saved	OK
Routing incoming communication [server]	Configure LSTS server firewall to route incoming simulator data to field operation network	Connection established between LSTS server and Neptus Workstation	OK
Testbed powering up	Power up!	Wait for system in "SERVICE" and SatComms task active	OK
Starting Simulator	Power up and run script "LSTS"	Simulator ready to receive data	OK[†]
Configuring Satellite	Enable satellite and configure last passage parameter	Set parameter and warns about sent option state	OK
Starting transmission!	Enable send option	Wait for satellite to appear and starts sending data	OK
Checking transmission	Check if DUNE is transmitting OK	HumSat terminal confirms transmission OK	OK
Checking Simulator reception	Check if simulator is receiving packets	Simulator receiving packets	OK
Checking Neptus reception	Check if Neptus is receiving data	Neptus shows incoming MessageParts	OK
Checking message reconstruction in Neptus	Check if data received is being correctly reconstructed	Neptus shows data reconstructed correctly	OK

[†] Only on a second attempt. On the first one, LSTS server was routing data to an unavailable port, causing the script to crash.

4.5.3.3 Field trials

Field trials were devised to confirm the results of the "Communication Dry-Run" scenario, and an identical operation setup was used. For the flight the Testbed was replaced by the real X8 vehicle. The HumSat SDR was installed vertically in the X8 belly, to optimise the available space, and the UHF antenna on the nose of the vehicle (opposite to the Pitot tube), as seen in Figure 4.16.

As before, both Manta gateways are capable of creating a communication network, each with a different external IP. Making the required configurations, gateway A (Figure 4.17a) emulates the spacecraft and its ground station, while gateway B (Figure 4.17b) is the common UAV field operation setup.

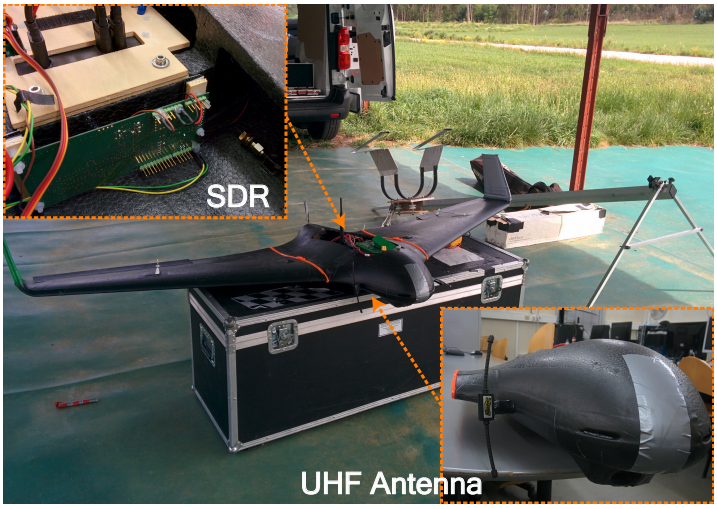
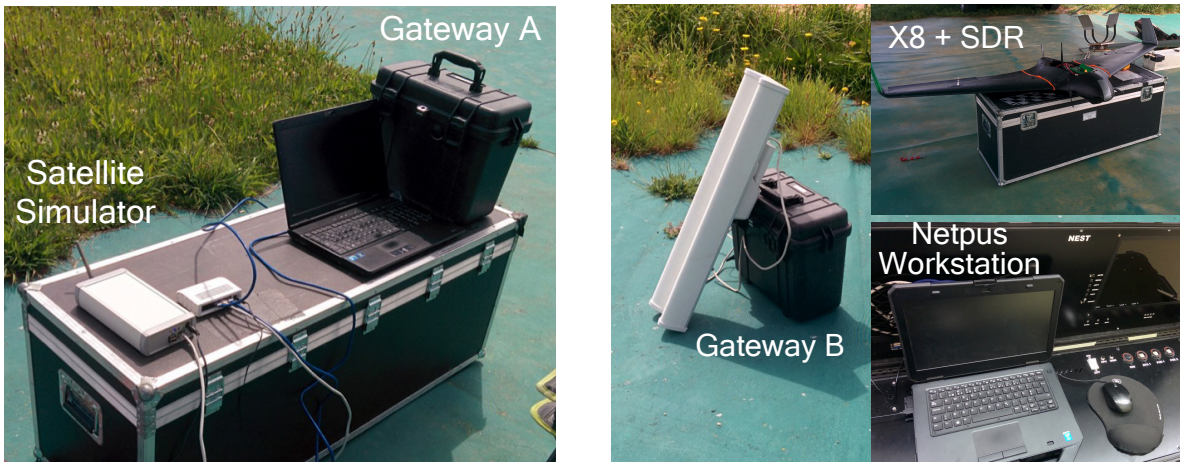


Figure 4.16 – *X8 vehicle equipped with the HumSat SDR and the UHF antenna.*



(a) *Network A* **(b)** *Network B*

Figure 4.17 – *Field trials operational setup.*

The test script, step by step, with the corresponding achieved results, is displayed in Table 4.4. As before, all tests were successful.

Within the field trials, it was possible to understand what could be achieved using just one satellite, and the current HumSat version. In particular, for a communication window with the satellite of about 5 minutes, about 45 kbytes could be transmitted by a vehicle. Although this is not much, if one envisions a multi-vehicle scenario, for a single satellite, larger pieces of information (*e.g.* an image, an environmental log or some navigational data) could be transmitted, and later reconstructed, if that data is shared among vehicles (and all transmitting together at a scheduled moment).

The tests reported here, performed in April 2017, will have to be repeated when the spacecraft carrying the HumSat payload is finally launched (possibly by mid 2019).

Table 4.4 – *Field mission script.*

Op. Phase	Test	Description	Expected Outcome	Results
Setup	Configure network interface in Simulator	Manual configuration of eth0	Connection established between gateway and simulator	OK
	Configuring Simulator *NeptusConnections*	Configure IP and port values	Connection established with LSTS server	OK
	Connecting communication gateways to internet	Enable "Mobile Internet" in both gateways and give external IPs to POC at LSTS.	Mobile Internet successfully established and external IP attributed.	OK
	Routing incoming communication [client]	Add iptable rule to route incoming data from LSTS server to Neptus workstation	Iptable rule successfully saved.	OK
	Routing incoming communication [server]	Configure LSTS server firewall to route incoming simulator data to field operation network	Connection established between LSTS server and Neptus Workstation	OK
Pre-flight	Powering up UAV	Power up UAV and check all systems	Everything working as expected	OK
	Checking SDR communication	Check if Satcomms is working properly	Satcomms reports status active	OK
	Checking SDR range	Do SDR + UHF antenna range test on the ground	Receive data successfully when UAV is away (as far as possible)	OK
	UAV takeoff	Catapult launch	UAV in air and OK	OK
Flight	Surveying plan upload	Make survey plan is above fire location and upload it to vehicle	Vehicle synchronizes plan successfully	OK
	Configuring Satellite	Enable satellite and configure last passage parameter	Set parameter and warns about sent option state	OK
	Starting transmission!	Enable send option	Wait for satellite to appear and starts sending data	OK
	Surveying Plan Execution	Start plan previously uploaded	Plan execution starts	OK
	Checking transmission	Check if DUNE is transmitting OK	HumSat terminal confirms transmission OK	OK
	Checking Simulator reception	Check if simulator is receiving packets	Simulator receiving packets	OK
	Checking Neptus reception	Check if Neptus is receiving data	Neptus shows incoming MessageParts	OK
	Checking message reconstruction in Neptus	Check if data received is being correctly reconstructed	Neptus shows data reconstructed correctly	OK[†]
	Waiting for end of transmission	Loiter away from fire after survey completed while communication window is open.	Loiter while transmitting.	OK
	UAV Land	UAV retrieval	UAV landing safely!	OK

[†] On the first flight there were some problems receiving all MessageParts, since the UAV was forced to fly away from the simulator area due to very strong winds. On the second trial the flight took place at the determined area, and all data was received and reconstructed.

CHAPTER 5

Thermal Analysis of Spacecraft and Small Satellites

Having presented what can be done with small satellites (including a practical application), the design phases a mission goes through, and what are their basic components, this chapter is focused on the design of a single component, the thermal control subsystem. Firstly, the chapter discusses what are the functions of the subsystem and what are the design steps an engineer needs to take to reach a solution. Still, the design process cannot be undertook without an understanding of how a spacecraft is influenced by the space thermal environment, neither how heat is conducted within the spacecraft itself. An overview of what are the most common technologies to control the heat distribution in small satellites is given afterwards, together with two computational methods used for these analyses. To make this theoretical exercise more concrete, a practical case of a CubeSat thermal analysis is presented, based on what was done in Ref. [45]. Apart from just looking at a spacecraft interior heat distribution, this chapter also presents what are the ensued accelerations from the emitted thermal radiation, based on the published Ref. [46].

5.1 The thermal subsystem – Objectives and design

The thermal control subsystem is responsible for maintaining the temperatures within the spacecraft at specified ranges. Those limits are derived by the components constrains, for all operation modes and thermal environments that the spacecraft might be exposed to. This task has to be fulfilled both in space, by limiting temperature gradients, and time, so that there is no significant differences during the lifetime of the spacecraft (*i.e.* always keeping a stable temperature). If this system fails, there might be pointing and alignment problems with respect to the platform, payload complications, or even the loss of the spacecraft.

Apart from determining the spacecraft temperatures, the thermal subsystem defines the hardware needed to control them. The characteristics of the subsystem are driven by the amount of heat that has to be dissipated to fulfil the components survival and operational temperature requirements [54]. Moreover, it is preferable to keep the temperatures of the spacecraft and its components close to their cooler limit, as this would generally mean a longer operational life time.

The design of a thermal subsystem, like any other, starts with a gathering of requirements and constraints, as is depicted in the flow diagram of Figure 5.1. Although general requirements are usually vague, *e.g.* “provide adequate margins”, these have to be refined for all the equipment, including allowable temperature ranges, maximum gradients, and stability requirements. Power dissipation and modes of operation are also relevant, as these might dictate equipment location and pointing constraints. More general spacecraft data is also used to characterise its thermal environment, like orbital parameters and attitudes. When collecting this data it is important to look for critical equipment (with the most stringent requirements) and events, which would drive the design.

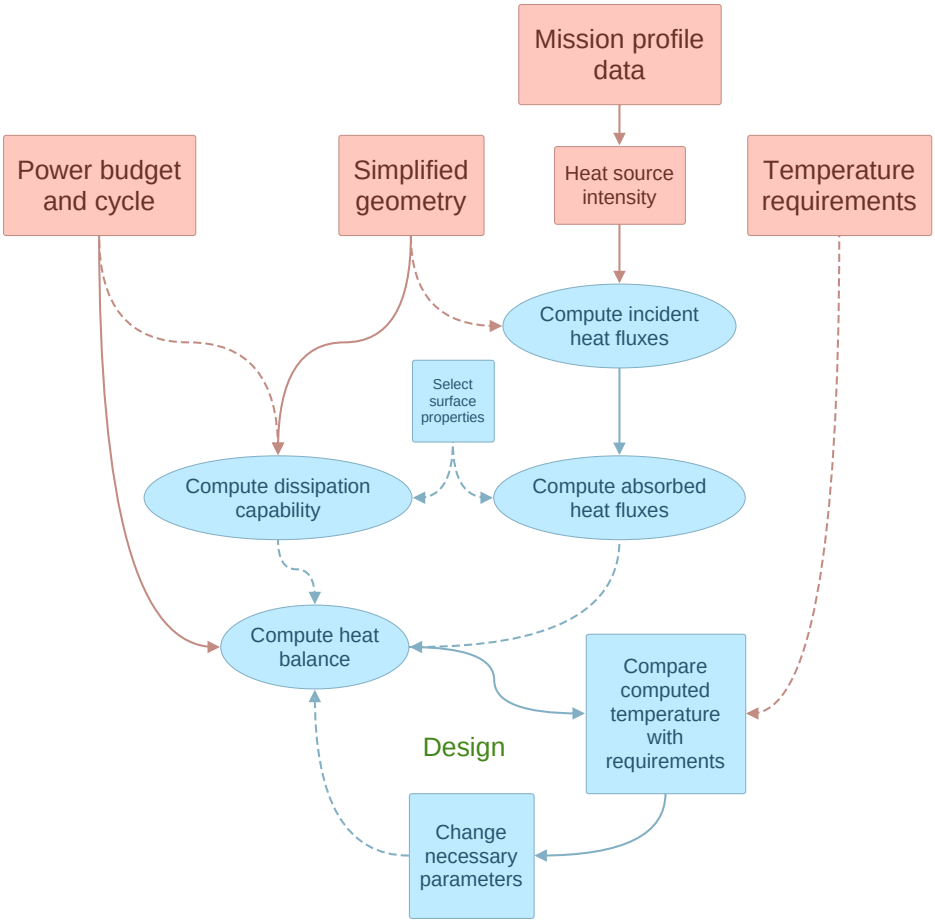


Figure 5.1 – *Flow diagram of thermal analysis design steps (adapted from Ref. [207]).*

At this point a preliminary design, with hardware configurations and coatings, together with the first temperature profiles, including external loads and dissipated heat, may be obtained. Firstly, only passive methods are used, as these minimise mass, cost, and complexity, moving to active control equipment if necessary. Two worst case conditions are usually modelled, either the spacecraft is exposed to the Sun and working at maximum power dissipation, *i.e.* the hot scenario, or it is in eclipse and operating with minimum power dissipated, *i.e.* the cold scenario. Iteratively, the design will reach a stable configuration after a few cycles, depending on the engineer experience, from where power and mass budgets may be obtained. In a concept definition phase it is better to

perform several parametric analyses with small models than to consider detailed ones in a large model, so that an engineer understands what might affect the design of the spacecraft.

Safety margins are common in most engineering approaches, and result from the uncertainties in matching models to reality. For thermal design, there are numerous uncertainties, which include contact conductances definitions, insulation characteristics, or methodological limitations [208, 209]. Thus, depending on the mission phase, larger or tighter margins have to be applied, according to the standards [210]. For example, during an initial concept design a margin of $\pm 10\,^{\circ}\mathrm{C}$ is recommended [60] (or up to $\pm 15\,^{\circ}\mathrm{C}$ [209]), whereas for later phases a $\pm 5\,^{\circ}\mathrm{C}$ margin must be considered. Nevertheless, because of the several uncertainties involved, some of which with no analytical solution, it is essential to perform several tests on engineering models, apart from thermal vacuum tests for the full spacecraft.

5.2 Space thermal environment

Space is a very harsh environment, due to the extreme temperatures that a spacecraft is subjected to. As an example, for a simple $1\,\mathrm{m}^2$ aluminium plate, the surface temperature can go from $436\,\mathrm{K}$ ($163\,^{\circ}\mathrm{C}$) when exposed to the Sun, to $3\,\mathrm{K}$ ($-270\,^{\circ}\mathrm{C}$) if in total darkness. The two main methods of heat transfer in space are conduction and radiation, since there is no convection medium. Although as a first approximation it might be enough to determine maximum and minimum temperatures (by doing a simple radiation energy balance), once a project reaches a detail design phase, even the conductivity between the components has to be studied.

Other important aspects of the Space environment, even though these are not discussed here, include the high levels of harmful radiation (which can damage electronic components, for instance), an almost perfect vacuum (requiring careful selection of materials and components), and particle impact (which can be as small as paint splinters travelling at about $8\,\mathrm{km/s}$) [54, 209, 211].

When designing the system, apart from the space environment, it is important to analyse both the ground and launcher environments. If the spacecraft is supposed to enter in a planetary atmosphere, a completely different thermal environment has also to be considered.

5.2.1 Radiation energy balance

Heat transfer by radiation is subjected to Stefan-Boltzmann's law,

$$q_{\mathrm{rad}} = \sigma_0 T^4, \tag{5.1}$$

which relates the fourth power of the temperature, T, with the thermal energy radiated per unit area per unit time, or heat flux, q_{rad}. The coefficient of proportionality is the Stefan-Boltzmann's constant, $\sigma_0 = 5.669 \times 10^{-8}\,\mathrm{W/(m^2K^4)}$. To obtain the total thermal energy, Q_{rad}, the flux is multiplied by the radiating surface area, A_{rad}.

Equation (5.1) is for an idealised black body, characterised by absorbing all incident electromagnetic radiation, which is not true for a real, or grey, body. For those, as they will emit less energy than a black body, the material's emissivity, $\epsilon < 1$, has to be used

$$Q_{\text{rad}} = q_{\text{rad}} A_{\text{rad}} = \epsilon \sigma_0 T^4 A_{\text{rad}}. \tag{5.2}$$

While in orbit, a spacecraft usually reaches a thermal equilibrium with its surroundings, having its temperatures oscillate between a maximum, when the spacecraft sees the Sun, and a minimum, when in eclipse. Therefore, the temperature is determined by an energy balance, between received, q_{in}, dissipated, q_d, and lost thermal radiation, q_{out}, written as

$$q_{\text{in}} + q_d - q_{\text{out}} = 0. \tag{5.3}$$

While the dissipated flux is associated to the generated heat by the electronic components, the radiated flux, or lost radiation, is related to the grey body emission (Equation (5.2)) of the spacecraft to Deep Space (which is assumed to be at 3 K).

The incident radiation value has to be decomposed in several components, including the Sun, Albedo (*i.e.* sunlight reflected by the Earth), and Earth infrared (IR) radiation fluxes,

$$q_{\text{in}} = q_S + q_E + q_A. \tag{5.4}$$

The first component, the Sun's radiation flux, depends on the solar flux, $G_s = 1\,367\,\text{W/m}^2$ (a mean value for Earth at 1 AU) [208], the material's absorptivity on the visible spectrum, α_S, and the angle between the solar ray and the surface's normal, θ_S. When a surface has solar panels, part of this incident flux is used to generate energy. Thus, that part has to be taken from the thermal balance, which yields a Sun's radiation flux of

$$q_S = G_S \alpha_S \cos\theta_S - q_{Gen}. \tag{5.5}$$

The value for the generated energy depends on the solar array efficiency, η,

$$q_{Gen} = \eta G_S \cos\theta_S. \tag{5.6}$$

While for the Sun all radiation is considered to be parallel, since the source is far away, the same cannot be said for the Albedo and the Earth's infrared radiation. In these cases, a view factor parameter, F, related to how the source illuminates the surface, has to be added to compute the radiation flux, according to the formulas discussed in subsubsection 5.2.1.1. Using the Earth view factor, F_E, the IR flux coming from the Earth is determined by the material's absorptivity (in this case the infrared one, α_{IR}), and the IR radiation emitted by the Earth (which is related to the

planet's average temperature and assumed to be $q_{\mathrm{IR}} = 230\,\mathrm{W/m^2}$ [209]),

$$q_E = q_{\mathrm{IR}} \alpha_{\mathrm{IR}} F_E. \tag{5.7}$$

The last incoming flux is simply the Sun radiation reflected by the Earth, defined by Earth's Albedo, a_E. Although this value is assumed to be about 36.5%, it can have high variability, for example, with cloud cover, snow or ice, and if over land or the ocean [208, 209]. Moreover, there is also a view factor parameter, F_A, related to the Earth's one and the angle made by the spacecraft, Earth and Sun given according to Ref. [212] by

$$F_A = F_E \cos\left(0.9\theta_A\right). \tag{5.8}$$

The 0.9 coefficient is used to account for the sunlight rays still heating the spacecraft when it is just above the shadow of the Earth [213]. With these, the Albedo radiation flux is simply

$$q_A = G_S a_E \alpha_S F_A \tag{5.9}$$

While the value for the solar flux, G_s, is more stable, although it involves variabilities along the year (about $\pm$3.5%), the Albedo, a_E, and Earth's infrared flux, q_{IR}, are much more erratic [208]. Limitations on Albedo and Earth IR values used for detailed analysis have been recognised, and thus NASA funded studies and statistical analysis of both parameters, according to orbit inclination and beta angle[i], exposure time, and the material sensitivity to IR and solar energy. Even though the IR absorptivity, as well as the visible one, depends on the material properties, the convention adopted here is that the infrared emissivity, ϵ, is equal to α_{IR}, and that the solar absorptivity α_S is equal to the emissivity in the visible wavelength.

5.2.1.1 View factors

View factors, sometimes called geometric configuration factors, or form factors, represent the fraction of total radiated energy from any source incident on a surface. For enclosed regions, the sum of view factors is one and reciprocally, $A_i F_{ij} = A_j F_{ji}$. Considering two elemental areas on two surfaces, dA_i and dA_j (one emitting and the other receiving), connected by a line of length r, which makes an angle θ with the surfaces' normal, as illustrated in Figure 5.2, the view factor can be calculated as

$$F_{ij} = \frac{1}{A_i} \int_{A_i} \int_{A_j} \frac{\cos\theta_i \, \cos\theta_j}{\pi r^2} \, dA_i \, dA_j. \tag{5.10}$$

Several formulas for particular geometries are available in the literature (Refs. [208, 212, 214, 215]).

[i] The orbit beta angle, $\pm 90°$, is defined as the minimum angle between the plane of the orbit and the solar vector. With increasing beta angle the Albedo is reduced as well as the eclipse time (reaching zero for high enough beta).

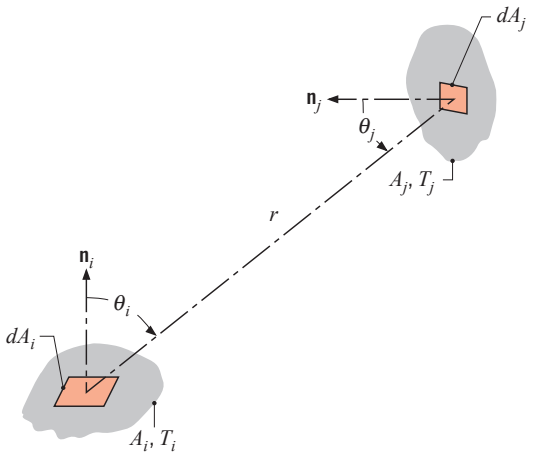


Figure 5.2 – *Schematic of view factor parameters for two elemental surfaces (image from Ref. [214]).*

For the Earth view factor alone there are many formulas and approximation methods. For example, according to the standards of the European Cooperation for Space Standardization (Ref. [215]), used by ESA, the simplest formula for the view factor is approximated by

$$F_E = B_0 + B_1 \cos\theta_E + B_2 \cos^2\theta_E + B_3 \cos^4\theta_E + B_4 \cos^6\theta_E, \tag{5.11}$$

where θ_E is the angle between the surface's normal and the planet centre (as shown in Figure 5.3). This formula is just for a flat plate around the Earth absorbing and emitting on one side, while there are others for other configurations.

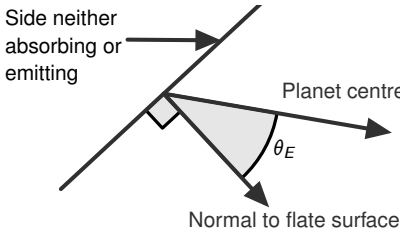


Figure 5.3 – *Schematic of the angle between surface's normal and planet centre (adapted from Ref. [215]).*

The B coefficients of Equation (5.11) are truncated power series [215], given by:

$$B_0 = \frac{2}{7\pi}\left(\frac{577}{105} - 7\cos\varpi + \frac{4}{3}\cos^3\varpi - \frac{2}{5}\cos^5\varpi + \frac{4}{7}\cos^7\varpi\right), \tag{5.12a}$$

$$B_1 = \frac{1}{2}\sin^2\varpi, \tag{5.12b}$$

$$B_2 = \frac{8}{7\pi}\left(\cos\varpi - 2\cos^3\varpi + 4\cos^5\varpi - 3\cos^7\varpi\right), \tag{5.12c}$$

$$B_3 = \frac{4}{7\pi}\left(-\cos\varpi + \frac{40}{3}\cos^3\varpi - \frac{91}{3}\cos^5\varpi + 18\cos^7\varpi\right), \tag{5.12d}$$

$$B_4 = \frac{8}{35\pi}\left(5\cos\varpi - 35\cos^3\varpi + 63\cos^5\varpi - 33\cos^7\varpi\right), \tag{5.12e}$$

with ϖ a parameter that depends on the radius of the Earth, r_E, and the orbital altitude, h,

$$\varpi = \arcsin \frac{r_E}{h + r_E}. \tag{5.13}$$

Another method to compute the Earth view factor is to use plotted data, represented in Figure 5.4, which depends on all the parameters discussed (*i.e.* orbit altitude and angle, and surface's normal direction).

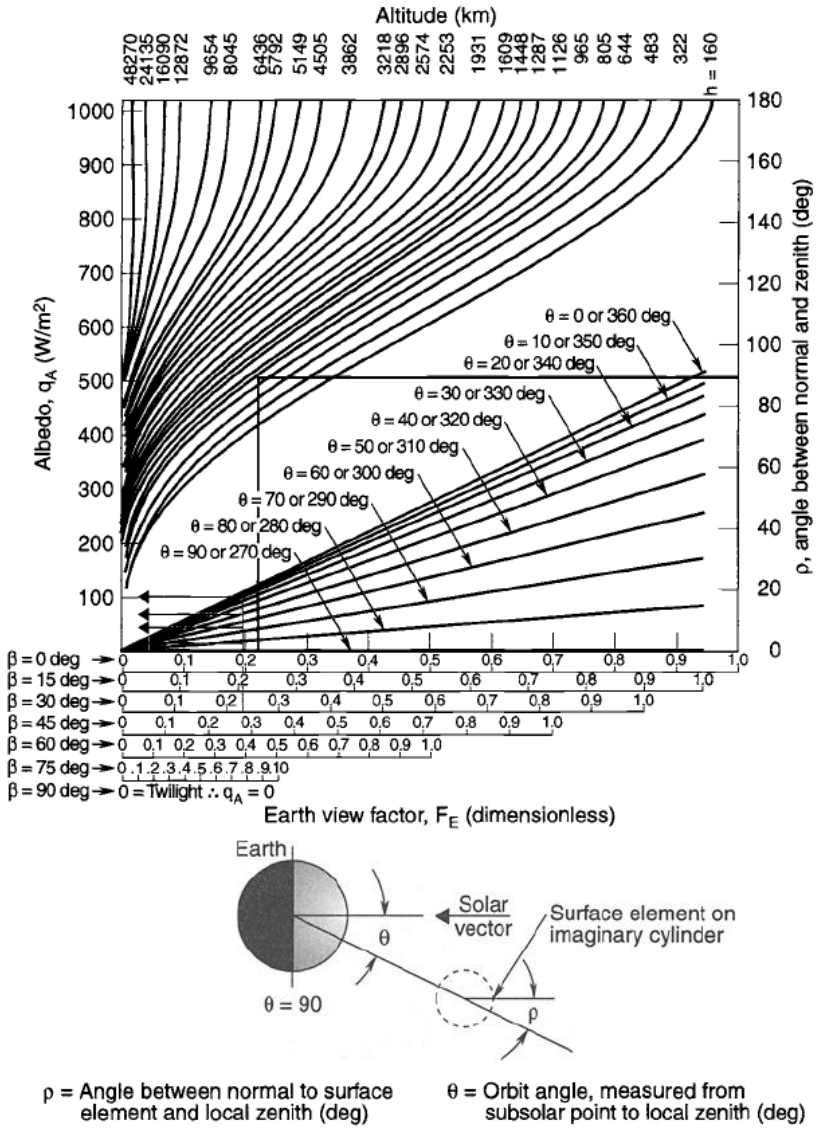


Figure 5.4 – *Albedo flux (for $a_E = 0.38$) on a surface element in Earth's orbit (image from Ref. [215]).*

According to Ref. [213], this can be approximated by

$$F_E = \varpi^{2.1} \left(\sin \frac{\rho}{2} \right)^{\Phi}, \tag{5.14}$$

with ρ as the angle between the surface's normal and local zenith (as shown in Figure 5.4), and Φ

as a function of ϖ,

$$\Phi = -21.232 + 226.81\varpi - 780.65\varpi^2 + 1\,394.6\varpi^3 - 1\,380\varpi^4 + 723.36\varpi^5 + 160.31\varpi^6. \quad (5.15)$$

5.2.1.2 Simple analyses

At first a steady state energy balance is usually performed to assess extreme working conditions. Using Equation (5.3) with Equation (5.2) it is possible to write a simple balance, now with surface area and temperature explicitly present,

$$q_{\text{in}} A_{\text{surf}} + q_d = \epsilon \sigma_0 T^4 A_{\text{rad}}. \quad (5.16)$$

For the case of a simple flat plate at 1 AU, pointing at the Sun with one side, with no power dissipation, and far from Earth, Equation (5.16) yields

$$T = \sqrt[4]{\left(G_s \frac{\alpha_S}{\epsilon} \frac{A_{\text{surf}}}{A_{\text{rad}}} \right) \Big/ \sigma_0}. \quad (5.17)$$

If $A_{\text{surf}} = A_{\text{rad}}$, as is the case for a flat plate with an adiabatically insulated side, the temperature only depends on the material's ratio α_S/ϵ, while if both sides are emitting (and only one receiving), then $2A_{\text{surf}} = A_{\text{rad}}$, as plotted in Figure 5.5. If it where a sphere, then $A_{\text{surf}} = \pi r^2$ and $A_{\text{rad}} = 4\pi r^2$, which means a ratio of $A_{\text{surf}}/A_{\text{rad}} = 1/4$. For the case of a cube with one side facing the Sun, useful for a first order approximation on the average temperatures for CubeSats, the ratio is $A_{\text{surf}}/A_{\text{rad}} = 1/6$.

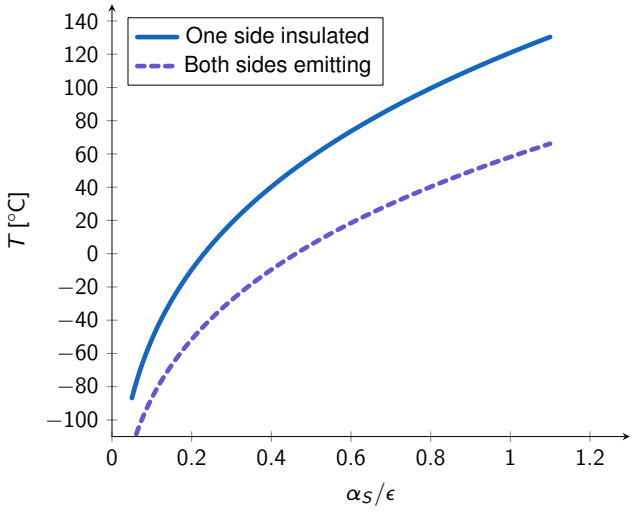


Figure 5.5 – *Temperature evolution for a flat plate normal to the Sun at* 1 AU *as a function of material optical characteristics (i.e. absorptivity and emissivity).*

Considering now a flat plate with a solar array on one side, the one pointing at the Sun (considered the top face), and the other side looking at the Earth (considered the bottom face). Solving again Equation (5.16) for T, but not discarding all incident components (as before), then

the maximum temperature of this plate would be

$$T = \sqrt[4]{\frac{G_s\alpha_S - \eta G_S + q_{\text{IR}}\alpha_{\text{IR}}F_E + G_S a_E \alpha_S F_A}{\sigma_0\left(\epsilon_{\text{top}} + \epsilon_{\text{bottom}}\right)}}. \tag{5.18}$$

Conversely, when this plate does not see the Sun, *i.e.* in eclipse, the minimum temperature obtained would be

$$T = \sqrt[4]{\frac{q_{\text{IR}}\alpha_{\text{IR}}F_E}{\sigma_0\left(\epsilon_{\text{top}} + \epsilon_{\text{bottom}}\right)}}. \tag{5.19}$$

5.2.2 Thermal conductivity and contact conductance

The phenomenon of conduction results from particles in a solid medium interacting with each other. When warming up one side of a solid, the heat passed to that section will be distributed throughout the whole solid, creating a heat flow. This depends on the material's thermal conductivity, k, the component cross sectional area where heat is flowing, A_{cross}, and the temperature difference. Thus, the heat flowing in one dimension between two arbitrary points (i and j) is given by

$$Q_{\text{cond}_{ij}} = \frac{kA_{\text{cross}}}{\Delta x}\left(T_i - T_j\right), \tag{5.20}$$

where Δx is the distance from one point to the other. Making an analogy with electrical circuits and Ohm's law, where heat flow is the current and temperature is the potential, it is possible to define the thermal resistance as

$$R_{ij} = \frac{\Delta x}{kA_{\text{cross}}}. \tag{5.21}$$

When two solids touch each other, heat will be conducted between them as well and, for vacuum conditions, that heat flow can be described by a contact conductance, h_c, expressed through [216]

$$Q_{\text{cond}_{ij}} = h_c A_{\text{apparent}}\left(T_i - T_j\right). \tag{5.22}$$

Contact conductance requires thus a more complicate treatment, with several parameters influencing it, including not only the apparent area of contact, A_{apparent}, and the thermal conductivity of each material, but also the rugosity of that contact surface and the pressure between the solids.

There have been several models proposed to obtain the value of h_c, with much theoretical and empirical work performed [208, 209, 217, 218]. Most of these models consider two surfaces pushed together and thus depend on many parameters characterising the contact between the two materials, as depicted in Figure 5.6. These include an effective thermal conductivity ($k_s = \frac{2k_1k_2}{k_1+k_2}$), the effective Root Mean Square (RMS) surface roughness ($\sigma_s = \left(\sigma_1^2 + \sigma_2^2\right)^{1/2}$), and the effective absolute mean asperity ($m_s = \left(m_1^2 + m_2^2\right)^{1/2}$). However, the absolute mean asperity is not always known, and so relations between it and the surface roughness (for $0.216\,\mu\text{m}$ to $9.6\,\mu\text{m}$) has been experimentally determined to either be $m = 0.125\left(\sigma \times 10^6\right)^{0.402}$ [219] or $m = 0.076\left(\sigma \times 10^6\right)^{0.52}$ [208].

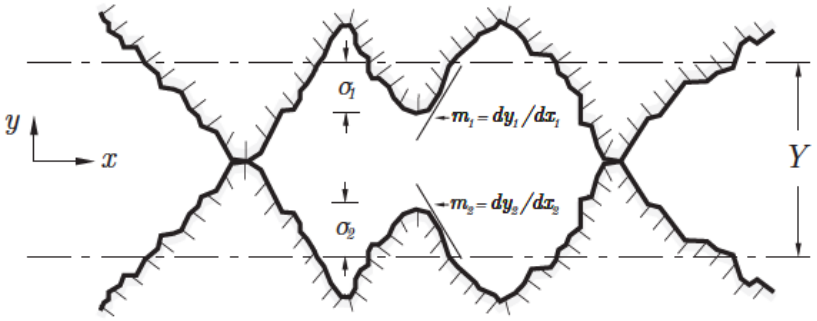


Figure 5.6 – *Schematic of a detail of a contact between two materials (image adapted from Ref. [220]).*

5.2.2.1 Contact conductance – Non bolted joints

For non bolted joints there are several methods to determine the contact conductance, especially if there is any filling material between the contact surfaces, and the filling type.

For a joint where there is no interstitial material, and for low applied pressures (typically encountered in microelectronic applications), a simple model assuming a conforming rough surfaces relatively smooth and in vacuum gives a contact conductance of

$$h_c = 1.25 \frac{k_s m_s}{\sigma_s} \left(\frac{P}{H_c} \right)^{0.95}, \tag{5.23}$$

where P is the applied pressure and H_c the lesser microhardness of the materials involved [219]. If a filling material is added to the interface, the total thermal contact conductance is then given by

$$\frac{1}{h_{c_{\text{total}}}} = \frac{1}{h_{c_1}} + \frac{1}{k_{\text{int}}/t_{\text{int}}} + \frac{1}{h_{c_2}}, \tag{5.24}$$

which depends on the conductance between each contact surface involved, and both the conductivity and thickness of the interstitial material, k_{int} and t_{int}, respectively [216].

If the interstitial material used is also slightly compressible, then Equation (5.24) acquires a dependence on the pressure and on the Young's module of the material, E, and thus is written as

$$\frac{1}{h_{c_{\text{total}}}} = \frac{1}{h_{c_1}} + \frac{1}{k_{\text{int}}/t_{\text{int}}\,(1 - P/E)} + \frac{1}{h_{c_2}}. \tag{5.25}$$

Some of the most common materials used to fill contact gaps include adhesives, epoxies, metallic foils or coatings. These are placed between the contact surfaces and then compressed by them, deforming and filling the cavities, as illustrated in Figure 5.7. This way, the contact area is increased, together with the contact conductance. There are a few important characteristics for these filling materials, in particular they should have a high thermal conductivity, a capacity to deform at low pressures, and a minimal thickness. Furthermore, for Space applications fluid materials (like greases) should not be used, since they would leak and disappear when in vacuum, or vaporise at high temperatures.

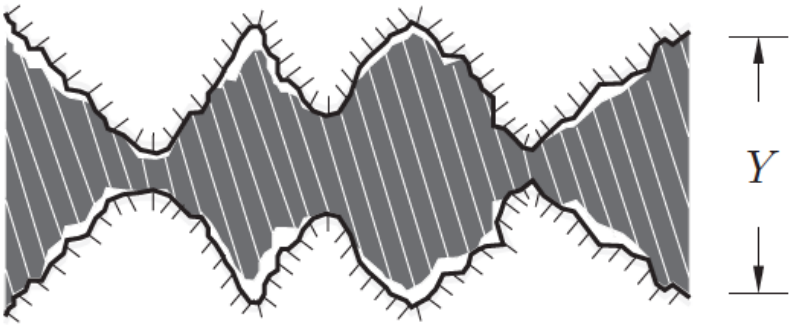


Figure 5.7 – *Illustration of a filling material applied in a contact interface (image adapted from Ref. [220]).*

According to some studies, for a given thickness of the interstitial material and high pressures the thermal conductivity plays the main role [213, 216], and thus Equation (5.24) can be simplified even further to

$$\frac{1}{h_{c_{\text{total}}}} = \frac{1}{k_1/t_1} + \frac{1}{k_{\text{adhesive}}/t_{\text{adhesive}}} + \frac{1}{k_2/t_2}. \tag{5.26}$$

5.2.2.2 Contact conductance – Bolted joints

When analysing bolted joints there are several other models, mostly empirical, which consider above all the pressure that the bolts produce. However, this limits the applicability of these models to similar conditions or geometrical designs.

One of the simplest, is a plastic model relating the applied pressure and the microhardness of the materials involved, and related to experimental data [221], much similar to Equation (5.23). This model proposes that the thermal contact conductance is

$$h_c = 1.45 \frac{k_s m_s}{\sigma_s} \left(\frac{P}{H_c} \right)^{0.985}. \tag{5.27}$$

Although it is well correlated with experimental data, this model has an absolute error between 50% and 100% [220].

There is also a model proposed by ESA to represent the joint thermal conductance, apart from how to use fasteners in spacecraft applications [222]. According to their standards, the contact pressure for a bolted joint is assumed to be constant and calculated as

$$P = \frac{F_v}{A_{\text{contact}}}, \tag{5.28}$$

where A_{contact} is the area of the contact, and F_v is the nominal preload of the fastener used to hold the joint (given as a percentage of its yield load). Using tabulated values of the contact conductivity, k_{contact}, for different materials, which depend on surface finish and contact pressure, the conductance is

$$h_{c_1} = k_{\text{contact}} A_{\text{contact}}. \tag{5.29}$$

Assuming a lateral conductance $h_{c_2} = 0.3\,\mathrm{W/K}$, a typical value for honeycomb panels, total conductance is given by

$$h_{c_{\text{total}}} = \frac{1}{1/h_{c_1} + 1/h_{c_2}}. \tag{5.30}$$

5.3 Thermal control technology

There are several ways to make sure temperatures are stable and within a predefined range. The two main categories, active and passive means, are set apart by the amount of power consumption needed to work.

Some of the most used passive control techniques include surfaces' coating, *e.g.* by applying selected paints, and thermal insulation using, for example, thermal blankets. When possible, on some available of the surfaces, radiators (*i.e.* panels made of materials with high emissivity and low absorption) are employed to radiate excess heat. Apart from these, which work mostly by emitting radiation or limiting emission, within the spacecraft itself, there are many techniques used, from physical rearrangement of equipment to thermal straps or adhesives.

If passive methods are still not enough, active means have to be implemented. Among these the simpler, compact, and less power consuming ones are heaters, which are basically resistances releasing heat through the Joule effect. Others like cryogenerators, and heat pipes, are more complicated systems and only applied in specific cases, or in conventional spacecraft. A common application case of active control is the use of heaters for the batteries, which have limited temperature ranges of operation.

Adding all up, the mass of a typical thermal control system would range from 2% to 6% of the spacecraft dry mass, depending if more passive or active control is used [207]. In terms of power consumption, it ranges from 2% (for a non propulsion spacecraft) to 15% (for a planetary spacecraft) [54, 207].

5.3.1 Passive methods

Surface coatings are the primary method of thermal control, both outside and inside the spacecraft. There are several types of coatings with different values of emissivity and absorptivity (as plotted in Figure 5.8). For example, white paints ($\epsilon = 0.85$ to 0.91 and $\alpha_S = 0.18$ to 0.28) or silver or aluminium backed Teflon ($\epsilon = 0.66$ to 0.78 and $\alpha_S = 0.05$ to 0.16) are commonly used on the outside to minimise absorbed energy and maximise the emitted one, whereas polished aluminium or gold are used to minimise both emission and absorption ($\epsilon = 0.03$ to 0.1 and $\alpha_S = 0.09$ to 0.3) [54, 208]. Conversely, on the interior of the vehicle, usually a high radiative heat exchange is looked for, and black paints are used ($\epsilon = 0.84$ to 0.89 and $\alpha_S = 0.92$ to 0.98 [208]). Although coatings have been studied to reduce problems of stability, outgassing, and mechanical adhesion, they degrade over time increasing the absorptivity (with minor impact on emissivity) [209].

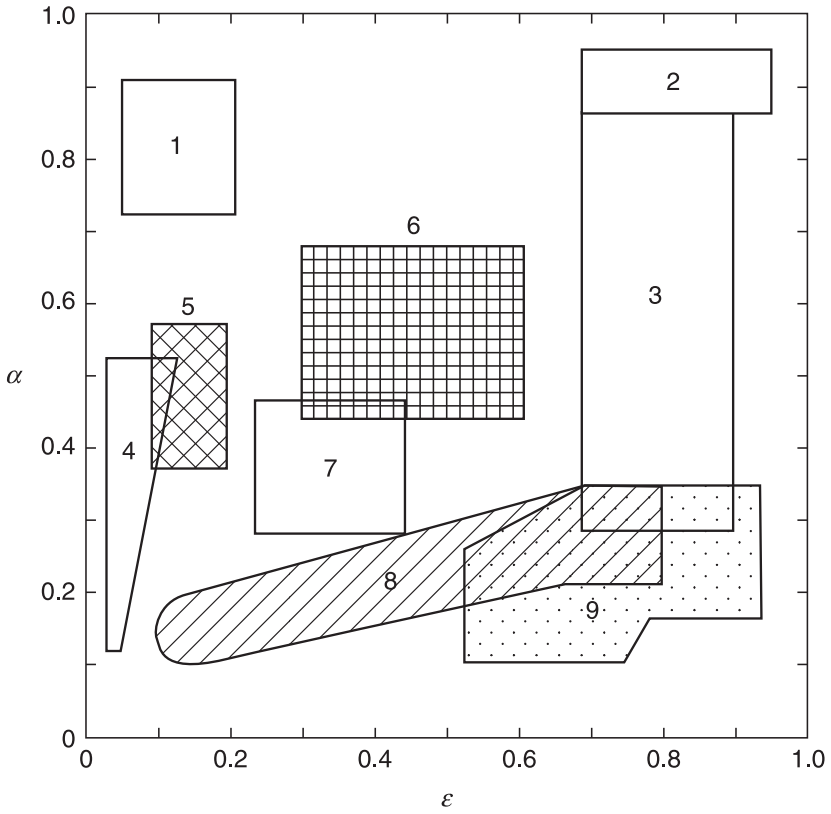


Figure 5.8 – *Absorptivity versus emissivity for different surface thermal control coatings (image adapted from Ref. [209]). The plotted coatings are: selective black (1); black paints (2); grey and pastel paints (3); polished metals (4); unpolished bulk metals (5); sandblasted metals and conversion coatings (6); metallic coatings (7); dielectric films on polished metals (8); white paints, second surface mirrors, metallized polymers (9).*

Radiators are ultimately surfaces that emit IR radiation to space, according to the emissivity and temperature of the surface. To maximise IR emissions, most radiators have high IR emissivities and low absorptivity ($\epsilon > 0.8$ and $\alpha_S < 0.2$) [54]. Therefore, even faces pointed to Sun can work as radiators, as long as the absorptivity is minimised. For some cases, gradients of temperature are not significant, or there is no face with enough area to work as a radiator. In these cases a deployable panel or a body mounted one, isolated from the rest of the spacecraft, may be used. Because of the coatings and materials degradation, it is usual to oversize radiators so that they meet the needed requirements at the end of their lives. While spacecraft panels used as radiators have their mass in the structure subsystem budget, and thus a virtually null mass for the thermal subsystem, radiators built out of deployable panels can reach $12\,\mathrm{kg/m^2}$ [208].

Multilayer thermal blankets (MLI) are the preferred method for insulating components and equipment, either from releasing or receiving too much heat. Although sometimes MLI almost cover completely the spacecraft, with just a few cut-outs (*e.g.* for radiators), they are also typically used to protect propulsion system components. These blankets work by combining several low emittance layers with low conductivity ones, for instance, Mylar or Kapton sheets with an aluminium or gold finish, separated to minimise conduction between layers. Heat transfer on MLI occurs both by conduction, minimised by low density, low conductive layers and by a design with minimal

contact points, and radiation, minimised by using reflective surfaces as much as possible. It is very hard to separate the two, and usually there is no analytical definition of conductivity and radiation in terms of fundamental variables, like temperature, density or material properties. Thus, it is usual to characterise MLI by an apparent thermal conductivity, or an effective emittance, obtained experimentally, related to each other by $\epsilon_{\text{eff}} = \frac{K_{\text{app}}(T_2 - T_1)}{l\sigma_0\left(T_2^4 - T_1^4\right)}$, where l is the thickness of the MLI [208]. Studies have shown that 25 layers are usually sufficient, producing blankets with effective emittance from 0.015 to 0.030 [54]. It is important to ground these blankets, as is shown in Figure 5.9, as they are prone to accumulate static charges and might cause short circuits.

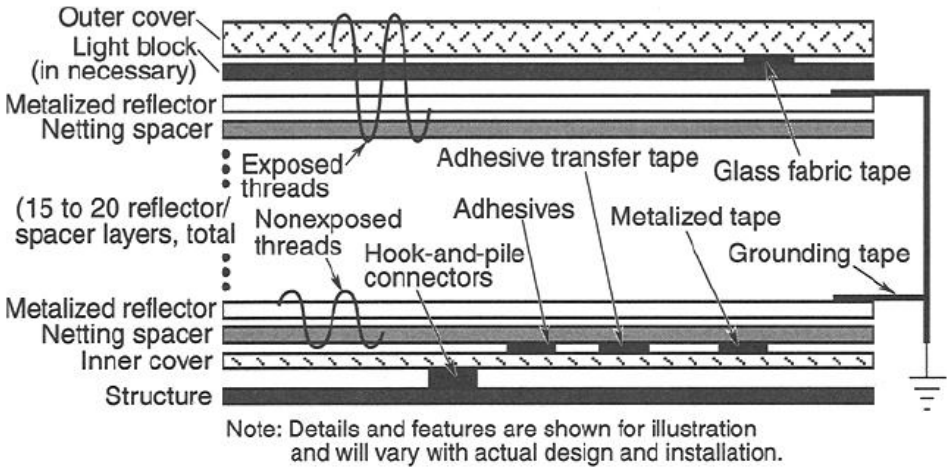


Figure 5.9 – *Typical composition of a multilayer thermal blanket (image from Ref. [208]).*

For some applications, conduction through the mounting structure, or emitted radiation, is not enough to cool down a component, and thus is necessary to add an additional heat path to a colder element. For example, in small satellites, in particular CubeSats, is important to make sure there are thermal conductive paths between internal heat generating components and exterior surfaces, so that heat is correctly distributed. To accomplish this, flexible mechanically compliant joints, providing an attachment and a thermal path, can be used. These joints are usually in the form of flexible strips, cables or braids, made of high conductivity material (*e.g.* cooper, silver or carbon fibres), and bulky pieces at each end, used for attachment (like the ones depicted in Figure 5.10). The performance of these thermal straps is commonly assessed with the strap linear conductance [209].

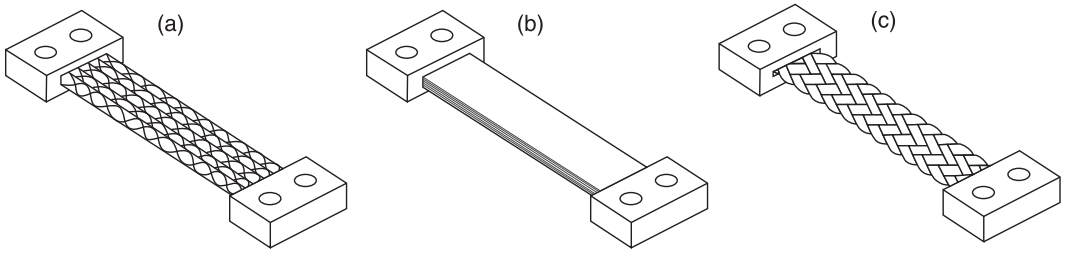


Figure 5.10 – *Thermal strap different configurations, including fibre bundles (a), multi-foil (b), and braids (c) (image from Ref. [209]).*

5.3.2 Active methods

Almost all spacecraft carry heaters, even if just to warm it up at the beginning of life, when passive methods are oversized. Coupled with thermostats, and commanded by the onboard computer (and a relay), precise temperature control can be achieved for particular components. Another possible application is to warm up equipment before turning it on, like for hydrazine propulsion thrusters. Patch heaters are the most commonly used, as the one from Figure 5.11, which are composed of an electrical resistance (usually more than one for redundancy) enclosed by two sheets of electric insulating material, like Kapton. A fuse is also used to protect the spacecraft from short circuits. Due to their low mass and volume several hundred thermostats might be used in a single spacecraft [54].

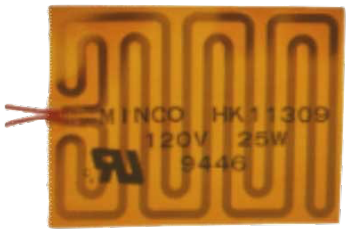


Figure 5.11 – *Heater made of a flexible metal printed circuit sandwiched between Kapton layers (image from ESA).*

Other active methods, like louvre, heat pipes and cryogenic coolers exist, but are usually not used for micro and nano satellites, as they tend to be heavy and bulky, and thus are not discussed here. Nevertheless, there is research for miniaturisation of louvres for use in smaller spacecraft, as they respond quickly to environmental thermal changes [223].

5.4 Computational analysis methods

To perform either basic or complex analysis, the first step is always to build a geometric mathematical model, representing the physical surfaces of the spacecraft and its components. This model is used to calculate radiation view factors, for instance, and external fluxes. Non-relevant details, from the thermal point of view, can be excluded when developing this model.

The next step is to build a thermal mathematical model to predict temperatures, which is basically a translation of the geometrical one by applying thermal elements and their equations. Each node of the model can be considered isothermal, coupled to its neighbours through conduction or radiation heat transfer paths [207]. There are two main approaches to this model, either using a Lumped-Parameter (LP) representation, where the characteristics are “lumped” or concentrated in a single point in space, or a Finite Element Method (FEM) one, where the characteristics are distributed over an area. Both methods on their own have been applied for practical cases, with appropriate software, since each has its own limitations and errors. Sometimes both are combined to solve difficult problems, for instance, when meshes cannot be easily generated for LP methods.

Parametric runs, where parameters are varied across a range, are sometimes used to establish optimum dimensions and characteristics, for example, radiator or heater sizes [54]. Nevertheless, worst case solutions, both hot and cold, have to be obtained to size the thermal system, using steady state calculations first. After determining the temperature limits, transient analyses are run to obtain temporal evolution, and verify that the thermal requirements are met for the full orbit.

For the case of FEM methods, their main strength is the mesh schemes that can be created, usually with hundreds of elements, and, for example, are extensively used for circuit board analysis [208]. The nodes of each element, either one, two or three dimensional, are located in their corners, with variations within an element calculated by interpolation. These meshes tend to be very fine since they are driven by structural analysis requirements, and thus represent an increase in computational cost and time, without any real additional information.

For LP methods, the characteristics of small volumes of the geometrical model are replaced by a single node. Each of these nodes, located in the centre of the small volume, represent two thermal network elements, the temperature (or the potential), and the thermal mass (or the capacitance), C. Therefore, the temperature distribution can be considered linear.

Finite thermal mass nodes, of diffusion nodes, represent normal materials that change temperature as a result of a heat flow [208], and thus are mathematically defined by

$$\sum Q - \frac{C\Delta T}{\text{time}} = 0. \tag{5.31}$$

The thermal capacitance of a node, a function of the material density, ρ, specific heat, c_p, and element volume, V, is written as

$$C = \rho V\, c_p. \tag{5.32}$$

The arithmetic node, or zero capacitance, although not representing a physical quantity, is used for numerical or result output reasons, and is translated by an instantaneous response to temperature changes. Finally, the boundary node, or infinite capacitance, represents an element that will never change temperature, independently of how much heat is flowing, and thus can be used to translate a boundary condition. A typical example of an arithmetic node is a bolt, while deep space is represented by a boundary node. Unlike LP methods, FEM only allows for diffusion and boundary elements (equivalent to the respective LP nodes), and not arithmetic ones.

To link nodes to each other conductors, G, have to be created. These can be either linear, representing conduction, which according to Equation (5.20) are

$$G = \frac{kA}{\Delta x}, \tag{5.33}$$

or non linear ones, for radiation heat transfer,

$$G_{ij} = \sigma_0\, \epsilon\, F_{ij}\, A_{ij}, \tag{5.34}$$

which depends on the view factor between the two surfaces i and j. As with electrical circuits, parallel conduction paths can be summed together ($G_{\text{total}} = G_1 + G_2 + \cdots + G_n$), whereas series ones have an inverse relation ($1/G_{\text{total}} = 1/G_1 + \cdots + 1/G_n$).

5.5 A practical case

Several practical cases have been used to understand how thermal analyses works, and to analyse its challenges and outputs. From all those cases, the one presented here is focused on developing a solution to control the maximum temperature of a field-programmable gate array device. This FPGA is going to be flown in a CubeSat mission during 2018, and there is a need to rapidly access its temperature, during the CubeSat design phase. Besides this main FPGA device, several other electronic devices, distributed over two PCBs, are also modelled.

5.5.1 Geometric model

The design process for any new satellite is highly iterative, in particular when the project is still in a preliminary phase. Therefore, the geometric model, for any type of simulation, has to be parametrised to account for any changes. Only the final version of the model is presented here, for simplicity, and the discussion of how this design has been obtained is found in Section 5.5.2. Nevertheless, several simplifications were performed, since only the temperature distribution for some components, and not the spacecraft as a whole, had to be studied.

The test region is bound by the dimensions of a 1U CubeSat. While the boundaries radiate to outer space, the internal components are only thermally coupled with the inner walls. The exterior boundaries are covered for most part with solar panels, giving an average emissivity and absorptance around $\epsilon = 0.78$ and $\alpha = 0.37$ respectively. A schematic picture of the spacecraft interior can be seen in Figure 5.12.

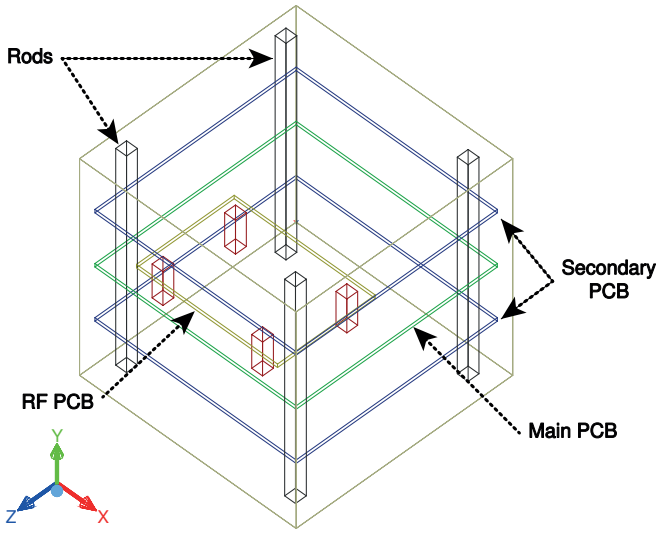


Figure 5.12 – *Basic model structure, with each component labelled.*

For this simplified analysis, it was assumed that the spacecraft contains only three large PCBs. The top and bottom PCBs, shown in Figure 5.12, are considered secondary (*i.e.* are not the focus of this simulation), while the middle one has the main components to be analysed. A fourth, and smaller, PCB (the RF PCB) is only connected to the middle one. All PCBs have a thickness of 1.6 mm and are made of ten layers of Cu-Pure (with a density equal to $\rho = 8\,933\,\mathrm{kg/m^3}$, a specific heat of $c_p = 195\,\mathrm{J/kg\,K}$ and a conductivity $k = 387.6\,\mathrm{W/m\,K}$ [224]), inside a FR-4 substrate ($\rho = 1\,250\,\mathrm{kg/m^3}$, $c_p = 1\,300\,\mathrm{J/kg\,K}$ and $k = 0.35\,\mathrm{W/m\,K}$ [224]). The emissivity and absorptance of FR-4 are $\epsilon = 0.9$ and $\alpha = 0.9$, respectively. The PCBs position inside the CubeSat and their dimensions are shown in Table 5.1.

Table 5.1 – *PCBs position and dimensions (all values in* cm*).*

Component	Dimensions		Position		
	Width	Length	X	Y	Z
Main PCB	9.29	9.29	0.36	5.00	0.36
Secondary PCB 1			0.36	2.50	0.36
Secondary PCB 2			0.36	7.50	0.36
RF PCB	6.51	4.51	2.05	6.00	4.91

Attached to the walls, and used as a support to all other components, four main rods are placed in each corner. Each rod is made of aluminium, presenting a density $\rho = 2\,710\,\mathrm{kg/m^3}$, a specific heat $c_p = 900\,\mathrm{J/kg\,K}$, a conductivity $k = 218\,\mathrm{W/m\,K}$, an emissivity $\epsilon = 0.09$, and a absorptance of $\alpha = 0.4$ [224]. Furthermore, there are four smaller secondary rods that hold the RF PCB. Their dimensions and positions are shown in Table 5.2.

Table 5.2 – *Dimensions and positions of the main and secondary rods (all values in* cm*).*

Component	Dimensions			Position		
	Outer Radius	Inner Radius	Height	X	Y	Z
Rod 1	0.25	0.15	10.00	0.50	0.00	0.97
Rod 2				8.67		0.73
Rod 3				8.67		8.70
Rod 4				0.50		8.33
Secondary Rod 1	0.25	0.15	1.56	2.54	4.80	5.34
Secondary Rod 2				7.68		5.34
Secondary Rod 3				7.14		8.69
Secondary Rod 4				2.54		8.69

These rods are in reality composed of an inner tube (a threaded rod), that links the bottom and the top of the spacecraft, and hollow spacers between the PCBs, holding them in place. For example, the four main rods have a total of 16 hollow spacers, four bellow each PCB plus four on the top. However, in an attempt to simplify the model, each rod was modelled as a single component, with a thermal resistance between the rod and the PCB, instead of several different components. This resistance is sized according to the real contact area between the PCBs and the hollow spacers, following the equations of Section 5.2.2. Furthermore, since both the PCBs

and the hollow spacers have a poor contact with the inner tube (*i.e.* the thermal conduction is very limited), an extra thermal resistance inside the rod (located at each PCB height) was added.

With the stack and the structural parts modelled, the electronic packages were included. The first components are mounted on the main PCB (the middle one of Figure 5.12), including a main chip, two memories, and a transceiver. All of them are enclosed in a protective aluminium casing from external radio frequency interferences, as represented in Figure 5.13. The casing measures $6.51\,\text{cm} \times 4.53\,\text{cm}$, with a height of $0.54\,\text{cm}$, and its walls have a thickness of $1\,\text{mm}$. Besides protecting the packages from the outside environment, it also separates them (*i.e.* one side has the main chip and the memories, and another has the transceiver, divided by a $1\,\text{mm}$ thick wall).

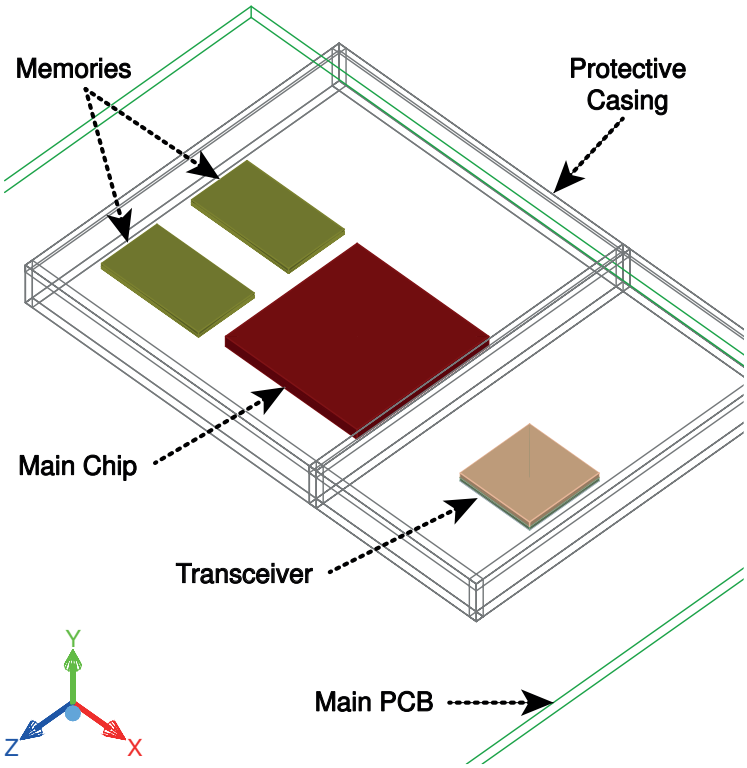


Figure 5.13 – *Main electric components of the main PCB.*

The main chip is a Xilinx System on a Chip (SoC), of the family Zynq-7000 (model number *cl484 xc7z020*), imported from available Icepak libraries [225]. With this template, the only parameters that have to be adjusted are its position in the main model, and the power of the junction node. The two memories are Double Data Rate type three Synchronous Dynamic Random-Access Memory (DDR3L SDRAM), with 4Gb x16 (model number *MT41K256M16TW-107*), commercialised by Micron [226]. Finally, there is an *AD9364* radio frequency agile transceiver, from Analog Devices [227]. As there is no Icepak model available for these last components, a standard package was added and adapted according to the components data sheets. Their main characteristics and position are listed in Table 5.3.

Table 5.3 – *Electronic packages position and characteristics (all values in* cm*).*

Component	Characteristics			Position		
	Width	Length	Thickness	X	Y	Z
Main Chip	1.90	1.90	0.14	3.64		2.11
Memory 1	1.40	0.80	0.11	1.95	5.16	2.01
Memory 2						3.31
Transceiver	1.00	1.00	0.15	6.71		2.69

On the middle of the RF PCB there is a single small ($0.3\,\text{cm} \times 0.3\,\text{cm} \times 0.09\,\text{cm}$) electronic component, an amplifier, shown in Figure 5.14. The package is an adaptation of a 3 V General Purpose, GSM Power Amplifier, model number *RF5110G*, distributed by Qorvo [228]. The RF PCB is also fully covered by another aluminium radio frequency shielding ($6.51\,\text{cm} \times 4.51\,\text{cm} \times 0.54\,\text{cm}$ with a 1 mm thickness). Furthermore, there is a Thermal Strap (TS) linking the amplifier and the shield, made of a Pyrolytic Graphite Sheet (PGS), with a thickness of $25\,\mu\text{m}$ [229]. Although it measures in total $1.6\,\text{cm} \times 0.3\,\text{cm}$, the strap is folded in itself to form a close loop between the amplifier and the shield (as depicted in Figure 5.14).

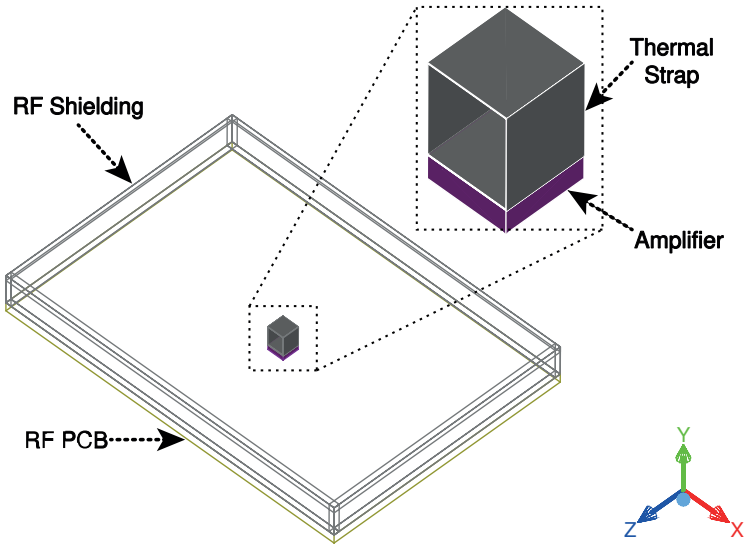


Figure 5.14 – *Amplifier, shielding and a zoom of the thermal strap, all on the RF PCB.*

5.5.2 Assumptions and simulated cases

5.5.2.1 Global assumptions

Although only the most relevant simulations analysed are described here, various validation and trial runs were performed before, not only to determine what is the best configuration, but to test different modes of operation. These validation runs were also used to establish global parameters. Moreover, for almost all simulations, both steady state conditions and transient ones were simulated. While the steady state gave operational limits, the transient runs showed how the

temperature evolved, and thus only the data for these transient conditions is presented at the result Section 5.5.3.

There are several mission parameters still to be defined, as this is a preliminary analysis. Therefore, some major assumptions had to be made, with the first one being the model initial temperature ($10\,^{\circ}\mathrm{C}$). This value was selected since it is within the range of the temperatures experienced inside the launcher.

The other major assumption taken was the CubeSat orbit, based on an educated guess, so that design assumptions could be taken. Thus, the orbit was assumed to be a Sun-synchronous one, with an altitude of $400\,\mathrm{km}$, which is a typical value for this kind of missions. Having the orbit, and resorting to the ESA TOPIC software, the maximum and minimum incident fluxes were assessed within a three years window of the launch. These fluxes feed the thermal numerical model as the worst environmental conditions that the CubeSat would experience during its lifetime. The orbit parameters, more exactly the $5\,550\,\mathrm{seconds}$ orbital period (about $92.5\,\mathrm{minutes}$), was also used to determine the length of the transient simulations (since the conditions are expected to repeat after each orbit cycle).

Other runs were used, for instance, to understand the impact of the rods conduction. On those sensitivity runs, the parameters used for the thermal resistance of the rods were varied slightly, to study their influence in the model, in an attempt to approximate the conduction of the rods to real conditions. Tests to simulate the amplifier transient behaviour, using different methods, were also performed.

5.5.2.2 Simulated cases

One of the electronic components that generates more heat is the amplifier. Besides being the smallest component, it has the highest power consumption of all of them. Moreover, unlike the main chip, it cannot be turned off. Therefore, the aspect that most defines the system under study is the amplifier operational mode.

The two relevant distinct cases are when the amplifier is turned off, and when it is turned on. Then, when the amplifier is turned on, there are also two different modes of operation, even though the activity always follows a squared wave pattern. For the first and shorter mode, the amplifier is active for $5\,\mathrm{seconds}$ and turned off for $20\,\mathrm{seconds}$, whereas on a second and longer mode, the amplifier works for $10\,\mathrm{seconds}$, followed by another $20\,\mathrm{seconds}$ of inactivity. This has then an impact in the transient conditions, and thus creates the options tree of Figure 5.15.

Verifying that the temperature distribution was outside the desired region, a third level of options was added. The same operational conditions described above were tested, but now, in an attempt to mitigate the encountered higher temperatures, and dissipate as much heat as possible, a thermal strap was added to the model. Several configurations were tried, and the one that proved most efficient is the loop one discussed before.

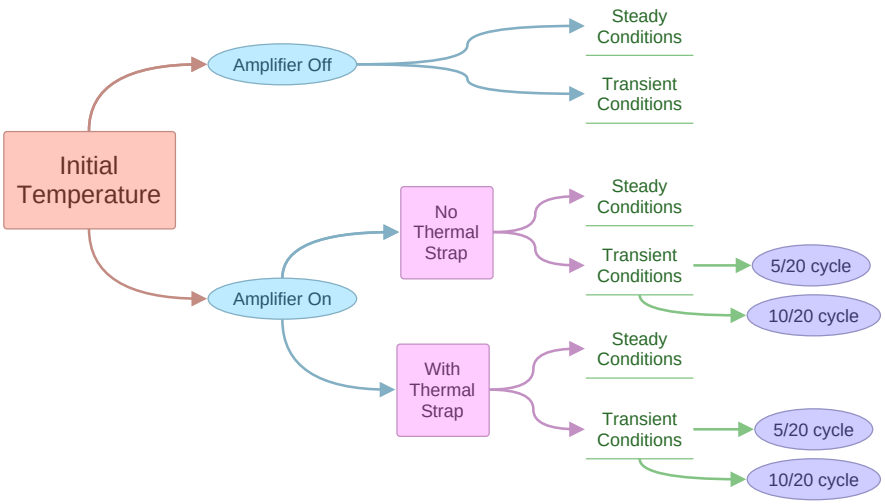


Figure 5.15 – *Schematic of the options simulated.*

5.5.2.3 Operational conditions

To respect manufacturer specifications, most components should work at a temperature bellow 80 °C. The maximum survival temperature of these components is 120 °C. However, the efficiency of the components is highly affected by increasing temperatures, and thus they work better with lower temperatures. Thus, the objective of the simulations is to guarantee that the temperatures of the electronic components remain below the maximum operational temperature, and that they do not reach the survival one, in any case.

Table 5.4 lists the power consumption for all components, considering two distinct cases, when the amplifier is operational and when it is turned off. The only two that do not have a steady power consumption is then the amplifier and its RF PCB.

Table 5.4 – *Power consumption of each component for the two main different cases.*

Object	Power [W]	
	Amp. Off	Amp. On
Amplifier	0	2
Main Chip	1.8	
Memory 1	0.25	
Memory 2	0.25	
Transceiver	1	
Main PCB	0.5	
Top PCB	0	
Bottom PCB	1	
RF PCB	0	0.25
Total Power	**4.8**	**7.05**

5.5.3 Results and discussion

5.5.3.1 Amplifier off

After modelling the full system, the first step was to determine the temperature distribution when the amplifier is turned off. This can be considered the baseline for the system, giving figures of merit for the temperatures of the main electronic components. Moreover, the worst case conditions are used as representative of the system, so the hottest point of each electronic component has to be determined.

As seen in Figure 5.16, with the amplifier off, the main chip is the hottest component (with a maximum temperature around $63\,^{\circ}\mathrm{C}$), closely followed by the transceiver. Their temperature difference is approximately $4\,\mathrm{degree}$, whereas the memories are about $12\,\mathrm{degrees}$ colder than the main chip. Between the memories the temperatures differ less than $1\,\mathrm{degrees}$. The amplifier temperature is even further away from the one of main chip, with less $28\,\mathrm{degrees}$. After $33\,\mathrm{minutes}$ of continuous operation, all components reach a temperature plateau, with differences bellow $0.01\,\mathrm{degrees}$.

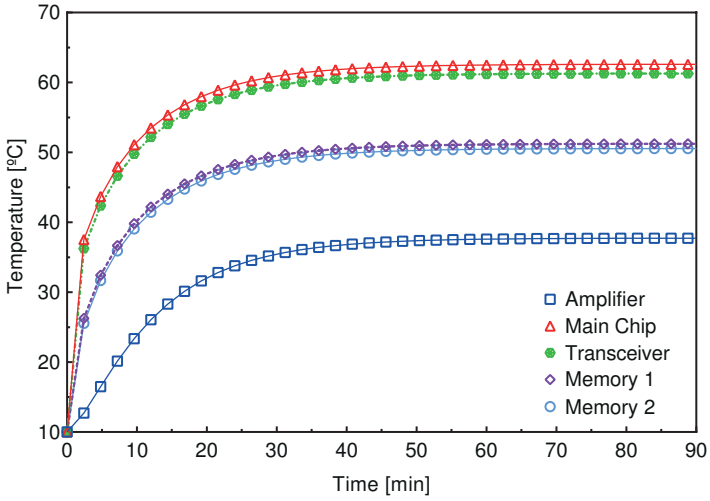


Figure 5.16 – *Temperature evolution for a full orbital period for all electronic components when the amplifier is off.*

As the main chip and the transceiver have similar behaviour, and since these are the components that show the highest temperatures, from this point forward the main chip is used as representative of the others.

5.5.3.2 Amplifier on

When the amplifier is turned on, the produced excess heat represents a rise of up to $4\,\mathrm{degrees}$ for the main chip, as plotted in Figure 5.17. This is the worst case and occurs when there is no thermal strap and the operation cycle of the amplifier is a $10/20\,\mathrm{seconds}$ one. This temperature rise is also seen in the other components. However, the same is not true when just looking to the amplifier.

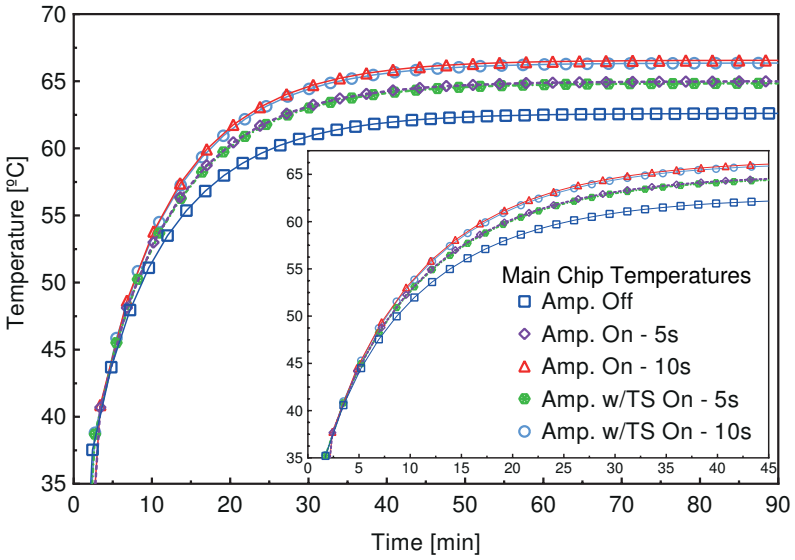


Figure 5.17 – *Temperature evolution of the main chip for all transient cases, including a zoom of the first* 45 minutes.

As soon as the amplifier is turned on, and after a 20 seconds hiatus, temperatures arose well above the 80 °C limit. The difference could reach up to 94 degrees, comparing to when the amplifier was turned off. Looking just to the first 5 minutes of operation (Figure 5.18), for better readability, the maximum temperature of the amplifier, without a thermal strap and between the two modes of operation, the 5/20 seconds and the 10/20 seconds cycles, differs around 7 degrees. Nevertheless, the warming up and cooling down in both cycles are very similar.

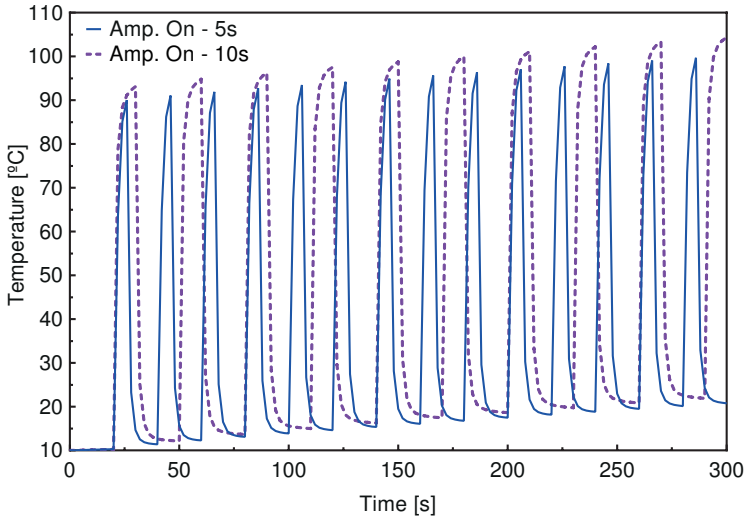


Figure 5.18 – *Temperature evolution for the amplifier, without a thermal strap, during the first* 5 minutes*, working either with a* 5/20 seconds *cycle or a* 10/20 seconds *one.*

Adding the thermal strap between the amplifier and the shielding case yields a significant change, resulting a decrease in the maximum temperature of more than 25 degrees. This is a strong argument for the thermal strap use, and is reflected in Figure 5.19. Furthermore, the temperature cycle is almost equal to both cases, with only a lower temperature. This similarity

is an extra evidence that what is making the temperature decrease is the addition of the thermal strap, and not the operational cycle.

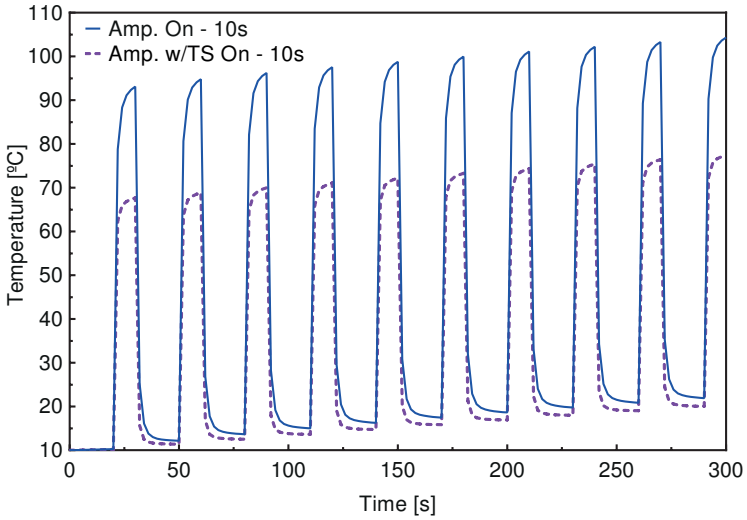


Figure 5.19 – *Comparison of the temperature evolution for the amplifier with and without the thermal strap, working with a* 10/20 seconds *cycle, for the first* 5 minutes.

Since the temperature is constantly rising, and the cycles of operation are very similar (*i.e.* warm up and cool down), Figure 5.20 shows only the maximum temperature reached for each cycle of operation and configuration. There the differences in temperature with the use of a thermal strap, and between the cycles, are clearly visible. The maximum temperature of the amplifier has fallen from about 131 °C to around 103 °C, when working on a 10/20 seconds cycle, or from 124 °C to around 99 °C for the 5/20 seconds cycle. Nevertheless, even with the thermal strap, the temperatures are above the 80 °C limit after about 6 minutes when operating within a 10/20 seconds cycle. The other mode takes about 1 minute more to reach that limit.

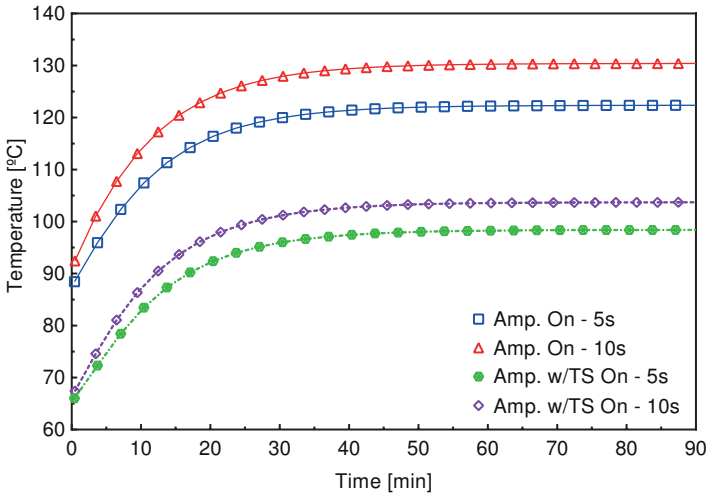
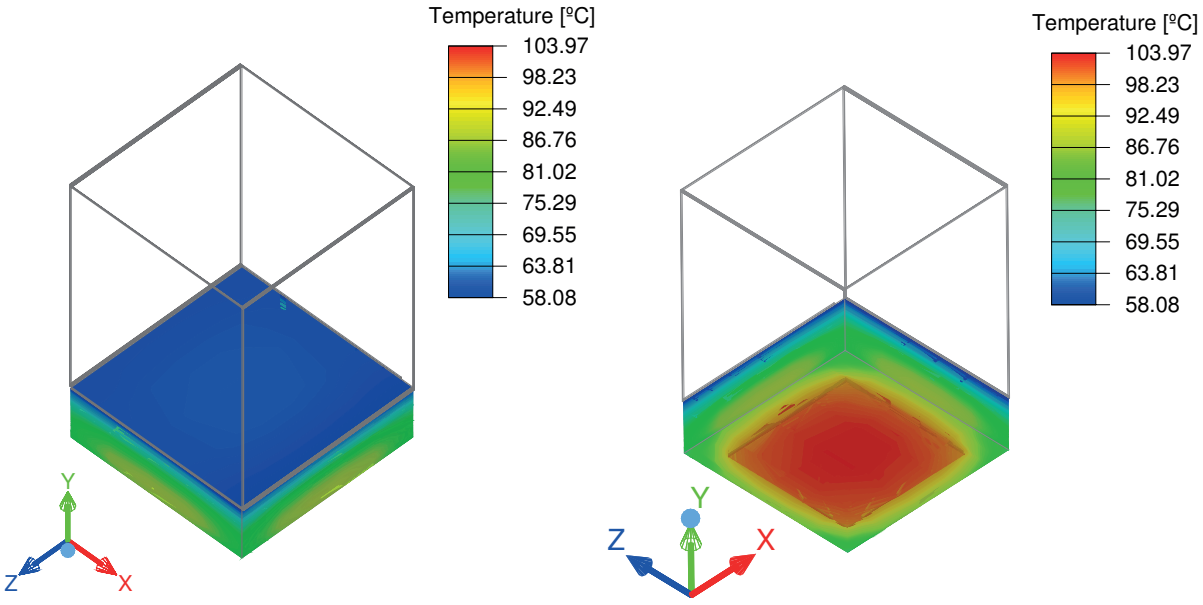


Figure 5.20 – *Maximum temperature evolution of the amplifier with different operational cycles, with and without the thermal strap.*

5.5.3.3 Temperature distribution – Amplifier on

Apart from registering the hottest points of the model, it is also interesting to look for the actual temperature distribution. For example, with the amplifier working with a 10/20 seconds cycle and the thermal strap, the hottest point of the amplifier is at a temperature of about 104 °C (Figure 5.21), whereas the thermal strap is only at 61 °C (Figure 5.22). This temperature difference is explained by the distribution of heat inside the amplifier. Because of the internal configuration and materials of the amplifier most of the heat is carried to its thermal pad, at the bottom, while few goes to the top, as illustrated in Figure 5.21b.



(a) *Amplifier seen from the top* **(b)** *Amplifier seen from the bottom*

Figure 5.21 – *Temperature distribution of the amplifier after a full orbital period (*90 minutes*).*

At the same time, with this strap configuration in a closed loop, both sides are symmetric and conduct similar amounts of heat to the enclosing casing (Figure 5.22). This yields a temperature difference of almost 15 degrees between the thermal strap top and bottom.

As a result of the heat distribution of the amplifier, the PCB that supports it (the RF PCB) is very hot underneath and around the amplifier (as is depicted in Figure 5.23). The rest of the board remains moderately cool, since the PCB is not very good at transporting heat. Nevertheless, what is carried by it is conducted to the supporting rods, and from them to the main PCB beneath.

The shield casing, that receives the heat from the amplifier through the thermal strap, does not seem to have reached its heat carrying capacity, as shown in Figure 5.24. The hottest points of the casing are close to where the thermal strap is attached, and in the connection between the case and the RF PCB. Nonetheless, the temperature range displayed is less than 2 degrees.

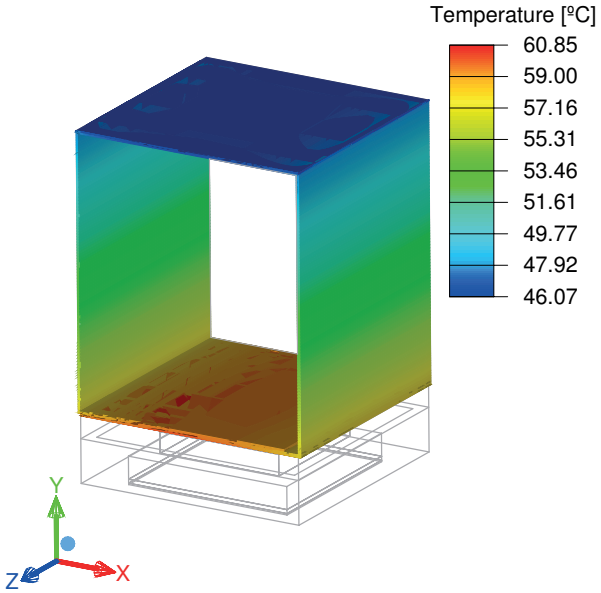
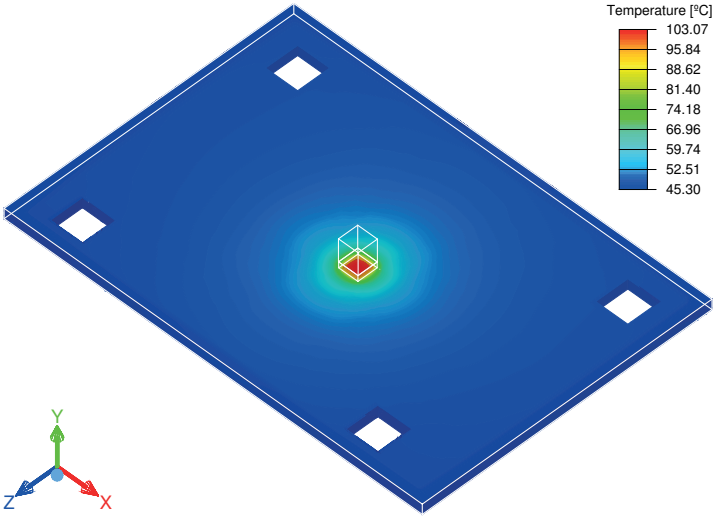
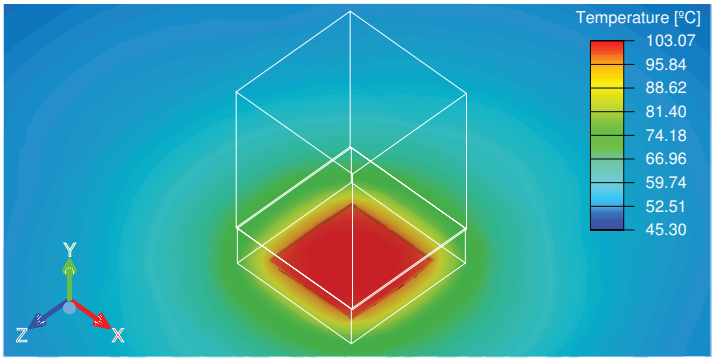


Figure 5.22 – *Thermal strap temperature distribution after* 90 minutes.

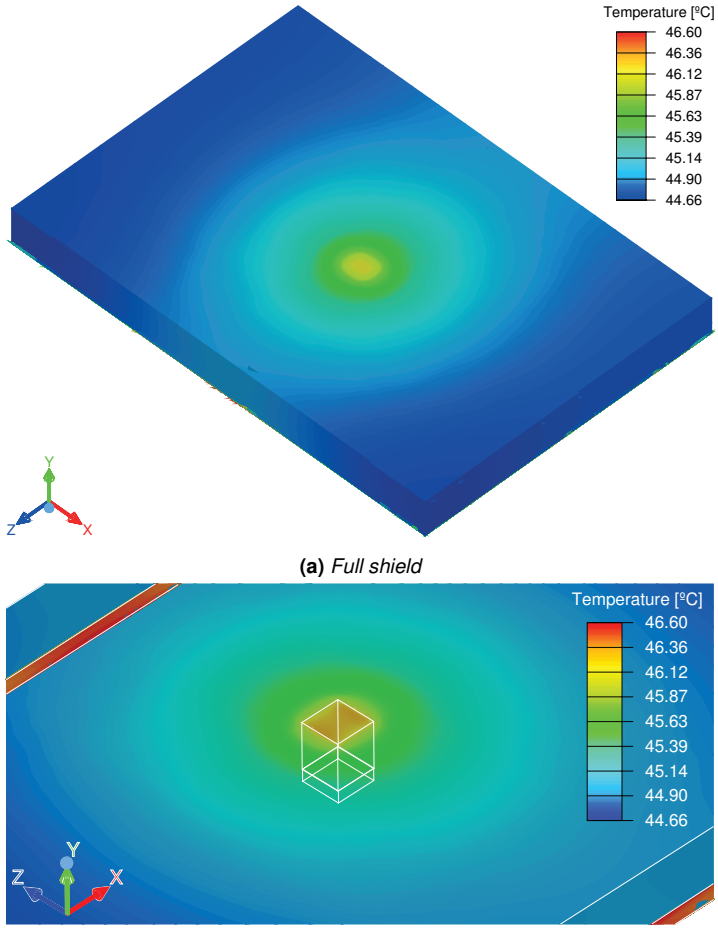


(a) *Full view of the RF PCB*



(b) *Close up of the amplifier location*

Figure 5.23 – *Temperature distribution of the RF PCB, which supports the amplifier, after* 90 minutes.



(a) *Full shield*

(b) *Close up of the amplifier location*

Figure 5.24 – *Temperature distribution of the amplifier shield casing after* 90 minutes.

5.5.4 Analysis summary

An inescapable fact is that when the amplifier is turned on, regardless of the working cycle or configuration, all components will have higher temperatures. Furthermore, the most problematic electronic component is clearly the amplifier, reaching sooner or later temperatures higher than the recommended ones.

Comparing the different configurations, with or without the thermal strap, it is evident that its use is fundamental, with temperatures falling up to 27 degrees. Conversely, changing the amplifier mode of operation does not have a significant impact on the temperatures reached.

Since the casing is still only moderately warm, a possible solution would be to extend the thermal strap to encapsulate both the entire amplifier, as well as the surrounding PCB area, increasing thus the contact surface. By doing that, the limitations arising from the heat distribution inside the amplifier and the PCB could be minimised.

An additional solution to this problem would be to add another thermal strap. This could be linked to the bottom of the RF PCB. However, a new heat sink would have to be selected, since

the main PCB beneath it is not an option (due to its low conductivity). If this connection is added, it should be properly electrically isolated (to prevent short circuits), and making sure that the PGS thermal strap fragility is respected.

5.6 Another approach to thermal analysis and induced accelerations

The methods discussed so far are mainly used to determine the temperature distribution within the spacecraft and its components, to access operation conditions. However, sometimes it is necessary to understand what are the implications, system and mission wise, of those temperatures. For example, as was mentioned before, the spacecraft thermal environment influences its trajectory, when far from the Sun, which is relevant when designing interplanetary travels.

To study the effects produced by the exterior temperatures of a spacecraft, LP and FEM methods are computationally heavy, difficult to set up or simply cannot provide the data intended. Therefore, another method to obtain this information is presented here, the Pointlike source one, based on previous works. To show the benefits of this method a test case is also discussed, the New Horizons spacecraft, one of those where the effect is more evident (spacecraft equipped with RTGs travelling to the outer planets).

5.6.1 Pointlike source method

5.6.1.1 Motivation

The purpose of the pointlike source method is to be both flexible and computationally fast, while still giving relevant results for a spacecraft thermal radiation environment, and keeping all physical features of the problem scrutinisable [32]. Several test situations can be modelled with this method, to assess the results robustness, and verify that the simplicity and transparency do not come at the expense of accuracy [33].

The pointlike source method is capable of taking into account several parameters with large degrees of uncertainty. This is an important feature when modelling situations where there is not much accurate design data available, or when the material's state evolution is unknown (*e.g.* when they are subject to extended periods of degradation in space). This is achieved by giving a representative statistical distribution to each parameter according to the information available, and using a Monte Carlo simulation, which generates a large number of random values, to get a probability distribution of the final result [34, 40].

Although the method is also discussed here, it has already proven its reliability and robustness within the context of the Pioneer anomaly and the Cassini solar conjunction experiment. In those cases it yielded results in agreement with radiometric navigation data, with a high confidence level, and verified by finite-element models results [35, 36]

5.6.1.2 Radiative momentum transfer

The physical formulation of this method is based on the representation of the spacecraft thermal emissions with a number of criteriously placed pointlike sources, distributed over its external surface. Although there are different types of sources available to model surface emissions, depending on the object and its characteristics, this method uses mostly Lambertian ones. Always employing the Poynting vector field (for both radiation emission and reflection), the time-averaged one for a Lambertian source with an emissive power W, and located at $\mathbf{x}_0$, is given by

$$\mathbf{S}_{\text{Lamb}}(\mathbf{x}) = \frac{W}{\pi||\mathbf{x}-\mathbf{x}_0||^2}\left(\mathbf{n}\cdot\frac{\mathbf{x}-\mathbf{x}_0}{||\mathbf{x}-\mathbf{x}_0||}\right)\frac{\mathbf{x}-\mathbf{x}_0}{||\mathbf{x}-\mathbf{x}_0||}, \tag{5.35}$$

where $\mathbf{n}$ represents the surface normal.

With the Poynting vector flux, E_{ilum}, passing through an illuminated surface, S, with normal vector $\mathbf{n}_{\text{ilum}}$, which is computed with the integral over the full surface,

$$E_{\text{ilum}} = \int_S \mathbf{S}\cdot\mathbf{n}_{\text{ilum}}\, dA, \tag{5.36}$$

it is possible to derive the amount of power illuminating that surface, W_{ilum}.

The radiation absorbed by the illuminated surface produces a radiation pressure which, for an opaque unit surface, is given by the radiation power flux divided by the speed of light ($p_{\text{rad}} = E/c$). This pressure has a symmetrical equivalent on the emitting surface. For the case of a non opaque surface (*i.e.* when there is transmission), the value for the pressure is multiplied by an absorption coefficient. Radiation reflection by a surface is discussed below, and can be treated as a re-emission of part of the absorbed radiation.

Having the radiation pressure, it is possible to obtain the force exerted on that surface,

$$\mathbf{F}_{\text{rad}_{\text{absorb}}} = \frac{1}{c}\int_S \mathbf{S}\cdot\mathbf{n}_{\text{ilum}}\frac{\mathbf{S}}{||\mathbf{S}||}dA. \tag{5.37}$$

This integral, or any over the emitting surface, has to be taken over a closed surface enveloping the absorbing or emitting surfaces, respectively. Moreover, a proper balance is needed, when there is a set of emitting and absorbing surfaces, casting shadows in each other.

5.6.1.3 Reflection modelling – Phong shading

In order to compute the radiation reflection it is necessary to resort to a set of techniques and algorithms, called the Phong Shading method, which has been used for a long time to render illumination in three-dimensional computer graphics [230]. With this method the reflections on the various surfaces can be modelled in a simple and straightforward way, besides gaining a more accurate account of the thermal radiation exchanged between the surfaces. However, this methodology has to be adapted from an intensity based formulation (*i.e.* with energy per unit of the

projected emitting surface), to a Poynting vector based one (where the energy flux per unit surface is used instead).

The Phong Shading method has two parts to it, a diffusive and specular reflection model, and an interpolation of curved surfaces represented by polygons. The Phong reflection model combines several empirical formulas together with parameters characterising the material (including the ambient, diffusive, and specular reflection constants, k_a, k_d, and k_s respectively) and the radiation (including the respective light source intensities, i_a, i_d, and i_s). The illumination value of any given point in a surface is then given by

$$I_\mathrm{p} = k_\mathrm{a} i_\mathrm{a} + \sum_{m \in \text{lights}} \left[k_\mathrm{d} (\mathbf{l}_m \cdot \mathbf{n}) i_\mathrm{d} + k_\mathrm{s} (\mathbf{r}_m \cdot \mathbf{v})^\alpha i_\mathrm{s} \right]. \tag{5.38}$$

As can be seen, the illumination value also depends on the surface normal, $\mathbf{n}$, and its "shininess" constant, α, representing the mirror-like aspect of that surface. Other parameters that need to be used are the direction of the mth light source, of the reflected ray, and of the observer, represented by $\mathbf{l}_m$, $\mathbf{r}_m$, and $\mathbf{v}$ respectively.

Although the formulation of Equation (5.38) is general to any problem, for reflection on surfaces of a spacecraft in space there are some constrains and simplifications that need to be applied. Firstly, since the background radiation does not exist in space, the ambient light parameters k_a and i_a are not relevant for the problem. Both diffusive and specular intensities, i_d and i_s, should be equal as they represent the same radiation source. Finally, although for thermal radiation the important part of the spectrum is the infrared, there should be no problem in applying a method devised for visible light, as long as the natural wavelength dependence of the material constants are taken into consideration.

As explained before, adapting the previous intensity formulation to one using the Poynting vector field, each reflection component can be calculated separately for any point on the reflecting surface, $\mathbf{x}'$. While the diffusive (d) part is given by

$$\mathbf{S}_\mathrm{rd}(\mathbf{x}, \mathbf{x}') = \frac{k_\mathrm{d} |\mathbf{S}(\mathbf{x}') \cdot \mathbf{n}|}{\pi ||\mathbf{x} - \mathbf{x}'||^2} \, \mathbf{n} \cdot (\mathbf{x} - \mathbf{x}') \, \frac{\mathbf{x} - \mathbf{x}'}{||\mathbf{x} - \mathbf{x}'||}, \tag{5.39}$$

the specular (s) one is

$$\mathbf{S}_\mathrm{rs}(\mathbf{x}, \mathbf{x}') = \frac{k_\mathrm{s} |\mathbf{S}(\mathbf{x}') \cdot \mathbf{n}|}{\frac{2\pi}{1+\alpha} ||\mathbf{x} - \mathbf{x}'||^2} \left[\mathbf{r} \cdot (\mathbf{x} - \mathbf{x}') \right]^\alpha \frac{\mathbf{x} - \mathbf{x}'}{||\mathbf{x} - \mathbf{x}'||}. \tag{5.40}$$

Both components depend on the incident radiation, $\mathbf{S}(\mathbf{x}')$, and on the material respective coefficients, k_d and k_s, as expected.

The reflected radiation field is then fully defined by adding up Equation (5.39) and Equation (5.40). Any number of reflection steps can be considered with these equations, by simply iteratively applying them to each reflector, and performing a discretisation of the reflection surface in several pointlike reflector sources, if necessary.

5.6.1.4 Reflections computation

To model an actual spacecraft it is necessary to begin by distributing radiation sources over the relevant surfaces, and determine the radiation field, using Equation (5.35). With Equation (5.36) it is possible to estimate the energy flux, and with it determine how many sources are necessary to properly model the radiation emitted by any surface.

The next step is to compute the emitted radiation force of each surface i (with normal $\mathbf{n}_i$), which is done with

$$\mathbf{F}_{\mathrm{rad}_{\mathrm{emit}_i}} = \frac{2}{3}\frac{W_i}{c}\,\mathbf{n}_i. \tag{5.41}$$

This has to be added to the absorption force on the illuminated surfaces, Equation (5.37). Although at this stage a first approximation of the total thermal radiation can be derived, the reflection field has to be computed, applying Equation (5.39) and Equation (5.40) into Equation (5.37), and add them to the previous result.

With this full thermal radiation force, for one reflection step, and with the mass of the spacecraft, m_{SC}, the thermal acceleration is given by

$$\mathbf{a}_{\mathrm{rad}} = \frac{1}{m_{\mathrm{SC}}}\left(\mathbf{F}_{\mathrm{rad}_{\mathrm{emitted}}} + \mathbf{F}_{\mathrm{rad}_{\mathrm{absorbed}}} + \mathbf{F}_{\mathrm{rad}_{\mathrm{reflected}}}\right). \tag{5.42}$$

5.6.2 New Horizons model

5.6.2.1 Physical setup

To model the thermal emissions, a geometric model of the spacecraft has to be built first. A simple model without small geometric details (compared to the overall dimensions) is enough, since only the basic features have a significant impact on the results (as shown in Ref. [32, 33]).

For the case of the New Horizons spacecraft, Figure 5.25, apart from a few protuberances it can be represented by a simple polyhedron shaped main body (the bus), with a RTG attached to its side, and a main high gain communication antenna on top of it.

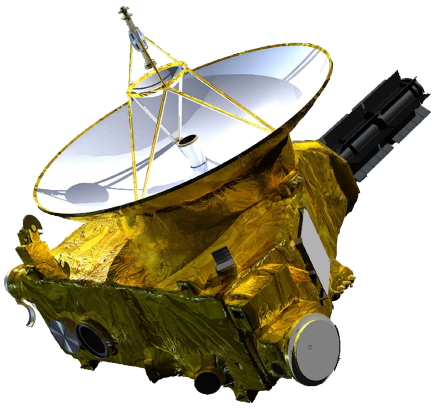


Figure 5.25 – *Artistic impression of the New Horizons spacecraft (image adapted from Ref. [231]).*

According to the available specifications [232], the main body is symmetric with respect to the X-Y plane, as seen in Figure 5.26. It measures $2\,\mathrm{m}$ (in the X axis), with a height ranging from $0.7\,\mathrm{m}$ to around $0.3\,\mathrm{m}$ (in the Y direction). Its width ranges from $0.3\,\mathrm{m}$ in the narrowest point to $2\,\mathrm{m}$ in the widest one. Housing most of the electronics and payload instruments, it has an evenly distributed thermal radiation emission, because of the multilayer thermal blankets. These cover most of its surface, stabilising the spacecraft's temperature and making it reasonably homogeneous. The reflection by the main body is also influenced by the use of these thermal blankets.

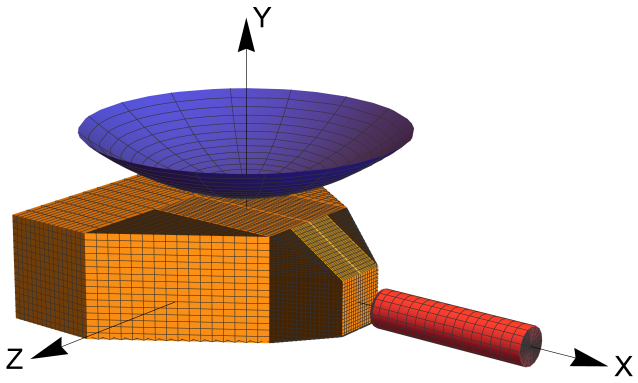


Figure 5.26 – *Model of the New Horizons used for the analysis, showing the antenna, main body, and RTG.*

The main antenna dish, capable of providing a data rate of $600\,\mathrm{bps}$ for data downlink at $36\,\mathrm{AU}$, has also its back covered with MLI. The antenna has a parabolic shape with about $2.1\,\mathrm{m}$ in diameter, and a depth in its centre of $0.4\,\mathrm{m}$. Although not represented in Figure 5.26, since its contribution is negligible to the calculations, the antenna is supported by a structure attached to the main body, which keeps the two separated by $0.12\,\mathrm{m}$ (in the closest point).

The RTG is also connected to the main body, in this case by an adaptor collar and a support structure, to isolate the two both electrically and thermally [41]. With a somewhat cylindrical shape, the RTG measures about $1\,\mathrm{m}$ in length and has a $0.3\,\mathrm{m}$ diameter, which does not take into account the cooling fins (seen in Figure 5.25).

When it was launched, New Horizons had a total mass of $478\,\mathrm{kg}$, part of it the hydrazine propellant and the helium pressurant for the propulsion tanks (about $77\,\mathrm{kg}$) [233]. The trajectory it took was so optimised and well executed that, by the time it reached Pluto, an estimated $47\,\mathrm{kg}$ of propellant was still available.

Within this trajectory there were moments where the spacecraft would be performing scientific experiments, trajectory correction manoeuvres, or simple maintenance, and was operating in a three-axis control mode. However, there were others moments when the spacecraft would be in a spin stabilised mode, rotating around its Y axis (seen in Figure 5.26), called hibernation periods [41]. Its main antenna would be pointing to Earth either listening or transmitting data. During these periods, where there is no manoeuvre, it would be possible to detect any kind of subtle non-gravitational accelerations, using a trajectory determination method with an accurate enough capacity.

5.6.2.2 Power supply

The New Horizons spacecraft is powered by that single F-8 RTG, equipped with about 9.8 kg of plutonium-238 dioxide [234]. With a half-life of 87.7 years, and an initial thermal output of 3 948 W, the power produced by the New Horizons RTG has a time evolution given by

$$W_{\text{thermal}}^{\text{RTG}}(t) = 3\,948 \times e^{-t\,\log(2)/87.7}\,\text{W}, \tag{5.43}$$

where the time, t, is expressed in years, with $t = 0$ corresponding to the moment of launch.

Although Equation (5.43) gives the thermal power produced, thermocouples have a very low efficiency, and thus only a small fraction of the energy is converted in electrical power. At the time of launch, the RTG supplied the spacecraft with 246 W, decreasing to only about 200 W when Pluto was encountered. This reduction in electrical output reveals that the thermocouples efficiency decreases over time faster than the Plutonium half-life, as seen on the data shown in Figure 5.27.

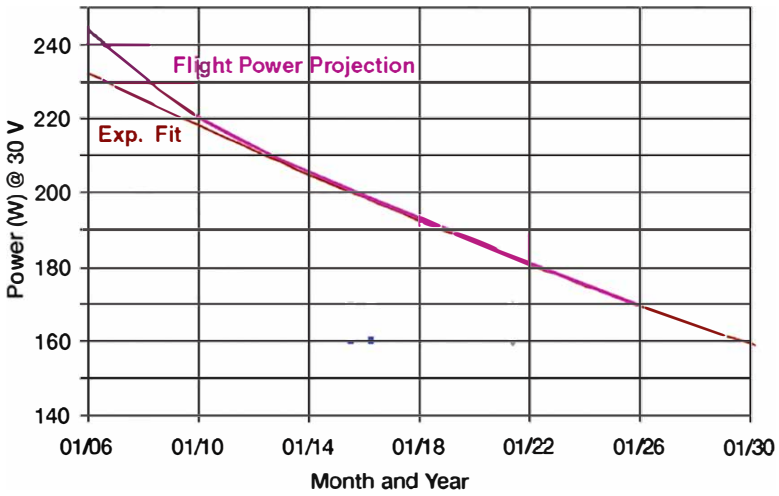


Figure 5.27 – *RTG electrical power output evolution with time (image adapted from Ref. [41]).*

Performing a fit to the data of Figure 5.27, and assuming a behaviour similar to the thermal output one (only with a smaller half-life), the electrical power evolution can be expressed by

$$W_{\text{electric}}^{\text{RTG}}(t) = 241.3 \times e^{-t\,\log(2)/39.1}\,\text{W}. \tag{5.44}$$

The electric power, given by Equation (5.44), represents the power emitted by the main bus ($W_{\text{Bus}}(t) = W_{\text{electric}}^{\text{RTG}}(t)$), and can be directly introduced into Equation (5.35), since even if it takes a while all of that power is transformed into heat. Conversely, for the power emitted by the RTG a balance between thermal and electric power has to be made, to respect the energy equilibrium ($W_{\text{RTG}}(t) = W_{\text{thermal}}^{\text{RTG}}(t) - W_{\text{electric}}^{\text{RTG}}(t)$), before it can be introduced in Equation (5.35).

5.6.2.3 Thermal emissions modelling

With the geometric model and the power emission defined, it is necessary to study the distribution of sources over the external surfaces. This is done first for the RTG, as it is the component with the highest thermal emitted radiation, followed by the main body.

Being a cylindrical body, emitting in all directions (mainly about its longitudinal axis), the radiation emitted by the RTG is either symmetric or perpendicular to the spin axis of the spacecraft, and thus it cancels out ($\mathbf{F}_{\text{rad}_{\text{emitted}}} = 0$). Looking at Figure 5.26, the only component of the radiation pressure that produces an acceleration is the one illuminating the main antenna. Nevertheless, the sources of Equation (5.35) have to be evenly distributed over the surface of the RTG, to correctly represent the emitted thermal radiation field. However, those sources are for flat surfaces, and thus the curved cylinder had to be discretised as a n regular polygonal (where n represents the number of faces) with m cross sections parallel to the polygonal base.

With either four or eight cross (or axial) sections, and 4, 8, 16 and finally 32 sources in the azimuthal direction (corresponding to the number of faces), a convergence analysis for the energy flux (Equation (5.36)) was performed. The energy difference between the two axial discretisations is negligible (about 0.02%) when considering the level of accuracy of the method. Conversely, for the azimuthal direction, when using either 2 or 16 sources, the difference can reach about 2%. Between a 16-sided polygon and a 32-sided one the question is no longer the energy flux difference, only 0.018%, but the computational effort required for the possible level of accuracy. Therefore, the RTG representation selected has 16 sources in the azimuthal direction, divided by four axial sections, as can be seen in Figure 5.28.

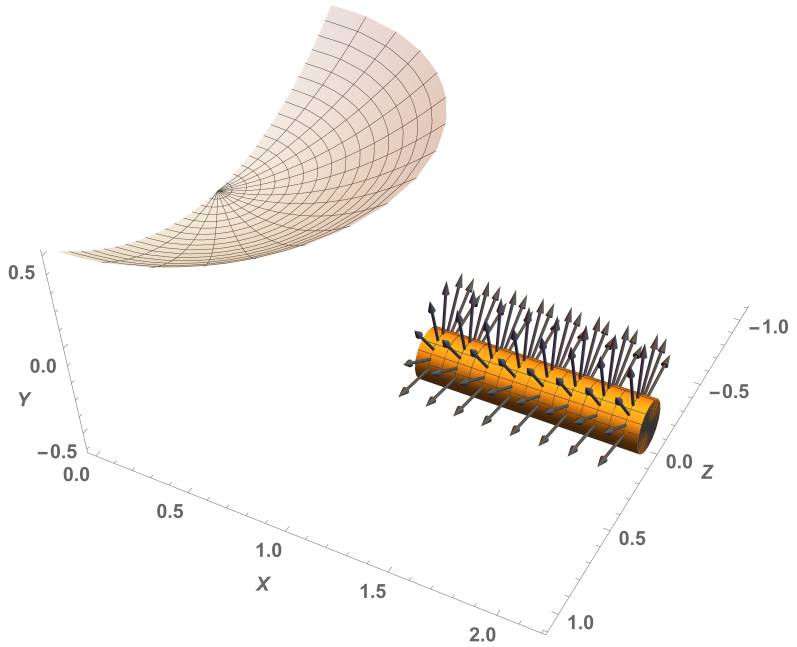


Figure 5.28 – *Schematic of the eight times sixteen Lambertian sources (represented by the arrows) distribution used to represent the RTG thermal emissions. Only sources of the upper half of the RTG are shown, for simplicity, together with the illuminated part of the high gain antenna.*

The main body of the New Horizons, the only other source of thermal radiation, had to be split in smaller parts since there are surfaces pointing in separate directions, and thus producing forces with different components. Furthermore, the total power ($W_{\text{Bus}}(t)$) was divided by each surface so that an even distribution is obtained at the end, an assumption based on the use of MLI over the entire body. To accomplish this, the emitted power for each surface is taken to be proportional to its area fraction, *i.e.* $W_{A_i}(t) = f_{A_i} \times W_{\text{Bus}}(t)$, where the area fraction is given by the area of surface i divided by the total body area ($f_{A_i} = A_i/A_{\text{total}}$). These body surfaces illuminate the main antenna, or simply irradiate to deep space, so while the former produces a radiation pressure (according to Equation (5.37)), the latter has a simpler treatment (Equation (5.41)).

Besides dividing the total emitted power, each surface has to discretised with a different number of Lambertian sources. For the case of the top wall, the most important one that illuminates the antenna, the difference in energy flux is 0.04% between modelling it with a single centred source or 16 distributed ones. This difference is much smaller (about 0.001%) when changing from 8 to those 16 sources. Therefore, considering the computational power required, the top wall is represented by 16 sources, as is illustrated in Figure 5.29.

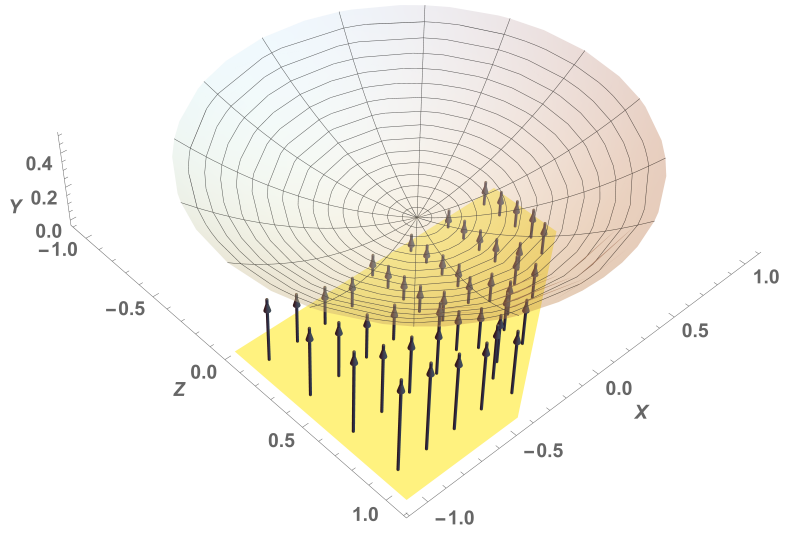


Figure 5.29 – *Schematic of the sixteen Lambertian sources used for the main body top wall (for simplicity, and for being symmetrical, only half of the wall is represented).*

For the other surfaces of the main body, illuminating the antenna, a similar process showed that the difference between four and eight sources was less than 0.0007%, and thus eight sources were used. Moreover, combining the energy flux passing through the antenna of all of those surfaces yields only about 3% of the total bus power.

The surfaces of main body that do not illuminate the antenna are either on the bottom or on the sides, radiating all their energy to deep space. For symmetry reasons, and due to the spin stabilisation, only the bottom contributes to the thermal acceleration generated. Thus, the resultant force of those surfaces is computed using Equation (5.41), with $W_i = f_{A_i} W_{\text{Bus}}$.

5.6.3 Results and discussion

By creating baseline scenarios, some initial results were assessed before going to a comprehensive statistical analysis. This not only provides figures of merit for the variables, but also gives an insight on the impact of the different parameters on the final result. Conversely, with the Monte Carlo method it is possible to study a broad range of parametric values, all statistically distributed.

5.6.3.1 Baseline scenarios

The two instants where there is more information about the spacecraft parameters are at launch and at the moment when the New Horizons encounters Pluto. For example, the thermal output of the RTG and the electrical power generated are at their maximum when the New Horizons was launched, providing an upper bound for the thermal accelerations, and thus is used in the following assumptions. Nonetheless, the Pioneer anomaly has already shown that any acceleration generated by thermal emissions is concealed by the solar pressure effect up to the asteroid belt [38].

With some of the values for the launch fixed (*i.e.* $m_{\mathrm{NH}} = 478\,\mathrm{kg}$, $W_{\mathrm{Bus}}(t = 0) = 240.4\,\mathrm{W}$, $W_{\mathrm{RTG}}(t = 0) = 3\,707\,\mathrm{W}$), the first hypothesis taken was that there were no reflections ($k_{\mathrm{d}} = k_{\mathrm{s}} = 0$), and thus the acceleration was given by just the emitted and absorbed radiation,

$$\mathbf{a}_{\mathrm{Hyp\,1}} = (-5.4\,\mathbf{e}_X + 8.5\,\mathbf{e}_Y + 0\,\mathbf{e}_Z) \times 10^{-10}\ \mathrm{m/s^2}. \tag{5.45}$$

This initial computation allows for confirming some expected results, *e.g.* the null acceleration on the $\mathbf{e}_Z$ direction (due to spacecraft symmetry in the X-Y plane). The result also reveals that if the spacecraft was not spin stabilised, there would be a significant acceleration in the $\mathbf{e}_X$ direction, compared to the $\mathbf{e}_Y$ component.

For the second hypothesis a reflection is added to the computation, by defining the reflection coefficients (diffusive and specular) and the shininess constant. Looking at information about the MLI manufacturer for the New Horizons, up to 95% of the total incident radiation can be reflected back, although in a very diffusive form and with a small shininess. Representing this with $k_{\mathrm{d}} = 0.85$, $k_{\mathrm{s}} = 0.1$, and $\alpha = 3$, the full model gives an acceleration of

$$\mathbf{a}_{\mathrm{Hyp\,2}} = (-7.2\,\mathbf{e}_X + 14.9\,\mathbf{e}_Y + 0\,\mathbf{e}_Z) \times 10^{-10}\ \mathrm{m/s^2}. \tag{5.46}$$

Although the null and non-null component distribution still holds, there is a considerable rise of the modulus values when considering reflections, in particular for the $\mathbf{e}_Y$ direction (which almost doubles).

To understand how the diffusive and specular reflection components impact the final result, a new hypothesis was formulated, based on a 60% total reflectance, which is a typical value available in the literature for aluminised kapton (like the New Horizons one) with the aluminium on the inside [235]. Assuming a 75% diffusive component (*i.e.* $k_{\mathrm{d}} = 0.45$ and $k_{\mathrm{s}} = 0.15$), the new

acceleration is

$$\mathbf{a}_{\text{Hyp 3}} = (-6.4\,\mathbf{e}_X + 12.5\,\mathbf{e}_Y + 0\,\mathbf{e}_Z) \times 10^{-10}\ \text{m/s}^2. \tag{5.47}$$

The hypothesis described above would be enough to start a parametric analysis. However, one more test case was studied, for completeness, where the total reflection is kept close to the third hypothesis (65%), but the components are different, with 85% for the diffusive one ($k_\text{d} = 0.55$ and $k_\text{s} = 0.10$). The result acceleration, and the starting point for the parametric analysis, is now

$$\mathbf{a}_{\text{Hyp 4}} = (-6.6\,\mathbf{e}_X + 12.9\,\mathbf{e}_Y + 0\,\mathbf{e}_Z) \times 10^{-10}\ \text{m/s}^2. \tag{5.48}$$

5.6.3.2 Parametric study

To plot the thermal acceleration evolution along the New Horizons trajectory, using an exponential fit, is is necessary to have three values defined. Considering the first two are at the launch and at the encounter, where the parameters are known, the third was assumed to be at half of the trip.

The mass is the only parameter where a statistical variation was not considered, as it is well defined for all instants. While launch and encounter values have been mentioned before, for half of the trip it was assumed that half of the propellant spent had already been used, which is in agreement with available data (Ref. [42]). Therefore, the mass of the New Horizons at half the trip is 461 kg.

Although the values for the energy produced by the RTG and consumed by the main body are given by Equation (5.43) and Equation (5.44) respectively, there is still some uncertainty here. As such, a normal distribution was used for each value, with an associated standard deviation, σ. While low confidence values have a 3.5% deviation of the obtained power result, high confidence ones have only 1.5%.

The parameters with the highest uncertainty are the reflection coefficients, for all previously mentioned reasons. Not giving a higher weight to any particular value, a uniform distribution for the diffusive component was used (from 0.55% to 0.95% of the total reflection). The specular component is obtained from this range using the relation between them (*i.e.* $k_\text{s} = k_\text{total} - k_\text{d}$). As a degradation of optical properties with longer periods of space exposure is expected, the total reflection was assumed to be decreasing with time. Thus, it goes from a $k_\text{total} = 0.8$ value at launch, to $k_\text{total} = 0.5$ when reaching Pluto, passing through $k_\text{total} = 0.65$ at half way.

With these defined statistical ranges, and using a Monte Carlo simulation, with 10^6 random values, the Y component of the thermal acceleration density distribution can be computed. For example, for the time of the encounter ($t = 9$ years), this acceleration has a normal characteristic (plotted in Figure 5.30) and a value, for a 2σ confidence level, of

$$(a_\text{NewHorizons})_Y = (11.5 \pm 0.3) \times 10^{-10}\ \text{m/s}^2, \tag{5.49}$$

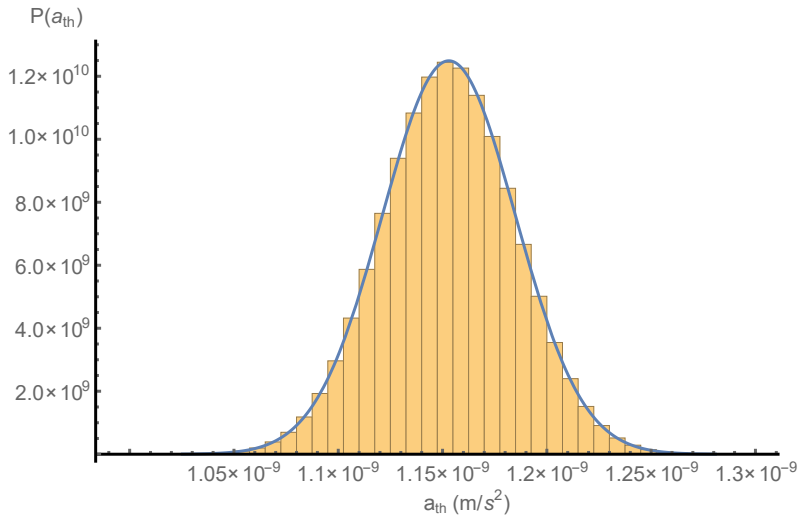


Figure 5.30 – *Thermal acceleration probability distribution, for the time of encounter with Pluto, in the Y direction, overlaid by the derived normal distribution.*

Combining this with the other two instants, launch and half way through the mission, the range for the thermal accelerations can be estimated for a 20 years period (as depicted in Figure 5.31). It not only shows the decrease with RTG Plutonium depletion, but fits well with the previous estimated non gravitational accelerations (Ref. [42]).

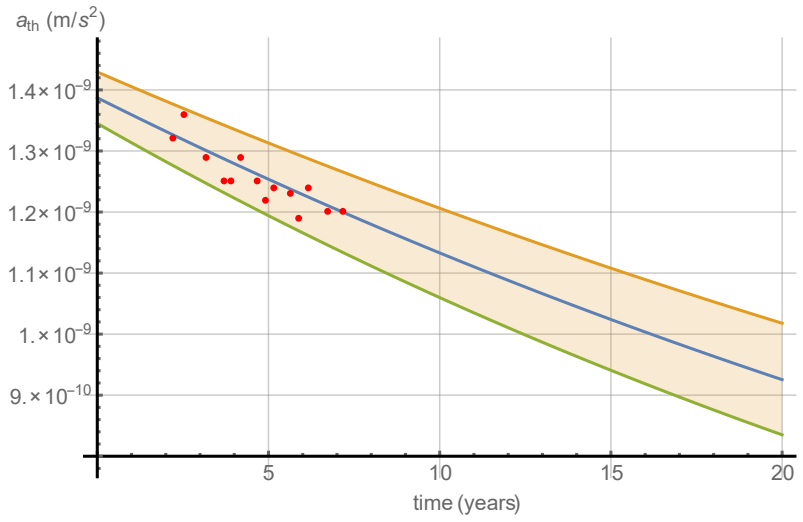


Figure 5.31 – *Thermal acceleration exponential fit for* 20 years *since launch (Pluto was reached after nine years) along the spacecraft Y axis, with the* 2σ *confidence region around it, and with measured data from Ref. [42].*

These results indicate that there is a non-negligible thermal acceleration in the Y direction, which, although small, may produce a significant trajectory offset with time. Assuming, for instance, that the New Horizons did not made any trajectory correction manoeuvres after the Jupiter flyby, in February 2007, then the difference in position would be of the order of $\Delta Y \approx 2 \times 10^4$ km, once it finally reached Pluto, 6 years afterwards.

5.6.3.3 Results of the thermal effects on attitude

With the pointlike source method, apart from the resultant thermal radiation force, each area element force (and its location) can be computed, with sufficient small error so that the thermal moment and its effects can be estimated. A first order method can be used (*cf.* Appendix B) to determine the attitude in both spin stabilisation and three-axis mode cases. The known variables for this problem are the centre of mass location (the reference frame origin of Figure 5.26), the spacecraft nominal spin rate ($\omega_0 = 5\,\text{rpm}$ [41]), and the principal moments of inertia of the inertia tensor ($A = \mathbf{I}_{XX} = 161.38\,\text{kg/m}^2$, $B = \mathbf{I}_{YY} = 402.12\,\text{kg/m}^2$ and $C = \mathbf{I}_{ZZ} = 316\,\text{kg/m}^2$ [236]).

Calculating the radiation forces (Equation (5.37)) for each element, and adding up their moment contributions (Equation (B.1)), the main resulting thermal moment at launch is

$$\mathbf{M}(t=0) \approx \mathbf{M}_Z = (+5.76 \pm 0.25) \times 10^{-7}\ \text{N m}. \tag{5.50}$$

Being this the upper bound of the resulting moment, the remaining components (M_X and M_Y of the order of $1 \times 10^{-12}\,\text{N m}$) can be discarded, as was expected and stipulated in Equation (B.2).

Spin stabilised case. In a passive spin mode, the Euler angles as a function of time are obtained from replacing Equation (5.50) into Equation (B.11). The results for the maximum expected deviations for ψ and ν, and their respective rates $\dot{\psi}$ and $\dot{\nu}$, are approximately

$$|\psi| \lesssim (12.7 \pm 0.6) \times 10^{-9}\,\text{rad}, \tag{5.51}$$
$$|\dot{\psi}| \lesssim (9.14 \pm 0.4) \times 10^{-9}\,\text{rad/s}, \tag{5.52}$$
$$|\nu| \lesssim (17.9 \pm 0.8) \times 10^{-9}\,\text{rad}, \tag{5.53}$$
$$|\dot{\nu}| \lesssim (9.14 \pm 0.4) \times 10^{-9}\,\text{rad/s}. \tag{5.54}$$

The frequency of these effects is so small that they are most probably difficult to detect. In fact, the attitude control system of the New Horizons is only capable of knowing the spin axis attitude to $471\,\mu\text{rad}$ [41], which is already four orders of magnitude higher than what would be required to detect these thermal effects. Nevertheless, this small wobble could be detected from Earth during communication with the spacecraft (due to the line-of-sight misalignment), if there is enough sensitivity to signal intensity decays.

With some rough approximations, the gain of parabolic antennae has a relation with the pointing accuracy given by $\Delta G(\theta) = -24\theta\Delta\theta/\theta^2_{3\text{dB}}$, for θ smaller than the half power beamwidth, $\theta_{3\text{dB}}/2$ [237]. Here the gain variation within an angle θ from boresight, $\Delta G(\theta)$, is given in dB, for a small deviation, $\Delta\theta$. While ΔG tends to zero in the boresight direction, and thus making it difficult to observe, the maximum reduction is seen for $\theta = \theta_{3\text{dB}}/2$ [237]. Therefore, for the case of the high gain antenna of the New Horizons ($\theta_{3\text{dB}} = 0.3^\circ$ [238]), and assuming the deviation obtained in Equation (5.53) ($\Delta\theta = \nu = 1.8 \times 10^{-8}\,\text{rad}$), the expected gain reduction is $4.1 \times 10^{-5}\,\text{dB}$.

Three-axis mode case. The three axis mode has a different treatment (using Equation (B.3) and Equation (5.37)), and the resulting angular velocity around the Z axis, produced by thermal effects at launch, is also very small,

$$\delta\dot{\omega}_Z \simeq (18.2 \pm 0.8) \times 10^{-10}\,\mathrm{rad/s}. \tag{5.55}$$

However, this effect is cumulative, growing in time, making it easier to detect, in principle. Nevertheless, the spacecraft would still have to be commanded not to perform any manoeuvre to correct for this effect, for example, for 30 consecutive days, since many manoeuvres are made when in the three-axis mode. This is a process similar to what was done during the Cassini Solar conjunction experiment [40].

Since the New Horizons turns about $5 \times 10^{-6}\,\mathrm{rad}$ per day, the largest possible accumulated rotation for those 30 days would have a deviation of $1.5 \times 10^{-4}\,\mathrm{rad}$. Translated to a gain reduction, this yields about $0.34\,\mathrm{dB}$, in the direction of the maximum gain variation.

CHAPTER 6

Conclusions

This concluding chapter gives an overview of the main take-home messages of this thesis and what has been learned in the process. A brief discussion of future actions is also presented, mainly for the proposed satellite communication protocol and the thermal analyses performed.

6.1 Design and development of small satellite missions

Small satellites, in particular micro and nano ones, clearly have several advantages for particular missions. Their lower developing costs allow for building a constellation, instead of a single spacecraft, which boosts their application. In fact, different payloads could be combined in a constellation to provide a comprehensive image, apart from larger surface and temporal coverages. Nevertheless, small satellites should work together with conventional ones, as they are complementary.

The faster development cycle of small satellites, in part a result of the extensive use of commercial-off-the-shelf components, also allows for a higher flexibility and greater number of mission opportunities. Moreover, newer technologies, either more advanced, cheaper, or both, can be incorporated in the design.

With less cost and complexity, smaller teams, even at the University or departmental level, are capable of developing their own spacecraft. This is an important benefit since more science oriented missions with faster research outcomes are possible. For example, the University of Vigo has already launched three nano satellites, has three more on track to be launched soon, and two others under study.

There is also a strong pedagogical component in these spacecraft, as their projects mimic conventional missions. Additionally, they provide a systematic opportunity to plan, design, build and test complex systems in a multidisciplinary environment, especially if concurrent design approaches are used. Micro and nano satellite missions can then provide an important set of skills for a new generation of space engineers and researchers. These can either be graduate or undergraduate students, as the design and development phases are within a student's academic programme duration, as well as young engineers, who can build their competences while the project is being developed. Spacecraft operations can also be handled by students, for instance.

In spite of their advantages, micro and nano satellites have important limitations and cannot fulfil all kinds of missions, in particular in the context of ocean observation and research. A clear limitation is the communication capability, when compared to larger conventional satellites. Nevertheless, as discussed in Chapter 4, the successful use of small satellites to build a communication network is closely linked to specific technologies. For instance, new and miniaturised high gain antennae, improved software defined radios, high efficient amplifiers, and better orbit and attitude control, must still be further developed. Another limitation, relevant for operating oceanographic payloads, besides the power and mass restrictions, is the pointing accuracy that these spacecraft can achieve. For example, $2°$ for sensing accuracy, which represents an uncertainty of $14\,\mathrm{km}$ for a $400\,\mathrm{km}$ altitude orbit, and less than $5°$ for control, is what has been obtained by CubeSats so far. However, this is not enough since accuracies closer to $0.02°$, representing ground uncertainties of $140\,\mathrm{m}$, are necessary for most ocean applications. Nonetheless, improvements capable to achieve these accuracies are already estimated for future CubeSat missions.

6.2 Oceanography and network operations

All the micro and nano satellites found in the survey of Chapter 3 fit into one of the three main categories: ocean imaging, data relay and space-borne ship-tracking (using AIS). Of the three, the latter category is the one with more missions found, since it has fostered more interest from both private and public institutions. This can be clearly explained by its strategic and economical benefits, considering increasing ship traffic and global trade, and the limitations of ground base alternatives. Thus, spacecraft carrying AIS receivers are expected to be continuously launched, even though it may not be as their primary payload.

Conversely, ocean imagers and other oceanographic remote sensing instruments have been scarcely implemented in micro and nano satellites. In fact, most remote sensing spacecraft for ocean research are among the heaviest and most complex ones ever launched (*e.g.* **EnviSat**, **TOPEX/Poseidon**, and **Aqua**). However, substantial interest for newer, cheaper, and more accessible instruments, with low operational costs, is constantly being demonstrated by the oceanographic community. Small satellites can prove to be the answer to many problems, as long as they are not used to replace conventional spacecraft.

Although there is still some uncertainty about when and which remote sensing instruments could be adapted to fit micro and nano satellites, three applications were shown to have a good potential. Firstly, ocean colour instruments are the ones that clearly can be easily adapted for small satellites, because of its size, mass and power consumption. Moreover, as these spacecraft tend to be at lower altitudes, better resolutions can be obtained. In terms of applications, imagers are important sensors for coastal region studies, for instance, with both scientific and economic ramifications, since they can be used for detecting concentrations of phytoplankton blooms or plumes.

Another application that can be very straightforwardly applied to small satellites, and with much potential, is GNSS reflectometry. By simply using two GNSS receivers, and some computational treatment, ocean altimetry and wind speed and direction can be obtained. This is not without limitations, but might give a larger number of measurements with a temporal coverage not achievable with conventional spacecraft.

Finally, one of the instruments that would potentially bring more scientific, economic and security benefits is the radar-based one, and especially SAR with its observation capabilities despite a cloudy coverage. A wide range of applications could be devised, including traffic monitor, ocean dynamics and bathymetry (to name a few), if a SAR would be adapted to a micro satellite. However, it might be one of the most difficult instruments to adapt to these platforms, since there are significant technical challenges to overcome, from the sheer size to power requirements. Nevertheless, much research in this field is being performed, financed by countries with large territorial waters, which could represent a breakthrough in the next five to ten years.

Although not directly performing ocean observation, small satellites with communication and data relay capabilities can be very useful in aiding an oceanborne constellation network in the open ocean, to send its data to land based facilities, or be commanded by them. This is also especially relevant for countries with an extensive continental shelf, like Portugal, that might need to mobilise vast sea and airborne resources for effective monitoring and surveillance.

Nowadays, vehicle networks, like the one from LSTS, which have been deployed all around the world and that have many hours of accumulated operations, depend on having a vessel close by, with a large overhead cost, and sometimes with satellite communication. Even though there are several conventional satellite communication systems, these solutions have a wide range of prices for both the provider (with constellations costing more than $2\,\text{billion dollars}$) and the user (with values from $0.21\,€/\text{kbyte}$ to about $3\,€/\text{kbyte}$, for data, or up to $\$1.50\,/\text{minute}$ for voice communication). Examples of these systems include the real time large bandwidth and power consumption system INMARSAT, the Argos with its limited bandwidth and communication gaps but less power consumption, or the in-between system which offers both options, the Iridium system. Therefore, these ocean networks of autonomous vehicles would benefit from a dedicated and especially designed small satellite communication system, like the HumSat system from UVigo. This one, although recent, has proven its use with two launches and several ground terminals deployed around the world (from Antarctica, to South and North America, and also Europe).

To test the benefits of this system of systems (*i.e.* an ocean network with a small satellite constellation) and the communication issues that might arise from this combination, a HumSat SDR system was integrated on a small low cost UAV. As discussed in Chapter 4, despite the current HumSat limitations, as is for example the amount of data that can be transmitted, the software written for the LSTS toolchain, and the data parsing, allowed for making the SDR a viable communication channel. With several test runs, and a few more happening soon, important conclusions have been drawn, which will influence the next version of the HumSat system, and the SDR prototype.

6.3 Thermal design and its effects

The thermal subsystem was shown in Chapter 5 to be very important when designing any type of spacecraft, from CubeSats to large conventional satellites. In fact, the practical case of Section 5.5 revealed an electrical component with temperatures higher than the survival one, which would go undetected, if thermal analysis were not conducted, until it was too late. Thus, a spacecraft should always go through a proper thermal analysis, or otherwise some components might not function as desired, or even have shorter life spans than expected.

With temperatures estimated by hand calculations, combined with requirements gathered from other subsystems, preliminary analyses and designs for the thermal subsystem may be easily obtained. However, whenever more detailed analyses are required, calculations become harder to perform. In particular, there are several unknown parameters that need to be obtained, *e.g.* optical surface properties and how they degrade over time, besides view factors between surfaces. Contact conductance is another parameter difficult to obtain as all models are based on empirical data for very particular cases. Apart from these unknown parameters, there are also uncertainties associated, for instance with the spacecraft thermal environment characterisation. A simple example is the attitude of the spacecraft, which determines the albedo and Earth view factors and the faces that see the Sun.

All of these unknowns and uncertainties might have an important impact on the final thermal result, and while it might be enough to increase safety margins for preliminary phases, they have to be thoroughly studied for more detailed phases. Furthermore, the spacecraft models created for this analysis phase can be computational heavy, adding to the previous difficulties.

When thermal problems are encountered there are several technologies and methods that can be applied to solve them, or at least minimise them. These solutions can be either passive or active ones, most of which with extensive flight heritage. Although with active solutions there is a higher control of the temperatures, these come at a cost, namely on the mass and on the power consumption. That is why passive options tend to be preferred as much as possible, especially in small satellites where an increase in mass or power has an impact on the payloads it can carry. For the CubeSat preliminary design example discussed, passive control technologies have proven to be fundamental to deal with the overheating discovered on some electronic components (with temperature differences reaching $27\,^{\circ}\mathrm{C}$).

Even with proper thermal analysis, and including thermal control technology whenever needed, only with tests of both single components and the full system can a spacecraft be certified to have a correct operation. Therefore, prior to launch, all spacecraft should go through thermal vacuum tests, where the maximum incident fluxes are simulated, as well as their time variability. Moreover, both the Earth's and the launcher's thermal environments should be accounted for, as there may be moments during these phases where survival thermal limits are not respected.

Also within Chapter 5, the effects of the spacecraft thermal environment, in particular the emitted thermal radiation, on the accelerations suffered by the spacecraft were also studied. This was

based on an already developed method for the Pioneer and Cassini spacecraft, which combined a pointlike source method with the Phong shading model. One of the biggest advantages of this method was its flexibility and how it could be used to quickly get an estimation of the thermal accelerations.

This method was applied this time to the New Horizons spacecraft, given its similarities with the previous ones, namely its trajectory taking it to the outer solar system, using a spin stabilised approach most of that time, and the use of a RTG as power source. Within the carried out computations, it was determined that a thermal induced acceleration exists and is of the order of $(11.5 \pm 0.3) \times 10^{-10}$ m/s^2 (with a 2σ confidence level), when New Horizons encountered Pluto. Since the spacecraft always has the main antenna pointing to Earth during spin stabilised operations (to have a constant link with the spacecraft), this acceleration is in that direction. Due to the spacecraft's geometrical configuration, more precisely the X-Y plane symmetry, the thermal acceleration is null in the perpendicular axis. Any other component of the acceleration that might exist is cancelled out by the spacecraft spin.

The method used for acceleration calculations was expanded here to determine resultant moments, which could cause attitude oscillations. Although small, these attitude effects have been determined and could possibly be detected during communication with the spacecraft (in the transmitted signal gain variation). Even in three-axis mode operations there is a cumulative attitude effect, however a dedicated experiment would have to be developed to detect these (like the one Cassini did).

An advantage of using a Monte Carlo approach, together with a statistical distribution of the parameters, to determine these results is that, even if the effects that influence the outcome could be refined, *e.g.* with more information on the material's optical properties, this would just reduce the confidence regions, and would not produce completely different results.

This method could be applied to other spacecraft with similar characteristics to determine thermal accelerations of future missions. With that, new and improved trajectories taking advantage of those accelerations could be potentially calculated and used for interplanetary travels. Conversely, the thermal acceleration values should also be used when doing fuel expenditure calculations, to maximise their utilisation.

6.4 Future Work

6.4.1 Communication integrated network

There are some hardware and software modifications to the current HumSat solution that could largely improve the system. The first, and which is already being implemented, is a centralised full-duplex communication capability. This would increase the communication network robustness, and allow for both data transmission and command reception by any asset in the network, without having to use two SDRs.

The second most relevant shortcoming is the data length capabilities of the current solution. With just 32 bytes of data, simple variables like the vehicle's estimated state have to be decomposed in several small messages, which all have to be sent to the satellite to be able to reconstruct the data on the ground. To solve this issue, two approaches can be followed. One of the solutions, on the IMC communication side, is a minimalistic version of the protocol for this particular communication channel, so not to have the usual long headers. This would also benefit underwater communication, which suffers from the same problem. Another option is on the HumSat protocol side, with an increase of data capabilities. In fact, with the most recent advances, messages with up to 100 bytes of data can possibly be achieved. If this proves successful, less messages would be transmitted for a single variable, which would definitely improve the success rate of data reconstruction on the Neptus Workstation (*i.e.* the oceanborne network ground station).

All of these new capabilities and approaches must be tested in the field as soon as possible. Even if a full small satellite constellation is not available, it can be replaced by multiple UAVs acting as relay nodes for testing purposes. This way, scalability issues and synergies of the SDR satellite technology with other network communication links can be inferred. An added gain of this solution is the minimisation of logistical costs, associated with spacecraft launches, before solutions can be fully implemented and validated.

Still, a full small satellite communication service will require a considerable initial investment. Both the design and development costs of all the spacecraft required for the constellation, and the costs of launching them to the correct final positions (to have a reasonable coverage), have to be accounted for. Nonetheless, this substantial investment would be, in principle, smaller than the conventional options, considering the reduced cost of small satellites, when compared with conventional commercial ones.

6.4.2 Thermal analysis

Despite the different solutions tested for the CubeSat case, the temperature of its amplifier is still above the recommended operational limits, for long periods of operation. Some solutions have already been proposed in Chapter 5, in particular to extend the thermal strap that is already there, or to add a new one connected to another heat sink. Nevertheless, the analyses carried out were only preliminary in nature, to give figures of merit for the temperatures achieved.

If the CubeSat moves to a detailed design phase, it is necessary to build new analyses. These should have more information about the spacecraft's internal components distribution, power consumptions and materials used. The spacecraft orbit and attitude would also have to be better defined, apart from the rest of the thermal environment the spacecraft is subject to.

It is also recommended to perform laboratory tests to validate the assumptions made, together with these new simulations. One of the tests, and which should have the highest priority, is the conduction behaviour between a stack of PCBs and the supporting rods.

In what concerns the thermal accelerations of the New Horizons, it would be interesting to actually measure them, and thus to validate the used method for the Pioneer and Cassini spacecraft, boosting the confidence for future analyses. To accomplish this, NASA and the Johns Hopkins University Applied Physics Laboratory would have to look for accelerations in the Doppler shifts on the tracking algorithms used, for different and larger periods.

Conversely, for the attitude wobbling, the intensity variations during transmissions could be enough to validate the results. Nevertheless, a dedicated experiment could be devised and later included in the mission extension of the New Horizons. These intensity variations, or the results of the dedicated experiment, would validate this new model feature.

References

[1] C. L. Sabine, The Oceanic Sink for Anthropogenic CO2, Science 305 (5682) (2004) 367–371. doi:10.1126/science.1097403.

[2] J. C. J. H. Aerts, W. J. W. Botzen, K. Emanuel, N. Lin, H. de Moel, E. O. Michel-Kerjan, Evaluating Flood Resilience Strategies for Coastal Megacities, Science 344 (6183) (2014) 473–475. doi:10.1126/science.1248222.

[3] I. S. Robinson, Discovering the Ocean from Space, Springer Berlin Heidelberg, Berlin, Heidelberg, 2010. doi:10.1007/978-3-540-68322-3.

[4] R. K. Pachauri, M. R. Allen, V. R. Barros, J. Broome, W. Cramer, R. Christ, J. A. Church, L. Clarke, Q. Dahe, P. Dasgupta, N. K. Dubash, O. Edenhofer, I. Elgizouli, C. B. Field, P. Forster, P. Friedlingstein, J. Fuglestvedt, L. Gomez-Echeverri, S. Hallegatte, G. Hegerl, M. Howden, K. Jiang, B. J. Cisneroz, V. Kattsov, H. Lee, K. J. Mach, J. Marotzke, M. D. Mastrandrea, L. Meyer, J. Minx, Y. Mulugetta, K. O'Brien, M. Oppenheimer, J. J. Pereira, R. Pichs-Madruga, G.-K. Plattner, H.-O. Pörtner, S. B. Power, B. Preston, N. H. Ravindranath, A. Reisinger, K. Riahi, M. Rusticucci, R. Scholes, K. Seyboth, Y. Sokona, R. Stavins, T. F. Stocker, P. Tschakert, D. van Vuuren, J.-P. van Ypserle, Climate Change 2014: Synthesis Report. Contribution of Working Groups I, II and III to the Fifth Assessment Report of the Intergovernmental Panel on Climate Change, Tech. rep., IPCC, Geneva, Switzerland, hdl:10013/epic.45156 (2014).

[5] Y. Ma, H. Wu, L. Wang, B. Huang, R. Ranjan, A. Zomaya, W. Jie, Remote sensing big data computing: Challenges and opportunities, Future Generation Computer Systems 51 (2015) 47–60. doi:10.1016/j.future.2014.10.029.

[6] SpaceWorks Enterprises Inc, Nano/Microsatellite Market Forecast, 8th Edition, Tech. rep., retrieved February 03, 2018 (2018).
URL http://spaceworksforecast.com/

[7] Y. Sharay, N. U, TecSAR Satellite –- Novel Approach in Space SAR Design, in: Proceedings of IRSI (International Radar Symposium India), 2005.

[8] G. Zhou, S. Reichle, UAV-based multi-sensor data fusion processing, International Journal of Image and Data Fusion 1 (3) (2010) 283–291. doi:10.1080/19479832.2010.497343.

[9] E. Bitton, K. Goldberg, Hydra: A framework and algorithms for mixed-initiative UAV-assisted search and rescue, in: 2008 IEEE International Conference on Automation Science and Engineering, IEEE, 2008, pp. 61–66. doi:10.1109/COASE.2008.4626527.

[10] P. McGuillivary, J. B. Sousa, R. Martins, Connecting the dots. networking maritime fleets of autonomous systems for science and surveillance, Marine Technology Reporter (2012) 32–38.

[11] J. Fortuna, F. Ferreira, R. Gomes, A. S. Ferreira, J. B. Sousa, Using low cost open source UAVs for marine wild life monitoring - Field Report*, IFAC Proceedings Volumes 46 (30) (2013) 291–295. doi:10.3182/20131120-3-FR-4045.00055.

[12] J. Eckert, D. Eckhoft, R. German, Flying Ad-Hoc Network communication for detecting thermals: Feasibility and insights, in: Third International Conference on Innovative Computing Technology (INTECH 2013), IEEE, 2013, pp. 333–338. doi:10.1109/INTECH.2013.6653654.

[13] J. P. Ryan, S. B. Johnson, A. Sherman, K. Rajan, F. Py, H. Thomas, J. B. J. Harvey, L. Bird, J. D. Paduan, R. C. Vrijenhoek, Mobile autonomous process sampling within coastal ocean observing systems, Limnology and Oceanography: Methods 8 (8) (2010) 394–402. doi:10.4319/lom.2010.8.394.

[14] J. Ryan, M. McManus, R. Kudela, M. Lara Artigas, J. Bellingham, F. Chavez, G. Doucette, D. Foley, M. Godin, J. Harvey, R. Marin, M. Messié, C. Mikulski, T. Pennington, F. Py, K. Rajan, I. Shulman, Z. Wang, Y. Zhang, Boundary influences on HAB phytoplankton ecology in a stratification-enhanced upwelling shadow, Deep Sea Research Part II: Topical Studies in Oceanography 101 (0) (2014) 63–79. doi:10.1016/j.dsr2.2013.01.017.

[15] J. Pinto, M. Faria, J. Fortuna, R. Martins, J. Sousa, N. Queiroz, F. Py, K. Rajan, Chasing fish: Tracking and control in a autonomous multi-vehicle real-world experiment, in: 2013 OCEANS - San Diego, San Diego, California, 2013, pp. 1–6. doi:10.23919/OCEANS.2013.6741228.

[16] M. Faria, J. Pinto, F. Py, J. Fortuna, H. Dias, R. Martins, F. Leira, T. A. Johansen, J. Sousa, K. Rajan, Coordinating UAVs and AUVs for oceanographic field experiments: Challenges and lessons learned, in: 2014 IEEE International Conference on Robotics and Automation (ICRA), IEEE, Hong Kong, 2014, pp. 6606–6611. doi:10.1109/ICRA.2014.6907834.

[17] J. Das, F. Py, J. B. Harvey, J. P. Ryan, A. Gellene, R. Graham, D. A. Caron, K. Rajan, G. S. Sukhatme, Data-driven robotic sampling for marine ecosystem monitoring, The International Journal of Robotics Research 34 (12) (2015) 1435–1452. doi:10.1177/0278364915587723.

[18] Council of the European Union, European Union Maritime Security Strategy, 11205/14 (2014).

[19] Directorate-General for Maritime Affairs and Fisheries, Blue Growth Opportunities for marine and maritime sustainable growth, Tech. rep., European Commission, Luxembourg (2012). doi:10.2771/43949.

[20] B. Narheim, O. Olsen, O. Helleren, R. Olsen, A. Beattie, R. Zee, A Norwegian Satellite for Space-based Observations of AIS in the High North, in: 22nd Annual AIAA/USU Conference on Small Satellites, Logan, Utah, 2008, sSC08-III-3.

[21] N. G. Orr, J. Cain, L. Stras, R. E. Zee, Space Based Ais Detection With the Maritime Monitoring and Messaging, in: 64th International Astronautical Congress, 2013, pp. 1–9.

[22] G. Mantzouris, P. Papadopoulos, N. Nikitakos, M. Manso, G. Markarian, Experiments on Pico-Satellites for Maritime Security Applications, Tech. rep., paper ID: 067.

[23] T. Eriksen, A. N. Skauen, B. Narheim, O. Helleren, O. Olsen, R. B. Olsen, Tracking ship traffic with Space-Based AIS: Experience gained in first months of operations, in: 2010 International WaterSide Security Conference, Vol. 1, IEEE, 2010, pp. 1–8. doi:10.1109/WSSC.2010.5730241.

[24] Y. Nakamura, K. Nishijo, N. Murakami, K. Kawashima, Y. Horikawa, K. Yamamoto, T. Ohtani, Y. Takhashi, K. Inoue, Small Demonstration Satellite-4 (SDS-4): Development, Flight Results, and Lessons Learned in JAXA's Microsatellite Project, in: 27th Annual AIAA/USU Conference on Small Satellites, Logan, Utah, 2013.

[25] S. Hardhienata, R. H. Triharjanto, M. Mukhayadi, LAPAN-A2: Indonesian Near-Equatorial Surveilance Satellite, in: 18th Asia-Pacific Regional Space Agency Forum, Singapore, 2011.

[26] G. Haller, Lagrangian Coherent Structures, Annual Review of Fluid Mechanics 47 (1) (2015) 137–162. doi:10.1146/annurev-fluid-010313-141322.

[27] B. Bagdatli, K. Griendling, D. Kalpakchian, E. Jones, S. Ussery, J. Ball, J. Kallman, D. Mavris, A method for examining the impact of interoperability on mission performance in a system-of-systems, in: 2010 IEEE Aerospace Conference, IEEE, 2010, pp. 1–15. doi:10.1109/AERO.2010.5446884.

[28] C. Fuchs, A. S. Ferreira, J. B. Sousa, G. Gonçalves, Adaptive Consoles for Supervisory Control of Multiple Unmanned Aerial Vehicles, in: M. Kurosu (Ed.), Human-Computer Interaction. Interaction Modalities and Techniques, Springer Berlin Heidelberg, 2013, pp. 678–687. doi:10.1007/978-3-642-39330-3_73.

[29] A. S. Ferreira, J. Pinto, P. S. Dias, J. B. Sousa, The LSTS software toolchain for persistent maritime operations applied through vehicular ad-hoc networks, in: 2017 International Conference on Unmanned Aircraft Systems (ICUAS), IEEE, 2017, pp. 609–616. doi:10.1109/ICUAS.2017.7991471.

[30] A. Castro, R. Walker, F. Emma, F. Aguado Agelet, R. Tubio, W. Balogh, The HumSAT system and the ESA GEOID Initiative, European Space Agency Bulletin 149 (2012) 45–50.

[31] Estrutura de Missão para a Extensão da Plataforma Continental, A EMEPC, visited May 25, 2015. Personal communication. (2015).
URL https://www.emepc.pt/

[32] O. Bertolami, F. Francisco, P. J. S. Gil, J. Páramos, Thermal analysis of the Pioneer anomaly: A method to estimate radiative momentum transfer, Physical Review D 78 (10) (2008) 103001. doi:10.1103/PhysRevD.78.103001.

[33] O. Bertolami, F. Francisco, P. J. S. Gil, J. Páramos, Estimating Radiative Momentum Transfer Through a Thermal Analysis of the Pioneer Anomaly, Space Science Reviews 151 (1-3) (2010) 75–91. doi:10.1007/s11214-009-9589-3.

[34] F. Francisco, O. Bertolami, P. J. S. Gil, J. Páramos, Modelling the reflective thermal contribution to the acceleration of the Pioneer spacecraft, Physics Letters B 711 (5) (2012) 337–346. doi:10.1016/j.physletb.2012.04.034.

[35] B. Rievers, C. Lämmerzahl, High precision thermal modeling of complex systems with application to the flyby and Pioneer anomaly, Annalen der Physik 523 (6) (2011) 439–449. doi:10.1002/andp.201100081.

[36] S. G. Turyshev, V. T. Toth, G. Kinsella, S.-C. Lee, S. M. Lok, J. Ellis, Support for the Thermal Origin of the Pioneer Anomaly, Physical Review Letters 108 (24) (2012) 241101. doi:10.1103/PhysRevLett.108.241101.

[37] J. D. Anderson, P. A. Laing, E. L. Lau, A. S. Liu, M. M. Nieto, S. G. Turyshev, Indication, from Pioneer 10/11, Galileo, and Ulysses Data, of an Apparent Anomalous, Weak, Long-Range Acceleration, Physical Review Letters 81 (14) (1998) 2858–2861. doi:10.1103/PhysRevLett.81.2858.

[38] J. D. Anderson, P. A. Laing, E. L. Lau, A. S. Liu, M. M. Nieto, S. G. Turyshev, Study of the anomalous acceleration of Pioneer 10 and 11, Physical Review D 65 (8) (2002) 082004. arXiv:0104064, doi:10.1103/PhysRevD.65.082004.

[39] B. Bertotti, L. Iess, P. Tortora, A test of general relativity using radio links with the Cassini spacecraft, Nature 425 (6956) (2003) 374–376. doi:10.1038/nature01997.

[40] O. Bertolami, F. Francisco, P. J. S. Gil, J. Páramos, Modeling the nongravitational acceleration during Cassini's gravitation experiments, Physical Review D 90 (4) (2014) 042004. doi:10.1103/PhysRevD.90.042004.

[41] G. H. Fountain, D. Y. Kusnierkiewicz, C. B. Hersman, T. S. Herder, T. B. Coughlin, W. C. Gibson, D. A. Clancy, C. C. DeBoy, T. A. Hill, J. D. Kinnison, D. S. Mehoke, G. K. Ottman, G. D. Rogers, S. A. Stern, J. M. Stratton, S. R. Vernon, S. P. Williams, The New Horizons Spacecraft, Space Science Reviews 140 (1-4) (2008) 23–47. doi:10.1007/s11214-008-9374-8.

[42] G. D. Rogers, S. H. Flanigan, D. Stanbridge, Effects of Radioisotope Thermoelectric Generator on Dynamics if the New Horizons Spacecraft, Advances in the Astronautical Sciences 151 (AAS 14-122) (2014) 801–812.

[43] A. G. C. Guerra, F. Francisco, J. Villate, F. Aguado Agelet, O. Bertolami, K. Rajan, On small satellites for oceanography: A survey, Acta Astronautica 127 (2016) 404–423. doi:10.1016/j.actaastro.2016.06.007.

[44] A. G. Guerra, A. S. Ferreira, M. Costa, D. Nodar-López, F. A. Agelet, Integrating small satellite communication in an autonomous vehicle network: A case for oceanography, Acta Astronauticadoi:10.1016/j.actaastro.2018.01.022.

[45] A. G. C. Guerra, D. Nodar-López, R. Tubó-Pardavila, Thermal analysis of the electronics of a CubeSat missionSubmitted to Applied Thermal Engineering. arXiv:1803.10468.

[46] A. G. C. Guerra, F. Francisco, P. J. S. Gil, O. Bertolami, Estimating the thermally induced acceleration of the New Horizons spacecraft, Physical Review D 95 (12) (2017) 124027. doi:10.1103/PhysRevD.95.124027.

[47] National Research Council (U.S.) - Committee on Scientific Accomplishments of Earth Observations from Space, Earth Observations from Space: The First 50 Years of Scientific Achievements, Vol. 244, National Academies Press, Washington, D.C, 2008.

[48] V. Kuznetsov, V. Sinelnikov, S. Alpert, Yakov Alpert: Sputnik-1 and the first satellite ionospheric experiment, Advances in Space Research 55 (12) (2015) 2833–2839. doi:10.1016/j.asr.2015.02.033.

[49] C. Lafleur, The Spacecrafts Encyclopedia, visited November 10, 2015 (2014).
URL http://claudelafleur.qc.ca/Spacecrafts-index.html

[50] R. Sandau, Status and trends of small satellite missions for Earth observation, Acta Astronautica 66 (1-2) (2010) 1–12. doi:10.1016/j.actaastro.2009.06.008.

[51] R. Sandau, International study on cost-effective earth observation missions outcomes and visions, Revue Française de Photogrammétrie et de Télédetection (185) (2007) 5–10.

[52] P. Fortescue, J. Stark, G. Swinerd, Spacecraft Systems Engineering, 4th Edition, Wiley, Hoboken, N.J, 2011.

[53] K. Briess, F. Baumann, S. Trowitzsch, Present and Future Picosatellite Missions at TU Berlin, in: 8th IAA Symposium on Small Satellites for Earth Observation, Berlin, 2011, pp. 49–52.

[54] W. J. Larson, J. R. Wertz, Space Mission Analysis and Design, 3rd Edition, Microcosm Press, Kluwer Academic Publishers, Boston, 1999.

[55] M. Swartwout, The First One Hundred CubeSats: A Statistical Look, Journal of Small Satellites 2 (2) (2013) 213–233.

[56] The CubeSat Program, CubeSat Design Specification, retrieved November 11, 2017 (2015).
URL http://www.cubesat.org/

[57] ESA-ESTEC Requirements & Standards Division, ECSS-E-ST-10C Rev.1 – System engineering general requirements, Tech. rep., European Space Agency, Noordwijk, the Netherlands (2017).
URL http://ecss.nl/standard/ecss-e-st-10c-rev-1-system-engineering-general-requirements-15-february-2017/

[58] European Space Agency, Concurrent Design Facility – Space Engineering & Technology, visited January 18, 2018 (2017).
URL http://www.esa.int/Our{_}Activities/Space{_}Engineering{_}Technology/CDF

[59] M. Bandecchi, B. Melton, B. Gardini, F. Ongaro, The ESA/ESTEC concurrent design facility, in: EuSEC 2000, Munich, 2000.

[60] ESA-ESTEC Requirements & Standards Division, ECSS-E-TM-10-25A – Engineering design model data exchange (CDF), Tech. rep., European Space Agency, Noordwijk, the Netherlands (2010).
URL http://ecss.nl/hbstms/ecss-e-tm-10-25a-engineering-design-model-data-exchange-cdf-20-october-2010/

[61] ESA Space Debris Mitigation Working Group, ESA Space Debris Mitigation Compliance Verification Guidelines, Tech. rep., European Space Agency, eSSB-HB-U-002 (2015).

[62] European Space Agency, ESA Academy / Education / ESA, visited November 12, 2017 (2017).
URL http://www.esa.int/Education/ESA{_}Academy

[63] D. Selva, D. Krejci, A survey and assessment of the capabilities of Cubesats for Earth observation, Acta Astronautica 74 (2012) 50–68. doi:10.1016/j.actaastro.2011.12.014.

[64] C. H. Verlag, Handbook of Space Technology, John Wiley & Sons, Ltd, Chichester, UK, 2009. doi:10.1002/9780470742433.

[65] M. Macdonald, V. Badescu, The International Handbook of Space Technology, Springer Berlin Heidelberg, Berlin, Heidelberg, 2014. doi:10.1007/978-3-642-41101-4.

[66] Innovative Solutions In Space, ISIS-Innovative Solutions In Space | The nanosatellite specialist, visited November 30, 2017 (2017).
URL https://www.isispace.nl/

[67] D. Schmuland, R. Masse, C. Sota, Hydrazine Propulsion Module for CubeSats, in: 25th Annual AIAA/USU Conference on Small Satellites, Logan, Utah, 2011, sSC11-X-4.

[68] L. NanoAvionika, Reaction Wheels System "SatBus 4RW0", visited November 30, 2017 (2017).

URL https://n-avionics.com/cubesat-components/attitude-control-systems/cubesat-reaction-wheels-control-system-satbus-4rw/

[69] GomSpace, GOMspace | Nanosatellites, visited November 30, 2017 (2017).
URL https://gomspace.com

[70] International Telecommunication Union, Prague Declaration on Small Satellite Regulation and Communication Systems, retrieved October 11, 2015 (2015).
URL http://www.itu.int/en/ITU-R/space/workshops/2015-prague-small-sat

[71] United Nations Office for Outer Space Affairs, Convention on International Liability for Damage Caused by Space Objects, adopted by the General Assembly in its resolution 2777 (XXVI), opened for signature on 29 March 1972, entered into force on 1 September 1972. Retrieved October 11, 2015 (1971).
URL http://www.unoosa.org/oosa/en/ourwork/spacelaw/treaties/liability-convention.html

[72] W. J. Ubbels, M. Buscher, Status of ITU-R studies related to small satellites, iTU Symposium and Workshop on small satellite regulation and communication systems (2015).

[73] United Nations Office for Outer Space Affairs, International Telecommunication Union, Guidance on Space Object Registration and Frequency Management for Small and Very Small Satellites, Tech. Rep. April, retrieved October 11, 2015 (2015).
URL http://www.unoosa.org/oosa/en/spaceobjectregister/resources/index.html

[74] International Telecommunication Union, Studies to accommodate requirements in the space operation service for non-geostationary satellites with short duration missions, Tech. Rep. November, world Radiocommunication Conference 2015 - Provisional Final Acts (2015).

[75] W. Shiroma, L. Martin, J. Akagi, J. Akagi, B. Wolfe, B. Fewell, A. Ohta, CubeSats: A bright future for nanosatellites, Open Engineering 1 (1) (2011) 9–15. doi:10.2478/s13531-011-0007-8.

[76] M. Swartwout, Secondary spacecraft in 2015: Analyzing success and failure, in: 2015 IEEE Aerospace Conference, IEEE, 2015, pp. 1–12. doi:10.1109/AERO.2015.7119175.

[77] T. O. Fossum, Intelligent Autonomous Underwater Vehicles, Tech. rep., Norwegian University of Science and Technology (2016).

[78] A. Thompson, Y. Chao, S. Chien, J. Kinsey, M. M. Flexas, Z. Erickson, J. Farrara, D. Fratantoni, A. Branch, S. Chu, M. Troesch, B. Claus, J. Kepper, Satellites to Seafloor: Toward Fully Autonomous Ocean Sampling, Oceanography 30 (2) (2017) 160–168. doi:10.5670/oceanog.2017.238.

[79] C. Garcia-Soto, J. Vazquez-Cuervo, P. Clemente-Colón, F. Hernandez, Satellite oceanography and climate change, Deep Sea Research Part II: Topical Studies in Oceanography 77-80 (2012) 1–9. doi:10.1016/j.dsr2.2012.07.004.

[80] H. J. Kramer (Ed.), Observation of the Earth and Its Environment: Survey of Missions and Sensors, 3rd Edition, Springer Berlin Heidelberg, Berlin, Heidelberg, 1996. doi:10.1007/978-3-642-97678-0.

[81] Planet Labs Inc., planet - Approach, visited January 13, 2018 (2017).
URL https://www.planet.com/company/approach/

[82] T. Kuwahara, K. Yoshida, Y. Sakamoto, Y. Tomioka, K. Fukuda, M. Fukuyama, International Scientific Micro-satellite RISESAT based on Space Plug and Play Avionics, in: 26th Annual AIAA/USU Conference on Small Satellites, Logan, Utah, 2012.

[83] European Space Agency, RISESat, visited September 30, 2015 (2015).
URL https://directory.eoportal.org/web/eoportal/satellite-missions/r/risesat

[84] H. Klinkrad, P. Beltrami, S. Hauptmann, C. Martin, H. Sdunnus, H. Stokes, R. Walker, J. Wilkinson, The ESA Space Debris Mitigation Handbook 2002, Advances in Space Research 34 (5) (2004) 1251–1259. doi:10.1016/j.asr.2003.01.018.

[85] E. A. Taylor, J. R. Davey, Implementation of debris mitigation using International Organization for Standardization (ISO) standards, Proceedings of the Institution of Mechanical Engineers, Part G: Journal of Aerospace Engineering 221 (6) (2007) 987–996. doi:10.1243/09544100JAERO233.

[86] European Space Agency, QSat-EOS, visited October 1, 2015 (2015).
URL https://directory.eoportal.org/web/eoportal/satellite-missions/q/qsat

[87] B. S. Aso, T. Yasaka, Y. Tani, T. Hanada, M. Murozono, M. Omura, Y. Tsuruda, S. Onishi, K. Arai, M. Cho, M. Nishio, QSAT-EOS: 50kg-class Small Satellite for Earth Observation System Demonstration, in: 28th International Symposium on Space Technology and Science, Okinawa, 2011.

[88] R. B. Wallace, H. Baumann, J. S. Grear, R. C. Aller, C. J. Gobler, Coastal ocean acidification: The other eutrophication problem, Estuarine, Coastal and Shelf Science 148 (2014) 1–13. doi:10.1016/j.ecss.2014.05.027.

[89] S. Massey, COPPER: IR Imaging and Radiation Studies Overview Payloads Spacecraft Bus Conclusion, retrieved October 1, 2015 (2012).
URL http://mstl.atl.calpoly.edu/{~}bklofas/Presentations/SummerWorkshop2011/Massey{_}COPPER.pdf

[90] European Space Agency, COPPER, visited September 7, 2015 (2015).
URL https://directory.eoportal.org/web/eoportal/satellite-missions/c-missions/copper

[91] AXELSPACE Cooperation, Micro-Satellite for Monitoring Polar Ice WNISAT-1, visited September 7, 2015 (2013).
URL http://en.axelspace.com/solution/wnisat1/

[92] S. Kim, T. Eishima, N. Miyashita, Y. Nojiri, Y. Nakamura, WNISAT - Nanosatellite for North Arctic Routes and Atmosphere Monitoring, in: 24th Annual AIAA/USU Conference on Small Satellites, Logan, Utah, 2010.

[93] European Space Agency, ParkinsonSat, visited September 29, 2015 (2015).
URL https://directory.eoportal.org/web/eoportal/satellite-missions/p/parkinsonsat

[94] European Space Agency, TUBSAT, visited September 29, 2015 (2015).
URL https://directory.eoportal.org/web/eoportal/satellite-missions/t/tubsat

[95] V. Carrara, H. K. Kuga, P. M. Bringhenti, M. J. de Carvalho, M. J. M. de Carvalho, Attitude Determination, Control and Operating Modes for CONASAT Cubesats, in: 24th International Symposium on Space Flight Dynamics (ISSFD), Laurel, Maryland, 2014.

[96] European Space Agency, Fedsat, visited September 29, 2015 (2015).
URL https://directory.eoportal.org/web/eoportal/satellite-missions/f/fedsat

[97] T. Hayashi, Y. Okamoto, K. Yokoyama, S. Hosokawa, T. Takahashi, K. Nakazawa, T. Takashima, S. Watanabe, T. Hashimoto, M. Nomachi, Y. Masumoto, Data Collection by Means of Formation Flight of Small Satellites with Gravity Gradient Attitude Stabilization, in: 55th International Astronautical Congress of the International Astronautical Federation, the International Academy of Astronautics, and the International Institute of Space Law, American Institute of Aeronautics and Astronautics, Reston, Virigina, 2004. doi:10.2514/6.IAC-04-IAA.4.11.4.04.

[98] F. M. Pranajaya, R. E. Zee, J. Cain, R. Kolacz, Nanosatellite Tracking Ships: Cost-Effective Responsive Space, in: The 4S Symposium - Small Satellites Systems and Services, Funchal, 2010.

[99] D. Bedard, A. Spaans, Responsive Space for the Canadian Forces, in: 5th Responsive Space Conference, Los Angeles, 2007.

[100] M. Takai, T. Ohtani, Y. Nakamura, Y. Takahashi, K. Inoue, JAXA's technology demonstration mission SDS-4, in: 2013 IEEE International Geoscience and Remote Sensing Symposium - IGARSS, IEEE, 2013, pp. 839–842. doi:10.1109/IGARSS.2013.6721289.

[101] Gunter Dirk Krebs, Triton 1, 2, visited September 29, 2015 (2015).
URL http://space.skyrocket.de/doc{_}sdat/triton-1.htm

[102] Gunter Dirk Krebs, TT 1, visited September 29, 2015 (2015).
URL http://space.skyrocket.de/doc{_}sdat/tt-1.htm

[103] Gunter Dirk Krebs, Perseus-M 1, 2, visited September 21, 2015 (2015).
URL http://space.skyrocket.de/doc{_}sdat/perseus-m.htm

[104] Wikipedia, Perseus-M, visited September 21, 2015 (2015).
URL https://en.wikipedia.org/wiki/Perseus-M

[105] Gunter Dirk Krebs, DX 1, visited September 23, 2015 (2015).
URL http://space.skyrocket.de/doc{_}sdat/dx-1.htm

[106] D. D. Villiers, R. V. Zyl, ZACube-2: The successor to Africa's first nanosatellite, in: Southern African Amateur Radio Satellite Association Space Symposium, Pretoria, 2015.

[107] European Space Agency, LambdaSat, visited September 29, 2015 (2015).
URL https://directory.eoportal.org/web/eoportal/satellite-missions/l/lambdasat

[108] European Space Agency, LAPAN-A2, visited October 1, 2015 (2015).
URL https://directory.eoportal.org/web/eoportal/satellite-missions/l/lapan-a2

[109] J. Block, A. Bäger, J. Behrens, T. Delovski, L.-C. Hauer, M. Schütze, R. Schütze, T. Spröwitz, A self-deploying and self-stabilizing helical antenna for small satellites, Acta Astronautica 86 (2013) 88–94. doi:10.1016/j.actaastro.2011.10.012.
URL http://linkinghub.elsevier.com/retrieve/pii/S0094576511003146

[110] M. R. Aherne, J. T. Barrett, L. Hoag, E. Teegarden, R. Ramadas, Aeneas – Colony I Meets Three-Axis Pointing, in: 25th Annual AIAA/USU Conference on Small Satellites, Logan, Utah, 2011.
URL http://digitalcommons.usu.edu/smallsat/2011/all2011/85/

[111] Union of Concerned Scientists, UCS Satellite Database, retrieved September 9, 2015 (2015).
URL https://www.ucsusa.org/nuclear-weapons/space-weapons/satellite-database#.WjJw7VVl-Uk

[112] Gunter Dirk Krebs, Rubin 9, visited September 23, 2015 (2015).
URL http://space.skyrocket.de/doc{%}7B{_}{%}7Dsdat/rubin-9-ais.htm

[113] European Space Agency, VesselSat, visited September 23, 2015 (2015).
URL https://directory.eoportal.org/web/eoportal/satellite-missions/v-w-x-y-z/vesselsat

[114] European Space Agency, SDS-4, visited September 24, 2015 (2015).
URL https://directory.eoportal.org/web/eoportal/satellite-missions/s/sds-4

[115] Gunter Dirk Krebs, SeaHawk 1, 2, visited September 29, 2015 (2015).
URL http://space.skyrocket.de/doc{_}sdat/seahawk.htm

[116] European Space Agency, CYGNSS, visited September 29, 2015 (2015).
URL https://directory.eoportal.org/web/eoportal/satellite-missions/c-missions/cygnss

[117] R. Rose, S. Gleason, C. Ruf, The NASA CYGNSS mission: a pathfinder for GNSS scatterometry remote sensing applications, in: C. R. Bostater, S. P. Mertikas, X. Neyt (Eds.), SPIE 9240, Remote Sensing of the Ocean, Sea Ice, Coastal Waters, and Large Water Regions, 2014, p. 924005. doi:10.1117/12.2068378.

[118] exactEarth Ltd., The exactView™ Constellation - Product Information, retrieved September 15, 2015 (2015).
URL https://www.exactearth.com/technology/exactview-constellation

[119] Gunter Dirk Krebs, LatinSat A, B, C, D / AprizeSat 1, ..., 10 / exactView 3, 4, 5, 5R, 6, 11, 12, 13, retrieved September 23, 2015 (2015).
URL http://space.skyrocket.de/doc{_}sdat/aprizesat-1{_}latinsat-1.htm

[120] European Space Agency, OrbView-2, visited November 18, 2015 (2015).
URL https://directory.eoportal.org/web/eoportal/satellite-missions/o/orbview-2

[121] European Space Agency, TerraSAR-X, visited November 18, 2015 (2015).
URL https://directory.eoportal.org/web/eoportal/satellite-missions/t/terrasar-x

[122] I. S. Robinson, Measuring the Oceans from Space: The principles and methods of satellite oceanography, 1st Edition, Springer-Verlag Berlin Heidelberg, New York, 2004.

[123] A. F. Shchepetkin, J. C. McWilliams, The regional oceanic modeling system (ROMS): a split-explicit, free-surface, topography-following-coordinate oceanic model, Ocean Modelling 9 (4) (2005) 347–404. doi:10.1016/j.ocemod.2004.08.002.

[124] J. Das, K. Rajany, S. Frolovy, F. Pyy, J. Ryany, D. A. Caron, G. S. Sukhatme, Towards marine bloom trajectory prediction for AUV mission planning, in: 2010 IEEE International Conference on Robotics and Automation, IEEE, Anchorage, Alaska, 2010, pp. 4784–4790. doi:10.1109/ROBOT.2010.5509930.

[125] M. Bernstein, R. Graham, D. Cline, J. M. Dolan, K. Rajan, Learning-based event response for marine robotics, in: 2013 IEEE/RSJ International Conference on Intelligent Robots and Systems, IEEE, 2013, pp. 3362–3367. doi:10.1109/IROS.2013.6696835.

[126] Committee on Earth Observation Satellites, The CEOS Database: Missions, Instruments and Measurements, visited October 12, 2015 (2014).
URL http://database.eohandbook.com/

[127] European Space Agency, Satellite Missions Directory - Earth Observation Missions - eoPortal, visited June 20, 2017 (2017).
URL https://directory.eoportal.org/web/eoportal/satellite-missionshttps://directory.eoportal.org

[128] D. B. Chelton, J. C. Ries, B. J. Haines, L.-L. Fu, P. S. Callahan, Satellite Altimetry, in: L.-L. Fu, A. Cazenave (Eds.), Satellite Altimetry and Earth Sciences - A Handbook of Techniques and Applications, 1st Edition, Vol. 69 of International Geophysics, Elsevier, 2001, Ch. 1, pp. 1–131. doi:10.1016/S0074-6142(01)80146-7.

[129] S. Martin, An Introduction to Ocean Remote Sensing, 2nd Edition, Cambridge University Press, New York, 2014.

[130] M. Burford, A. Revill, J. Smith, L. Clementson, Effect of sewage nutrients on algal production, biomass and pigments in tropical tidal creeks, Marine Pollution Bulletin 64 (12) (2012) 2671–2680. doi:10.1016/j.marpolbul.2012.10.008.

[131] A. E. Parker, R. C. Dugdale, F. P. Wilkerson, Elevated ammonium concentrations from wastewater discharge depress primary productivity in the Sacramento River and the Northern San Francisco Estuary, Marine Pollution Bulletin 64 (3) (2012) 574–586. doi:10.1016/j.marpolbul.2011.12.016.

[132] National Aeronautics and Space Administration, NASA Pace, visited November 18, 2015 (2015).
URL https://pace.oceansciences.org/

[133] International Ocean-Colour Corrdinating Group, International Ocean Colour Coordinating Group, visited November 18, 2015 (2015).
URL http://www.ioccg.org/

[134] European Space Agency, OceanSat-2, visited October 12, 2015 (2015).
URL https://directory.eoportal.org/web/eoportal/satellite-missions/o/oceansat-2

[135] European Space Agency, HY-1B, visited November 18, 2015 (2015).
URL https://directory.eoportal.org/web/eoportal/satellite-missions/h/hy-1b

[136] Cloudland Instruments, Seahawk Cubesat Project, visited October 13, 2015 (2015).
URL http://cloudlandinstruments.com/?page{_}id=7

[137] European Space Agency, GRACE, visited October 14, 2015 (2015).
URL https://directory.eoportal.org/web/eoportal/satellite-missions/g/grace

[138] H. M. Dierssen, A. E. Theberge, Bathymetry: Assessment, in: Encyclopedia of Natural Resources: Water, CRC Press, 2016, pp. 629–636. doi:10.1081/E-ENRW-120048588.

[139] S. Vignudelli, H. M. Snaith, F. Lyard, P. Cipollini, F. Venuti, F. Birol, J. Bouffard, L. Roblou, Satellite radar altimetry from open ocean to coasts: challenges and perspectives, in: R. J. Frouin, V. K. Agarwal, H. Kawamura, S. Nayak, D. Pan (Eds.), SPIE 6406, Remote Sensing of the Marine Environment, 2006, p. 64060L. doi:10.1117/12.694024.

[140] European Space Agency, Jason-1, visited October 14, 2015 (2015).
URL https://directory.eoportal.org/web/eoportal/satellite-missions/j/jason-1

[141] European Space Agency, EnviSat, visited November 4, 2015 (2015).
URL https://directory.eoportal.org/web/eoportal/satellite-missions/e/envisat

[142] European Space Agency, Jason-2, visited October 14, 2015 (2015).
URL https://directory.eoportal.org/web/eoportal/satellite-missions/j/jason-2

[143] European Space Agency, CryoSat-2, visited October 14, 2015 (2015).
URL https://directory.eoportal.org/web/eoportal/satellite-missions/c-missions/cryosat-2

[144] European Space Agency, SARAL, visited October 14, 2015 (2015).
URL https://directory.eoportal.org/web/eoportal/satellite-missions/s/saral

[145] J. Richard, V. Enjolras, L. Rys, J. Vallon, I. Nann, P. Escudier, Space Altimetry from Nano-Satellites: Payload Feasibility, Missions and System Performances, in: IGARSS 2008 - 2008 IEEE International Geoscience and Remote Sensing Symposium, Vol. 3, IEEE, 2008, pp. III – 71–III – 74. doi:10.1109/IGARSS.2008.4779285.

[146] Y. Zheng, The GANDER Microsatellite Radar Altimeter Constellation for Global Sea State Monitoring, in: 13th Annual AIAA/USU Conference on Small Satellites, Logan, Utah, 1999.

[147] R. da Silva Curiel, G. Jolly, Y. Zheng, The GANDER constellation for maritime dissaster mitigation, Acta Astronautica 44 (7-12) (1999) 685–692. doi:10.1016/S0094-5765(99)00064-8.

[148] N. Stacy, 6U Radar Altimeter Concept, in: 6U Cubesat Low Cost Space Missions Workshop, Canberra, 2012.

[149] A. Mroczek, G. Jacobs, Nanosats for Radar Altimetry, in: 29th Annual AIAA/USU Conference on Small Satellites, Logan, Utah, 2015, sSC15-XII-7.

[150] J. Zec, W. Jones, R. Alsabah, A. Al-Sabbagh, RapidScat Cross-Calibration Using the Double Difference Technique, Remote Sensing 9 (11) (2017) 1160. doi:10.3390/rs9111160.

[151] European Space Agency, QuikSCAT, visited October 15, 2015 (2015).
URL https://directory.eoportal.org/web/eoportal/satellite-missions/q/quikscat

[152] European Space Agency, DMSP, visited October 15, 2015 (2015).
URL https://directory.eoportal.org/web/eoportal/satellite-missions/d/dmsp-block-5d

[153] European Space Agency, Coriolis, visited October 15, 2015 (2015).
URL https://directory.eoportal.org/web/eoportal/satellite-missions/c-missions/coriolis

[154] European Space Agency, SMOS, visited October 16, 2015 (2015).
URL https://directory.eoportal.org/web/eoportal/satellite-missions/s/smos

[155] European Space Agency, Meteosat - First Generation, visited October 19, 2015 (2015).
URL https://directory.eoportal.org/web/eoportal/satellite-missions/m/meteosat-first-generation

[156] European Space Agency, EO-1, visited October 19, 2015 (2015).
URL https://directory.eoportal.org/web/eoportal/satellite-missions/e/eo-1

[157] European Space Agency, EnviSat AATSR Radiometer – Principles of Measurement, visited October 19, 2015 (2014).
URL http://envisat.esa.int/handbooks/aatsr/CNTR1-1-3.html

[158] A. Schmittner, J. C. Chiang, S. R. Hemming, Introduction: The ocean's meridional overturning circulation, in: Ocean Circulation: Mechanisms and Impacts - Past and Future Changes of Meridional Overturning, 2007, pp. 1–4. doi:10.1029/173GM02.

[159] National Aeronautics and Space Administration, Aquarius – Sampling Seas No 'Grain of Salt' Task, visited November 18, 2015 (2011).
URL https://www.nasa.gov/mission{_}pages/aquarius/news/aquarius20110525.html

[160] R. Rose, C. S. Ruf, H. Seki, Ocean altimetry and wind applications of a GNSS nanosatellite constellation, in: H. Shimoda, X. Xiong, C. Cao, X. Gu, C. Kim, A. S. Kiran Kumar (Eds.), SPIE 8528, Earth Observing Missions and Sensors: Development, Implementation, and Characterization II, 2012, p. 85280G. doi:10.1117/12.977595.

[161] M. Meerman, M. Unwin, S. Gleason, S. Jason, M. Sweeting, A Nanosatellite to Demonstrate GPS Oceanography Reflectometry, in: 16th Annual AIAA/USU Conference on Small Satellites, AIAA, Logan, Utah, 2002.

[162] G. Foti, C. Gommenginger, P. Jales, M. Unwin, A. Shaw, C. Robertson, J. Roselló, Spaceborne GNSS reflectometry for ocean winds: First results from the UK TechDemoSat-1 mission, Geophysical Research Letters 42 (13) (2015) 5435–5441. doi:10.1002/2015GL064204.

[163] A. Camps, N. Rodriguez-Alvarez, X. Bosch-Lluis, J. Marchan, I. Ramos-Perez, M. Segarra, L. Sagues, D. Tarrago, O. Cunado, R. Vilaseca, A. Tomas, J. Mas, J. Guillamon, PAU in SeoSAT: A proposed hybrid L-band microwave radiometer/GPS reflectometer to improve Sea Surface Salinity estimates from space, in: 2008 Microwave Radiometry and Remote Sensing of the Environment, IEEE, 2008, pp. 1–4. doi:10.1109/MICRAD.2008.4579467.

[164] L. d'électronique et traitement de signal, Advanced Algorithmic and Architecture Designs for Future Satellite Navigtion Receivers and GNSS-Reflectometry Applications, visited October 14, 2015 (2015).
URL http://esplab.epfl.ch/page-115178-fr.html

[165] European Space Agency, TechDemoSat-1, visited October 14, 2015 (2015).
URL https://directory.eoportal.org/web/eoportal/satellite-missions/t/techdemosat-1

[166] H. Carreno-Luengo, A. Camps, I. Perez-Ramos, G. Forte, R. Onrubia, R. Diez, 3Cat-2: A P(Y) and C/A GNSS-R experimental nano-satellite mission, in: 2013 IEEE International Geoscience and Remote Sensing Symposium - IGARSS, IEEE, 2013, pp. 843–846. doi:10.1109/IGARSS.2013.6721290.

[167] J. Pineda, V. Starczak, J. C. B. da Silva, K. Helfrich, M. Thompson, D. Wiley, Whales and waves: Humpback whale foraging response and the shoaling of internal waves at Stellwagen Bank, Journal of Geophysical Research: Oceans 120 (4) (2015) 2555–2570. doi:10.1002/2014JC010564.

[168] J. da Silva, M. Buijsman, J. Magalhaes, Internal waves on the upstream side of a large sill of the Mascarene Ridge: a comprehensive view of their generation mechanisms and evolution, Deep Sea Research Part I: Oceanographic Research Papers 99 (2015) 87–104. doi:10.1016/j.dsr.2015.01.002.

[169] M. K. Mishra, D. Ganguly, P. Chauhan, Ajai, Estimation of Coastal Bathymetry Using RISAT-1 C-Band Microwave SAR Data, IEEE Geoscience and Remote Sensing Letters 11 (3) (2014) 671–675. doi:10.1109/LGRS.2013.2274475.

[170] W. Pitz, D. Miller, The TerraSAR-X Satellite, IEEE Transactions on Geoscience and Remote Sensing 48 (2) (2010) 615–622. doi:10.1109/TGRS.2009.2037432.

[171] Earth Snapshot, ASAR Image Orthorectification, visited October 15, 2015 (2015).
URL http://www.eosnap.com/earth-observation/asar-image-orthorectification/

[172] S. W. McCandless Jr., C. R. Jackson, Chapter 1: Principles of Synthetic Aperture Radar, in: SAR Marine User's Manual, U. S. Department of Commerce, Washington, DC, 2004, pp. 1−24, retrieved October 14, 2015.
URL http://sarusersmanual.com/

[173] G. C. Staples, J. Hornsby, Turning the Scientifically Possible into the Operationally Practical: RADARSAT-2 Polarimetry Applications, in: Proceedings of IGARS −- IEEE International Geoscience and Remote Sensing Symposium, 2002. doi:10.1109/IGARSS.2002.1026153.

[174] U. Steinbrecher, T. Kraus, G. Castellanos Alfonzo, C. Grigorov, D. Schulze, B. Bräutigam, B. Braeutigam, TerraSAR-X: Design of the new operational WideScanSAR mode, in: Proceedings of the 10th European Conference on Synthetic Aperture Radar (EUSAR 2014), VDE, Berlin, 2014, pp. 189−192.

[175] M. Di Lazzaro, G. Angino, M. Piemontese, A. Capuzi, R. Leonardi, COSMO-SkyMed: The Dual-Use Component of a Geospatial System for Environment and Security, in: Proceedings of the 2008 IEEE Aerospace Conference, 2008.

[176] S.-R. Lee, Overview of KOMPSAT-5 Program, Mission, and System, in: Proceedings of IGARS −- IEEE International Geoscience and Remote Sensing Symposium, 2010.

[177] P. Snoeij, E. Attema, B. Duesmann, M. Davidson, N. Floury, B. Rosich Betlem amd Rommen, G. Levrini, GMES Sentinel-1 Mission, System and Products, in: Proceedings of 4th International POLinSAR 2009 Workshop, 2009.

[178] Government of Canada, Canada's Oceans Action Plan − For Present and Future Generations, Tech. rep., Communications Branch Fisheries and Oceans Canada, Ottawa, Ontario (2005).

[179] O. Bertolami, A. G. C. Guerra, F. Francisco, J. Villate, Pequenos satélites em Portugal, contribution to Portugal Space 2030, Fundação para a Ciência e a Tecnologia (2017).

[180] J. B. Sousa, J. Pereira, J. Pinto, P. C. Lourenfo, J. M. Galocha, J. Fontes, M. Silva, K. Rajan, T. A. Johansson, J. Alves, A. Munafò, K. Pelekanakis, R. Petroccia, M. Carreiro Silva, M. Incze, Rapid Environmental Picture Atlantic exercise 2015: A field report, in: OCEANS 2016 MTS/IEEE Monterey, IEEE, 2016, pp. 1−6. doi:10.1109/OCEANS.2016.7761496.

[181] J. Pinto, P. S. Dias, R. Martins, J. Fortuna, E. Marques, J. B. Sousa, The LSTS toolchain for networked vehicle systems, in: OCEANS 2013 MTS/IEEE Bergen: The Challenges of the Northern Dimension, IEEE, 2013, pp. 1−9. doi:10.1109/OCEANS-Bergen.2013.6608148.

[182] D. Merani, A. Berni, J. Potter, R. Martins, An Underwater Convergence Layer for Disruption Tolerant Networking, in: 2011 Baltic Congress on Future Internet and Communications, IEEE, 2011, pp. 103–108. doi:10.1109/BCFIC-RIGA.2011.5733227.

[183] B. G. Evans (Ed.), Satellite Communication Systems, IET, The Institution of Engineering and Technology, Michael Faraday House, Six Hills Way, Stevenage SG1 2AY, UK, 1999. doi:10.1049/PBTE038E.

[184] H. H. M. Sondaal, The current situation in the field of maritime communication satellites: INMARSAT, J. Space L. 8 (1980) 9.

[185] V. Spiridonov, Inmarsat systems and services, in: Proceedings of International Conference on Satellite Communications. ICSC'94, Vol. 1, Int. Centre for Sci. & Tech. Inf, 1994, pp. 45–52. doi:10.1109/ICSC.1994.523087.

[186] I. plc., inmarsat, visited June 15, 2017 (2013).
URL www.inmarsat.com

[187] P. Chini, G. Giambene, S. Kota, A survey on mobile satellite systems, International Journal of Satellite Communications and Networkingdoi:10.1002/sat.941.

[188] I. plc., Fleet One - INMARSAT terminal specification, retrieved June 15, 2017 (2014).

[189] Orbcomm, ORBCOMM, visited June 17, 2017 (2017).
URL www.orbcomm.com

[190] R. Hobby, An introduction to the Iridium, in: IEE Colloquium on Communication Opportunities Offered by Advanced Satellite Systems - Day 1, Vol. 1998, IEE, London, UK, 1998, pp. 1–1. doi:10.1049/ic:19980875.

[191] C. Fossa, R. Raines, G. Gunsch, M. Temple, An overview of the IRIDIUM (R) low Earth orbit (LEO) satellite system, in: Proceedings of the IEEE 1998 National Aerospace and Electronics Conference. NAECON 1998., IEEE, Dayton, OH, USA„ 1998, pp. 152–159, celebrating 50 Years (Cat. No.98CH36185). doi:10.1109/NAECON.1998.710110.

[192] I. Poole, Iridium satellite technology, theory and frequency bands, visited June 20, 2017 (2017).
URL http://www.radio-electronics.com/info/satellite/communications-systems/iridium-theory-history-technology-frequency.php

[193] Orbital ATK, Iridium NEXT - Fact Sheet, retrieved June 20, 2017 (2015).
URL https://www.orbitalatk.com/space-systems/commercial-satellites/communications-satellites/docs/FS002{_}11{_}OA{_}3862IridiumNEXT.pdf

[194] CLS America, Iridium Services & Hardware - 2016 Catalog, retrieved June 20, 2017 (2016).

[195] Rock Seven Mobile Services Ltd, RockBLOCK v2 - Developer Guide, retrieved June 20, 2017 (2016).
URL http://www.rock7mobile.com/downloads/RockBLOCK-Developer-Guide-Mk2.pdf

[196] Rock Seven Mobile Services Ltd, Rock Seven, visited June 22, 2017 (2014).
URL www.rock7mobile.com

[197] B. Yann, CLS America, Personal communication (2017).

[198] CLS America, Argos – Worldwide tracking and environmental monitoring by satellite, visited June 20, 2017 (2017).
URL http://www.argos-system.org/

[199] CLS America, Argos-3 – The New Generation, Tech. rep., retrieved June 22, 2017 (2011).
URL http://www.argos-system.org/argos-3/

[200] Elta, Terminals and Beacons – PMT Argos 3, retrieved June 21, 2017 (2017).
URL http://www.elta.fr/uploads/files/bb278d5679fa8671bbb3b2391d97c244f85ddfac.pdf

[201] CLS America, Argos-3 PMT-K – Platform messaging transceiver, retrieved June 22, 2017 (2009).

[202] F. Aguado Agelet, D. Nodar-López, A. G. Muiño, Satellite Communication Systems based on Small Satellite Platforms, in: 3rd IAA Conference On University Satellite Missions And Cubesat Workshop, International Academy of Astronautics, Rome, 2015, iAA-CU-15-0S-0P.

[203] European Space Agency, HumSat / GEOID / GENSO, visited June 7, 2015 (2017).
URL https://directory.eoportal.org/web/eoportal/satellite-missions/content/-/article/humsat

[204] A. G. C. Guerra, M. Costa, SatComms Task Software Files, found in *LSTS/dune* GitHub repository, within *feature/humsat* branch and on *dune/src/Transports/* folder (2017).
URL https://github.com/LSTS/

[205] FPVMODEL.COM, HAWKEYE UHF Dipole 433MHZ Antenna, visited April 12, 2017 (2015).
URL https://www.fpvmodel.com/hawkeye-uhf-dipole-433mhz-antenna{_}g847.html

[206] Universidade de Vigo, Universidade do Porto, Laboratoire d'Analyse et d'Architecture des Systèmes, Fire-RS - Wildfire Picosatellite Constellation & UAVs Remote Sensing: Active fire mapping and management (2016).

[207] J. R. Wertz, D. F. Everett, J. J. Puschell (Eds.), Space mission engineering: The new SMAD, Microcosm Press, Hawthorne, CA, 2011.

[208] D. G. Gilmore (Ed.), Spacecraft Thermal Control Handbook – Volume I: Fundamental Technologies, 2nd Edition, Aerospace Press, 2003.

[209] J. Meseguer, I. Pérez-Grande, A. Sanz-Andrés, Spacecraft Thermal Control, Woodhead Pub, Oxford, Philadelphia, 2012.

[210] ESA-ESTEC Requirements & Standards Division, ECSS-E-ST-31C – Thermal control, Tech. rep., European Space Agency, Noordwijk, the Netherlands (2008).
URL http://ecss.nl/standard/ecss-e-st-31c-thermal-control/

[211] ESA-ESTEC Requirements & Standards Division, ECSS-E-ST-10-04C – Space environment, Tech. rep., European Space Agency, Noordwijk, the Netherlands (2008).
URL http://ecss.nl/standard/ecss-e-st-10-04c-space-environment/

[212] T. C. Bannister, Radiation Geometry Factor between the Earth and a Satellite, Tech. Rep. July, National Aeronautics and Space Administration, Washington, D.C, nASA TN D-2750 (1965).

[213] L. Jacques, Thermal Design of the Oufti-1 nanosatellite, Ph.D. thesis, University of Liège (2009).

[214] T. L. Bergman, A. S. Lavine, F. P. Incropera, D. P. Dewitt, Fundamentals of Heat and Mass Transfer, 7th Edition, Wiley, Hoboken, NJ, 2011.

[215] ESA-ESTEC Requirements & Standards Division, ECSS-E-HB-31-01 Part 3A – Thermal design handbook – Part 3: Spacecraft Surface Temperature, Tech. rep., European Space Agency, Noordwijk, the Netherlands (2011).
URL http://ecss.nl/active-handbook/ecss-e-hb-31-01-part-3a-thermal-design-handbook-part-3-spacecraft-surface-temperature-5-december-2011/

[216] I. Savija, J. R. Culham, M. M. Yovanovich, E. E. Marotta, Review of Thermal Conductance Models for Joints Incorporating Enhancement Materials, Journal of Thermophysics and Heat Transfer 17 (1) (2003) 43–52. doi:10.2514/2.6732.

[217] M. Yovanovich, Four decades of research on thermal contact, gap, and joint resistance in microelectronics, IEEE Transactions on Components and Packaging Technologies 28 (2) (2005) 182–206. doi:10.1109/TCAPT.2005.848483.

[218] M. A. Lambert, L. S. Fletcher, Review of Models for Thermal Contact Conductance of Metals, Journal of Thermophysics and Heat Transfer 11 (2) (1997) 129–140. doi:10.2514/2.6221.

[219] M. Yovanovich, J. Culham, P. Teertstra, Calculating interface resistance, Electronics Cooling 3 (2) (1997) 24–29.

[220] A. Hasselström, U. Nilsson, Thermal Contact Conductance in Bolted Joints, Ph.D. thesis, Chalmers University of Technology, Sweden, diploma work no 85/2012 (2012).

[221] M. Cooper, B. Mikic, M. Yovanovich, Thermal contact conductance, International Journal of Heat and Mass Transfer 12 (3) (1969) 279–300. doi:10.1016/0017-9310(69)90011-8.

[222] European Space Agency, Threaded fasteners handbook, Tech. Rep. April, eCSS-E-HB-32-23A (2010).

[223] S. Z. Cao, X. K. Chen, G. Wu, J. P. Yang, R. Wang, Micro Louvers for Micro and Nano-Satellites Thermal Control, Advanced Materials Research 317-319 (2011) 1658–1661. doi:10.4028/www.scientific.net/AMR.317-319.1658.

[224] ANSYS, Icepak (2016).

[225] Xilinx Inc., Zynq-7000 - Package Thermal Models, retrieved March 21, 2017 (2017).
URL https://www.xilinx.com/support/download/index.html/content/xilinx/en/downloadNav/device-models/package-thermal-models/zynq-7000-ap-socs.html

[226] Micron Technology Inc., MT41K256M16TW-107 - Data Sheet, retrieved March 23, 2017 (2017).
URL https://www.micron.com/parts/dram/ddr3-sdram/mt41k256m16tw-107

[227] Analog Devices Inc., AD9364 - Data Sheet (Rev. C), retrieved April 11, 2017 (2017).
URL http://www.analog.com/en/products/rf-microwave/integrated-transceivers-transmitters-receivers/wideband-transceivers-ic/ad9364.html{#}product-overview

[228] Qorvo Inc., RF5110G - Data Sheet, retrieved April 11, 2017 (2017).
URL http://www.qorvo.com/products/p/RF5110G

[229] Panasonic Corporation of North America, Pyrolytic Graphite Sheet (PGS) Brochure, retrieved May 25, 2017 (2017).
URL https://na.industrial.panasonic.com/download/pyrolytic-graphite-sheet-pgs-brochure

[230] B. T. Phong, Illumination for computer generated pictures, Communications of the ACM 18 (6) (1975) 311–317. doi:10.1145/360825.360839.

[231] NASA, Johns Hopkins University Applied Physics Laboratory, Southwest Research Institute, PEPSSI Instrument Tastes Pluto's Atmosphere, visited March 9, 2017 (2015).
URL http://pluto.jhuapl.edu/News-Center/News-Article.php?page=20150701-2

[232] Johns Hopkins University Applied Physics Laboratory, New Horizons - Design and Build, retrieved April 1, 2017 (2016).
URL http://pluto.jhuapl.edu/Participate/museums/Design-and-Build.php

[233] Y. Guo, R. W. Farquhar, New Horizons Mission Design, Space Science Reviews 140 (1-4) (2008) 49–74. doi:10.1007/s11214-007-9242-y.

[234] G. Ottman, C. Hersman, The Pluto-New Horizons RTG and Power System Early Mission Performance, in: 4th International Energy Conversion Engineering Conference and Exhibit (IECEC), American Institute of Aeronautics and Astronautics, Reston, Virigina, 2006. doi:10.2514/6.2006-4029.

[235] I. Martínez, THERMO-OPTICAL PROPERTIES, visited December 10, 2016 (2016).
URL http://webserver.dmt.upm.es/{~}isidoro/dat1/Thermooptical.pdf

[236] G. H. Fountain, Personal communication (2017).

[237] G. Maral, M. Bousquet, Satellite Communications Systems: Systems, Techniques and Technology, 5th Edition, John Wiley & Sons, Ltd, Chichester, West Sussex, U.K., 2009.

[238] C. DeBoy, C. Haskins, T. Brown, R. Schulze, M. Bernacik, J. Jensen, W. Millard, D. Duven, S. Hill, The RF telecommunications system for the New Horizons mission to Pluto, in: 2004 IEEE Aerospace Conference Proceedings (IEEE Cat. No.04TH8720), IEEE, 2004, pp. 1463–1478. doi:10.1109/AERO.2004.1367922.

[239] I. G. Cumming, F. H. Wong, Digital processing of synthetic aperture radar data: algorithms and implementation, Artech House, Inc., Nortwood, MA, USA, 2005.

[240] H. Zebker, Lecture notes for Radar Remote Sensing: Fundamentals and Geophysical Application of Imaging Radar Systems, retrieved September 9, 2015 (2015).
URL http://web.stanford.edu/class/ee355/syllabus.htm

[241] M. Mohan, Synthetic Aperture Radar, Vol. 2, Artech House, Dedham, MA, 2013.

[242] W. E. Wiesel, Spaceflight Dynamics, 2nd Edition, McGraw-Hill, New York, 1997.

APPENDIX A

SAR Principles

Most radars mounted aboard spacecraft usually have their antenna at an incident angle, θ, with the vertical, or nadir (which represents the line between the spacecraft and the centre of the Earth). The notorious exception to a $\theta > 0$ is the altimeter, whose antenna points straight down to nadir, making the beam very localised. When the antenna incident angle is increased, so is the illuminated area by the radar beam, called the swath width, S (as is depicted in Figure A.1). Moreover, the illuminated region tends to be wider in the range direction (*i.e.* perpendicular to the projection of the orbit on the ground), and narrower in the azimuth one (*i.e.* parallel to the orbit projection). This is because the angle of the beam is inversely proportional to the length of the antenna. For side looking radars, as represented in Figure A.1, the length of the antenna in the motion direction, D, is commonly bigger than the perpendicular length, d.

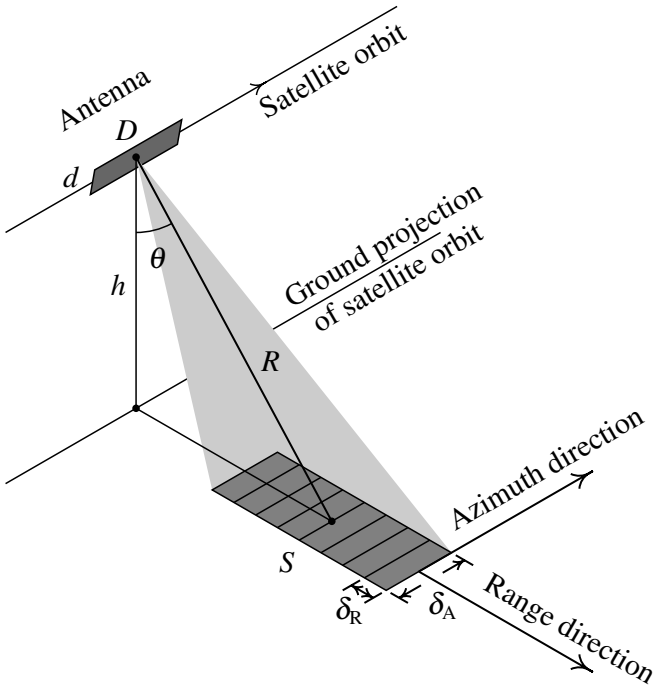


Figure A.1 – *Schematic of a side looking imaging radar system aboard a spacecraft, with the most relevant parameters.*

When a signal is sent from the radar to the ground, there would be a delay in the backscattered signal returning to the antenna from different points within the illuminated area. This occurs since

the distance from those points to the radar differs between them. Considering the range to a particular point in the ground is given by R_i (whereas R is the distance to the centre of the swath area), the time a signal takes to travel that distance, hit the ground, and return to the antenna is $2\,R_i/c$ (where c is the speed of light). Thus, the radar will only be able to distinguish apart two points in the ground, if the difference between their time delays is larger than the time each radar pulse lasts, τ. This is called the resolution distance, δ_{R}, of a radar in the range direction, and is given by

$$\delta_{\mathrm{R}} \approx \frac{c\tau}{2}. \tag{A.1}$$

With the equation above, in theory, by making the pulse shorter, better resolutions can be obtained. For example, for a spacecraft orbit altitude, h, of a few hundred kilometres, the radar needs to work with very short pulses, a few nanoseconds, to obtain a resolution of only tens of meters. However, to reduce the emitted pulse length it is necessary to increase its peak intensity, so that the reflected pulse has a minimum amount of energy for the antenna to distinguish it from the background noise. This peak energy can become so high that it would literally burn the antenna.

Consequently, to solve the problem a frequency-modulated (chirped) pulse, *i.e.* whose frequency decreases with time, can be sent instead. When it returns to the antenna the higher frequencies can then be delayed. This makes the time span, τ, equal to the inverse of the emitted pulse bandwidth, B (*i.e.* the difference between higher and lower frequencies), and in turn the resolution in the range direction equals to

$$\delta_{\mathrm{R}} \approx \frac{c}{2B}. \tag{A.2}$$

The range resolution value for a common radar, *e.g.* a bandwidth of $15\,\mathrm{MHz}$, is about $10\,\mathrm{m}$, using a tens of micro seconds emitted pulse. This cannot be much better, without either increasing the bandwidth (which has its own technical difficulties), or leaving the frequency ranges allowed for microwave radars, and into some which interfere with other telecommunication devices [122].

Conversely, the azimuth resolution, δ_{A}, depends on the range to the centre of the illuminated area, the length of the antenna, and the wavelength of the signal, λ. It represents the capability to distinguish, without interference, two independent pulses in the azimuth direction,

$$\delta_{\mathrm{A}} \approx \frac{\lambda R}{D}. \tag{A.3}$$

This means, for example, that for a wide $10\,\mathrm{m}$ antenna, the azimuth resolution is only tens of meters. In fact, for a reasonable image resolution, and a radar using microwaves, a several kilometre antenna would have to be used.

Another relevant parameter for radar systems is the Signal-to-Noise Ratio (SNR), whose expression is sometimes called the radar equation. Although there are various expressions, for different types of imaging radars [239, 240], a general one is

$$SNR = \frac{P_t\, G_t\, G_r\, \lambda^2\, A\, \sigma_0}{(4\pi)^3 R^4\, k\, T\, B\, F_n\, L_s}. \tag{A.4}$$

The numerator parameters include the average transmitted power, P_t, the transmitter and receiver antennae gains, G_t and G_r respectively, the target area, A, and the normalised cross section, σ_0 (*i.e.* the radiation power actually returned by the target, in the direction of the receiver), apart from the radar pulse wavelength. The denominator, aside from the range and the pulse bandwidth, is given by Boltzmann's constant, k, the radar absolute temperature, T, the value for the receiver noise, F_n, and a system loss parameter, L_s . When a single antenna is used, for both transmitter and receiver, G_t and G_r are equal.

The difference between SAR and most radars, and where it excels, is that SAR takes advantage of the fact the platform is moving with a certain speed with respect to the target. This means that since the moment a target is in view of the radar to when it finally leaves (the illumination time) the radar emits several pulses, which are all backscattered by the target. These are then synthesised electronically to form a coherent image. With this displacement and by synthesising, the radar would have a hypothetical antenna length equal to the distance that the satellite has moved while illuminating the target. Therefore, a much larger azimuth resolution is obtained, because the effective length of a SAR antenna, D_{SAR}, is of the order of the size of the illuminated region. However, the Doppler shift of the pulses received has to be recorded, so the system can distinguish pulses from different targets, along the azimuth direction [241].

Applying this SAR concept to the SNR equation, and considering the SAR minimum antenna area equal to $A_{min} = \delta_{\mathrm{R}}\delta_{\mathrm{A}}/\sin\theta$, the result is

$$SNR = \frac{P_t\, G_t\, G_r\, \lambda^3\, \sigma_0\, c}{128\, \pi^3\, R^3\, k\, T\, B\, F_n\, L_s\, v\, \sin\theta}, \tag{A.5}$$

where v represents a "velocity" and is given by $v = D/\tau$. Here the distinct $1/R^3$ SAR factor is evident. The equation also shows that either the signal is increased, by giving more power, gain, and using larger wavelengths, or the noise and losses are decreased, for instance having a greater "velocity" v (which requires shorter pulses and an upgraded discrimination of the incoming signal), or both, to improve SAR performance.

APPENDIX B

Modelling the Thermal Effects on the Attitude of the Spacecraft

B.1 Thermal moment relative to the centre of mass

The nominal axis of rotation of the New Horizons spacecraft, the $+Y$ axis along the direction of the antenna in Figure 5.26, is also its principal moment of inertia [41]. In Section 5.6.2 it is also clearly seen that the spacecraft is reasonably symmetric about the $X-Y$ plane. Therefore, the body reference frame of Figure 5.26 can be assumed as the principal reference frame, with origin at the centre of mass, and with moments of inertia A, B, and C.

If the sum of each individual thermal radiation force vector, $\mathbf{F}_i$, is given by $\mathbf{F}$, and its position relative to the centre of mass is $\mathbf{r}$, the yielding moment of force is

$$\mathbf{M} = \mathbf{r} \times \mathbf{F}_{\text{rad}} = \sum_i \mathbf{r}_i \times \mathbf{F}_{\text{rad}_i}. \tag{B.1}$$

Considering the spacecraft symmetry, and that the force is mainly in the $X-Y$ plane, the moment can by simplified to

$$\mathbf{M} = M\mathbf{e}_Z. \tag{B.2}$$

B.2 Rotation dynamics induced by thermal effects

Different dynamic conditions have to be considered depending on the mode of operations, since the attitude control system would have different behaviours. For example, in active spin mode the ADCS would be constantly controlling the spacecraft's attitude and thus no thermal effect would be identifiable. These effects would only be seen on the three-axis mode and spin stabilised cases, analysed bellow.

B.2.1 Three-axis mode case

For the three-axis mode, if there is no thrust firing, the rotation effect is a small one around the Z axis, given by

$$\delta\dot{\omega}_Z = M/C. \tag{B.3}$$

Moreover, this holds because the thermal moment has the direction of a principal axis.

B.2.2 Spin stabilised case

When the spacecraft is in a passive spin mode the ADCS gives it a nominal spin value, ω_0, around the principal Y axis. On this mode the rotational state evolution is characterised by the Euler equations [242], which in the the body reference frame are given by

$$M_X = A\dot{\omega}_X + (C - B)\omega_Y\omega_Z, \tag{B.4a}$$
$$M_Y = B\dot{\omega}_Y + (A - C)\omega_X\omega_Z, \tag{B.4b}$$
$$M_Z = C\dot{\omega}_Z + (B - A)\omega_X\omega_Y, \tag{B.4c}$$

When fixing the initial direction of the Y axis in space, the angular velocity at the beginning is $\boldsymbol{\omega} = \omega_0\mathbf{e}_Y$. This will be perturbed, by the applied moment, yielding

$$\boldsymbol{\omega} = \delta\omega_X\mathbf{e}_X + (\omega_0 + \delta\omega_Y)\mathbf{e}_Y + \delta\omega_Z\mathbf{e}_Z \tag{B.5}$$

Since the time components, $\delta\omega_i$ for $i = X,\ Y,\ Z$, are zero at the start, and remain very close to zero all the time, higher order terms can be neglected.

Combining Equation (B.1) with Equation (B.4), and considering that New Horizons has an almost flat body, with respect to the Y rotation axis (*i.e.* $B > A,\ C$), the perturbed components of the angular velocity are given by

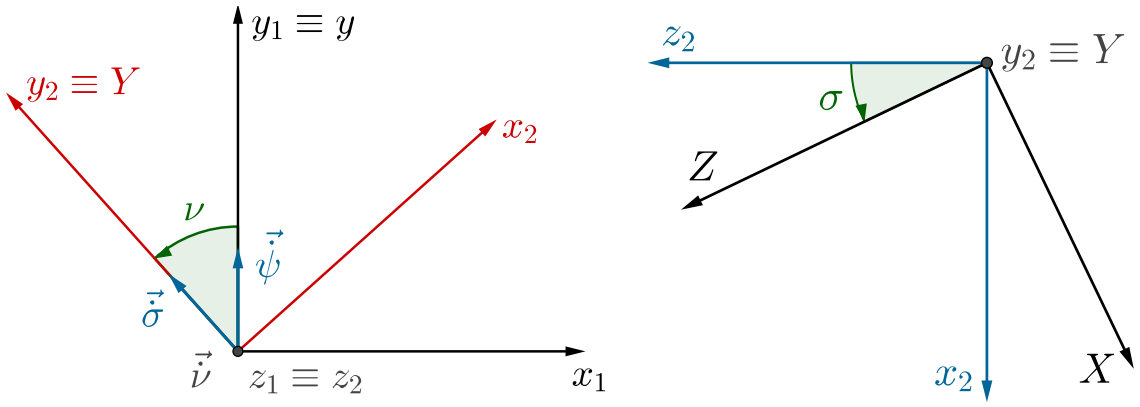
$$\delta\omega_X = \alpha_1\left[1 - \cos(\Omega t)\right], \tag{B.6a}$$
$$\delta\omega_Y = 0, \tag{B.6b}$$
$$\delta\omega_Z = \alpha_2\sin(\Omega t). \tag{B.6c}$$

The constants in these equations are

$$\alpha_1 = \frac{MR}{A\Omega}, \tag{B.7a}$$
$$\alpha_2 = \frac{M}{C\Omega}, \tag{B.7b}$$
$$\Omega = \omega_0\sqrt{(B/A - 1)(B/C - 1)}, \tag{B.7c}$$
$$R = \sqrt{\frac{A(B - C)}{C(B - A)}}. \tag{B.7d}$$

Furthermore, Ω is real, with the same sign of ω_0, since B is larger than the other principal moments of inertia.

As was mentioned before, New Horizons usually has its main antenna pointing towards Earth, during most of its journey. Defining the x axis of the non-rotating reference frame (x, y, z) to be directed away from Earth, to avoid Euler angle singularities (*i.e.* when precession and spin have the same direction), then the antenna is directed towards the negative x axis when the spacecraft is in the spin stabilised mode. With this the Euler angles can be successively constructed. Firstly, the precession, $\dot{\psi}$, is given by a rotation around the y axis, followed by the nutation, $\dot{\nu}$, as a rotation around a new z_1 axis. Finally the spin, $\dot{\sigma}$, comes from a rotation around the new $y_2 = Y$ axis. The sum of Euler angle frequencies is the angular velocity of the New Horizons, $\boldsymbol{\omega} = \dot{\boldsymbol{\psi}} + \dot{\boldsymbol{\nu}} + \dot{\boldsymbol{\sigma}}$. To have a better understanding of the rotations discussed, from an external observer point of view, the non-rotating reference frame with Euler angles is give in Figure B.1.



(a) *Nu rotation (ν), with z and $\dot{\nu}$ directed outwards.* **(b)** *Sigma rotation (σ), with Y directed outwards.*

Figure B.1 – *Transformation between the inertial reference frame (x, y, z) and the spacecraft's reference frame (X, Y, Z), using the Euler angles (ψ not shown) and frequencies.*

The Euler angle initial condition can be set to, without any loss of generality,

$$\psi(0) = 0, \qquad \nu(0) = \pi/2, \qquad \sigma(0) = 0. \tag{B.8}$$

For a small effect, ψ, $\dot{\psi}$, and $\dot{\nu}$ are also small, although the same cannot be said about σ, $\dot{\sigma}$, and $\nu \simeq \pi/2$. Combined with Equation (B.6), it is possible to define $\epsilon \ll 1 : \ \nu \equiv \frac{\pi}{2} - \epsilon \ \Rightarrow \ \sin\nu \simeq 1$, $\cos\nu \simeq \epsilon$. Consequently, the angular velocity can be approximated by

$$\delta\omega_X \simeq \dot{\psi}\cos\sigma - \dot{\nu}\sin\sigma, \tag{B.9a}$$

$$\omega_0 \simeq \dot{\psi}\epsilon + \dot{\sigma}, \tag{B.9b}$$

$$\delta\omega_Z \simeq \dot{\psi}\sin\sigma + \dot{\nu}\cos\sigma. \tag{B.9c}$$

Since ϵ and $\dot{\psi}$ are small enough to be neglected, and applying Equation (B.8) initial conditions, the solution for Equation (B.9b) is readily obtained,

$$\dot{\sigma} \simeq \omega_0 \quad \Rightarrow \quad \sigma(t) \simeq \omega_0 t. \tag{B.10}$$

With σ solved, the other variables, $\psi(t)$ and $\nu(t)$ in Equation (B.6) and Equation (B.8), can be computed using $\dot{\psi}$ and $\dot{\nu}$, which are obtained by inverting Equation (B.9a) and Equation (B.9c).

For the case $\Omega \neq \omega_0$, the solution is given by

$$\begin{aligned}\psi(t) = {} & \frac{(\alpha_1\Omega - \alpha_2\omega_0)\sin\Omega t\cos\omega_0 t}{\omega_0^2 - \Omega^2} \\ & + \frac{\left[\left(\frac{\alpha_1}{\omega_0}\right)(\omega_0^2 - \Omega^2) + (\alpha_2\Omega - \alpha_1\omega_0)\cos\Omega t\right]\sin\omega_o t}{\omega_0^2 - \Omega^2},\end{aligned} \tag{B.11a}$$

$$\begin{aligned}\nu(t) = {} & \frac{\left(\frac{\Omega}{\omega_0}\right)(\alpha_1\Omega - \alpha_2\omega_0)}{\omega_0^2 - \Omega^2} - \frac{(\alpha_1\Omega - \alpha_2\omega_0)\sin\Omega t\sin\omega_0 t}{\omega_0^2 - \Omega^2} \\ & + \frac{\left[\left(\frac{\alpha_1}{\omega_0}\right)(\omega_0^2 - \Omega^2) + (\alpha_2\Omega - \alpha_1\omega_0)\cos\Omega t\right]\cos\omega_0 t}{\omega_0^2 - \Omega^2}.\end{aligned} \tag{B.11b}$$

Whereas for $\Omega = \omega_0$ the condition

$$\sqrt{(B/A - 1)(B/C - 1)} = 1 \;\Leftrightarrow\; B = A + C, \tag{B.12}$$

is observed, which in turn implies that $R = \frac{A}{C}$ and $\alpha_1 = \alpha_2 = \frac{M}{C\omega_0}$. Using this the obtained solution is much simpler,

$$\psi(t) = \frac{\alpha_1}{2\omega_0}(2\sin\omega_0 t - \sin 2\omega_0 t) \tag{B.13a}$$

$$\nu(t) = \frac{\alpha_1}{\omega_0}(\sin^2\omega_0 t - 1 + \cos\omega_0 t). \tag{B.13b}$$

This solution does not reveal any resonance effect, as was expected, because it translates the gyroscopic stabilisation effect (which does not have any resonance component).

The general solution for the spin stabilised case, is thus either Equation (B.11) or Equation (B.13), together with Equation (B.10), depending on whether $B \neq A + C$ or $B = A + C$. Since the moment applied, M (Equation (B.1)), is expected to be small, the Euler angles ψ and ν also remain small, which validates the approximations used.

